Coherent Electric Field Control of Spin Systems for Quantum Technologies

Niccolò Fontana

St Edmund Hall

University of Oxford

A thesis submitted for the degree of

DPhil in Condensed Matter Physics

Michaelmas Term, 2025

Supervised by Dr Junjie Liu and Professor Arzhang Ardavan

Abstract

Spin systems offer a versatile platform for exploring fundamental phenomena and developing quantum technologies. Conventional manipulation of spin states with magnetic fields faces intrinsic limitations, including crosstalk and poor nanoscale confinement. Electric fields, by contrast, can be precisely localised, potentially opening new routes for scalable spin control and device integration.

This thesis investigates the electric-field control in spin systems exhibiting spin-electric coupling (SEC) and its relevance to quantum information and sensing. Chapter 2 presents a proof-of-concept electric-field quantum sensor based on an optically excited state in an organic molecular nanomagnet integrated into a capacitive device. Unlike conventional SEC that typically requires strong atomic spin-orbit coupling (SOC), the effect here arises from electric-field-induced redistribution of charge within the excited state. Notably, this mechanism yields a coupling strength comparable to that of SOC-driven systems, thus expanding the range of materials suitable for SEC studies.

In Chapter 3, we demonstrate the electric control of nuclear spins in magnetic defects within a semiconducting crystal. In this system, the electron-nuclear interaction, often suppressed in nuclear-spin qubits to preserve coherence, is harnessed to enhance nuclear SEC. The underlying mechanism relies on the electric field modulating the electron magnetic anisotropy, whose electric sensitivity is transferred to the nuclei via the hyperfine coupling. Using this approach, we were able to drive nuclear spin transitions using resonant electric fields. Building on these results, Chapter 4 investigates electrically driven electron transitions, proposing a resonator architecture for their investigation and analysing possible mechanisms that mediate them.

Finally, Chapter 5 explores the SEC in polyoxometalate molecular complexes and introduces strategies to generate and electrically control their clock transitions, that is, spin transitions whose energy is, to first order, independent of the magnetic field. We further propose a theoretical scheme for generating entanglement between two clock spins, marking a step toward the development of scalable multi-qubit platforms.

Taken together, the studies presented in this thesis advance spin-based quantum technologies by establishing a foundation for fully electrical control of spin systems.

"Your thesis has so many Greek characters, it looks like the Rosetta Stone."
Vittoria Lucchese, upon looking at this (Physics) DPhil thesis.

Acknowledgements

Before I began writing this thesis, the idea of producing 150-200 pages of (somewhat coherent) scientific content about my own work felt like preparing a long farewell message to my own sanity. The fact that I managed all this and am still standing is thanks to the support of my family, friends, and colleagues.

First and foremost, I would like to thank my two supervisors, Dr Junjie Liu and Professor Arzhang Ardavan. To Junjie, for the patience of a saint, his good humour, and above all his insight as an excellent experimental physicist. I was lucky to be his first (of what I believe will be many) DPhil student. If you are reading this as a student or PostDoc with Junjie, let me tell you, you are in good hands. To Arzhang, for his calm, thoughtful presence, something that balanced out my more erratic tendencies, and for his expertise and ideas that helped shape both this thesis and my next steps in life. Working with both has been a privilege.

During my time in Oxford, I had the pleasure of working with an amazing team. To Dr Gabriel Moise, without whose help with ESR equipment, lasers, DFTs and many other things, parts of this thesis would simply not exist. Another shout goes to Dr Sumin Lim and his great ideas in quantum information science. It is also thanks to you if I could put "for Quantum Technologies" in the title of this thesis. A person I cannot fail to mention is the (second) newest doctor in our group, Dr Mikhail V. Vaganov, whose scientific skills, programming expertise, and dedication helped me with most of the projects in this work. And lastly, to Soyoung Oh, a recent addition to the group, whose optimism and positive energy helped me push through the last months in the lab. I wish you a wonderful DPhil journey, and do not forget to enjoy the ride.

The engineering side of scientific research often goes unnoticed, yet behind any successful experiment there are always great technical staff. My gratitude goes to Dr William K. Myers, whose support in CAESR saved many otherwise doomed measurements, and to Mr Paul Pattinson, whose help in the cleanroom probably saved me from becoming permanently attached to the wire-bonder.

College life shapes much of the Oxford DPhil experience, and St Edmund "Teddy" Hall has been my refuge and my castle for the past four years. My thanks go to all the staff, especially Chery and Belinda, for the countless lovely lunches and for the wonderful Marston house where I lived for three years. Thanks also to Professor Carly Howett and Professor Jeffrey Tseng for giving me the opportunity to lecture and to be part of the SCR for a year. It was an honour and a joy.

To my dearest rowing team, thank you for giving me something to look forward to outside the lab and for keeping me (relatively) sane. The frosty winter outings and the bumps races are memories I will hold close, as are all the friends I made there, especially Ioannis "Freddo Espresso" Spanos. *Hall, Hall, Hall!*

To my friends Luca, Giovanni, Filippo, Rattan, Natalie, Dana and many more, thank you for the good times, the support, and the laughs. Life would not be the same without you. Even if with some of you we do not see each other often, scattered across the world as we are, I know I can count on you, and for that I am grateful.

Language switch!

A papà e mamma, per tutto quello che mi avete dato in questi anni, per aver condiviso con me i momenti bui, di insicurezza e di paura. Questa è anche una vittoria vostra. Da Belgioioso al mondo, non ci sono confini. E ovviamente ai nonni e agli zii, che mi hanno sempre voluto bene. Grazie.

L'ultimo e più importante ringraziamento va a Vittoria Lucchese, la mia fidanzata, che ha vissuto accanto a me ogni alto e basso di questo dottorato e di questa tesi con una pazienza e un affetto che non dimenticherò mai. A te dedico questo lavoro, per quanto posso. Non vedo l'ora di vivere con te tutte le avventure che ci aspettano. Grazie di cuore, Vicky.

Contents

Abbreviations

CT	Clock Transition
CTr	Charge-Transfer State
cw	Continuous Wave
DFT	Density Functional Theory
EDFS	Echo Detected Field Sweep
EDSR	Electric Dipole Spin Resonance
EFG	Electric Field Gradient
ENCT	Electro-Nuclear Coherence Transfer
ENDOR	Electron Nuclear Double Resonance
ESR	Electron Spin Resonance
mw	Microwave Radiation
NER	Nuclear Electric Resonance
NMR	Nuclear Magnetic Resonance
QIS	Quantum Information Science
rf	Radio-frequency Radiation
SE	Spin Echo
SEC	Spin-Electric Coupling
SNR	Signal-to-Noise Ratio
SOC	(Atomic) Spin-Orbit Coupling
SSC	Spin-Spin Coupling
ZFS	Zero-Field Splitting

1 Introduction

1.1 Magnetic Resonance

Electron Spin Resonance (ESR) and *Nuclear Magnetic Resonance* (NMR) are the primary experimental techniques explored in this thesis. The following section presents classical and quantum-mechanical descriptions of magnetic resonance, and highlights key experimental considerations. This discussion draws primarily from Ref. [1].

1.1.1 Classical Treatment

In a paramagnetic material, the unpaired electrons tend to align with an applied static magnetic field $\mathbf{B}$. This can be pictured as a *magnetic torque* τ acting on the spins[1], formally expressed as the vector product between $\mathbf{B}$ and the induced magnetization, $\boldsymbol{\tau} = \mathbf{M} \times \mathbf{B}$. This torque can also be written as the time derivative of the (classical) angular momentum $\mathbf{L}$, namely $\boldsymbol{\tau} = \mathrm{d}\mathbf{L}/\mathrm{d}t = \gamma^{-1}\mathrm{d}\mathbf{M}/\mathrm{d}t$, where $\gamma = q/(2m)$ is the particle's gyromagnetic ratio. The magnetization dynamics can then be described by

$$\frac{\mathrm{d}\mathbf{M}}{\mathrm{d}t} = \gamma(\mathbf{M} \times \mathbf{B}), \tag{1.1}$$

[1]This simplified picture works in scenarios where we describe the *ensemble* dynamics (macroscopic magnetization), rather than *single spins*, where it breaks down.

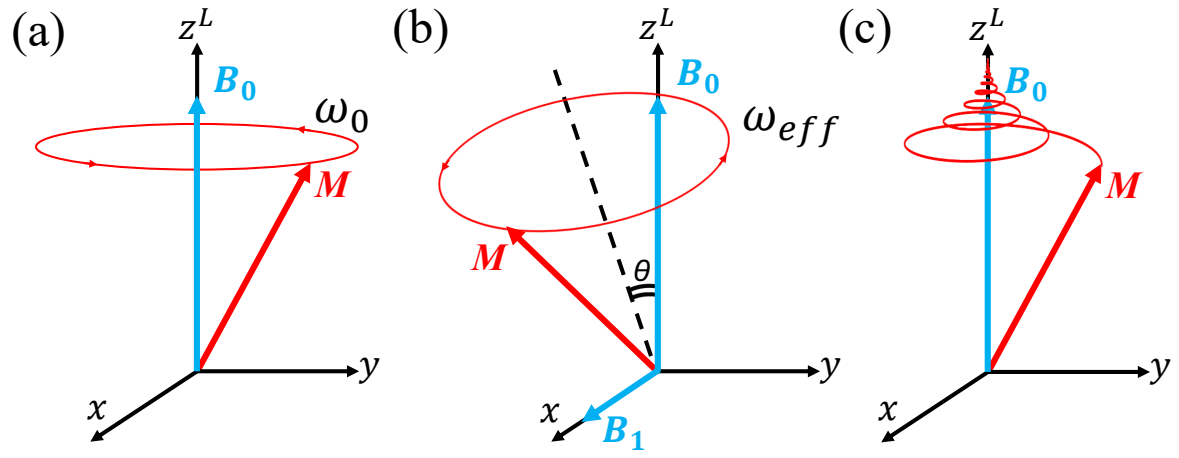

Figure 1.1: (a) Precession of the magnetization around the static magnetic field B_0, as described by the Bloch equation. In the laboratory frame, the oscillation frequency equals the Larmor frequency ω_0. (b) Applying an oscillating field B_1 at frequency ω_{mw} tilts the precession axis in the rotating B_1-frame by $\theta = \arctan(\Omega/(\omega_0 - \omega_{\mathrm{mw}}))$, where Ω is the Rabi frequency. (c) When relaxation processes are included, the magnetization relaxes towards its equilibrium orientation along B_0.

which is the vector form of the *Bloch equation*.

Applying a static[2] magnetic field B_0 to a paramagnetic sample causes the magnetization to precess about the field at a frequency $\omega_0 = \frac{g\,\mu\,B_0}{\hbar}$, known as the *Larmor frequency*. A pictorial representation of this precession is shown in Fig. 1.1(a). Next, consider applying a circularly polarised, time-varying magnetic field $\mathbf{B}_1 = B_1\,(\cos(\omega_{\mathrm{mw}}t),\,\sin(\omega_{\mathrm{mw}}t),\,0)^\top$ in the $\{x, y\}$ plane of the laboratory frame[3], where ω_{mw} denotes the microwave radiation frequency. Transforming to a frame co-rotating with $\mathbf{B}_1$ simplifies the solutions to Eq. 1.1 as follows:

$$\frac{\mathrm{d}M_x}{\mathrm{d}t} = -\Delta\omega\,M_y, \quad \frac{\mathrm{d}M_y}{\mathrm{d}t} = \Delta\omega\,M_x - \Omega\,M_z, \quad \frac{\mathrm{d}M_z}{\mathrm{d}t} = \Omega\,M_y, \tag{1.2}$$

where $\Delta\omega = \omega_0 - \omega_{\mathrm{mw}}$ is the difference between the system's natural and driving frequencies, or *detuning*, while Ω is the *Rabi frequency*, defined in direct analogy to the Larmor frequency, with B_1 replacing B_0, and describing the strength of the excitation. In the absence of a driving field, the magnetization simply precesses about the z-axis at the

[2]Throughout this thesis, the standard ESR convention is used: B_0 denotes the static magnetic field, while B_1 and B_2 represent the microwave (mw) and radio-frequency (rf) fields for electron and nuclear manipulation, respectively.

[3]By convention, the z-axis of the laboratory frame is aligned with B_0.

detuning frequency $\Delta\omega$. Once the drive is applied, however, the magnetization precesses about an *effective* magnetic field whose components are given by the off-resonance term $\Delta\omega$ and the drive term Ω. The tilt angle of this effective field is $\theta = \tan^{-1}(\Omega/\Delta\omega)$ (see Fig. 1.1(b)), and the corresponding precession frequency is given by

$$\omega_{\text{eff}} = \sqrt{\Omega^2 + \Delta\omega^2}. \tag{1.3}$$

When on resonance ($\Delta\omega = 0$), $\mathbf{M}$ precesses about an axis in the $\{x', y'\}$ (rotating-frame) plane ($\theta = 90°$). Driving the system at the Larmor frequency thus enables rotation of the overall magnetization, a key feature for both *resonance* and *detection* in magnetic resonance (see Subsec. 1.1.3).

To complete the classical picture, we must also account for *relaxation processes*, through which the magnetization returns toward its equilibrium value along B_0. While the microscopic origin is quantum-mechanical (Subsec. 1.1.4), we can model relaxation phenomenologically by adding exponential damping terms to Eq. 1.1, yielding:

$$\frac{\mathrm{d}\mathbf{M}}{\mathrm{d}t} = \gamma\left(\mathbf{M} \times \mathbf{B}\right) - \frac{M_x(t)\hat{x} + M_y(t)\hat{y}}{T_2} - \frac{(M_z(t) - M_z(0))\hat{z}}{T_1}. \tag{1.4}$$

Here, T_1 and T_2 are the longitudinal and transverse relaxation times, respectively, describing the recovery of M_z towards equilibrium along B_0 and the decay of the magnetization in the $\{x, y\}$ plane.

1.1.2 Introducing Quantum Mechanics: the Electron and Nuclear Spin Hamiltonian

While useful for building intuition, this classical model is insufficient to describe the experiments presented in this thesis. In magnetic resonance and quantum information science [2], it is often more convenient to represent spin states and their evolution on the *Bloch sphere*, illustrated in Fig. 1.2 for $S = \frac{1}{2}$. For *pure states*, the state vector $|\psi\rangle$ is represented by a unit vector pointing from the origin to a point on the surface of the Bloch sphere[4], and can be parameterised using spherical coordinates (θ, ϕ) and

[4]Pure states are distinguished from *mixed states*, which represent statistical ensembles of pure states. Mixed states are described by Bloch vectors with norm $||\vec{r}|| < 1$, i.e., they lie *inside* the Bloch sphere. For more details, see Subsec. 1.1.5.1.

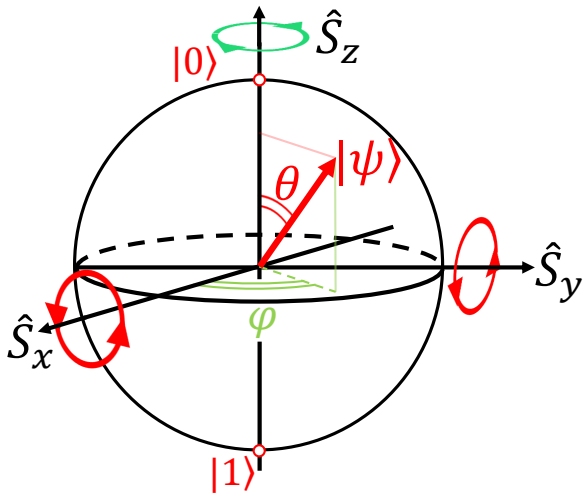

Figure 1.2: Schematic representation of the Bloch sphere for a simple two-level ($S = 1/2$) system. The *poles* of the sphere correspond to the computational basis states $\{|0\rangle, |1\rangle\}$, and any point on the sphere represents a superposition state $|\psi\rangle$. Applying a microwave magnetic pulse generates a rotation about $\hat{S}_x$ or $\hat{S}_y$, depending on the field polarization, with the pulse power and duration setting the rotation angle. Under certain conditions, discussed in Sec. 1.2, applying a DC electric-field pulse produces a rotation about the $\hat{S}_z$ axis (green).

a global phase γ, as $|\psi\rangle = e^{i\gamma}\left(\cos\theta\ |0\rangle + e^{i\phi}\sin\theta\ |1\rangle\right)$. Since the global phase factor $e^{i\gamma}$ has no measurable effect, it can be omitted, yielding

$$|\psi\rangle = \cos\theta\ |0\rangle + e^{i\phi}\sin\theta\ |1\rangle\,. \tag{1.5}$$

The corresponding spin operators, or *Pauli operators*, have eigenvalues corresponding to spin projections along the Cartesian axes $\{x, y, z\}$, where z is conventionally aligned with the applied static magnetic field B_0. Mathematically, they are described by

$$\hat{S}_x = \frac{\hbar}{2}\begin{pmatrix} 0 & 1 \\ 1 & 0 \end{pmatrix}, \quad \hat{S}_y = \frac{\hbar}{2}\begin{pmatrix} 0 & -i \\ i & 0 \end{pmatrix}, \quad \hat{S}_z = \frac{\hbar}{2}\begin{pmatrix} 1 & 0 \\ 0 & -1 \end{pmatrix}. \tag{1.6}$$

These Hermitian and unitary matrices satisfy the angular momentum commutation relations

$$[\hat{S}_i, \hat{S}_j] = i\hbar\,\epsilon_{ijk}\,\hat{S}_k, \tag{1.7}$$

where ϵ_{ijk} is the Levi-Civita symbol.

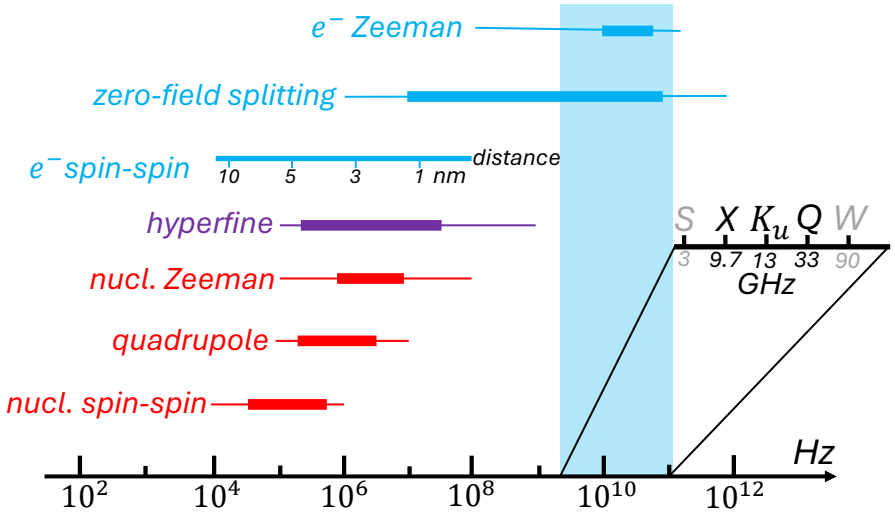

Figure 1.3: Energy scales (in Hz) of the electron (blue), nuclear (red), and hyperfine (purple) terms from Eq. 1.10. The close-up on the right shows typical ESR frequency bands, as well as K_u, which is relevant for Chapter 4. This figure has been adapted from Ref. [1].

Exponentiating the Pauli matrices generates unitary evolution operators of the form

$$U(\hat{n}, \alpha) = e^{-i\,\alpha\,\hat{\mathbf{S}}\cdot\hat{n}/\hbar}, \tag{1.8}$$

where $U(\hat{n}, \alpha)$ rotates the quantum state $|\psi\rangle$ by an angle α about the axis $\hat{n}$. In magnetic resonance, such rotations are typically implemented using oscillating magnetic fields that are resonant with the spin transition frequency. The rotation axis $\hat{n}$ is determined by the orientation and polarization of the applied field B_1, while the rotation angle α depends on both the pulse amplitude and duration. These fields commonly induce rotations about $\hat{S}_x$ or $\hat{S}_y$, as illustrated by red circular arrows in Fig. 1.2. Under certain conditions, rotations about $\hat{S}_z$, which corresponds to a relative phase accumulation φ (green arrow), can also be induced by static *electric* fields, as detailed in the discussion provided in Sec. 1.2.

In much of this thesis, we consider systems with total spin quantum number $S \geq 1$, having $2S+1$ sublevels with projections $m_s = -S, -S+1, \ldots, +S$. The spin operators generalise from Eq. 1.6 to

$$\begin{aligned} \langle m_s|\hat{S}_{x,y}|m_s'\rangle &= \frac{\hbar}{2}\left(\delta_{m_s,m_s'+1} \pm \delta_{m_s',m_s+1}\right)\sqrt{S(S+1) - m_s m_s'}, \\ \langle m_s|\hat{S}_z|m_s'\rangle &= \hbar\,\delta_{m_s,m_s'}\,m_s, \end{aligned} \tag{1.9}$$

where $\hat{S}_{x,y}$ couple states $|m_s\rangle \leftrightarrow |m_s \pm 1\rangle$ and $\hat{S}_z$ is diagonal. Also useful in magnetic resonance (Subsec. 1.1.3) are the *ladder operators*, $\hat{S}_\pm = \hat{S}_x \pm i\hat{S}_y$, which satisfy $\hat{S}_\pm|m_s\rangle = \sqrt{S(S+1) - m_s(m_s \pm 1)}\,|m_s \pm 1\rangle$.

We can now introduce the central mathematical object for most theoretical and experimental work in this thesis: the *Hamiltonian*, $\hat{\mathcal{H}}$, which encodes the total energy of the system. The general spin Hamiltonian for n electrons and m nuclei was first derived by Abragam and Pryce [3] to be:

$$\hat{\mathcal{H}} = \mu_B \sum_k^n \mathbf{B}_0^\top \cdot \mathbf{g}_{e,k} \cdot \hat{\mathbf{S}}_k + \sum_{\substack{k \\ S_k > 1/2}} \hat{\mathbf{S}}_k^\top \cdot \mathbf{D} \cdot \hat{\mathbf{S}}_k + \mu_N \sum_k^m \mathbf{B}_0^\top \cdot \mathbf{g}_{N,k} \cdot \hat{\mathbf{I}}_k + \sum_k \hat{\mathbf{S}}^\top \cdot \mathbf{A}_k \cdot \hat{\mathbf{I}}_k$$
$$+ \sum_{\substack{k \\ I_k > 1/2}}^m \hat{\mathbf{I}}_k^\top \cdot \mathbf{Q}_k \cdot \hat{\mathbf{I}}_k + \sum_{\substack{i,k \\ i \neq k}} \hat{\mathbf{I}}_i^\top \cdot \mathbf{d}_N^{(i,k)} \cdot \hat{\mathbf{I}}_k + \sum_{\substack{i,k \\ i \neq k}} \hat{\mathbf{S}}_i^\top \cdot \mathbf{d}_e^{(i,k)} \cdot \hat{\mathbf{S}}_k. \tag{1.10}$$

The physical origin of each term will be outlined in the next subsections. Here, $\hat{I}$ denotes nuclear spin operators and follows the same structure as $\hat{S}$, while $\hat{\mathbf{S}} = (\hat{S}_x, \hat{S}_y, \hat{S}_z)^\top$ is the vector of spin matrices. The $\prod_{k=1}^n \prod_{j=1}^m (2S_k + 1)(2I_j + 1)$ eigenstates and eigenvalues of $\hat{\mathcal{H}}$ correspond to the electron-nuclear spin states $|\psi\rangle$ and their associated energies. This equation is sometimes referred to as the *effective spin Hamiltonian*, which captures the spin interactions that influence the energy levels of a paramagnetic system in the presence of external magnetic fields and spin-spin interactions. The typical energy scales of each of the terms in Eq. 1.10 are schematically illustrated in Fig. 1.3, alongside representative excitation microwave bands relevant to ESR and this work.

1.1.2.1 Electron and Nuclear Zeeman Splitting

The coupling between spins and an external static magnetic field $\mathbf{B_0}$ is described by the *Zeeman interaction*. The presence of $\mathbf{B_0}$ lifts the *degeneracy* between spin states related by time-reversal symmetry. Following Eq. 1.10, the Zeeman Hamiltonian for n electrons and m nuclei is generally given by

$$\hat{\mathcal{H}}_B = \mu_B \sum_k^n \mathbf{B}_0^\top \cdot \mathbf{g}_{e,k} \cdot \hat{\mathbf{S}}_k + \mu_N \sum_k^m \mathbf{B}_0^\top \cdot \mathbf{g}_{N,k} \cdot \hat{\mathbf{I}}_k, \tag{1.11}$$

where $\mu_B = e\hbar/(2m_e)$ and μ_N are the *Bohr magnetons* for electrons and nuclei, respectively. Since μ_B is roughly three orders of magnitude larger than μ_N, NMR typically takes place

at MHz frequencies, while ESR lies in the GHz range (see Fig. 1.3). This difference in energy scales will be important in Chapter 3.

The g-factor in Eq. 1.11 is a dimensionless relativistic correction to the Zeeman interaction. It is generally a symmetric tensor ($g_{ij} = g_{ji}$) with six independent parameters. In most cases, however, its principal axes are taken to coincide with the molecular or crystal axes, although this is not universally true [4]. For example, in cubic-symmetry environments the g-tensor is isotropic, with $g_{xx} = g_{yy} = g_{zz}$. Lowering the symmetry to axial geometry introduces anisotropy such that $g_{xx} = g_{yy} \neq g_{zz}$, while in orthorhombic environments all three components differ, $g_{xx} \neq g_{yy} \neq g_{zz}$. The reference values for the free-electron g-factor[5] is $g_e \simeq 2.0023$, whereas nuclear g-factors span a much wider range, from 0.097 for ^{191}Ir to 5.58 for ^{1}H [1].

In addition to environmental symmetry, another important contribution to the g-factor comes from the *spin-orbit coupling* (SOC)[6], the relativistic interaction between an electron's spin and its motion in the electrostatic potential of the nucleus. This interaction can be expressed as the dot product between the *orbital* angular momentum $\gamma\hat{\mathbf{L}}$ and $\hat{\mathbf{S}}$, i.e., $\hat{\mathcal{H}}_{\mathrm{SOC}} = \lambda\,\hat{\mathbf{L}}\cdot\hat{\mathbf{S}}$, where the SOC constant $\lambda \propto Z^4$, with Z being the atomic number [5]. The SOC-corrected g-factor is

$$\mathbf{g} = g_e\,\mathbb{I} + 2\lambda\,\mathbf{\Lambda}, \tag{1.12}$$

where $\mathbf{\Lambda}$ is a symmetric tensor describing the second-order orbital correction to the energy levels, defined in Eq. A.5; a full derivation of Eq. 1.12 is given in App. A.1.1. This SOC contribution can be substantial in certain systems, particularly in lanthanide- and actinide-based compounds, where it can even drive g to negative values [6].

[5]The Dirac equation predicts $g = 2$, but higher-order quantum electrodynamics corrections give $g = 2\,(1+\alpha/2\pi+\dots)$, where $\alpha = e^2/(4\pi\varepsilon_0\hbar c)$ is the fine-structure constant. At X-band, this corresponds to a resonant-magnetic-field deviation of ~ 4 G, which is measurable with standard techniques but often negligible.

[6]This refers to the *atomic* spin-orbit coupling, which arises from localised (spin) states. It is distinct from the SOC observed in systems such as a two-dimensional degenerate electron gas, where the SOC involves k-dependent dispersion of delocalised, band-like electrons. Unless otherwise specified, all mentions of SOC throughout this thesis refer to the atomic type.

1.1.2.2 Zero-field Splitting

For systems with $S \geq 1$, electron-electron interactions lift the $(2S+1)$-fold degeneracy of the ground state. A useful heuristic picture is that each electron experiences the magnetic field produced by the others; thus, even in the absence of an external static field, a *pseudo*-Zeeman interaction acts on each electron. This effect is known as the *zero-field splitting* (ZFS). It is important to note that ZFS refers to the *intra-site* coupling between electrons within the same ion or molecule. This is fundamentally distinct (and subject to different physical constraints) from the *inter-site* interactions between electrons belonging to different systems (see Subsec. 1.1.2.5). Mathematically, the ZFS for n spectroscopically distinguishable systems[7] is described by

$$\hat{\mathcal{H}}_{\mathrm{ZFS}} = \sum_{k=1}^{n} \hat{\mathbf{S}}_k^T \cdot \mathbf{D} \cdot \hat{\mathbf{S}}_k, \tag{1.13}$$

where each term $\hat{\mathbf{S}}_k^T \cdot \mathbf{D} \cdot \hat{\mathbf{S}}_k$ represents the interaction between the $2S$ electrons within the k-th ion or molecule.

The tensor $\mathbf{D}$, which is symmetric and traceless[8], can be expressed in its principal-axis frame, and, neglecting the sum over different systems, Eq. 1.13 then reduces to

$$\hat{\mathcal{H}}_{\mathrm{ZFS}} = D_x \hat{S}_x^2 + D_y \hat{S}_y^2 + D_z \hat{S}_z^2 = D\left(\hat{S}_z^2 - \tfrac{1}{3}S(S+1)\right) + E\left(\hat{S}_x^2 - \hat{S}_y^2\right), \tag{1.14}$$

where $D = \frac{3}{2}D_z$ is the *axial* anisotropy and $E = (D_x - D_y)/2$ is the *transverse* component. Unless otherwise stated, both D and E will be treated as scalars, given in units of MHz.

The ZFS tensor has two main contributions:

$$\mathbf{D} = \mathbf{D}^{\mathrm{SSC}} + \mathbf{D}^{\mathrm{SOC}}, \tag{1.15}$$

where $\mathbf{D}^{\mathrm{SSC}}$ arises from first-order dipolar spin-spin coupling (SSC), and $\mathbf{D}^{\mathrm{SOC}}$ originates from second-order SOC. The SSC term dominates when SOC is weak, as in organic molecules and many light transition-metal complexes, while the SOC contribution becomes

[7] Here, "distinguishable" refers to molecules having different ZFS tensors and/or different spin quantum number.

[8] By magnetic-resonance convention, $\mathrm{Tr}(\mathbf{T}) = T_{xx} + T_{yy} + T_{zz} = 0$, which is achieved by subtracting $\frac{1}{3}\mathrm{Tr}(\mathbf{T})$ from each diagonal component. This procedure shifts all energy levels by the same constant, producing no measurable effect.

significant in heavy-metal compounds [7]. This distinction will be central in Chapter 2. The SSC can be expressed analogously to a classical magnetic dipole-dipole interaction. For two electrons i and j ($i \neq j$), the contribution is

$$\left(\mathbf{D}^{\mathrm{SSC}}\right)_{ij} = \frac{\mu_0 g_e^2 \mu_B^2}{4\pi\hbar|\mathbf{r}_{ij}|^3}\left[\hat{\mathbf{S}}_i^T \cdot \hat{\mathbf{S}}_j - \frac{3}{|\mathbf{r}_{ij}|^2}\left(\hat{\mathbf{S}}_i^T \cdot \mathbf{r}_{ij}\right)\left(\hat{\mathbf{S}}_j^T \cdot \mathbf{r}_{ij}\right)\right], \tag{1.16}$$

where $\mathbf{r}_{ij}$ is the displacement vector from spin j to i. On the other hand, the SOC contribution can be obtained using the same second-order perturbation theory employed for the SOC correction to the g-factor (App. A.1.1):

$$\mathbf{D}^{\mathrm{SOC}} = \lambda^2 \mathbf{\Lambda}, \tag{1.17}$$

where λ and $\mathbf{\Lambda}$ are defined as in the previous subsection.

1.1.2.3 Hyperfine Coupling

The *hyperfine* interaction describes the coupling between electron and nuclear spins, and constitutes one of the most important sources of information in ESR spectroscopy [8]; see Sec. 1.1.5 for more details. For a system with m nuclei, the general Hamiltonian reads

$$\hat{\mathcal{H}}_{hf} = \sum_k^m \hat{\mathbf{S}}^\top \cdot \mathbf{A}_k \cdot \hat{\mathbf{I}}_k, \tag{1.18}$$

where $\mathbf{A}_k$ is the hyperfine tensor coupling the general $2S+1$ electron spin operator $\hat{\mathbf{S}}$ to the k^{th} nucleus. Analogously to the ZFS case, $\mathbf{A}$ can be decomposed into a quantum-mechanical and a semi-classical dipole-dipole interaction

$$\mathbf{A} = A_{\mathrm{iso}}\,\mathbb{I} + \frac{\mathbf{g}\,\mathbf{T}}{g_e}, \tag{1.19}$$

where A_{iso} is the *Fermi contact interaction* [9], and the second term accounts for the anisotropic dipole-dipole coupling. $\mathbf{T}_{ij}$ is defined analogously to Eq. 1.16, and $\mathbf{g}$ is the SOC-corrected g-factor from Eq. 1.12. The SOC contribution to the hyperfine tensor follows from the orbital-nuclear interaction, $\hat{\mathcal{H}}_{LI} \sim \hat{\mathbf{L}} \cdot \hat{\mathbf{I}}$, which has the same structure as the electron SOC Hamiltonian. By analogy, one finds that $\mathbf{A}^{\mathrm{SOC}} \sim 2\lambda\,\mathbf{\Lambda}$ [1].

The Fermi contact term accounts for the *isotropic* part of the hyperfine interaction and arises from the quantum-mechanical limit of the dipole-dipole interaction, in which the

electron and nucleus are spatially coincident. Physically, it reflects the overlap of the electron and nuclear wavefunctions and is nonzero only for states with finite probability density at the nucleus (notably s-orbitals). The isotropic constant is then given by

$$A_{\text{iso}} = \frac{2\mu_0}{3\hbar}\, g_e\mu_B\, g_N\mu_N\, |\psi_e(0)|^2, \tag{1.20}$$

where $|\psi_e(0)|^2$ is the electron spin density at the nucleus. For isotopes of the same element[9], the ratio of A_{iso} values should scale with the ratio of their nuclear g-factors. This holds for most systems, although small deviations ($\lesssim 1\%$ [10]) can occur due to differences in nuclear charge distribution (finite size or shape), which slightly modify $|\psi_e(0)|^2$ at the nucleus. Such deviations are known as the *hyperfine anomaly*, or Bohr-Weisskopf effect [11].

1.1.2.4 Quadrupolar Coupling

For nuclei with spin $I \geq 1$, the charge distribution is non-spherical and gives rise to a *quadrupolar* contribution to the ESR Hamiltonian. This interaction is characterised by the nuclear electric quadrupole moment Q. For m nuclei, the corresponding Hamiltonian is

$$\hat{\mathcal{H}}_{NQ} = \sum_{k=1}^{m} \hat{\mathbf{I}}_k^T \cdot \mathbf{Q} \cdot \hat{\mathbf{I}}_k, \tag{1.21}$$

where $\mathbf{Q}$ is the quadrupolar coupling tensor. In its principal-axis system (and neglecting the summation over k), this reduces to

$$\hat{\mathcal{H}}_{NQ} = Q_x\hat{I}_x^2 + Q_y\hat{I}_y^2 + Q_z\hat{I}_z^2 = \frac{eQ\,V}{4I(2I-1)\hbar}\left[3\hat{I}_z^2 - I(I+1) + \eta\left(\hat{I}_x^2 - \hat{I}_y^2\right)\right], \tag{1.22}$$

where $\eta = (Q_x - Q_y)/Q_z$ is the asymmetry parameter ($0 \leq \eta \leq 1$), $V = (\nabla\mathbf{E})_{\max}$ is the principal component of the electric field gradient (EFG), and by convention $|Q_x| \leq |Q_y| \leq |Q_z|$. The EFG has contributions from both the surrounding electronic distribution and other nuclei. Although often negligible in many spin Hamiltonians, the quadrupolar term will play a central role in the experiment described in Chapter 3.

[9] Typically differing in g_N while sharing the same electronic configuration.

1.1.2.5 Inter-site Spin-spin Couplings

The interaction between electron spin centres located on different molecules or crystal sites (or nuclear spins on separate sites) may have different physical origins from the electron ZFS. As in earlier terms of the Hamiltonian, there are two contributions: a magnetic dipole-dipole interaction (analogous to Eq. 1.16) and a quantum-mechanical term known as the *exchange interaction*. The latter is described by the Heisenberg Hamiltonian,

$$\hat{\mathcal{H}}_{\text{exch}} = \hat{\mathbf{S}}_1^T \cdot \mathbf{J} \cdot \hat{\mathbf{S}}_2, \tag{1.23}$$

where indices 1 and 2 denote two distinct sites, and $\mathbf{J}$ is the exchange tensor (often called the J-coupling in ESR literature). Unlike in Eq. 1.13, one may have $S_1 \neq S_2$.

The exchange tensor $\mathbf{J}$ can be decomposed into an isotropic and an anisotropic component. The isotropic part, often described in terms of chemical bonding between two J-coupled $S = \frac{1}{2}$ electrons, dictates whether the ground state is a singlet (antiferromagnetic) or a triplet (ferromagnetic). The anisotropic part, by contrast, originates from spin-orbit coupling and dipolar contributions, and accounts for deviations from purely isotropic exchange.

Such inter-site exchange interactions are of particular interest in quantum information science (see Chapter 5), as they provide a mechanism to couple spins located at different sites [12].

1.1.2.6 Crystal Field Effect: High-rank Stevens Operators

In Eq. 1.10, we neglected the interaction between the electronic spins and the surrounding molecular or crystalline environment, commonly referred to as the *crystal field* (CF), which might be significant in certain transition-metals and lanthanide-based compounds [13]. A simple approach to estimate such CF effects is to compute the total Coulomb potential energy $W_{CF} = \sum_{i \in e^-} \sum_{j \in \text{env}} \frac{q_i q_j}{|\mathbf{r}_i - \mathbf{r}_j|}$, where the sums run over the unpaired electrons and the charges in the surrounding environment, respectively. The specific form of W_{CF} depends on the symmetry of the environment.

The connection between W_{CF} (and, hence, the environment's symmetry) and the spin Hamiltonian was formalised by Stevens [14]. The key idea is that, within a degenerate

manifold[10] of $\hat{\mathbf{S}}^2$ eigenstates, spatial operators can be replaced by equivalent spin operators of matching tensor rank. For example, a second-order term like xy transforms as $\hat{S}_x\hat{S}_y + \hat{S}_y\hat{S}_x$. This correspondence leads to the *Stevens operator formalism*, in which the CF Hamiltonian is expressed as

$$\hat{\mathcal{H}}_{\mathrm{CF}} = \sum_{k=2,4,6} \sum_{q=-k}^{+k} B_k^q \, \hat{O}_k^q(\hat{\mathbf{S}}), \quad \hat{O}_k^q(\hat{\mathbf{S}}) \sim \hat{S}_z^{k-|q|} \cdot \hat{S}_\pm^{+|q|}, \tag{1.24}$$

where B_k^q are the CF parameters, and $\hat{O}_k^q$ are the q^{th} components of a rank-k spherical tensor operator[11]. The full expressions of these operators, as defined in Refs. [14, 15], are provided in Appendix A.1.3. As W_{CF} is a scalar and therefore even under time reversal, and since the operators $\hat{O}_k^q$ transform as $(-1)^k\hat{O}_k^q$, only even k values contribute to time-even scalars consistent with the crystal field potential. Higher orders ($k \geq 8$) are generally negligible[12]. Note that the CF parameters can be directly related to previously discussed anisotropies; for example, $D = 3B_2^0$ and $E = B_2^2$.

1.1.3 The Resonance Phenomenon

All the terms described above are static (time-independent) contributions to the Hamiltonian, determined by the symmetry of the system and the underlying electronic and nuclear interactions. In contrast, magnetic resonance relies on the coupling between the system and an *oscillating* electromagnetic field that is close to resonance with a specific spin transition. The general idea of resonance is that the energy of the applied radiation matches the energy gap between two levels in the sample. From a simple angular-momentum perspective, the radiation carries a quantum of angular momentum that is absorbed by the spin system, promoting it to an excited state.

The time-dependent component of the Hamiltonian, written in standard ESR form, is

$$\hat{\mathcal{H}}_1(t) = \mu_B \, \mathbf{B}_1^\top(t) \cdot \mathbf{g} \cdot \hat{\mathbf{S}}, \tag{1.25}$$

[10] Collection of quantum states that are energetically or structurally grouped together based on a shared property, e.g., m_s, or m_I.

[11] A rank-k spherical tensor operator transforms under rotations like a spherical harmonic Y_k^q, carrying $2k+1$ components labelled by $q \in [-k, k]$.

[12] The $k = 0$ term corresponds to a constant and is omitted.

where the oscillating field is taken as $\mathbf{B}_1(t) = B_1 \cos(\omega_{\mathrm{mw}} t)$. Here ω_{mw} is the microwave angular frequency and B_1 is the field amplitude, proportional to the applied power. For a spin placed in a static field B_0, choosing[13] $\mathbf{B}_0 = B_0 \hat{z}$ and assuming an isotropic g_e-factor yields

$$\hat{\mathcal{H}}(t) = \hat{\mathcal{H}}_0 + \hat{\mathcal{H}}_1(t) = \mu_B g_e \Big(B_0 \hat{S}_z + \mathbf{B}_1^{\top}(t) \cdot \hat{\mathbf{S}} \Big). \tag{1.26}$$

If the oscillating field $\mathbf{B}_1$ is aligned *parallel* to B_0, the Hamiltonian remains diagonal, and (within the static Zeeman basis) no transitions are driven, since the field does not couple different spin states[14]. In quantum mechanics, however, transitions may still be induced if the eigenstates are not pure Zeeman states but are mixed by other interactions. This regime is known as *parallel-mode* ESR, in contrast to the conventional case where $\mathbf{B}_1 \perp \mathbf{B_0}$ (so-called *perpendicular-mode* ESR). In this thesis, unless explicitly stated otherwise (see Chapter 4), we will consider the perpendicular-mode case, where $\mathbf{B}_1$ lies in the transverse plane.

This can also be understood in terms of ladder operators. If the oscillating field $\mathbf{B}_1(t)$ lies in the transverse $(\hat{x}, \hat{y})$ plane, then $\hat{\mathcal{H}}_1(t)$ contains terms proportional to $\hat{S}_{\pm}$, which connect neighbouring Zeeman states $|m_s\rangle \leftrightarrow |m_s \pm 1\rangle$. In other words, the standard ESR selection rule is $\Delta m_s = \pm 1$, and analogously for nuclear transitions ($\Delta m_I = \pm 1$). Part of this thesis also deals with transitions driven *electrically*, rather than magnetically (see Sec. 1.2). In that case, the selection rules may change: under specific conditions, higher-order transitions with $\Delta m_s \geq 2$ become allowed. For example, double-quantum transitions ($\Delta m = \pm 2$) in both electron and nuclear spins appear in this work, as shown in Eqs. 3.2 and 4.2.

So far we have described resonance qualitatively, without considering transition strengths. In general, the transition rate is determined by the *Fermi Golden Rule*, which gives the probability per unit time of a transition from an initial state $|\psi_i\rangle$ to a final $|\psi_f\rangle$:

$$\mathcal{C}_{i \to f} = \frac{2\pi}{\hbar} \left| \langle \psi_i | \, \hat{\mathcal{H}}_1(t) \, | \psi_f \rangle \right|^2 \rho(E_f), \tag{1.27}$$

[13] This convention is adopted so that the quantization axis matches the eigenstates of $\hat{S}_z$; otherwise, a basis transformation is required.

[14] Classically, this is analogous to Fig. 1.1(b): a field parallel to B_0 cannot tilt the magnetization away from the z-axis.

where $\rho(E_f)$ is the density of final states. The matrix element $|\langle\psi_i|\,\hat{\mathcal{H}}_1\,|\psi_f\rangle|^2$ shows how strongly the oscillating perturbation couples the two states; thus the transition probability depends on the symmetry of the states and the form of the driving field[15]. Another factor is the population difference between the two levels, which is determined by temperature. At thermal equilibrium, the occupation probabilities follow the Boltzmann factor $e^{-E_i/k_BT}/Z$, which assigns higher probability to lower-energy states[16].

The discussion so far implicitly assumed that the applied radiation is exactly resonant with the Larmor frequency of the system. In practice, radiation that is slightly detuned from resonance can still drive transitions. In the rotating frame of the microwave field B_1, the Hamiltonian becomes[17]

$$\tilde{\mathcal{H}}_1 = (\omega_0 - \omega_{\mathrm{mw}})\,\hat{S}_z + \Omega\,\hat{S}_x, \tag{1.28}$$

which is now time-independent. The detuning $(\omega_0 - \omega_{\mathrm{mw}})$ quantifies the mismatch between the radiation and the Larmor frequency, while Ω is the Rabi frequency (see Sec. 1.1.1). Equation 1.28, derived in App. A.1.2, shows that even if the oscillating field is transverse (e.g., along $\hat{x}$), a residual longitudinal term $\hat{S}_z$ remains whenever the drive is detuned.

Finally, Eq. 1.25 applies to purely electronic spin transitions. For transitions involving both electronic and nuclear spins (as in Subsec. 1.1.5.4) the oscillating-field Hamiltonian takes a slightly different form (assuming isotropic g-factors):

$$\hat{\mathcal{H}}_2(t) = \mathbf{B}_2(t)\cdot\left(-\mu_N g_N\,\hat{\mathbf{I}} + \mu_B g_e\,\hat{\mathbf{S}}\right) = \hat{\mathcal{H}}_1^{(I)}(t) + \hat{\mathcal{H}}_1^{(S)}(t), \tag{1.29}$$

where $\mathbf{B}_2(t)$ is the applied radio-frequency field. The minus sign in the first term reflects the definition of the gyromagnetic ratio, which depends on the particle's electric charge; as electrons and nuclei have opposite charges, their couplings to the field appear with opposite signs.

[15]Group-theoretically, the tensor product $\Gamma^i \otimes \Gamma^{\hat{\mathcal{H}}_1} \otimes \Gamma^f$ must contain the totally symmetric representation for the matrix element to be non-zero.

[16]Here e^{-E_i/k_BT} gives the relative thermal weight of state i, with the lower-energy level being exponentially more populated than the excited level. $Z = \sum_i e^{-E_i/k_BT}$ is the partition function that ensures proper normalization.

[17]This expression assumes the rotating-wave approximation. Under strong driving, this breaks down, and an additional frequency shift (called *Bloch-Siegert*) arises. In X-band ESR, however, this is typically only a few tens of kilohertz and thus is often neglected [1].

1.1.4 Relaxation Mechanism

In Eq. 1.4, we introduced the longitudinal (T_1) and transverse (T_2) relaxation times in the classical Bloch model. We now explain their physical origin from a quantum-mechanical perspective. Just as in the Bloch picture, relaxation leads to an exponential decay of the magnetization, i.e., $\exp(-t/T_1)$, and $\exp(-t/T_2)$.

T_1 relaxation refers to the process by which a spin ensemble returns to thermal equilibrium along the direction of the static magnetic field B_0. This process arises through interactions between the spin system and its surrounding environment, i.e., the lattice, and is therefore often called *spin-lattice relaxation*. In solid-state systems, this exchange is primarily mediated by *phonons*, the quantised vibrations of the crystal lattice, whereas in liquids it is driven by stochastic molecular motion. On its own, a pure electron spin couples only weakly to lattice vibrations. However, SOC can act as the mechanism connecting the spin to environmental fluctuations, providing the dominant pathway for T_1 relaxation in many systems [16].

Since a change in the longitudinal magnetization M_z requires changing the spin quantum number m_s (or m_I in nuclear spins), such transitions can only occur if energy is exchanged between the environment and the spin-system *via* absorption or emission of a phonon. The simplest phonon-driven relaxation mechanism is the *direct process*, in which a phonon with frequency equal to the Larmor frequency ω_0 is absorbed or emitted by the spin system. In that case, the relaxation rate scales approximately as $T_1^{-1} \propto T$, because the phonon population increases linearly with temperature in the high-temperature regime[18].

More efficient two-phonon processes are commonly dominant in ESR [17]. These involve the absorption of a (THz) phonon with frequency $\omega_{\text{phonon}} \gg \omega_0$, which excites the system to a short-lived intermediate state, followed by the emission of a second phonon

[18] $f[\text{GHz}] \simeq 20.84 \cdot T[\text{K}]$, which means that carrying out an experiment at 20 K (as typical in this thesis) corresponds to roughly 400 GHz, significantly larger than the frequency range of standard ESR. Thus, one usually has $k_B T \gg \hbar\omega_0$, justifying the high-temperature approximation.

with energy[19] $\omega_{\text{phonon}} \pm \omega_0$. If the intermediate state is *virtual*, the relaxation proceeds via the *Raman process*, for which the relaxation rate scales as $T_1^{-1} \propto T^n$ with $n = 7$ or 9, depending on whether the system is Kramers or non-Kramers. Otherwise, if a real intermediate level exists at an energy matching available phonons (e.g., due to strong ZFS splitting), the mechanism is termed *Orbach process*, characterised by $T_1^{-1} \propto \exp(-\Delta/k_B T)$, with Δ being the energy separation. Which mechanism dominates therefore depends strongly on temperature.

In contrast, transverse relaxation (T_2) does not require an exchange of energy with the environment; instead, it describes the loss of coherence between individual spin packets[20] in the ensemble. Even though no energy is transferred, lattice fluctuations can still indirectly shorten T_2, as any stochastic modulation of the local magnetic field disrupts the phase relationship among spins and leads to dephasing. Another more efficient dephasing mechanism is driven by spin-spin coupling, hence the name *spin-spin relaxation*. Two nearby spins can undergo a *flip-flop* process in which they exchange their spin orientation without changing the total energy. If the flip-flop rate is $1/T_{\uparrow\downarrow}$, then the total transverse relaxation rate becomes

$$\frac{1}{T_2} = \frac{1}{T_{\uparrow\downarrow}} + \frac{1}{2T_1}, \tag{1.30}$$

where the factor of 1/2 reflects that a flip-flop process between two spins contributes twice as much to the dephasing of the transverse magnetization as a single spin flip governed by T_1 [1]. This leads to the commonly observed inequality $T_2 \leq 2T_1$, found in both ESR and NMR experiments.

Experimentally, T_2 is often not measured directly, because additional dephasing mechanisms, as B_0-field inhomogeneities, contribute to an *effective* decay time T_2^*. If each spin packet experiences a slightly different static field, i.e. $B_0 \pm \delta B_0$, then its Larmor frequency differs by $\delta\omega$, and the ensemble phase spreads out across the Bloch sphere

[19]The improved efficiency can be explained using the *Debye model*. The phonon density of states increases quadratically with frequency up to a cut-off (Debye frequency). Since ω_0 is much smaller than typical phonon frequencies, the density of phonons resonant with the direct process is essentially zero, while the density at THz frequencies is much larger.

[20]Ensemble of spins experiencing the same time-average local field.

at different rates. As a result, $1/T_2^* = 1/T_2 + \gamma \cdot \delta B_0$, so that $T_2^* \leq T_2$. The value of T_2^* determines the linewidth[21] in cw ESR ($\Gamma^{\text{inh}} = 1/T_2^*$), as well as the decay of the free-induction signal in pulsed ESR (see Subsec. 1.1.5).

As described above, the transverse decay in many paramagnetic systems follows a single-exponential function, $\exp(-t/T_2)$. In certain molecular systems, however, the decay is more accurately modelled by introducing a stretch parameter $2 \leq \alpha \leq 3$, so that the relaxation follows $\exp(-(t/T_m)^\alpha)$. Here, T_m is referred to as the *phase-memory time*, and it coincides with T_2 only in the case $\alpha = 1$ [18, 19]. For example, in the molecular nanomagnet[22] discussed in Chapter 5, we find $\alpha \simeq 2.55$ (see Fig. 5.2(b)). This non-exponential behaviour is caused by local magnetic field fluctuations driven by nuclear spin flip-flop nearby the electron spin system, and becomes significant in nuclear-spin-rich environments [20].

1.1.5 Pulse Sequences

Magnetic resonance experiments can be performed in two basic modes: continuous-wave (cw) and pulsed operation. In cw mode, the sample is irradiated continuously, and the observable is the change in magnetization due to spin population differences at resonance (Sec. 1.5). While cw spectroscopy is widely used in chemistry and structural biology, it will play only a minor role in this thesis. Our focus instead lies on pulsed magnetic resonance, which is essential for quantum-information applications. In this mode, short electromagnetic pulses are used to rotate the spin state by a controllable angle; the pulse duration and amplitude determine the rotation angle (*flip angle*, see Fig. 1.2), while its polarization the rotation axis. Pulse sequences then allow coherent control and readout of the time-evolving quantum state, including phase information.

To describe pulsed experiments rigorously and to interpret time-domain signals, we now introduce one of the central mathematical tools in magnetic resonance and quantum

[21] Inhomogeneous broadening (finite T_2^*) arises from static or slowly varying spatial variations of the magnetic field or spin environment, whereas *homogeneous* broadening (finite T_2) originates from dynamic stochastic processes that cause irreversible dephasing, such as spin-spin, or spin-lattice interactions.

[22] A type of molecule that exhibits magnetic properties at the molecular level.

mechanics: the density matrix ρ. The practical implementation of both cw and pulsed techniques is discussed in Sec. 1.5.

1.1.5.1 Density Matrix & the Product Formalism

The density ρ generalises the wavefunction $|\psi\rangle$, and is defined as a Hermitian, positive semidefinite operator with unit trace[23]. Formally,

$$\rho = \sum_i p_i |\psi_i\rangle\langle\psi_i|, \tag{1.31}$$

where the probabilities $p_i \geq 0$ satisfy the normalization condition $\sum_i p_i = 1$. A quantum state is said to be *pure* if $\rho^2 = \rho$, and *mixed* if its purity, defined as $\mathrm{Tr}[\rho^2]$, is strictly less than one. Physically, pure states correspond to a single wavefunction, while mixed states represent statistical mixtures of multiple states, that is, linear combinations weighted by classical probabilities rather than quantum amplitudes. In ensemble techniques such as liquid-state NMR, one often works with so-called *pseudo-pure states* [21]. In these systems, the macroscopic ensemble remains globally mixed, but one energy level possesses a slight excess population[24].

The density matrix evolves under unitary dynamics as $\rho(t) = U(t)\,\rho(t_0)\,U^\dagger(t)$. A pulse of duration t, with Rabi frequency Ω (proportional to the field strength B_1), rotating about axis $\hat{\mathbf{n}}$ by angle $\theta = \Omega t$, is described by

$$U(\theta, \hat{\mathbf{n}}) = e^{-i\theta\,(\hat{\mathbf{S}}\cdot\hat{\mathbf{n}})}. \tag{1.32}$$

In the product-operator convention of Ref. [1] adopted here, the unitary transformation $e^{-i\phi B} A e^{i\phi B} = C$ is shortened as $A \xrightarrow{\phi B} C$.

The simplest pulsed experiment is the *free induction decay* (FID). The system initially sits at thermal equilibrium[25], $\rho \propto -\hat{S}_z$. A $\pi/2$ pulse in the transverse plane then rotates

[23] In ESR and NMR, it is often convenient to treat the density matrix as traceless by subtracting the identity (thermal equilibrium is then $\rho \propto -\hat{S}_z$); this does not affect the dynamics.

[24] The density matrix is defined as $\rho = (1-\epsilon)\frac{\mathbb{I}}{N} + \epsilon|\psi\rangle\langle\psi|$, where $\mathbb{I}/N$ is the represents the maximally mixed state, while $|\psi\rangle\langle\psi|$ is the desired pure quantum state, with $\epsilon \ll 1$ quantifying the small deviation from the mixed state.

[25] This approximation arises from $\rho \approx \frac{1}{2}(\mathbb{I} - \epsilon\,\hat{S}_z)$, where $\epsilon \propto g\mu B_0/k_B T \ll 1$.

the magnetization onto the equator of the Bloch sphere, after which it precesses at the Larmor frequency and decays due to dephasing. In the rotating frame of B_1, we then have

$$\rho_{\mathrm{eq}} \simeq -\hat{S}_z \xrightarrow{\pi/2\,\hat{S}_y} -\hat{S}_x, \tag{1.33}$$

assuming a perfectly on-resonance pulse. A non-zero ESR signal can now be detected, since the observable in magnetic resonance is the transverse magnetization, i.e., the expectation values $\langle \hat{S}_x \rangle$ and $\langle \hat{S}_y \rangle$. Only these transverse components induce a measurable oscillating voltage in the detection circuitry (see Eq. 1.48), making the FID a direct measure of coherent spin precession. If there is a detuning between the mw and the Larmor frequency ($\Delta\omega \neq 0$), then the state becomes time-dependent immediately after the pulse, oscillating as $\rho(t) \simeq \hat{S}_x \cos(\Delta\omega\, t) - \hat{S}_y \sin(\Delta\omega\, t)$, as directly obtained from Eq. 1.28.

However, such FID signals are strongly affected by *inhomogeneous* dephasing: the signal envelope decays as e^{-t/T_2^*} due to static field variations and spectral broadening across the ensemble. This limitation motivated the development of more complex pulse sequences, such as the Hahn echo, described next.

1.1.5.2 Hahn Echo Sequence

One of the most widely used pulse sequences is the *Hahn (or spin) echo*, first introduced by Hahn [22], and it remains one of the standard methods to probe spin *coherences*. The motivation is to overcome the limitations of the FID, whose signal decays with the inhomogeneous time T_2^* due to field inhomogeneities. This is accomplished by applying a second pulse, after a free-evolution interval τ, that rotates the magnetization by π. The sequence is illustrated schematically in the top panel of Fig. 1.4, alongside the corresponding time evolution of the magnetization in the transverse plane.

Assuming an $S = 1/2$ ensemble, after a non-selective $\pi/2$ pulse[26], the system is left to evolve freely under the static Hamiltonian $\hat{\mathcal{H}}_0 \simeq \hat{S}_z$. The free-evolution propagator is $U = e^{it\hat{\mathcal{H}}_0}$, corresponding to a phase rotation about the z-axis. Due to inhomogeneous broadening, each spin packet accumulates a slightly different phase during this time: after a delay τ, the i-th packet is rotated to $+\hat{S}_y \sin(\delta\omega_i^{\mathrm{inh}}\,\tau) + \hat{S}_x \cos(\delta\omega_i^{\mathrm{inh}}\,\tau)$, where

[26]The following discussion assumes hard pulses, i.e., non-selective with respect to resonance offsets.

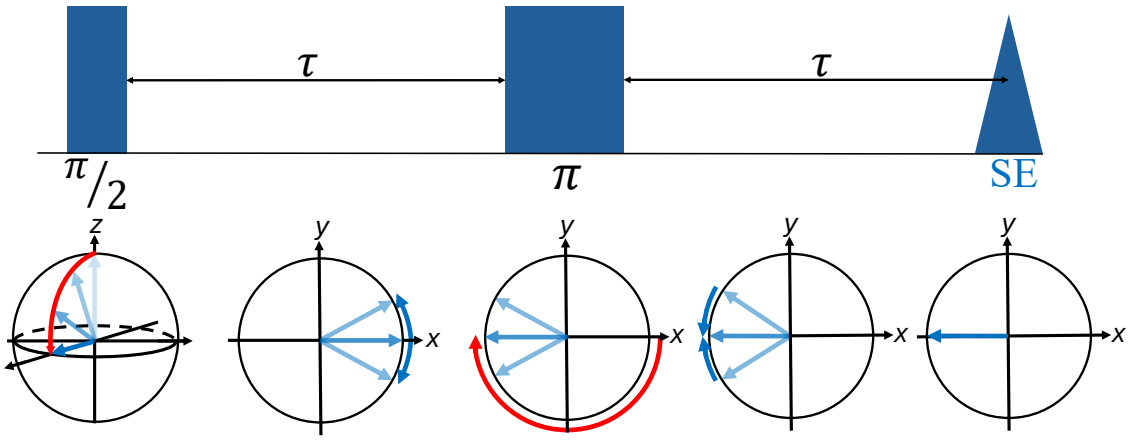

Figure 1.4: *Top:* The Hahn echo pulse sequence, consisting of a $\pi/2$ pulse that generates coherence between two states, followed by a refocusing π pulse, with an inter-pulse delay τ. *Bottom:* The evolution of spin packets (blue arrows) in the Bloch sphere representation for $S = 1/2$, illustrating the effects of the pulses (red arrows) and inhomogeneous broadening (blue curved arrows).

$\delta\omega_i^{\text{inh}}$ is the deviation from the mean Larmor frequency due to static field inhomogeneity. This is analogous to the FID dephasing process.

A subsequent π-pulse (e.g., along the y-axis) inverts the Bloch vector, resulting in $\hat{S}_y \sin(\delta\omega_i^{\text{inh}}\tau) - \hat{S}_x \cos(\delta\omega_i^{\text{inh}}\tau)$, i.e., each packet reverses its rotation. The density operator of packet i during the second free-evolution then becomes $\rho(t) = +\hat{S}_y \sin\Big(\delta\omega_i^{\text{inh}}(\tau - t)\Big) - \hat{S}_x \cos\Big(\delta\omega_i^{\text{inh}}(\tau - t)\Big)$. Notably, all packets rephase when $t = \tau$, that is, when the phase becomes independent of $\delta\omega_i^{\text{inh}}$. The resulting collective refocusing produces a signal at this time, referred hereafter to as spin echo (SE).

Contrary to the FID, the Hahn echo sequence refocuses phase accumulation caused by inhomogeneous broadening. As a result, the signal decay is now limited by the longer coherence time T_2, rather than by T_2^*; see Subsec. 1.1.4. In practice, one can measure T_2 by varying the inter-pulse delay τ in the echo sequence and recording how the echo amplitude decays. This makes the Hahn echo a central tool for magnetic resonance, which will be used extensively throughout this thesis.

Building on the basic echo, the *echo-detected field sweep* (EDFS) is performed by applying the Hahn echo sequence at a fixed microwave frequency and τ while sweeping the static

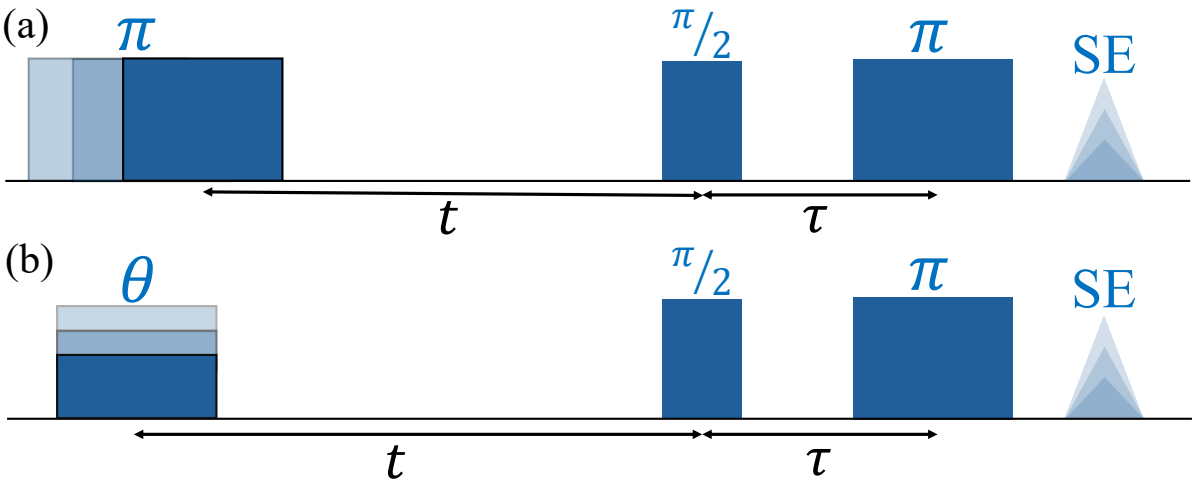

Figure 1.5: (a) Inversion-recovery pulse sequence consisting of an initial π-pulse, a free-evolution period t (on the order of T_1), and a final Hahn-echo readout. By varying t and monitoring the echo intensity, the spin-lattice relaxation time T_1 can be extracted. (b) Three-pulse nutation sequence of similar structure, where the first pulse is fixed in time but varied in duration or power, producing a rotation angle $\theta = \Omega t_p$, with Ω and t_p denoting the Rabi frequency and pulse length, respectively. The resulting echo amplitude oscillates as $\cos(\theta)$, from which Ω can be determined.

field B_0[27]. The resulting echo amplitude as a function of field produces the resonance spectrum, from which the effective spin Hamiltonian (Eq. 1.10) can be extracted.

1.1.5.3 Nutations and Inversion Recovery

More elaborate sequences also exist. For example, the three-pulse *inversion recovery* sequence ($\pi - t - \pi/2 - \tau - \pi - \tau -$ echo), shown in Fig. 1.5(a), is used to measure the longitudinal relaxation time T_1. The system begins at thermal equilibrium and the first π-pulse inverts the magnetization to $-\hat{z}$ on the Bloch sphere. If the intermediate delay $t \ll T_1$, the system has not yet relaxed back toward equilibrium, and the subsequent Hahn echo yields a "negative" (phase inverted relative to equilibrium) spin-echo. As t increases, the magnetization partially relaxes back toward equilibrium, causing the echo signal to pass through zero and eventually recover its positive (equilibrium) phase. When $t \gtrsim T_1$, the effect of the inversion is completely lost, and the system has fully returned to equilibrium, hence the name "inversion recovery". The echo amplitude thus

[27] Alternatively, one could fix the field and sweep the frequency, but here we used fixed-frequency resonators in all experiments.

follows the standard recovery law[28] $M(t) \sim \left(1 - 2e^{-t/T_1}\right)$. By fitting this function to the measured echo amplitude versus t, T_1 can be measured.

A related experiment is the three-pulse *nutation* sequence[29], shown in Fig. 1.5(b). Here, the first pulse is varied to produce a flip angle $\theta = \Omega t_p$, where $\Omega \propto B_1$ is the Rabi frequency and t_p is the pulse duration, while the rest of the sequence is held constant. The free-evolution interval is chosen such that $T_2 < t < T_1$, so that all transverse components have dephased, but the longitudinal population has not yet relaxed. After this delay, only the longitudinal component remains, and the $\pi/2$-pulse serves as a standardised readout, converting that population into a detectable SE. Since the magnitude of this longitudinal component depends on the initial flip angle θ, the echo amplitude oscillates as $\cos(\theta)$, allowing the Rabi frequency Ω to be extracted.

1.1.5.4 Electron Nuclear Double Resonance

We now briefly introduce another major technique used in ESR: Electron Nuclear Double Resonance (ENDOR). ENDOR is typically employed to characterise the influence of nuclear spins on the electron-spin Hamiltonian. The basic principle involves applying both mw and rf pulses to the sample, while sweeping the rf frequency and monitoring the echo-detected ESR signal. When the rf pulse is resonant with a nuclear spin transition, the electron-spin signal exhibits a characteristic intensity reduction (or dip). The *ENDOR efficiency*, which quantifies this effect, is defined as

$$F_{\mathrm{ENDOR}} = \frac{1}{2}\left|\frac{\mathcal{S}(\mathrm{off}) - \mathcal{S}(\mathrm{on})}{\mathcal{S}(\mathrm{off})}\right|, \tag{1.34}$$

where $\mathcal{S}$ denotes the electron-spin-echo intensity with the rf field turned on or off [1].

To illustrate this, consider a hyperfine-coupled (A_{iso}) electron-nuclear spin system with $S = 1/2$ and $I = 1/2$. In the *doubly rotating frame*, defined by the unitary transformation $U(t) = e^{-i(\omega_{\mathrm{mw}}\hat{S}_z + \omega_{\mathrm{rf}}\hat{I}_z)t}$, the effective Hamiltonian can be written as

$$\hat{\mathcal{H}}_0 = \Delta\omega_s\hat{S}_z + \Delta\omega_I\hat{I}_z + A_{\mathrm{iso}}\hat{S}_z\hat{I}_z, \tag{1.35}$$

[28] Assuming that the repetition time, i.e., the interval between two consecutive sequences, is much larger than T_1, as typical in experiments.

[29] In magnetic resonance, the term "nutation" refers to experiments where all parameters are kept fixed except one (typically a pulse flip angle or delay), while the spin echo is recorded.

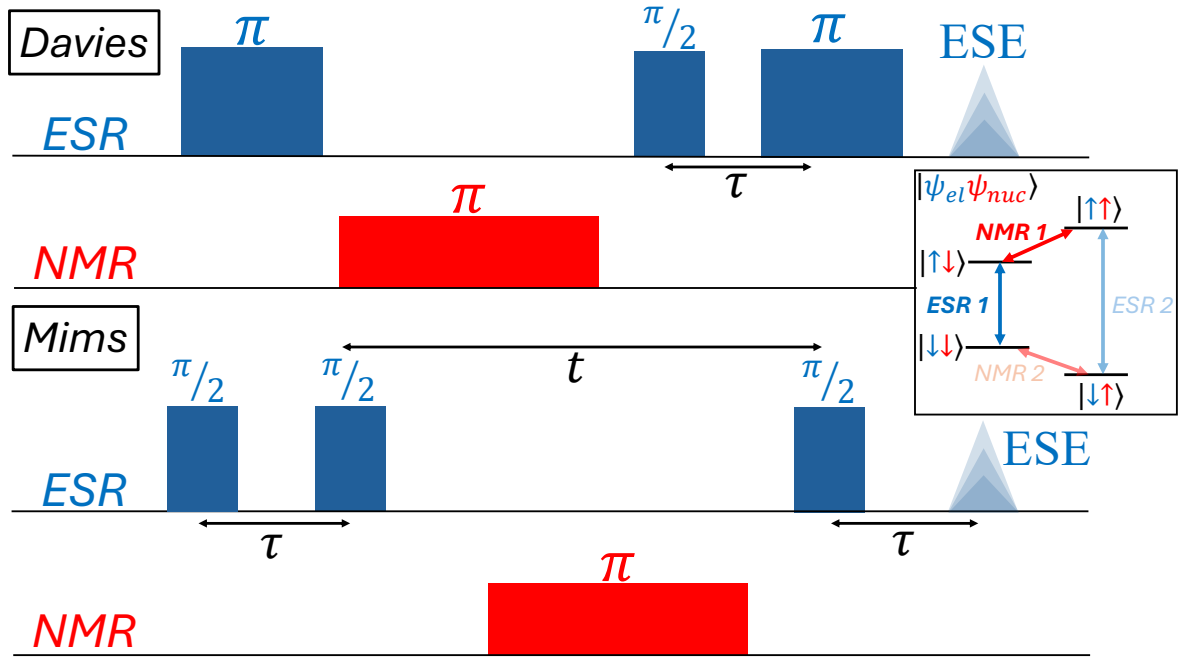

Figure 1.6: Davies (top) and Mims (bottom) ENDOR pulse sequences, as described in the main text. Blue and red pulses correspond to ESR and NMR frequencies, respectively. In both protocols, the frequency of the rf π-pulse is swept to extract the hyperfine coupling. *Inset:* Electron-nuclear states $|\psi_{el}\psi_{nuc}\rangle = |m_s, m_I\rangle$ for a electron system with $S = 1/2$ hyperfine-coupled to a nucleus with $I = 1/2$.

where $\Delta\omega_s = \omega_0^{(e)} - \omega_{\mathrm{mw}}$ and $\Delta\omega_I = \omega_0^{(n)} - \omega_{\mathrm{rf}}$ are the detunings of the microwave and radiofrequency fields, respectively. The eigenstates of this Hamiltonian, $|\psi_{\mathrm{el}}\psi_{\mathrm{nuc}}\rangle = |m_s, m_I\rangle$, are shown schematically in the inset of Fig. 1.6. Owing to the hyperfine interaction term $A_{\mathrm{iso}}\hat{S}_z\hat{I}_z$, each electron-spin state experiences a different effective nuclear field and vice versa. As a result, the pairs of ESR and NMR transition frequencies are individually addressable, with resonance frequencies $\omega_0^{(e)} \pm a_{\mathrm{iso}}/2$ and $\omega_0^{(n)} \pm a_{\mathrm{iso}}/2$.

The simplest ENDOR scheme was first introduced by Davies [23], and its pulse sequence is illustrated in Fig. 1.6 (top). The key principle is to detect nuclear transitions indirectly through their effect on the electron-spin echo intensity. A selective mw π-pulse (in blue) initially inverts one of the ESR transitions (for example, *ESR 1* in the figure), transferring the population between the two associated electron-spin states as $|m_s, m_I\rangle = |{\downarrow\downarrow}\rangle \leftrightarrow |{\uparrow\downarrow}\rangle$. At thermal equilibrium, the $|{\downarrow\downarrow}\rangle$ state has a higher population than $|{\uparrow\downarrow}\rangle$, and the initial π-pulse transfers this population difference into the higher energy level. If the following applied rf π-pulse (red) is on resonance with the nuclear transition ($\omega_{\mathrm{rf}} = \omega_0^{(n)} - \frac{A_{\mathrm{iso}}}{2}$ for

NMR 1), it flips the nuclear spin, transferring populations as $|{\uparrow\downarrow}\rangle \leftrightarrow |{\uparrow\uparrow}\rangle$. This rf-driven redistribution equalises the populations of the electron-spin states connected by *ESR 1*, thereby removing the net electron-spin polarization that would otherwise contribute to the Hahn-echo signal. Consequently, the subsequent Hahn-echo readout on *ESR 1* yields a vanishing (or strongly reduced) echo intensity under perfect nuclear-resonance conditions. By sweeping the rf frequency and recording the echo amplitude, one can therefore determine the NMR frequencies and extract the hyperfine coupling constant A_{iso}.

Davies ENDOR, however, requires that the initial mw π-pulse be *selective*. If the hyperfine splitting is small (typically $\lesssim 3$ MHz [1]), the mw pulse cannot selectively invert a single ESR line, and the method fails. In such cases, a different sequence, known as *Mims ENDOR* [24], can be used (bottom of Fig. 1.6). By detecting nuclear transitions via their influence on stored electron-nuclear populations rather than through population inversion, Mims ENDOR does not require selective microwave excitation.

In the Mims ENDOR experiment, three mw pulses are applied to the electron spins in the sequence $\pi/2 - \tau - \pi/2 - t - \pi/2$, producing a stimulated-echo signal. The first pulse creates a coherent superposition of electron spin states, while the second $\pi/2$ pulse rotates part of this transverse coherence back along the z-axis of the Bloch sphere, effectively storing it as a population difference (longitudinal magnetization) that can persist during the waiting period t. During this time, a rf pulse is applied to the coupled nuclear spins. If the rf frequency matches a nuclear resonance, it flips some of the nuclear spins and thereby alters the electron-nuclear population distribution established by the microwave pulses. The third $\pi/2$ pulse then converts these modified populations back into electron coherence, generating an echo whose intensity depends on whether the rf field was on nuclear resonance. The drawback of Mims ENDOR is the presence of *blind spots*, that is, specific rf frequencies where a dip is expected, but none is observed. This arises because the echo intensity is modulated by a factor $\frac{1}{4}\big(1 - \cos(a_{\mathrm{iso}}\,\tau)\big)$ [1], which goes to zero whenever $\tau = 2\pi n / a_{\mathrm{iso}}$ with $n \in \mathbb{Z}^+$. This can be mitigated by varying τ together with ω_{rf}, but this comes at the cost of longer acquisition times [24].

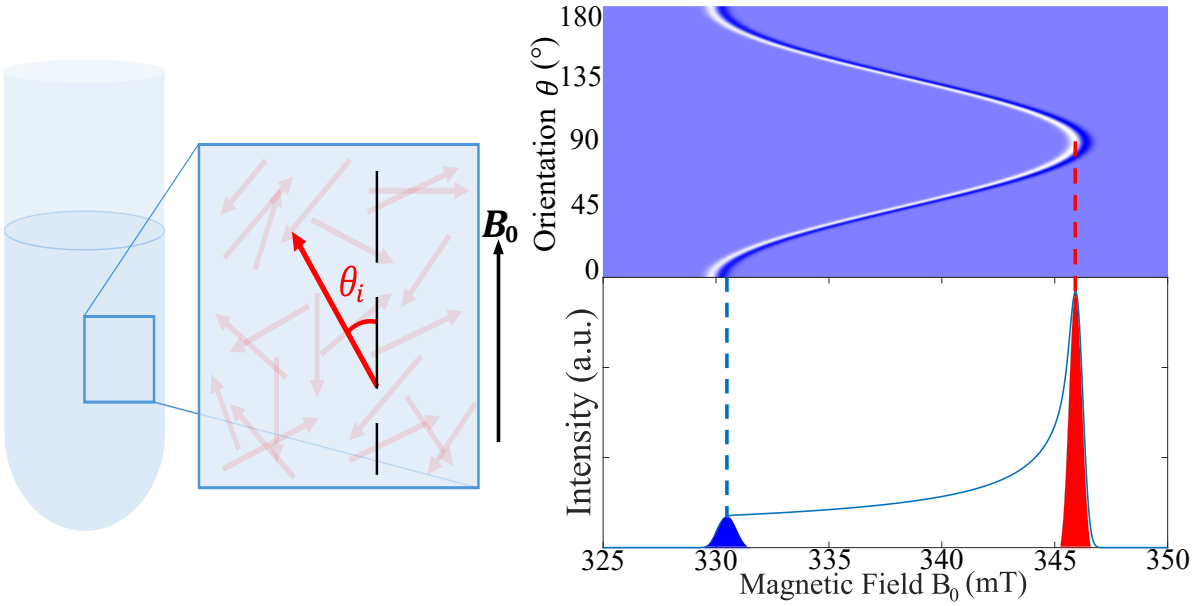

Figure 1.7: *Left:* Schematic representation of a randomly oriented ensemble of spin centres (red arrows), each forming an angle θ_i with the static magnetic field B_0. *Right:* (Simulated) Orientation-dependent (top) and corresponding absorption spectra (bottom) of an $S = 1/2$ system with axial symmetry and $g_\parallel > g_\perp$. This illustrates orientation selectivity: by varying the magnitude of B_0, different spin orientations satisfy the resonance condition and contribute to the signal.

Many additional pulse sequences exist in magnetic resonance; for an extensive review, see Ref. [1].

1.1.6 ESR of Disordered Spin Ensemble

In disordered spin ensembles (e.g., powders, or molecular spins in frozen solution), the principal axis of each spin centre points in a random direction relative to the external magnetic field B_0. Consequently, each spin effectively experiences a different Hamiltonian, and the measured signal represents an orientational average over all molecules.

To illustrate how ESR behaves in such systems, we consider a simple example: an ensemble of $S = 1/2$ spins with an axially symmetric g-tensor, with $g_\parallel > g_\perp$[30]. If the symmetry axis of spin i makes an angle θ_i with B_0, its Zeeman Hamiltonian becomes

$$\hat{\mathcal{H}}(\theta_i) = \mu_B B_0 \left(g_\parallel \hat{S}_z \cos\theta_i + g_\perp \hat{S}_x \sin\theta_i \right). \tag{1.36}$$

[30] $g_\parallel = g_z$ and $g_\perp = (g_x + g_y)/2$

A schematic of this is shown in the left panel of Fig. 1.7, whereas the right bottom panel shows the simulated powder-averaged ESR spectrum.

Each region of the broadened spectrum corresponds to contributions from spins at specific orientations θ_i. This is better visualised in the orientation-resolved spectrum (top right panel of Fig. 1.7), obtained using Eq. 1.36. For instance, near $B_0 \approx 347$ mT, the resonance is dominated by molecules with $\theta \approx 90°$ (red peak, symmetry axis perpendicular to the field), whereas at $B_0 \approx 331$ mT, molecules with $\theta \approx 0°, 180°$ (blue peak) contribute. Thus, by sweeping B_0 in a disordered sample, one effectively selects different molecular orientations, a phenomenon known as *orientation selection*. This concept will be central to the data analysis in Chapter 2.

Notably, in a randomly oriented ensemble, the number of spins pointing in each direction is not uniform: there is a larger population of spins oriented at $\theta = 90°$ than along the field axis. Geometrically, the set of orientations lies on a sphere, and the signal strength carries a weighting factor $\sin(\theta)$ that reflects how many spin centres occupy each angular slice. Since $\sin(\theta)$ is maximal at 90°, most spins lie in planes perpendicular to the field, resulting in a stronger signal at that angle, as displayed in the previous simulated spectrum.

1.2 Electric-field Effect in Electron Spin Resonance

1.2.1 Motivation & Theoretical Background

While magnetic resonance forms the backbone of all the experiments presented in this thesis, our primary focus is to investigate the effect of applying *electric* (E), rather than magnetic, fields to paramagnetic species. Specifically, we aim to assess whether such fields can be used for *coherent control*[31] of spin systems, and how this can be leveraged for quantum information science. In the following sections, we outline the theoretical framework, experimental techniques, and the overall plan of the thesis in this context.

Before proceeding, it is instructive to address the motivation for employing electric fields in the control of spin systems. At first sight, this may appear counterintuitive:

[31] Here, "coherent control" refers to the ability to manipulate both the amplitudes and phases of the quantum states in the system.

since spin is an intrinsically magnetic property, one would naturally expect magnetic fields to provide the most direct and efficient means of manipulation. The principal advantage of E-fields, however, lies in their ability to be spatially confined. This property follows directly from Gauss' laws:

$$\nabla \cdot \mathbf{E} = \frac{\rho}{\varepsilon}, \quad \nabla \cdot \mathbf{B} = 0. \tag{1.37}$$

The divergence of the electric field is determined by the local charge density (ρ), and hence electric fields can be readily localised through the placement of electrodes. In contrast, magnetic fields are divergenceless and therefore cannot be similarly confined to nanoscale regions. As a result, strong and highly localised electric fields can be generated in nanoscale device architectures, whereas magnetic fields necessarily extend over much larger spatial regions.

This scalability[32] makes electric-field-based control particularly advantageous for the coherent manipulation of spin systems in quantum technologies [25]. A key requirement for scalable architectures is the ability to manipulate and read out[33] spin states *locally*, thereby allowing a large number of qubits to be integrated within a small area. An additional advantage of electric fields is their reduced *cross-talk*: unlike magnetic fields, which are inherently long-ranged, electric fields minimise undesired interactions between neighbouring spin systems (or qubits, i.e., the basic unit of quantum information) [28].

Physically, the *spin-electric coupling* (SEC), the interaction between an applied electric field and the spin system, can arise from the electric-field-induced modulation of the crystal field. The applied field displaces ions and redistributes charge densities, thereby modifying the electronic cloud surrounding the magnetic ion. In turn, this alters the terms of the Hamiltonian that depend on the orbital angular momentum L. Mathematically, these modifications can be expressed as a change in the symmetric tensor $\mathbf{\Lambda} = \mathbf{\Lambda}(L)$,

[32] In the context of quantum information, this refers to the ability of a quantum computing system to increase the number of qubits and supporting components without exponential growth in resource overhead, while maintaining coherence, fidelity, and controllability necessary for reliable computation.

[33] Electric-field-based readout is *not* explored in this thesis. Nonetheless, significant progress has been made in this direction. For example, electrically detected magnetic resonance employs resistance measurements to probe spin states [26], while spin transistors exploit spin-polarised currents that vary according to the spin configuration [27].

defined in Eq. A.5, which encodes the orbital angular momentum eigenstates and their crystal-field-dependent energies. According to Eqs. 1.12 and 1.17, the effect of the electric field is then to shift both the g-tensor and the spin-orbit-induced ZFS as

$$\delta\mathbf{g}(\mathbf{E}) = 2\lambda\,\delta\mathbf{\Lambda}(\mathbf{E}) \qquad \delta\mathbf{D}^{\mathrm{SOC}}(\mathbf{E}) = \lambda^2\,\delta\mathbf{\Lambda}(\mathbf{E}), \tag{1.38}$$

leading to new spin-effective parameters $\mathbf{g}(\mathbf{E}) = \mathbf{g}(0) + \delta\mathbf{g}(\mathbf{E})$ and $\mathbf{D}^{\mathrm{SOC}}(\mathbf{E}) = \mathbf{D}^{\mathrm{SOC}}(0) + \delta\mathbf{D}^{\mathrm{SOC}}(\mathbf{E})$.

Eq. 1.38 highlights two important aspects. First, a stronger SOC constant λ enhances the magnitude of the electric-field-induced shifts, explaining why lanthanide ions, which are characterised by strong SOC, are a major focus in SEC studies [29, 30]. Second, the scaling differs: while the g-tensor varies linearly with λ, the ZFS contribution scales quadratically, making the ZFS generally more susceptible to electric modulation than the g-factor [30, 31].

A second contribution to the SEC originates from the electric modulation of spin-spin interactions, which directly affects the anisotropy parameters. This can be understood by considering that the application of an E-field displaces the electronic and nuclear wavefunctions, thereby modifying their average inter-spin distances. Since the dipolar SSC depends on $\langle 1/r^3 \rangle$, even small displacements lead to measurable changes in the anisotropy. For example, the electrically induced variation to the SSC anisotropy can be expressed as

$$\delta\mathbf{D}^{\mathrm{SSC}}(\mathbf{E}) \propto \left\langle 1/\delta r(E)^3 \right\rangle, \tag{1.39}$$

where $\delta r(E)$ denotes the electric-field-induced change in inter-spin distance. In this thesis, both SOC- and SSC-induced contributions to the SEC are described by a coupling constant κ (in units of Hz/(V/m)), which parametrises the strength of the interaction between the applied electric field and the spin Hamiltonian. For example, a linear electric-field dependence of the ZFS parameter D can be expressed as $\delta D(E) = \kappa \cdot E$.

A further point concerns the role of *inversion symmetry*. Since the electric field changes sign under spatial inversion, any linear coupling must vanish in centrosymmetric environments, where opposite field directions produce cancelling effects. In contrast,

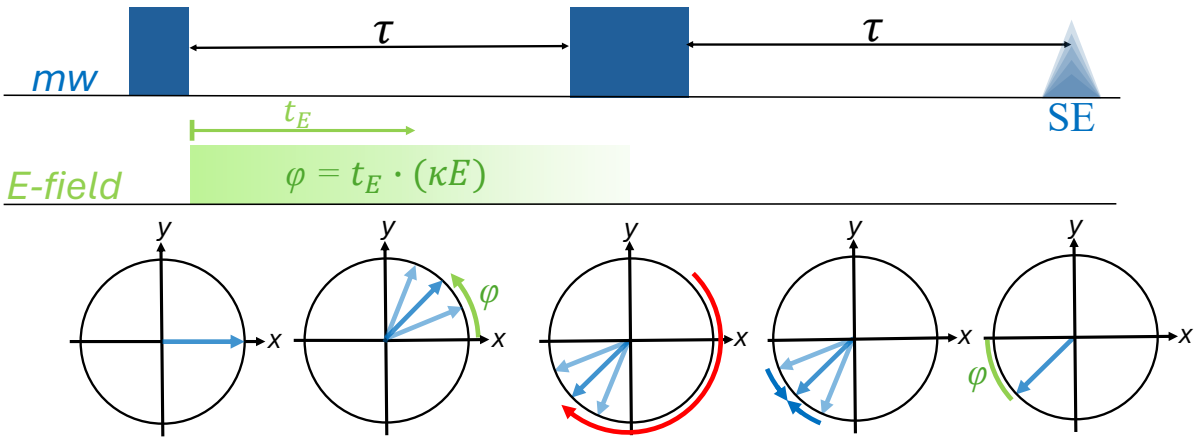

Figure 1.8: The Hahn-Mims pulse sequence (top), and the corresponding evolution of spin packets in the $\{x, y\}$-plane of the Bloch sphere (bottom). Application of a static electric field shifts the magnetization vector by an additional phase φ, which depends on both the electric-pulse parameters and the intrinsic spin-electric coupling constant κ of the system. The final (in-phase) echo is modulated by $\cos(\varphi)$, so that κ can be measured.

when inversion symmetry is broken (non-centrosymmetric systems), this cancellation no longer occurs, and linear SEC becomes allowed. Such behaviour has been analysed theoretically [32, 33] and confirmed in experiments [30, 34].

Experimentally, the SEC is most commonly quantified by measuring the electric-field-induced shift in the resonant frequency of a spin transition, known as the *Stark shift*[34] [34]. This approach is effective because the application of an external electric field modifies the effective spin Hamiltonian parameters, e.g., $D(E)$, which in turn alters the system's eigenstates and corresponding transition frequencies. In the following section, we identify and analyse the pulse sequence that enables a direct measurement of the Stark shift, thereby allowing the extraction of the SEC constant κ.

1.2.2 Hahn-Mims Sequence

We now introduce the pulse sequence that directly probes the SEC. This experiment was originally developed by Mims and is referred to hereafter as the *Hahn-Mims sequence* [35]. The corresponding pulse timing diagram is shown in the top panel of Fig. 1.8.

[34]The Stark shift is the electric-field analogue of the Zeeman effect and it lifts the degeneracy between states related by inversion symmetry, rather than by time-reversal symmetry.

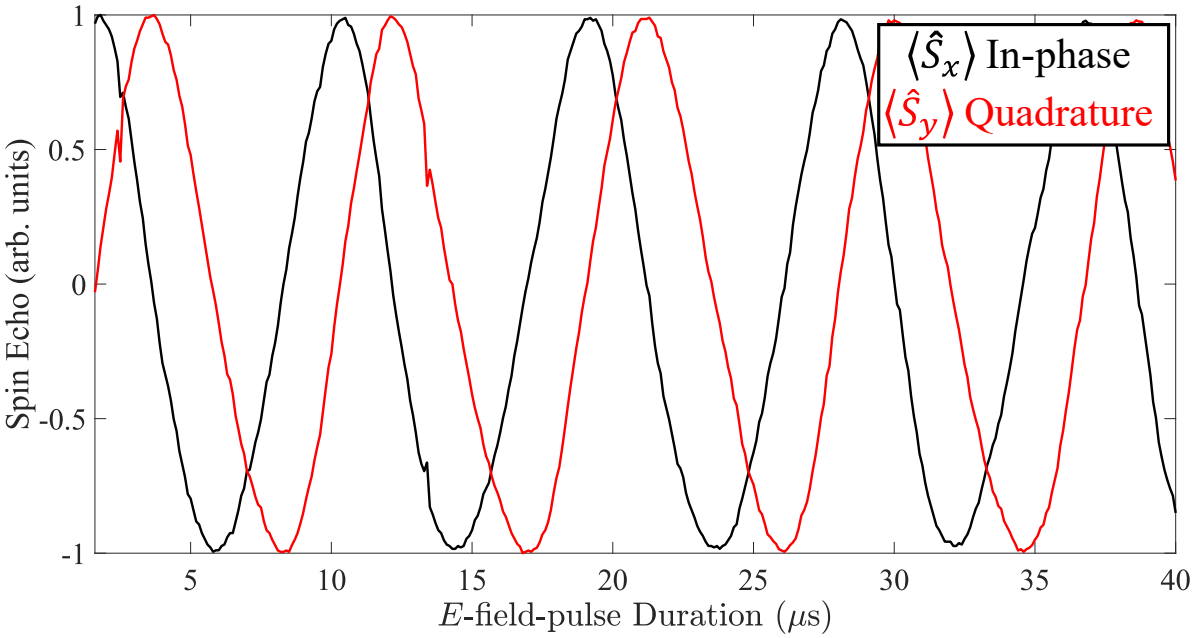

Figure 1.9: (Experimental) In-phase $\langle \hat{S}_x \rangle$ (black) and quadrature $\langle \hat{S}_y \rangle$ (red) components of the spin echo as a function of the electric-field-pulse duration (t_E in Fig. 1.8), showing the expected oscillatory behaviour. Fitting these oscillations yields a spin-electric coupling constant of approximately $\kappa \simeq 10$ Hz/(V/m). The data are measured on an iron defect in a ZnO host crystal; further details are provided in Chapter 4.

The sequence consists of a standard Hahn echo in which a static electric-field pulse E of variable duration is inserted after the $\pi/2$-pulse[35]. To understand the effect of this pulse, consider a simple two-level system. If a SEC exists, the energy levels are shifted by the Stark effect, which in practise means that the Larmor frequency ω_0 changes. By denoting this electric-field-induced shift by $\delta f(E)$, Eq. 1.28 becomes

$$\tilde{\mathcal{H}}_1(E) = (\omega_0(E) - \omega_{\mathrm{mw}})\,\hat{S}_z + \Omega\,\hat{S}_x = (\omega_0(E=0) + \delta f(E) - \omega_{\mathrm{mw}})\,\hat{S}_z + \Omega\,\hat{S}_x, \quad (1.40)$$

with $\delta f(E) = \kappa \cdot E$ in the case of a linear SEC. Thus, the net effect of the electric pulse is to shift the *phase of the transverse magnetization* by an amount that depends on the strength of the applied E-field, as well as the SEC constant κ.

The effect of the DC electric field can be modelled as a rotation about the z-axis of the Bloch sphere:

$$\hat{E} = \exp\!\left(i\hat{S}_z\,\kappa E t_E\right), \quad (1.41)$$

[35] In principle, the same effect could be obtained by varying the *amplitude* of the electric pulse, but this variant is not used in this thesis.

where t_E is the duration of the electric pulse, so that the E-field induced phase shift is $\varphi = \kappa E t_E$. Using this, the density matrix of the i-th packet after the $\pi/2$ pulse and the first free-evolution period τ becomes

$$\rho(t_E, \tau) = \hat{S}_y \sin(\delta\omega_i^{\text{inh}}\tau + \varphi(t_E)) + \hat{S}_x \cos(\delta\omega_i^{\text{inh}}\tau + \varphi(t_E)). \tag{1.42}$$

This is shown in the spin-packet time-evolution in the $\{x, y\}$ plane in the bottom panel of Fig. 1.8. The density $\rho(t_E, \tau)$ is identical to the standard Hahn-echo evolution, except for an additional phase term $\varphi(t_E)$ acquired during the DC electric pulse. Applying the refocusing π-pulse results in

$$\rho(t_E, \tau) \xrightarrow{\pi} -\hat{S}_y \sin(\delta\omega^{\text{inh}}(\tau - t) + \varphi(t_E)) + \hat{S}_x \cos(\delta\omega^{\text{inh}}(\tau - t) + \varphi(t_E)), \tag{1.43}$$

and at the echo time ($t = \tau$), the in-phase and quadrature components[36] read:

$$\langle \hat{S}_x \rangle(t_E) = \cos(\kappa E t_E), \qquad \langle \hat{S}_y \rangle(t_E) = \sin(\kappa E t_E). \tag{1.44}$$

By keeping the field amplitude E fixed and varying t_E, the oscillation of the spin echo allows one to extract the SEC strength κ. This approach is therefore *phase-sensitive*, and it is capable of detecting electric-field-induced frequency shifts down to a few tens of kHz (see, e.g., Fig. 5.5(c,d) in Chapters 5). The oscillations predicted by Eq. 1.44 are clearly visible in the experimental data shown in Fig. 1.9, where both $\langle \hat{S}_x \rangle$ and $\langle \hat{S}_y \rangle$ are plotted as a function of the electric-pulse duration t_E. These data were measured on an iron defect in a ZnO host crystal, and they will be presented in Chapter 4.

If the electric field pulse is extended beyond the refocusing π-pulse by an additional duration t', then

$$\rho(t_E, \tau{+}t') \xrightarrow{\hat{E}} -\hat{S}_y \sin\Big(\delta\omega^{inh}(\tau{-}t'){+}\kappa E(\tau{-}t')\Big){+}\hat{S}_x \cos\Big(\delta\omega^{inh}(\tau{-}t'){+}\kappa E(\tau{-}t')\Big). \tag{1.45}$$

In particular, if the electric pulse symmetrically overlaps both sides of the echo sequence, i.e., if $t' = \tau$, which implies $t_E = 2\tau$, then the phase accumulated before the π-pulse is exactly cancelled by the second half, and the original echo is fully recovered [30].

[36] These two components can be regarded as the orthogonal projections of the precessing magnetization in the transverse plane.

Following the discussion on randomly oriented spins in Subsec. 1.1.6, one might initially expect no net SEC effect in a disordered ensemble, since the electric field E is odd under parity[37]. Nevertheless, according to Eq. 1.44, two spins experiencing equal but opposite electric-field directions accumulate phases $\pm\varphi(E)$ and their combined echo components are $\langle\hat{S}_x\rangle = \cos(\varphi(E)) + \cos(-\varphi(E)) \neq 0$ and $\langle\hat{S}_y\rangle = \sin(\varphi(E)) + \sin(-\varphi(E)) = 0$. Thus, in a randomly oriented ensemble with a linear SEC, the quadrature component $\langle\hat{S}_y\rangle$ cancels out, while a net in-phase component $\langle\hat{S}_x\rangle$ survives and depends on the electric field. This effect was observed experimentally in an ensemble of molecular nanomagnets in Ref. [34], and it accounts for the behaviour seen in Fig. 2.5. See Sec.1.5.4 for the practical considerations of the devices employed to generate the DC E-field in this sequence.

1.2.3 Electric-Dipole Spin Resonance

So far, we have discussed spin manipulation using static electric fields. However, to achieve fully electrical control, one must also employ time-varying electric-field pulses resonant to spin transitions. The concept of Electric-Dipole Spin Resonance (EDSR), i.e., the electric analogue of ESR[38], was first introduced by Rashba in the context of quantum dots [36], and has since been experimentally demonstrated in a variety of semiconductor platforms [28, 37]. Rashba-type EDSR exploits Rashba and Dresselhaus SOC [38, 39], which couples the spin degree of freedom to the electron's *linear momentum* $\mathbf{k}$. While this framework successfully describes mobile or weakly confined electrons, it fails in strongly localised systems such as molecular magnets or defect centres in semiconductors (the central focus of this thesis; see, for instance, Sec. 1.4), where electrons lack translational motion and SOC is purely atomic.

A key advance relevant to this work came from Asaad *et al.* [40], building on the early proposal of Bloembergen [41], which demonstrated that localised spin systems can indeed be controlled electrically. In their experiment, manipulation of the quantum state of a single nuclear defect in silicon was achieved using resonant E-fields, thereby

[37] Intuitively, one might expect cancellation because opposite spin orientations would experience opposite Stark shifts. However, the Hahn-Mims sequence measures the sample magnetization, not the direct electric-field sensitivity of each individual spin.

[38] That is, spins are driven by resonant E-fields, rather than B-fields

achieving the first experimental demonstration of *Nuclear Electric Resonance* (NER). Unlike earlier approaches, which relied on transducing electric signals into effective magnetic fields via the electron-nuclear hyperfine interaction [42] (a process that strongly limits nuclear coherence), this work directly harnessed the coupling between the nuclear quadrupole moment and the electric-field gradient. This breakthrough provides the conceptual basis for Chapters 3 and 4, where we describe experiments targeting NER and EDSR, respectively.

In both EDSR and NER, the applied AC electric field $\tilde{\mathbf{E}}(t)$ couples to the electronic clouds or the crystal structure, which in turn modulate the spin system; a mechanism conceptually similar to the one discussed in Subsec. 1.2.1. For instance, this coupling may occur through the nuclear quadrupole interaction with the electric-field gradient, the hyperfine-mediated electric fields between electron and nucleus, or through crystal fields that modulate the ZFS or other anisotropies. In all cases, the applied AC field introduces a time-dependent perturbation to the Hamiltonian, as in Eq. 1.25. From a classical perspective, one may think of this in terms of Maxwell's equations: a time-varying E-field generates a magnetic response that can, in turn, drive spin transitions.

The general EDSR interaction Hamiltonian can be expressed as the time-dependent extension of the static Stevens operators in Eq. 1.24, in which the crystal-field parameters are modulated by the applied $E_1(t)$. Mathematically:

$$\hat{\mathcal{H}}_I^{\mathrm{EDSR}}(t) = \sum_{k=2,4,6} \sum_{q=-k}^{k} \delta B_k^q(t)\, \hat{O}_k^q(\hat{\mathbf{S}}), \quad \text{with} \quad \delta B_k^q(t) = \tilde{\kappa}_k^q E_1(t), \tag{1.46}$$

where $\tilde{\kappa}_k^q$ is the AC SEC constant. The time-varying $\delta B_k^q(t)$ acts analogously to the mw magnetic field $B_1(t)$ in conventional ESR, although the selection rules may differ (see Chapter 4). Similar expressions can be found for nuclear transitions, for instance, via modulation of the hyperfine or quadrupolar interaction, as described in Eq. 3.3 and 3.4. Note that no explicit time dependence of the g-factor is included, since in all the examples considered here the driving arises from modulation of magnetic anisotropies rather than Zeeman interactions.

One of the central aims of this thesis is to explore how resonant electric fields can be used to drive both nuclear and electronic spin transitions. To this end, Chapter 3 investigates how the coupling between electronic and nuclear degrees of freedom affects the strength and efficiency of NER. Chapter 4, in turn, focuses on achieving coherent EDSR control and detection by exploiting the electric sensitivity of the local environment surrounding the spin.

1.3 Kane Quantum Computer

We now consider the application of the electric-field control of spin systems in quantum computation, focusing on the Kane model[39]. In this approach, donor nuclear spins in silicon serve as qubits, with their states controlled through the hyperfine interaction with their bound electrons. Conceptually, the architecture can be viewed as an NMR-inspired system: local gate electrodes provide electric-field tuning of the effective spin parameters, closely paralleling the types of control mechanisms explored in most of the experiments described in this thesis.

The original model is based on phosphorus donors (^{31}P) in silicon. Each donor hosts a single bound electron with spin $S = 1/2$, coupled via the hyperfine interaction to the nuclear spin $I = 1/2$, which serves as the qubit. In isotopically enriched ^{28}Si crystals (where background nuclear and electronic spins are absent) the coherence time of the donor nuclear and electron can reach several hours and thousands of second at cryogenic temperatures (around 1.5 K), respectively [44]. This provides a compelling platform for quantum information science (QIS). To realise such systems in practice, donors are introduced by ion implantation [45], and patterned gate electrodes are fabricated on the silicon surface [40].

Two types of gates are used: A-gates, placed above each donor, and J-gates, positioned between neighbouring donors. The A-gates apply local electric fields that displace the electron wavefunction towards the surface and away from the phosphorus nucleus.

[39] Loss and DiVincenzo first proposed spin qubits based on single electrons confined in quantum dots [43]. While semiconductor quantum-dot architectures have since attracted considerable attention, they are not the focus of this thesis.

This reduces the Fermi contact hyperfine interaction (see Subsec. 1.1.2.3), thereby shifting the nuclear resonance frequency. In this way, each donor electron-nucleus pair functions as a voltage-tunable oscillator. When a global oscillating magnetic field is applied, only nuclei with resonance frequencies at or near that of the field undergo significant rotations. Thus, local electric-field tuning via the A-gates, combined with global microwave driving, enables qubit-selective control.

The J-gates, in contrast, regulate the electron-mediated coupling between adjacent nuclear spins by controlling the potential barrier between neighbouring donors. Adjusting this barrier modifies the overlap of the electron wavefunctions, and hence the strength of their exchange interaction. Crucially, quantum operations are performed in the regime where the exchange coupling J remains much smaller than the electron Zeeman splitting, ensuring that qubits can still be addressed individually.

After the desired operations are completed, the nuclear spin state is measured as follows. The exchange coupling J is gradually increased from its low operational value towards values comparable to the electron Zeeman splitting. In this regime, the nuclear and electron spin states hybridise through the hyperfine interaction. Under adiabatic ramping of J, the nuclear state is coherently mapped onto a correlated electron spin state (for example, a singlet or triplet). Readout is then achieved by spin-dependent tunnelling; only the electron singlet state can occupy the doubly charged donor configuration (D^-), while the triplet remains blockaded due to the Pauli exclusion principle[40]. The tunnelling probability distinguishes the two electron spin states, and the resulting charge change is detected capacitively by a nearby single-electron transistor. Since the electron spin encodes the nuclear state via adiabatic mapping, this enables reliable measurement of the nuclear qubit.

The Kane proposal remains actively studied, benefiting from decades of silicon-chip expertise. Its main (current) limitation is that single-electron transistors require cryogenic operation, which hinders scalability and limits energy-efficiency gains. We now briefly discuss alternative approaches, focusing on molecular-based QIS.

[40]Since the two-electron orbital wavefunction of the D^- state is symmetric.

1.4 Molecules in Quantum Information Processing

A variety of physical platforms have been proposed and experimentally explored for QIS, with the most significant progress achieved in superconducting quantum circuits [46], laser-cooled trapped ions [47], and neutral atoms [48]. Despite recent breakthroughs [49] and claims [50], several practical constraints still limit the realization of a scalable multi-qubit platform for fault-tolerant quantum computation. Most of these systems in fact require highly specialised infrastructure to preserve fragile quantum states and enable coherent operations; for instance, cryogenic cooling or ultra-high vacuum conditions. Solid-state approaches based on spin defects in semiconductors, as silicon [51], diamond [52], and SiC [53], have also been investigated. These systems offer the advantage of potential integration with existing semiconductor technologies or room temperature operations; however, challenges in reproducibly fabricating and controlling the defects may hinder their scalability.

Molecular systems have recently attracted considerable attention for applications in quantum technologies [54–56], owing to their unique *bottom-up* design flexibility. Unlike most other platforms, molecular qubits can operate in the sub-10 nm regime while still retaining tunability and structural flexibility. Their atomic-level programmability enables spin Hamiltonians to be tailored and allows controlled coupling to, for instance, optical [57], and mechanical [58] degrees of freedom. In principle, molecules provide access to a broad manifold of states, including electronic, vibrational, and vibronic excitations. However, these excitations typically suffer from ultrafast decoherence, with coherence times of only a few picoseconds [59], limiting their direct use in QIS. By contrast, molecular nuclear and electronic spins can exhibit much longer coherence times, reaching up to the millisecond scale at cryogenic temperatures [60].

As for all other platforms, the quest for fault-tolerant quantum computation remains central in molecular-spin-based QIS and entails long *coherence* [61] and *scalability* [62]. For the former, it is crucial to minimise environmental decoherence channels around the paramagnetic centres. Common strategies include engineering the ligand coordination sphere to suppress low-energy vibrational modes coupled to the spin [63], or isotopic

purification to reduce the density of surrounding nuclear spins, thereby mitigating hyperfine-driven dephasing [64]. Another route is the use of Kramers ions (half-integer spins), which benefit from time-reversal symmetry protection: spin-phonon coupling matrix elements between Kramers-conjugate states vanish due to the so-called *Van Vleck cancellation*, leading to reduced relaxation pathways [65][41]. Relaxation between Kramers-conjugate states can nevertheless proceed via higher-order Orbach or Raman processes [66]. However, these may be strongly suppressed when the ZFS exceeds the thermal energy $k_B T$, as is often the case in lanthanide complexes where strong SOC yields naturally large ZFS values [67]. Beyond these approaches, coherence can also be enhanced by diluting spin centres in diamagnetic host matrices to reduce dipolar interactions [68], or by operating at clock transitions (CT) [69], where the spin splitting is first-order insensitive to magnetic-field noise. We will return to CT in more detail in Chapter 5.

As for scalability, molecular spins are inherently zero-dimensional systems, but they can be integrated into higher-dimensional architectures through controlled intermolecular interactions. Coupling between molecular units can be engineered via covalent bonds or non-covalent interactions, enabling the construction of atomically precise qubit arrays [59]. Supramolecular assemblies such as metal-organic frameworks (MOFs) offer a particularly versatile route: their modular structure, based on metal nodes and organic linkers, allows tunable geometries and chemical environments, making it possible to embed spin-active centres into ordered and porous crystalline lattices [70]. In this way, MOFs provide a chemically programmable platform for arranging spins in extended networks while retaining atomic-level precision. Currently a limiting factor for MOFs-based quantum platforms is constituted by the challenging of *addressing* individual qubits.

Beyond such frameworks, scalability can also be pursued through surface deposition techniques that integrate molecular spins into ordered arrays on substrates [71, 72]. Another promising direction is the use of hybrid approaches, where molecular systems are coupled to external platforms that mediate interactions over longer distances. Examples include photonic cavities and waveguides for photon-mediated coupling [73], mechanical resonators

[41] Since the spin-phonon interaction V_{sp} is invariant under time-reversal, then $\langle\psi_1| V_{\mathrm{sp}} |\psi_2\rangle = 0$ if $|\psi_1\rangle = \mathcal{T}|\psi_2\rangle$, i.e., the two states are Kramer conjugate.

that enable interactions with phonons [74], and plasmonic nanostructures that confine electromagnetic fields at the nanoscale and thereby enhance spin-spin interactions [75].

Among these approaches, two particularly promising strategies have recently emerged. The first involves integrating molecules with superconducting coplanar resonators [76] or nanoconstrictions [77, 78], where a shared superconducting mode can mediate interactions between spatially separated spins. This architecture offers a path toward circuit-level integration of molecular qubits by combining local control with long-range coupling, though practical implementations are currently limited by weak molecule-photon couplings. The second strategy is based on molecular transistors, in which a single molecule is wired between source and drain electrodes and its quantum state can be probed electrically through changes in the junction current [42, 79, 80]. Such devices enable the manipulation and detection of coherent spin or nuclear spin states at the single-molecule level, and even the implementation of simple quantum algorithms, such as Grover's search, has been demonstrated in this setting [81]. Embedding these transistors into graphene nanoribbons may further enhance scalability by combining molecular precision with exceptional electronic transport properties [82, 83]. Nevertheless, significant challenges remain: the reliable fabrication of reproducible single-molecule junctions is technically demanding, and operation still generally requires cryogenic temperatures.

In terms of practical applications, molecular-spin quantum technologies have been proposed and explored for quantum simulations of the electronic structure and dynamics of realistic molecules and materials [59]. Such simulations could provide new insights into catalytic processes, light-harvesting systems, and even high-temperature superconductivity, all of which are central to energy production, storage, and transmission [84]. In addition, molecular spins offer significant potential for quantum sensing: their chemical tunability and biological compatibility allow them to be placed in close proximity to the target, which may enable high-precision detection of chemical interactions and biological processes [85, 86]. Beyond applied sensing, molecular spins have also been proposed for fundamental research, serving as nanoscale probes for exotic states of

matter such as polar skyrmions [87], charged quasi-particles [88], and even hypothetical particles relevant to dark matter detection [89].

Despite the possibility of combining the advantages of molecules and E-field control (Sec. 1.2), the exploration of spin-electric coupling in molecular systems has only recently begun. The first experimental detection was reported in Ref. [34], with subsequent demonstrations in [16, 30]. Nonetheless, this area remains relatively underexplored, motivating the experiments presented in Chapter 2 and Chapter 5. These focus on the quantum sensing of electric fields and the integration of molecular spins into multi-qubit platforms, respectively.

1.5 Practical Aspects

We have so far discussed the theoretical foundations and pulse sequences relevant to this thesis. We now turn to the experimental aspects, beginning with the physical observables in magnetic resonance and how they are detected in practice. Crucially, the measured response depends on whether the experiment is carried out in continuous-wave (cw) or pulsed mode.

In the cw case, the sample is continuously exposed to a steady microwave field while either the excitation frequency or the static magnetic field B_0 is swept. The readout relies on changes in the sample's magnetic susceptibility $\chi = dM/dB_0$ at resonance. Indeed, when the excitation matches a spin transition, the spins interact with the microwave photons, giving rise to both absorption and dispersion in the system's response. The absorptive part corresponds to the energy transfer from the field to the spin system, while the dispersive response arises when the excitation is detuned from resonance, causing the magnetization to lag in phase with the driving field and producing a reactive (out-of-phase) component of the susceptibility [90]. Formally, this behaviour is expressed as

$$\chi = \chi' + i\,\chi'', \tag{1.47}$$

where χ'' and χ' denote the absorptive and dispersive components, respectively. Variations in χ alter the coupling between the spin system and the resonant microwave field, thereby

modifying the resonator response (see next subsection) and changing the microwave power reflected at the source-resonator interface, which is the experimentally detected quantity.

In pulsed mode, by contrast, the spin system is driven out of equilibrium by short microwave bursts. Once the excitation ends, the spins precess freely around the static magnetic field, generating a macroscopic transverse magnetization. The experimentally detected signal arises from the voltage induced in the detection circuitry by the changing magnetic flux produced by this precessing magnetization, as dictated by Faraday's law of induction:

$$V(t) \propto \frac{dM_{\perp}(t)}{dt}. \tag{1.48}$$

Here, $M_{\perp}(t)$ denotes the component of the magnetization vector perpendicular to the static magnetic field B_0. Since $M_{\perp}(t)$ is time-dependent, the acquired signal reflects the real-time dynamics of the system. This represents a key advantage of pulsed magnetic resonance techniques: they enable full access to the spin dynamics in the time domain, allowing for the probing of decoherence mechanisms and the implementation of quantum control protocols.

1.5.1 ESR Cavity Resonators

In magnetic resonance experiments, detection sensitivity and control over spin dynamics can be greatly enhanced by using a *cavity resonator*[42], which provides a controlled electromagnetic environment that strongly enhances spin-photon interactions. Resonators can be generally regarded as lumped-element LC circuits, where the inductance and capacitance determine the natural oscillation frequency. Unlike free space, where radiation spreads in all directions, a cavity confines the electromagnetic field into discrete spatial and frequency modes. These modes concentrate the field energy into specific patterns and frequencies, reinforcing the signal through constructive interference. This allows photons to interact multiple times with the spin ensemble, thereby increasing the effective coupling.

[42]Other types of resonators, such as coplanar waveguides or loop-gap resonators [1], also exist but lie outside the scope of this thesis.

In practice, losses arise from an effective resistance R in the equivalent RLC model of the cavity. The associated figure of merit is the *quality factor* Q, which characterises how efficiently the resonator stores energy compared to the energy lost per cycle, and can then be expressed as

$$Q = \frac{\text{energy stored}}{\text{energy dissipated per cycle}} = \frac{\omega}{\delta\omega} = \omega\tau_\gamma, \tag{1.49}$$

where τ_γ is the average photon lifetime in the cavity and $\delta\omega$ is the resonator bandwidth, i.e., the frequency range over which the cavity effectively stores and exchanges energy. A narrower bandwidth (high Q) implies longer photon storage and stronger spin-photon coupling, but at the cost of addressing only spins with resonance frequencies lying within that narrow window. Conversely, a broader bandwidth (low Q) excites a wider range of spin frequencies but with weaker interaction strength.

While the Q-factor is widely used to characterise resonators, it depends on several factors, including the material properties of the cavity. In some cases, however, one is solely interested in the effect of the cavity *geometry*; for example, when comparing the performance of different resonator designs. For this purpose, it is useful to introduce a material- and coupling-independent metric known as the *geometric factor* G [91], defined as

$$G = \frac{\omega\mu_0 \int dV\, |\mathbf{B}(\mathbf{r})|^2}{\int dS\, |\mathbf{B}(\mathbf{r})|^2}, \tag{1.50}$$

and expressed in units of Ω. The volume integral is proportional to the total magnetic energy stored inside the cavity, while the surface integral quantifies the energy lost to surface currents at the cavity walls. The geometric factor is related to the quality factor by $Q = G/R_s$, where R_s is the surface resistance of the cavity material. This will play a central role in Chapter 4 (see Fig. 4.4).

Another important consideration is the choice of *cavity mode*, each associated with a distinct electromagnetic field pattern and resonance frequency (unless degenerate). A useful figure of merit for characterizing a mode is the *magnetic mode volume* V_B,

$$V_B = \frac{\int dV\, |\mathbf{B}(\mathbf{r})|^2/\mu(\mathbf{r})}{|\mathbf{B}(\mathbf{r}_{\max})|^2/\mu(\mathbf{r}_{\max})}, \tag{1.51}$$

where $\mathbf{r}_{\max}$ denotes the point of maximum magnetic field. Smaller V_B indicates stronger field localization and therefore higher possible coupling for a spin placed at the field maximum. When the sample is introduced, an equally important parameter is the *filling factor* η, which quantifies the fraction of the cavity's magnetic energy overlapping with the sample,

$$\eta = \frac{\int_{\text{sample}} dV\, |\mathbf{B}(\mathbf{r})|^2}{\int_{\text{resonator}} dV\, |\mathbf{B}(\mathbf{r})|^2}. \tag{1.52}$$

Maximizing η ensures that a larger portion of the resonator field couples to the sample, thereby enhancing sensitivity, particularly for compact spin ensembles.

Finally, the coupling strength between the resonator and an external mw or rf sources needs also to be considered. In practice, this is typically achieved by introducing an aperture in the resonator, antenna, or loop probe [92], which enables energy exchange between the feedline and the resonator. The strength of this coupling determines how efficiently energy flows into and out of the cavity and is conventionally classified into three regimes. In the *undercoupled* case, internal cavity losses dominate over the energy transferred from the source, so only a limited fraction of the input power excites the mode; while such cavities can store energy well (i.e., relatively high Q), energy leaks out too slowly to be efficiently extracted for most applications. At the opposite extreme, an overcoupled cavity dissipates more power into the feedline than is dissipated internally, resulting in a reduced Q and, consequently, a broader resonance bandwidth. In this regime, energy leaks out faster than it is lost inside, which is advantageous for pulsed ESR since fast energy dumping and broadband excitation are far more critical than sensitivity at a single frequency. The intermediate point, known as *critical coupling*, occurs when internal and external losses are balanced[43]. In this case, the input power is absorbed most efficiently by the cavity, providing the optimal operating point for continuous-wave ESR.

[43] From an electronics perspective, this corresponds to perfect impedance matching, where the input sees no reflection at resonance.

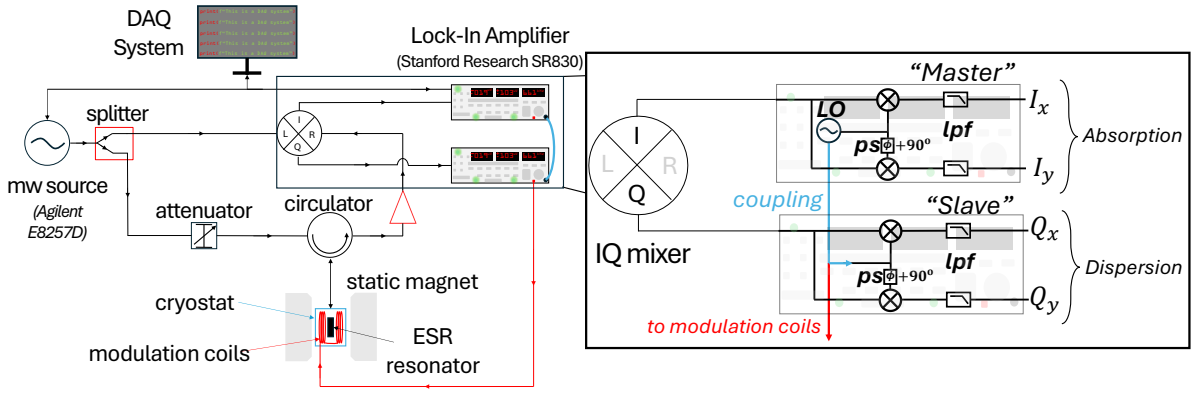

Figure 1.10: Schematic of the home-built cw magnetic resonance spectrometer, based on IQ-mixing and lock-in detection (details provided in the main text). *Close-up:* Our detection scheme employs two coupled lock-in amplifiers, allowing the simultaneous measurement of both the absorption and dispersion components of the ESR signal. In the inset: *ps*: phase shifter. *lpf*: low-pass filter. *LO*: local oscillator.

1.5.2 Continuous-wave Spectrometer

Continuous-wave ESR spectrometers typically operate by combining *field modulation* with *lock-in detection*. In field modulation, a small ($\lesssim 1$ mT) alternating[44] magnetic field B_{mod} is superimposed on the main static magnetic field. This periodic modulation converts variations in susceptibility into an oscillating detector response at the modulation frequency. By referencing the detection to this frequency, a lock-in amplifier (LIA) can then recover weak resonance signal from the noisy background. Internally, the LIA contains a reference oscillator at frequency ω_{mod} (the *LO* in the inset of Fig. 1.10), two phase-sensitive detectors (in-phase and quadrature, IQ, mixers; see Subsec. 1.5.3.1), and low-pass filters. The incoming signal $\mathcal{S}(t)$, which carries a time dependence due to the field modulation, is *mixed* (multiplied) with the reference $\sin(\omega_{\text{mod}}t)$ as well as $\cos(\omega_{\text{mod}}t)$, producing sum and difference frequencies[45]. The subsequent low-pass filtering effectively averages the mixed signal in time, isolating only the components at the reference frequency (*demodulation*). In this way, the LIA extracts the modulated ESR response with high sensitivity while strongly rejecting broadband noise.

[44] Typically in the hundreds of kHz to few MHz range.

[45] From the trigonometric identities $\cos(x)\sin(y) = \frac{1}{2}[\sin(x+y) - \sin(x-y)]$ and $\sin(x)\sin(y) = \frac{1}{2}[\cos(x-y) - \cos(x+y)]$.

By writing the combined static and modulating field as $B(t) = B_0 + B_{\mathrm{mod}} \sin(\omega_{\mathrm{mod}} t)$ with $B_{\mathrm{mod}} \ll B_0$ (as typical in experiments), the ESR signal can be Taylor-expanded as

$$\mathcal{S}(t) = \mathcal{S}(B(t)) \simeq \mathcal{S}(B_0) + \left.\frac{d\mathcal{S}}{dB}\right|_{B_0} B_{\mathrm{mod}} \sin(\omega_{\mathrm{mod}} t) + \ldots \tag{1.53}$$

In the LIA, this signal is mixed with the reference $\sin(\omega_{\mathrm{mod}} t)$ and integrated over a period, $\int_0^{T=2\pi/\omega_{\mathrm{mod}}} \mathcal{S}(t) \sin(\omega_{\mathrm{mod}} t)\, dt$. By orthogonality of trigonometric functions, only the components at the modulation frequency ω_{mod} with the reference survive, as the constant term $\mathcal{S}(B_0)$ and any off-frequency contributions average to zero. The non-vanishing term is therefore proportional to $d\mathcal{S}/dB\big|_{B_0}$; this means that in cw ESR with field modulation, the recorded signal corresponds to the *first derivative* of the absorption spectrum (since the dispersion is often disregarded [93]) with respect to the magnetic field [1].

Our home-built continuous-wave spectrometer, schematically shown in Fig. 1.10, employs an Agilent E8257D microwave source (maximum output power 16 dBm) to excite the sample in the resonator, as well as serving as the *LO* for the IQ mixer. In this setup, the Stanford Research SR830 LIA modulates the magnetic field (via the red coils in the schematic), causing the total signal emerging from the resonator to oscillate at $\omega_{\mathrm{sig}} = \omega_{\mathrm{LO}} + \omega_{\mathrm{mod}}$, i.e., the modulation frequency superimposed on the microwave carrier. The IQ mixer *downconverts*[46] this signal by mixing it with the *LO*, producing two orthogonal outputs (I and Q) at the difference frequency $\omega_{\mathrm{sig}} - \omega_{\mathrm{LO}} = \omega_{\mathrm{mod}}$. This shifts the spin-dependent signal directly to the modulation frequency, where the LIA operates at maximum sensitivity and can efficiently extract the ESR response while suppressing noise. This allows detection of extremely weak signals, down to 2 nV, providing the high sensitivity required for molecular and spin-based ESR measurements [94].

In our spectrometer, two LIAs are employed, as highlighted in the close-up of the figure, with their modulation frequencies and phases locked together (blue connector in the schematic). This configuration allows each channel to be optimised independently, thereby increasing overall sensitivity. By setting the reference phases of the two LIAs 90° apart,

[46] Down- and upconversion shift a signal to lower and higher frequencies, respectively. If ω_i is the incoming frequency and ω_{LO} is the local oscillator frequency, then $\omega_{d,u} = \omega_i \mp \omega_{\mathrm{LO}}$.

the in-phase (I) channel measures the absorptive component, while the quadrature (Q) channel simultaneously captures the dispersive one.

This setup differs from standard spectrometers, which typically employ automated frequency control to lock the microwave source to the cavity resonance, thereby suppressing resonance-frequency drifts caused by dispersion [95]. Such drifts may distort lineshapes and reduce measurement accuracy, so in most conventional experiments the absorptive component is used as the primary readout [96]. In contrast, our approach offers two main advantages: (i) it preserves phase information, allowing simultaneous access to both the absorptive and dispersive components of the ESR response, and (ii) because the noise in the two channels is largely uncorrelated, the combination of χ' and χ'' (Eq. 1.47) effectively increases the measured signal amplitude to $\sqrt{(\chi')^2 + (\chi'')^2} \sim \sqrt{2}\,\chi''$, resulting in an overall SNR improvement [93].

1.5.3 Broadband Pulsed Spectrometer

The spectrometer used for pulsed experiments, shown schematically in Fig. 1.11, is centred around the Arbitrary Waveform Generator (AWG, Zurich Instruments HDAWG). The AWG is a programmable device that produces voltage waveforms with user-defined shapes and precise timing. In our case, it generates and synchronises the mw pulse sequences that manipulate the spin ensemble, while also triggering the oscilloscope (Tektronix DPO 7254) for time-resolved data acquisition. In pulsed ESR, the oscilloscope records the spin response in real time, e.g., the echo described in Subsec. 1.1.5.2.

After the computer uploads the desired pulse sequence[47], the AWG generates two low-frequency signals at ω_{awg}, which are fed into the I and Q ports of an IQ mixer (#1 in the schematic). Because typical AWGs are limited to the kHz-hundreds of MHz range, they cannot directly produce the GHz-frequency mw pulses required for ESR. Instead, the IQ mixer performs *upconversion* by combining the AWG outputs with a continuous carrier at frequency ω_{LO} from the source, yielding a signal[48] at $\omega_R = \omega_{\mathrm{LO}} + \omega_{\mathrm{awg}}$. For instance, in an X-band configuration with $\omega_{\mathrm{LO}} = 9.6$ GHz and $\omega_{\mathrm{awg}} = 100$ MHz, the resulting output

[47] Custom Python codes were developed for this purpose.

[48] The IQ mixer also generates a component at $\omega_{\mathrm{LO}} - \omega_{\mathrm{awg}}$, which is suppressed by a low-pass filter.

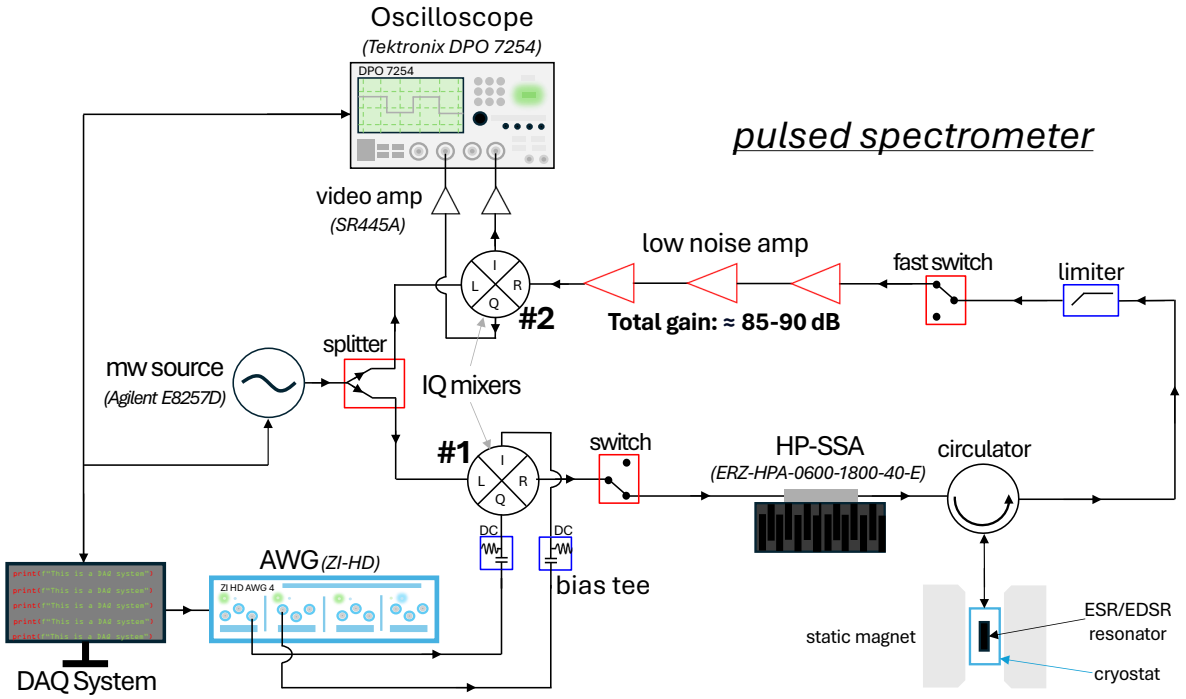

Figure 1.11: Schematic of the home-built pulsed spectrometer, whose frequency working range is between 6 and 18 GHz. DAQ System: Data-Acquisition System; AWG: Arbitrary Wave Generator; HP-SSA: High-Power Solid State Amplifier.

is $\omega_R = 9.7$ GHz, suitable for spin excitation. To suppress leakage of the unmodulated carrier from the *LO*, which could otherwise introduce DC offsets or baseline distortions, the AWG signals are DC-biased to minimise carrier bleedthrough (see Subsec. 1.5.3.1).

The upconverted pulses are subsequently amplified by a broadband high-power solid-state amplifier (Erzia 0600-1800-40-E), which provides a typical gain of 46 dB across 6-18 GHz. This broad bandwidth enables operation not only in the *X*-band (relevant for Chapters 2 and 3), but also in the K_u-band, crucial for the custom resonator described in Chapter 4. To suppress spurious microwave leakage that may accumulate in the IQ mixer, transmission lines, or other components, a fast microwave switch is inserted before the amplifier. The switch is set *ON* only during the intended pulse window, otherwise providing ~ 60 dB suppression in the *OFF* state. This ensures that only the desired pulses are amplified and delivered to the resonator, thereby reducing noise and preserving signal fidelity.

After interacting with the sample, the mw signal first passes through a limiter, which protects the downstream electronics by capping the maximum power released from the

resonator to a level compatible with the rest of the detection chain (in our case ∼20 dB). The signal then reaches a fast diode switch, controlled by the AWG (connection omitted in the schematic for clarity). During the pulse sequence, this switch attenuates the incoming signal by ∼ 50 dB, effectively generating a *"defence" pulse*. This temporary gating period blocks both the strong reflections and the transient energy released by the resonator after excitation. This transient energy, known as *ringing*, arises from the finite decay time of the stored electromagnetic energy and can last several microseconds[49]. To prevent this, the defence pulse is extended beyond the excitation window, remaining active until the resonator energy has sufficiently dissipated. Resonators with shorter decay times require shorter defence windows, which in turn permits reduced interpulse delays (e.g., smaller τ in a Hahn echo), improving flexibility and potentially enhancing signal strength[50]. Once the defence pulse ends, the switch opens, and the desired spin response can propagate unattenuated.

The surviving signal is then amplified by a cascade of low-noise amplifiers (LNAs), providing a total gain of ∼85-90 dB. This is subsequently fed into a second IQ mixer (#2), referenced to the same local oscillator as the first, which *downconverts* the I and Q components to the baseband frequency ω_{awg}. This step is crucial because most oscilloscopes cannot directly digitise GHz signals but can readily sample signals in the MHz range. Importantly, any spin-echo response generated by the sample will appear at ω_{awg} (or its harmonics). By Fourier transforming the oscilloscope's time-domain trace, the relevant spectral component can be isolated with high sensitivity, effectively suppressing broadband noise. Moreover, frequency-domain analysis preserves the phase information of the signal, making it particularly valuable for phase-sensitive measurements.

1.5.3.1 IQ Mixer Calibration

We briefly outline the calibration procedure for the IQ mixers used in the broadband operations described in the previous section. Calibration is essential because, without it, leakage from the LO (mw source) into the output port, as well as imperfections in

[49] For high-Q, critically coupled resonators.

[50] The duration of the defence pulse can be optimised experimentally, e.g., by applying soft pulses to monitor the resonator's ringing time.

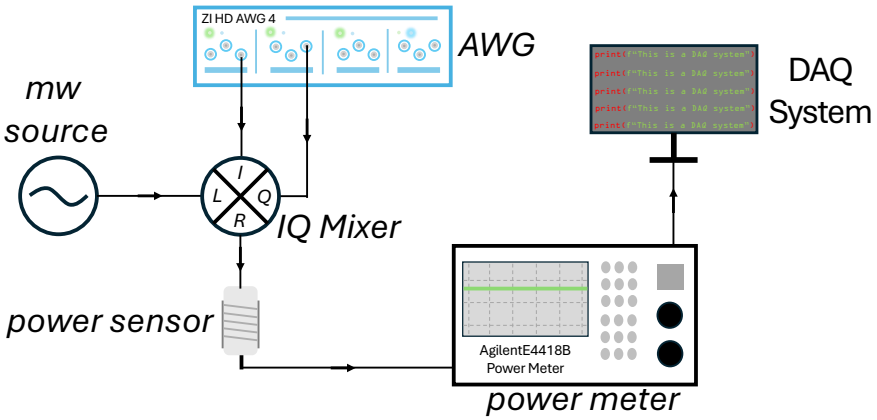

Figure 1.12: The circuit schematic for the calibration of IQ mixers.

the I/Q balance, would obscure the weak spin-dependent signal. This requirement is not unique to ESR: similar up- and downconversion stages appear in superconducting qubits, silicon single-electron transistors, and quantum dots [97], where mixer calibration is likewise a critical step. The schematic of the calibration circuit is shown in Fig. 1.12.

The IQ mixer receives the local-oscillator signal at its L port, while the AWG applies DC biases (typically a few mV) to the I and Q channels. The resulting output is monitored at the R port using a power meter (in our case, Agilent E4418B). By systematically sweeping the DC offsets applied to I and Q, one finds the bias point that minimises the residual output power at the LO frequency. This condition corresponds to maximal suppression of LO leakage, ensuring that the mixer is correctly balanced. Minimising LO leakage is thus important because any residual carrier signal reduces the available dynamic range and can mask the weak ESR response.

In practice, the optimal DC offsets depend on frequency, and thus the calibration must be repeated at each operating frequency of interest. While some groups have implemented automated calibration routines to handle many mixers simultaneously in multi-qubit platforms [98], here the procedure is performed manually. Once the optimal offsets are identified, they are recorded and subsequently applied using bias tees, as shown for the upconverting IQ mixer (#1) in Fig. 1.11.

1.5.4 DC Electric Field Devices

In Subsec. 1.2.2, we introduced the Hahn-Mims sequence but did not address an important practical challenge: how to apply a controlled DC $E-$field pulse to the sample while it is placed inside an ESR cavity. In what follows, we outline the general requirements for devices capable of delivering such pulses and briefly review the solutions that have been proposed in the literature.

The first practical consideration is that the device must fit within the limited space of the resonant cavity. Commercial ESR resonators typically allow only a few millimetres of clearance[51], as they are designed to accommodate sample tubes with frozen solutions or powders. Custom cavities with larger sample spaces could, in principle, host bigger electrodes, but this comes at the cost of increased mode volume and therefore weaker field amplitudes (see Eq. 1.51). Thus, comparable spatial constraints apply to both commercial and custom resonators. Within these limits, the device must provide sufficient sample volume while generating an E-field strong enough to shift the ESR resonance frequency by more than the intrinsic spin-echo linewidth.

A second key requirement is to minimise the device's perturbation of the resonator's oscillating field profile. In practice, this means limiting the use of metallic or other conductive materials which, while necessary for delivering $E-$fields to the sample, introduce mw (or rf) reflections and Ohmic losses that degrade the resonator performance. This trade-off has been a central challenge in previous SEC studies [16, 30, 34].

Two main designs have been developed so far. The first involves supplying the E-field by inserting two thin conducting wires into the sample solution, a straightforward method effective for liquids or dissolved powders. This configuration enabled the first detection of SEC in molecular nanomagnets [34] and electric-field-modulated ESR [16]. A fundamental limitation, however, is that the field strength scales inversely with the wire separation: reducing the gap increases the E-field amplitude but also introduces stronger field inhomogeneity. As a result, different spins experience different local E-fields, acquiring unequal E-field-induced phase shifts. This effect is similar to inhomogeneous

[51] For example, 5 mm in the Bruker ER-4118X-MD5 (X-band) resonator used in Chapter 2.

broadening in conventional ESR and ultimately may lead to the reduction of the SEC signal. An alternative approach, which works also for solid-state samples, is to employ a parallel-plate capacitor inserted inside the resonator [30]. To minimise the perturbation of the cavity mode, the electrodes are typically fabricated as thin metallic layers patterned on a printed circuit board (PCB). These layers consist of a ∼10-20 nm seed layer of Cr or Ti, followed by a ∼100-200 nm Au film deposited by thermal evaporation. This design has the advantage of delivering the required E-field to the sample while having comparatively good field homogeneity.

Beyond the wire and parallel-plate capacitor approaches discussed above, there are other designs to consider, though not employed in this thesis. One such option is a "hybrid" design for solid samples, where one face of the sample is metal-plated and contacted with a wire, while the opposite face is coupled to a PCB electrode (as in the parallel-plate method) using, for instance, vacuum grease. This arrangement could, in principle, generate strong and relatively homogeneous $E-$fields, with the maximum field strength set by the sample width. Another possible design would employ *interdigitated* 2D electrodes, onto which the sample is deposited in liquid form and subsequently dried, leaving the material adhered to the capacitor surface. This design raises two considerations: (i) field homogeneity is limited by the finite thickness of the dried sample, since the $E-$field lies in the plane of the electrodes. Thinner, more uniform layers could be achieved through techniques such as spin coating. (ii) Molecules deposited on top of the metallic electrodes contribute to the ESR signal but do not experience the applied $E-$field, thereby reducing the measurable SEC effect. A possible mitigation strategy is to use photolithographic masking to restrict the sample deposition to the electrode gaps, ensuring that only molecules within the active field region contribute.

The specific device implementations adopted in this thesis will be discussed in detail in the relevant chapters. In particular, Chapter 2 introduces an additional design constraint not discussed here: the electrodes must also be transparent to UV radiation, as the study relies on optical initialization.

This work appears in arXiv:2506.19640, and it has been accepted for publication in the Journal of the American Chemical Society.

2

Spin-Electric Coupling in Optically Excited Molecules

2.1 Electric-field Quantum Sensing using Molecular Spins

Quantum sensing is an emerging field that harnesses the fundamental properties of quantum systems to measure physical quantities with exceptional precision [99]. By exploiting uniquely quantum resources such as superposition, coherence, and entanglement, these sensors can access regimes of sensitivity that are unattainable with classical approaches [100]. This framework has enabled remarkable advances across diverse platforms, including nitrogen-vacancy centres in diamond [101], superconducting circuits [102], and cold atoms [103]. Quantum sensing of electric fields, in particular, has seen rapid development through systems like Rydberg atoms [104], trapped ions [105], and superconducting circuits [106], which offer excellent sensitivity via strong coupling to electric fields. Yet, these platforms typically operate at micrometre to millimetre scales, limiting their spatial resolution and hindering their ability to access electric fields near surfaces or within heterogeneous environments [107].

Molecular electron spins have long been studied as promising candidates for magnetic field sensing due to their well-defined spin states and intrinsic coupling to magnetic fields

via the Zeeman effect [55]. As outlined in Sec. 1.4, another strength lies in the ability to extensively tailor their properties through chemical design, enabling controlled coupling to electric [30], optical [57], and mechanical [58] degrees of freedom, as well as impressively long phase coherence times, up to one millisecond at 10 K [60]. Building on these advantages, recent efforts have begun exploring molecular spins for electric field sensing. Molecular systems offer a compelling route, as their intrinsically nanoscale dimensions enable high spatial resolution and placement in direct proximity to the sensing target [59].

Progress toward electric field sensing with molecular systems has revealed that molecular spins can exhibit strong coupling to electric fields [30, 34, 108, 109]. However, to achieve sufficient sensitivity using electron spin resonance, a significant spin polarization in magnetically diluted samples is desirable, often necessitating low temperatures. An alternative route to large spin polarisations is offered by light-induced species such as spin-correlated radical pairs[1] (SCRPs), which have shown room-temperature operation, owing to the generation of polarised spin states through spin-selective processes during their formation [110]. SCRPs have been widely investigated as potential candidates for spin qubits, particularly for implementing 2-qubit gates, where two electron spins are correlated via, for instance, the zero-field splitting, or $J-$coupling [59]. Quantum teleportation has already been successfully demonstrated using SCRPs, highlighting their ability to embody entangled states between two electron spins within a molecule [111].

Recently, Xie *et al.* [56] showed that SCRPs can be used to sense electric fields by enclosing one of the radicals inside a cyclophane host molecule. In their system, the local electric field within this host changes the distance between the two spins, producing a measurable shift in the spin-echo signal. Crucially, however, such electric field effects on light-induced spin states have, until now, not been demonstrated using externally applied (and controllable) E-fields.

In this chapter, we present a proof-of-principle demonstration of a spin-based quantum sensor for electric fields, implemented in an optically excited molecular state. We first

[1] A spin-correlated radical pair refers to two radicals formed by photoinduced charge separation, in which the electron spins remain quantum-mechanically correlated in either a singlet ($S = 0$) or triplet ($S = 1$) configuration.

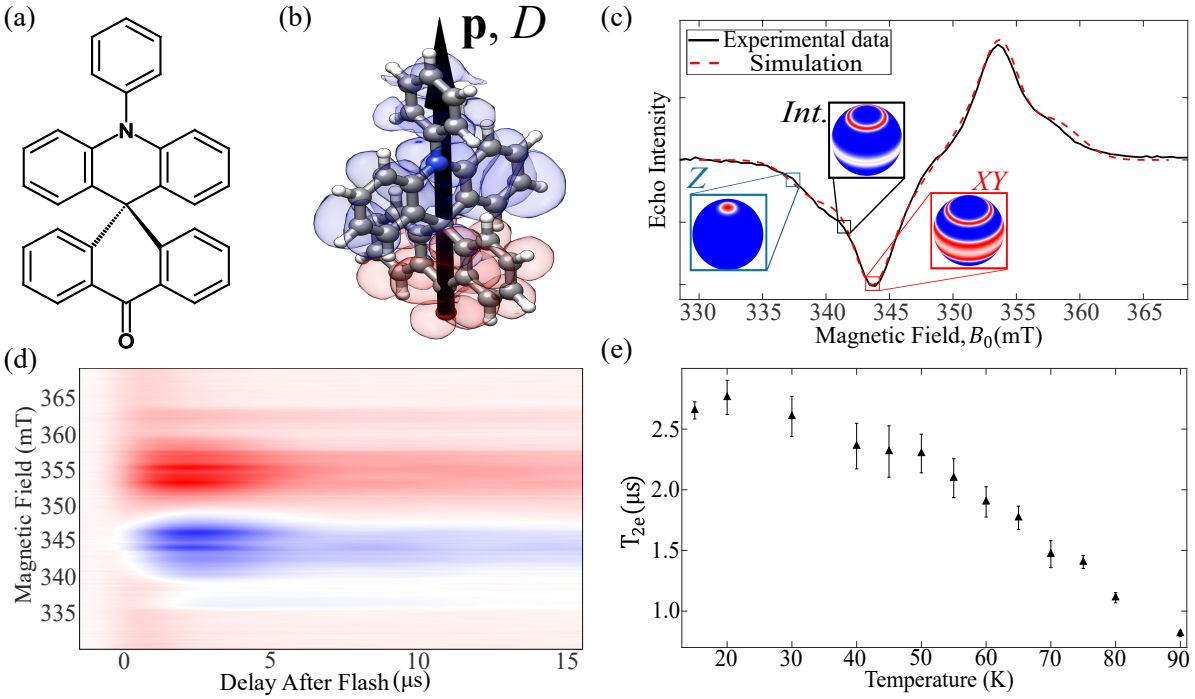

Figure 2.1: Magnetic and optical characterization of ACRSA, whose molecular structure is shown in (a). (b) DFT-calculated electron (red) and hole (blue) densities of the ^{3}CT state, together with the simulated orientation of the molecular dipole moment **p** and ZFS D. (c) Experimental and simulated EDFS of ACRSA in PMMA at 20 K, showing the relevant B_0-field positions and the corresponding orientation selection on the unit sphere (with red denoting stronger contributions to the resonance). (d) Transient ESR spectrum demonstrating that spectral features persist for (at least) 15 μs after photoexcitation. (e) Electronic coherence time as a function of temperature.

describe the optical and magnetic properties of the sample used in this work, followed by the design of the device architecture that enables the application of DC electric fields while preserving optical initialization and magnetic control. Finally, we develop a quantitative model based on the spin Hamiltonian to elucidate the microscopic origin of the observed spin-electric coupling (SEC).

2.2 Characterization of ACRSA

The system under investigation is the commercially available molecular semiconductor ACRSA (chemical formula: $C_{32}H_{21}NO$, IUPAC name: 10-phenyl-10H,10'H-spiro[acridine-9,9'-anthracen]-10'-one). Its structure consists of an electron-donating acridine moiety and an electron-accepting anthracenone unit, rigidly and orthogonally coupled through a

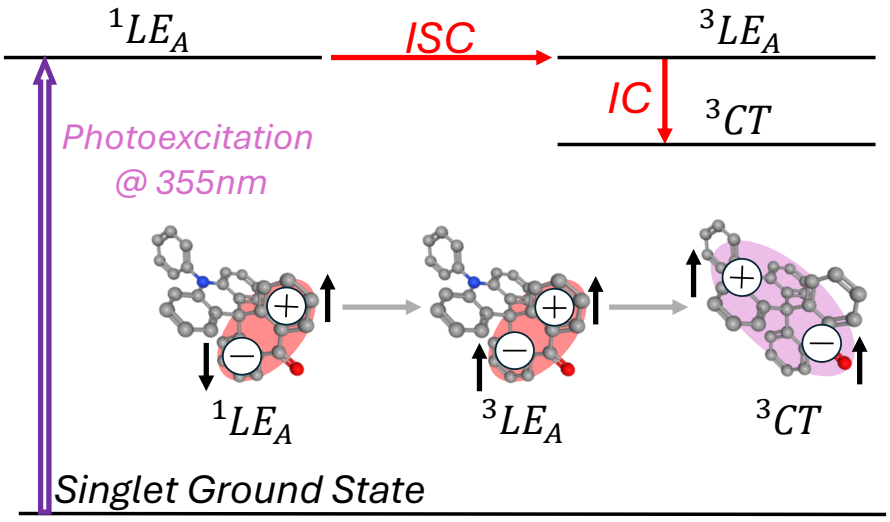

Figure 2.2: Optical-relaxation diagram of ACRSA, adapted from [112], showing the main photophysical processes following excitation at 355 nm. The diagram illustrates the sequence of intersystem crossing (ISC) and internal conversion (IC) that leads to the formation of the triplet charge-transfer state (^{3}CT), where the electron and hole are spatially separated across different moieties of the molecule. *Inset:* Schematic depiction of the evolution of the electron-hole distribution within ACRSA.

spiro-bond (Fig. 2.1(a)). In what follows, we define the direction connecting the oxygen and nitrogen atoms as the *molecular major axis*.

ACRSA is a well-known organic blue-green emitter, exhibiting a fluorescence maximum at roughly 490 nm [113]. Its photophysical properties have been extensively investigated, both theoretically [114] and experimentally [115], particularly in the context of organic-based solid-state lighting and display technologies [116–118]. This interest stems from the fact that, unlike conventional light-emitting compounds, ACRSA and related molecules can achieve high performance without incorporating heavy metals, thereby reducing material costs and environmental impact [119]. This purely organic character is also relevant to the present study, as it implies that atomic spin-orbit coupling (SOC) plays only a minor role in the spin dynamics of ACRSA [7].

2.2.1 Optical Properties of ACRSA

The optical response of ACRSA is governed by a cascade of relaxation pathways following photoexcitation. Among these, intersystem crossing (ISC) and internal conversion (IC) play a central role in the formation of the excited quantum state investigated here (see Fig.

2.2). ISC involves a non-radiative transition between electronic states of different spin multiplicity, typically converting an excited singlet into a triplet configuration through coupling between electronic and vibrational degrees of freedom. IC, on the other hand, is a rapid (10^{-11}-10^{-14} s) non-radiative relaxation process that redistributes population among excited vibrational levels as the molecule relaxes within its potential-energy surface [120].

Previous studies have examined the electronic structure and photochemistry of ACRSA under different solvents and excitation wavelengths [112, 113]. These works established that the molecule supports both charge-transfer[2] (CTr) and locally excited (LE) states [121]. In CTr states, an electron is transferred from the donor to the acceptor moiety, creating an electron-hole pair delocalised across the two units, while in LE states the charge densities are localised within a single moiety [122].

The main relaxation pathways upon excitation at 355 nm (the wavelength used in this work) in ACRSA are summarised in the *Jablonski diagram* in Fig. 2.2 and are based on Ref. [112]. After optical excitation, a vibronically assisted[3] transition initially promotes the molecule from the singlet ground state to a singlet LE state localised on the anthracenone moiety (^1LE_A). From there, population is transferred via ISC into a triplet LE state (^3LE_A), which subsequently relaxes via IC into the metastable CTr triplet state (^3CT), characterised by spatial separation of the electron and hole across the molecule (see Density Functional Theory, DFT, in Fig. 2.1(b)). Excitation at other wavelengths, by contrast, can preferentially access different LE states depending on the photon energy [112]. In this work, however, we focus on the CTr state, whose spatially separated electron-hole pair generates a larger electric dipole moment $\mathbf{p}$, thereby enhancing the electric interaction ($\sim \mathbf{p} \cdot \mathbf{E}$) and, therefore, the molecule's sensitivity to external E-fields (see Sec. 2.5).

An important factor for our quantum sensor is the time the photoexcited electron-hole pair remains separated prior to recombination (that is, relaxes back to a singlet state), which, along with the spin coherence time, determines the overall sensor performance.

[2]In most literature the acronym for charge-transfer states is CT. However, to avoid confusion with spin clock transitions, which are central to Chapter 5, we use CTr throughout this chapter.

[3]The vibronic coupling is defined as the interaction between a molecule's electronic and vibrational degrees of freedom.

This can be measured using transient ESR (trESR), where a short laser pulse excites the system while continuous resonant microwave radiation probes the ESR response. The signal is then recorded as a function of the time elapsed after the laser pulse, commonly referred to as the *Delay After Flash* [123], thereby tracking the evolution of spin sublevel populations over time. Fig. 2.1(d) shows the trESR spectrum of ACRSA at 20 K, excited with a 355 nm laser (0.1 W, corresponding to 2 mJ/pulse at 50 Hz repetition rate). Notably, the characteristic ESR features, described in the next subsection, remain clearly observable for at least 15 μs after photoexcitation.

2.2.2 Magnetic Properties in ACRSA

As detailed in Subsec. 2.2.1, optical excitation at 355 nm populates a metastable charge-transfer triplet state in ACRSA. The corresponding X-band echo-detected field sweep (EDFS), recorded at 20 K for a solution of ACRSA dissolved in poly(methyl methacrylate) (PMMA, 5% by weight, or ~ 90 μM), is shown in Fig. 2.1(c). This spectrum is described using the spin Hamiltonian for an axially symmetric triplet state ($S = 1$):

$$\hat{\mathcal{H}} = D\left(\hat{S}_z^2 - \tfrac{1}{3}S(S+1)\right) + \mu_B g B_0\left(\hat{S}_z\cos\theta + \hat{S}_x\sin\theta\right), \tag{2.1}$$

where θ denotes the angle between the molecular major axis and the external magnetic field B_0 (see Fig. 2.3(a)). This coordinate choice is justified by DFT calculations performed with the ORCA package [124] (App. A.2.1), which indicate that the principal axis of the ZFS is aligned within $\lesssim 3^\circ$ of the ACRSA symmetry axis. Fitting the experimental spectrum (red dotted line) using the EasySpin MATLAB library [125] yields $|D| \simeq 317$ MHz and a g-factor close to the free-electron value, $g \simeq g_e$. In addition, a distribution of D values (*strain*) of roughly 150 MHz is required to reproduce the experimental linewidth, whose origin is attributed to inhomogeneous broadening arising from local variations such as differences in molecular packing, or slight structural distortions.

The overall shape of the EDFS in Fig. 2.1(c) highlights two key features of the system: (i) as discussed in Subsec. 1.1.6, the measured spectrum in frozen solutions represents the orientationally averaged response of all possible molecular orientations, resulting in a broad, structured spectrum rather than discrete resonance peaks; and (ii) the presence of

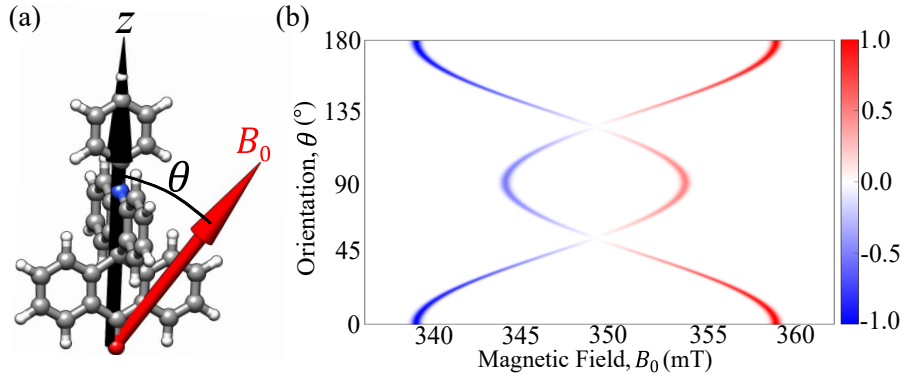

Figure 2.3: (a) Molecular major axis of ACRSA (black arrow) aligned with the DFT-calculated principal axis of D spanning an angle θ with the applied magnetic field B_0 (red arrow). (b) Simulated orientation-dependent spectra of ACRSA at X-band, computed using Eq. 2.1, where blue and red correspond to emission and absorption components, respectively. The simulation illustrates the effect of orientation selection, showing how varying B_0 selectively probes different subsets of molecular orientations within the frozen solution.

both absorption and emission components (appearing as positive and negative signals, respectively) indicates that the system is spin polarised [123].

The phenomenon described in (i) underlies the concept of *orientation selection*, which is central to the SEC measurements discussed in Sec. 2.4. This effect is illustrated in Fig. 2.3(b), which shows the simulated θ-dependent spectra for ACRSA at X-band, computed using Eq. 2.1. As the static magnetic field B_0 is varied, different molecular orientations satisfy the resonance condition, meaning that each field value selectively probes a distinct subset of orientations within the ensemble. In our study, SEC measurements are performed at three representative field positions, indicated in Fig. 2.1(c). At $B_0 = 337.5$ mT (Z), the external field is nearly aligned with the molecular anisotropy axis (see inset of the figure), at 341.5 mT (Int.), it forms an intermediate angle of approximately 45°, while at 344 mT (XY), it is predominantly perpendicular to that axis. The corresponding orientational distributions for these field positions are analysed in greater detail in Sec. 2.5.

By fitting the spectrum in Fig. 2.1(c) and assuming an easy-plane anisotropy ($D > 0$, in line with the DFT results), the light-induced spin polarisation at zero field is found to be ∼95% in the $|m_s = 0\rangle$ sublevel and 2.5% in each of the $|m_s = \pm 1\rangle$ states, indicating nearly complete spin polarisation. This is markedly higher than the thermal population

differences typically observed in molecular magnets exhibiting significant SEC at 20 K, where, for example, only a 1.7% population imbalance is found in $S = 1$ antiferromagnetic rings [34] and between 1% and 2.8% in $S = 5/2$ Mn-based complexes [126]. This demonstrates that, in theory, optically excited molecules offer a more direct route toward room-temperature operation than conventional ground-state molecular spin systems.

DFT calculations further elucidate the microscopic origin of D in Eq. 2.1. In contrast to previous reports [30, 34], the dominant contribution to the ZFS in ACRSA arises from spin-spin interactions between the optically generated electron and hole wavefunctions, whose spatial distributions are shown in Fig. 2.1(b), rather than from strong atomic SOC. This finding is consistent with the absence of heavy atoms in ACRSA [123, 127].

Finally, Fig. 2.1(e) presents the temperature dependence of the electron coherence time (T_{2e}). At 20 K, T_{2e} exceeds 2.5 μs, and it remains above 1 μs at liquid-nitrogen temperature. Although the coherence times at $\sim$ 80 K would, in principle, still permit SEC measurements, the signal-to-noise ratio (SNR) of the transient-echo signal becomes too weak to resolve electric-field-induced modulations. For this reason, and since the SNR ultimately sets the sensitivity of our molecular sensor (see App. A.2.3), all SEC data presented in this chapter were acquired at 20 K, where the SNR is sufficient for unambiguous detection. It should be noted that T_{2e} is considerably shorter than the recombination time of the photoexcited electron-hole pair ($>$ 15 μs from Fig. 2.1(d)), indicating that the latter timescale does not limit the sensing protocols employed in this study.

2.3 Parallel-plate Capacitor Design

As discussed in Subsec. 1.5.4, the design of the devices used to apply the DC E-field in SEC measurements is constrained by the limited space within the magnetic-resonant cavity and by the need to minimise disturbances to its electromagnetic mode. In the present study, an additional condition is that the device must remain transparent to UV excitation, so that the laser pulse can initialise the system into the desired triplet state. A simple option would be to insert a pair of wires directly into the solution

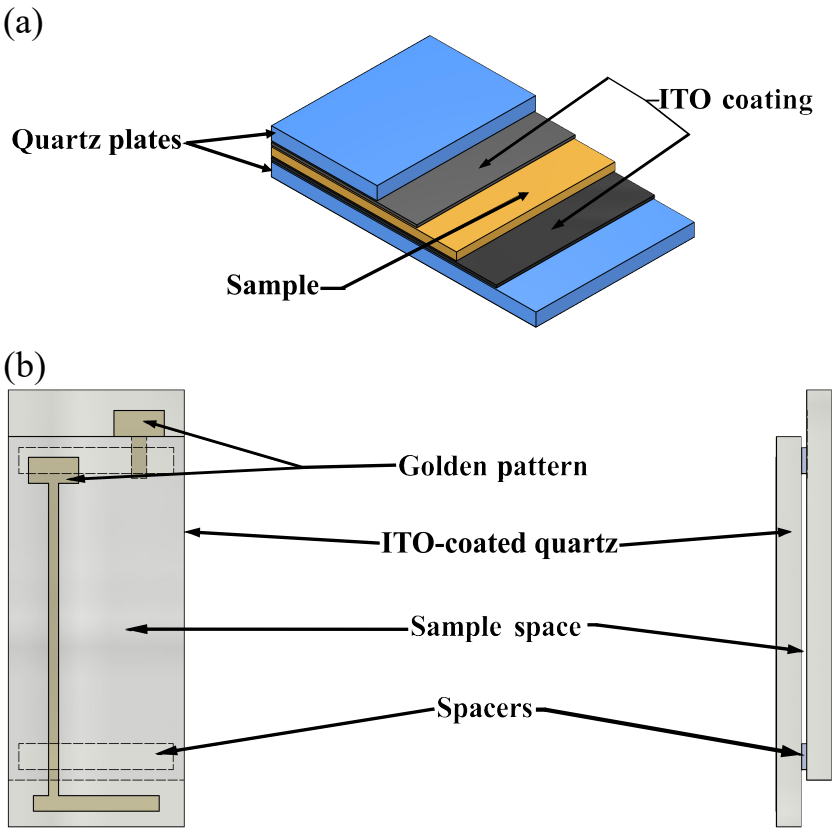

Figure 2.4: (a) A false-colour scheme of the E-field device used in the measurements. The DC electric-field pulse is generated by applying a voltage across a parallel-plate capacitor, whose electrodes are made from quartz coated with indium-tin oxide. These electrodes are nearly perfectly transparent to UV and microwave excitations, thus allowing both the initial laser and ESR pulses to interact with the sample. (b) A more detailed schematic of the device, illustrating the T-shaped golden patterns and the offset between the two plates. These features ensure multiple wire bondings between the device and the E-field supply.

and apply the electric field across them. Such a setup, however, would generate weak and inhomogeneous fields and would not represent a viable device concept, since any practical sensor requires the molecular material to be incorporated into a defined device architecture rather than left dissolved in solution. A more suitable approach is to use a parallel-plate capacitor geometry, in which the ACRSA:PMMA film is dried between two UV-transparent electrodes. In this configuration, the achievable field strength is set by the film thickness, and the parallel-plate design ensures reasonable spatial homogeneity while remaining compatible with optical initialization.

In our study, the electrodes are fabricated from 7.3 mm $\times$ 3.5 mm $\times$ 0.5 mm quartz chips, whose dimensions match the Bruker ER-4118X-MD5 X-band resonator used here. Each

chip is coated with a few hundred nanometres of indium-tin oxide (ITO), a transparent conductive oxide that combines optical transmission with electrical conductivity and is widely used in organic solar cells [128]. The ITO-coated quartz substrates therefore serve a dual role: they permit laser excitation and microwave ESR pulses to reach the sample, while keeping the amount of conductive material inside the resonator minimal. On top of the ITO layer, T-shaped gold patterns (∼150 nm thick) are defined by optical lithography (SUSS MJB4 mask aligner). These gold features are wire-bonded to copper electrodes plated onto a thin 25 mm × 3.5 mm PCB, which provides mechanical support and the electrical interface to the E-field pulse generator. The complete device layout, including the plate offset that accommodates multiple wire bonds to the copper contacts, is shown in Fig. 2.4.

The electrode separation was chosen to optimise the trade-off between the applied E-field strength and the accessible sample volume. A gap of 200 μm was selected as a practical compromise, providing a sufficiently large sample volume to yield measurable signals while maintaining a field strength capable of modulating the desired spin transitions. With the voltage set to 300 V (using an Avtech AVR-4-B, used in all subsequent SEC measurements), this configuration produces a field of $\sim$ 15 kV/cm across the plates and accommodates a frozen sample volume of approximately 3.5 μl.

2.4 Spin-Electric Coupling Measurements

We now characterise the SEC of ACRSA at 20 K using the Hahn-Mims pulse sequence described in Sec. 1.2.2. The only modification, illustrated in Fig. 2.5(a), is the inclusion of an initial 355 nm laser pulse to populate the CTr triplet state, which is the focus of our study. The interpulse delay across all measurements was set to $\tau = 2$ μs, corresponding to approximately 75% of the coherence time at this temperature, $T_{2e} \simeq 2.7$ μs (see Fig. 2.1(e)).

Fig. 2.5(b) shows a representative SEC measurement at the Int. field position ($B_0 =$ 341.5 mT in Fig. 2.1(c)), obtained using an electric-field pulse of fixed amplitude $E \simeq$ 15 kV/cm and variable duration between 0 and $2\tau = 4$ μs. The in-phase echo component

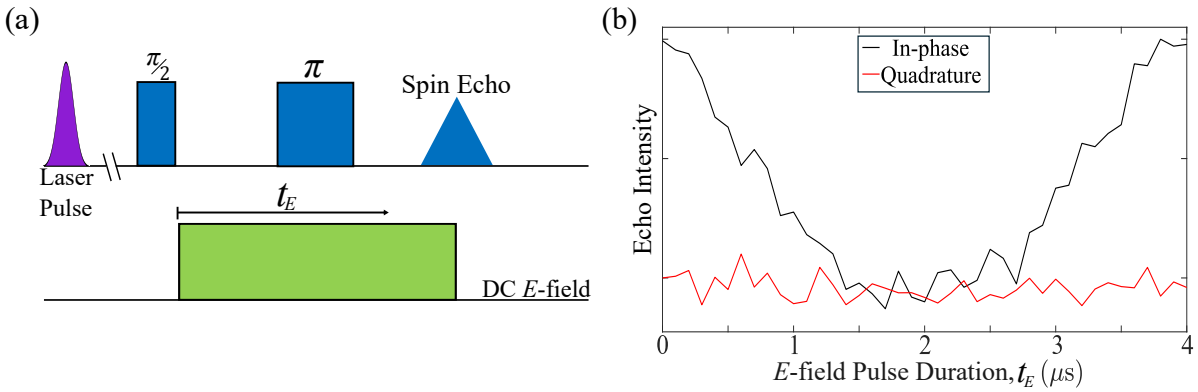

Figure 2.5: (a) Hahn-Mims sequence including the initial laser pulse used to initialise the triplet state. (b) (Experimental) In-phase and quadrature components of the echo intensity as a function of the electric-field-pulse duration t_E, measured at 20 K at the Int. field position. The absence of a quadrature response in a spin ensemble indicates that the SEC in ACRSA is linear, i.e., the resonance shift induced by the electric field scales as $\delta f \propto E$.

(black) decreases as the electric-field pulse extends from 0 to τ and recovers at 2τ, demonstrating coherent electric-field modulation of the spin transition [126]. In contrast, the quadrature component (red) remains constant, which, combined with the random orientation of the molecular ensemble, indicates that the response arises from a first-order SEC process, that is, the frequency shift $\delta f(E)$ depends linearly on the applied electric field (see the final part of Sec. 1.2.2).

To obtain a more complete picture of the SEC in ACRSA, analogous measurements were performed at the Z ($B_0 = 337.5$ mT) and XY ($B_0 = 344.0$ mT) field positions. As discussed in Sec. 2.2.2, varying B_0 modifies the θ-dependent orientational distribution of molecules resonant with the mw excitation (orientation selection), thereby allowing the angular dependence of the SEC to be experimentally assessed. The corresponding results are shown in the top panels of Fig. 2.6, where the E-field-pulse duration was varied between 0 and $\tau = 2$ μs (rather than 2τ, as in Fig. 2.5). Panels (a) and (b) correspond to the $\mathbf{E} \parallel \mathbf{B_0}$ and $\mathbf{E} \perp \mathbf{B_0}$ configurations, respectively.

When $\mathbf{E} \parallel \mathbf{B_0}$ (Fig. 2.6(a)), the strongest SEC response, i.e., the most pronounced echo modulation, is observed at the Z field position. This behaviour can be understood by noting that DFT simulations on the excited CTr state predict an electric dipole moment $\mathbf{p}$ approximately aligned with the principal axis of D. Since this anisotropy axis is itself

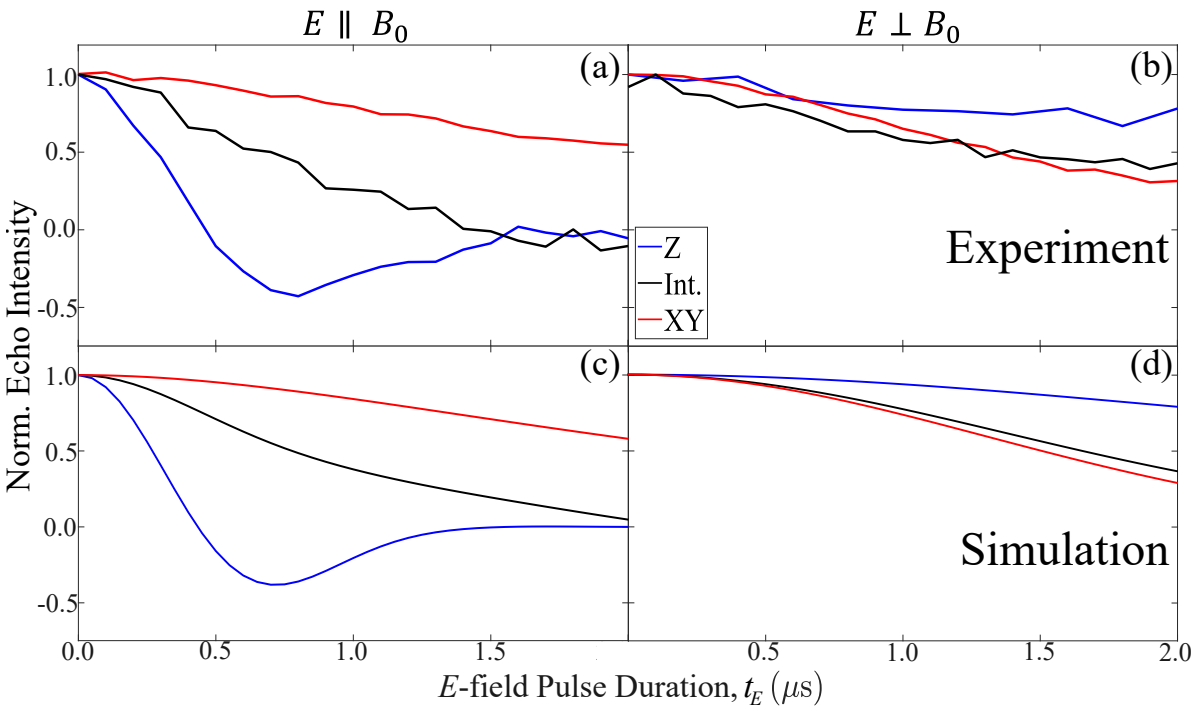

Figure 2.6: (a,b) Experimental spin-echo intensities as a function of the E-field pulse duration at the three field positions considered in this work, for (a) $E \parallel B_0$ and (b) $E \perp B_0$. (c,d) Corresponding simulations based on the model discussed in Sec. 2.5.

nearly parallel to B_0 at the Z position (see the inset of Fig. 2.1(c)), the applied electric field in this configuration is effectively aligned with the molecular dipole moment, i.e., $\mathbf{p} \parallel \mathbf{E}$. Such alignment maximises the electric coupling energy and, consequently, the strength of the SEC. At other field positions, the molecular orientations resonant with B_0 are progressively tilted away from $\mathbf{E}$, thereby increasing the misalignment between $\mathbf{p}$ and $\mathbf{E}$ and resulting in a correspondingly weaker SEC response.

In the $\mathbf{E} \perp \mathbf{B_0}$ configuration (Fig. 2.6(b)), the ESR spectrum and the angular distribution of molecular orientations remain unchanged owing to the random orientation of spins in the frozen solution, whereas the relative alignment between the applied $\mathbf{E}$ and $\mathbf{p}$ is modified, leading to different SEC responses. As a result, the strongest SEC response is observed at the XY position, while the weakest occurs at Z, consistent with this position now corresponding approximately to $\mathbf{p} \perp \mathbf{E}$.

In the next section, we develop a quantitative model based on the spin Hamiltonian and DFT calculations to reproduce this angular dependence, estimate the SEC strength

in ACRSA, and elucidate its microscopic origin.

2.5 Modelling the Spin-Electric Coupling

We now introduce a theoretical model to quantitatively describe the SEC in ACRSA. The working assumption is that the dominant contribution to this effect arises from the modulation of the zero-field splitting parameter D in Eq. 2.1. This hypothesis is supported by the observation that both the electric dipole moment $\mathbf{p}$ and D originate from the same underlying charge-transfer process; upon photoexcitation, an electron-hole pair is generated, whose spatial separation defines $\mathbf{p}$, while their mutual spin-spin interaction gives rise to D, as confirmed by DFT calculations. When an external electric field is applied, it perturbs this electron-hole interaction through its coupling to $\mathbf{p}$, thereby altering the molecular geometry and/or electronic structure and ultimately leading to a change in D (see Eq. 1.39).

Assuming a linear response, as supported by Fig. 2.5(b), the dependence of the ZFS on an external electric field for the configuration $\mathbf{E} \parallel \mathbf{B_0}$ (cf. Eq. 2.4) can be expressed as:

$$D(E) = D(0) + \kappa E \cos(\theta), \tag{2.2}$$

where κ is the SEC constant (in Hz/(V/m)), and $D(0)$ is the unperturbed anisotropy. Note that, since $\mathbf{p} \parallel D$ (Sec. 2.4), in this case θ also corresponds to the angle between the electric dipole moment $\mathbf{p}$ and the applied electric field $\mathbf{E}$. Although Eq. 2.2 resembles the form commonly used to describe SEC effects in single-ion spin systems [30, 108, 126, 129], its microscopic origin in ACRSA is fundamentally different. Here, D arises from the magnetic dipole interaction between the electron and hole, which localise on distinct parts of the molecule, rather than from atomic SOC associated with transition-metal or lanthanide centres. The presence of a substantial molecular dipole moment $\mathbf{p}$ ($\sim$ 23 D, according to DFT calculations) in ACRSA enables an electrostatic interaction between the electron-hole pair and an external electric field, with the coupling strength directly governed by the electric polarizability of the molecule [30].

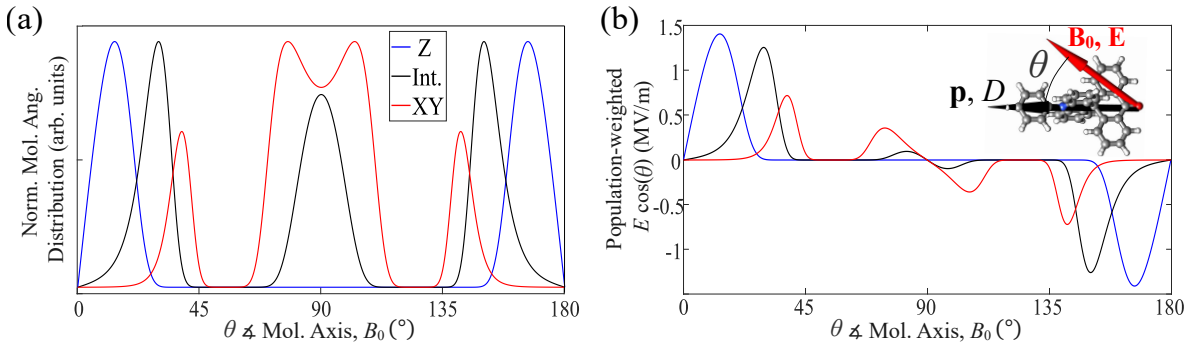

Figure 2.7: (a) (Simulated) Angular distribution of resonant molecules as a function of the angle θ between the external magnetic field $\mathbf{B_0}$ and $\mathbf{p}/D$, as illustrated in the inset of panel (b). The three distributions correspond to the magnetic-field values used in the SEC study (see Fig. 2.1(c)). (b) (Simulated) Effective electric field, calculated as the projection of the electric field along the $\mathbf{p}/D$ axis ($E \cdot \cos(\theta)$, with $E = 15$ kV/cm) weighted by the $\mathbf{B_0}$-dependent molecular population shown in (a). This represents the strength of the interaction between the electric field and the molecular ensemble, which takes into account the angular distribution variations at different B_0.

While Eq. 2.2 accounts only contribution from molecules with a specific orientation θ, it is essential to account for orientational averaging to model SEC in a solution. At each resonant field B_0, the ensemble of molecules does not share a single orientation but instead spans a distribution of angles θ, with each orientation experiencing a distinct modulation of D. Fig. 2.7(a) shows the simulated orientational distributions for the three experimental field positions. At the Z-position (blue trace), most resonant molecules lie within a narrow angular range centred around $\simeq 15°$ (or equivalently, 165°) with respect to $\mathbf{B_0}$. By contrast, the XY-position exhibits a broad population around $\theta \simeq 90°$, with a noticeable subpopulation at smaller angles ($\lesssim 45°$), explaining why its SEC, although weaker, is still detectable at this position even when $\mathbf{E} \parallel \mathbf{B_0}$. On the other hand, panel (b) shows the corresponding simulated population-weighted effective electric fields (assuming $E_{\max} \simeq 15$ kV/cm), which quantify the coupling strength of a molecule at a given orientation θ to the applied electric field. These effective fields are computed as the projection of the electric field along the $\mathbf{p}/D$ axis, $E \cdot \cos(\theta)$, weighted by the B_0-dependent molecular populations from panel (a).

Using these simulations together with Eq. 2.2, we computed the SEC oscillations shown

in Fig. 2.6(c) and extracted a SEC coupling parameter of

$$\kappa = (0.59 \pm 0.03)\ \text{Hz/(V/m)}, \quad \sigma = (0.15 \pm 0.01)\ \text{Hz/(V/m)}. \tag{2.3}$$

Here, σ accounts for a Gaussian broadening of the SEC strength, which is required to reproduce the damping of the oscillations that cannot be explained by orientational averaging alone (see Fig. 2.9(a)). Inhomogeneity of the applied E-field within the capacitor and/or strain in D can contribute to this effect. The close agreement between the experimental and simulated echo modulations provides initial evidence that our model captures the essential features of the SEC in ACRSA, supporting the proposed mechanism based on an electric modulation of D.

The SEC strength can then be extracted as the ratio between the electrically induced resonance-frequency shift and the applied field. For the Z position, we obtain $\delta f/E = (0.51 \pm 0.02)$ Hz/(V/m). Notably, this value is comparable to those reported for molecular samples exhibiting much stronger atomic SOC [34, 126, 130], indicating that pronounced SOC is not strictly required to observe sizeable spin-electric coupling, contrary to common expectations [16, 30].

Using this $\delta f/E$, we estimate the minimum detectable E-field of our molecular-based sensor. As detailed in App. A.2.3, this is limited by the SNR of the transient echo signal from ACRSA, which defines the weakest E-field-induced modulation of the spin echo that can be reliably resolved. We find $E_{\text{min}} \simeq 1.2$ kV/cm, corresponding to a resonance shift of $\delta f(E_{\text{min}}) \simeq 63$ kHz, or roughly a 29% change in echo intensity for $\tau = 2\ \mu$s (as calculate from $1 - \cos(2\pi\delta f(E_{\text{min}})\tau)$). Enhancing the ESR signal, e.g., by increasing the triplet-state yield, would improve the SNR and, in turn, the sensor performances. Besides boosting the signal, the sensitivity (i.e., E_{min}) can also be improved by increasing[4] κ and/or T_2. While enhancing κ requires molecular engineering or the use of alternative SCRP systems, T_2 can be extended through established approaches such as reducing the environmental nuclear-spin bath, for instance, by deuterating the host matrix [60].

[4] A longer T_2 would lead to the same SNR with a larger τ, hence enabling the same modulation to the spin echo with a smaller E-field.

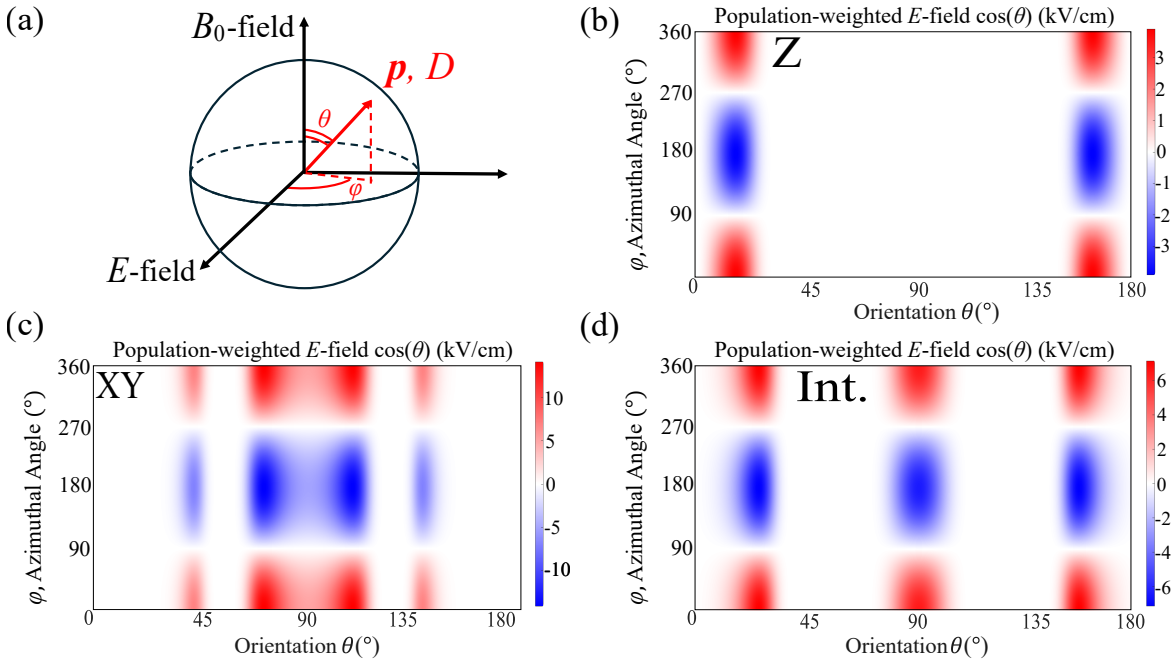

Figure 2.8: Schematic illustration of the molecular orientation (red arrow), with the molecular major axis labelled as "$\mathbf{p}, D$", in the configuration $E \perp B_0$. In contrast to the $E \parallel B_0$ case, the angle between the E-field and the molecular axis (determining the strength of the spin-electric coupling) depends on both the polar angle θ, and the azimuthal angle φ between the plane spanned by $\{E,\ B_0\}$ and the molecular axis. (b-d) Angular dependence of the population-weighted effective E-field for the Z (b), XY (c), and Int. (d) field positions.

So far, we have considered only the case where the applied E-field is aligned with B_0. In this configuration, the angle θ simultaneously specifies the orientation of B_0 relative to the anisotropy axis D (which sets the resonance condition) and the orientation of $\mathbf{E}$ relative to the molecular dipole moment $\mathbf{p}$. By contrast, the case of $\mathbf{E} \perp \mathbf{B_0}$ requires an additional degree of freedom: the azimuthal angle φ, defined as the angle between $\mathbf{p}$ and the plane spanned by $\mathbf{E}$ and $\mathbf{B_0}$. A schematic illustration is shown in Fig. 2.8(a). In this case, Eq. 2.2 must be rewritten to explicitly include φ, yielding

$$D^{E \perp B_0}(E) = D(0) + \kappa \cdot E \sin(\theta)\cos(\varphi). \tag{2.4}$$

The resulting population-weighted E-fields for the three molecular orientations are shown in panels (b-d) of the figure. The additional modulation by $\cos(\varphi)$ leads to a weaker response compared to the $E \parallel B_0$ case. This follows from observing, for instance, the behaviour at $\theta \simeq 15°$ in panel (b): the signal is maximised at $\varphi = 0°$, but vanishes around $\varphi = 90°, 270°$. Upon $\varphi-$orientational averaging, this effect diminishes the net

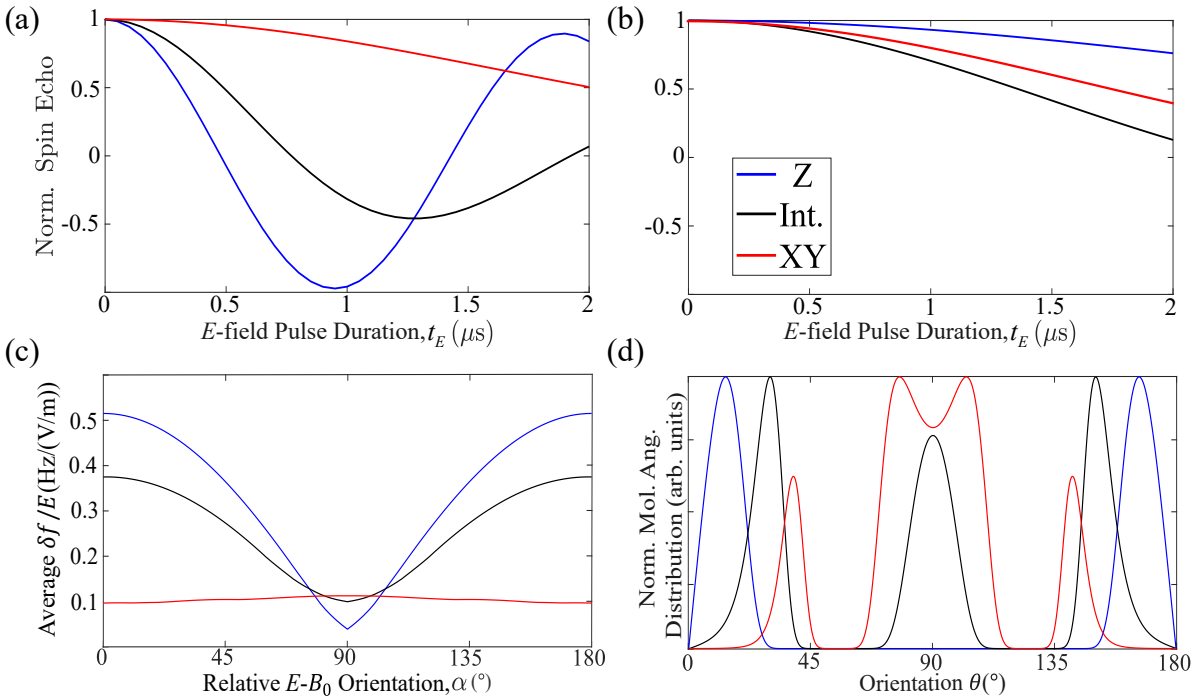

Figure 2.9: (a, b) Simulated SEC oscillations calculated without including a Gaussian distribution (σ in Eq. 2.3) of SEC strengths for $E \parallel B_0$ (a) and $E \perp B_0$ (b). (c) Angular dependence of the SEC strength as a function of the angle α between B_0 and the applied E-field. (d) Molecular θ-distribution for $D = -317$ MHz, showing no difference compared to Fig. 2.7(a) and thus confirming that our model is independent of the sign of the magnetic anisotropy.

SEC, explaining the overall weaker modulations observed in Fig. 2.6(b) compared to panel (a). The corresponding simulations in Fig. 2.6(d), performed using the same κ and σ values as in Eq. 2.3, accurately reproduce this behaviour and show good agreement with the experimental data.

More generally, for an applied field that forms an angle α with $\mathbf{B_0}$, the relative angle Ω between $\mathbf{E}$ and $\mathbf{p}$ is given by $\cos(\Omega) = \cos(\alpha)\cos(\theta) + \sin(\alpha)\sin(\theta)\cos(\varphi)$. Fig. 2.9(c) shows the resulting variation of the E-field-induced frequency shift $\delta f(E = 15$ kV/cm) as a function of α. The response is generally strongest for the Z position, while the XY orientation remains nearly constant and exceed the Z response only in a narrow window around $\alpha = 90°$. This angular dependence can be exploited for sensing applications: by comparing the relative SEC amplitudes for different molecular orientations, one can extract both the direction and magnitude of the applied E-field relative to the known orientation of B_0.

Finally, we assess whether the sign of the ZFS, assumed positive throughout this chapter as predicted by DFT, influences our SEC analysis. The sign of D determines the ordering of the triplet sublevels and thus which m_s projections are preferentially populated upon photoexcitation into the CTr triplet state [127], potentially affecting the SEC. EasySpin-based simulations indicate that for $D < 0$, the initial population is primarily in the $|m_s = \pm 1\rangle$ states, rather than in $|m_s = 0\rangle$ as in the $D > 0$ case. Despite this change in sublevel populations, Fig. 2.9(d) shows that the resulting molecular orientation distributions remain indistinguishable from those obtained with $D > 0$ (cf. Fig. 2.7(a)), with the same holding true for the SEC oscillation simulations. We therefore conclude that our model is independent of the sign of D.

2.6 Conclusion & Future Directions

In this chapter, we have demonstrated the presence of a sizeable spin-electric coupling (SEC) in a spin-polarised charge-transfer state in ACRSA, a commercially available organic molecule. The coupling between the magnetic and electric degrees of freedom in this system originates from the formation of an intramolecular electron-hole pair, which simultaneously induces charge and spin separation. The former gives rise to an electric dipole moment $\mathbf{p}$, while the associated spin-spin interaction produces a zero-field-splitting (D) parameter. When an external electric field is applied, it interacts with the dipole moment $\mathbf{p}$, perturbing either the molecular geometry or the electronic structure, thereby modifying the charge separation and, in turn, modulating D.

Importantly, this mechanism demonstrates that a substantial SEC can emerge even in the absence of strong atomic spin-orbit coupling (SOC). Previous studies have often considered SOC to be a prerequisite for measurable SEC, therefore focusing primarily on transition-metal or lanthanide-based compounds where SOC is inherently strong [30, 108, 126, 129]. In contrast, ACRSA is an organic molecule composed solely of light elements, whose spin Hamiltonian is governed predominantly by spin-spin interactions rather than SOC, yet it still exhibits a clear SEC response. This finding significantly broadens the range of

candidate materials for SEC-active systems and is particularly appealing for quantum information applications, where strong SOC typically limits spin coherence times [16, 30].

While this work constitutes a proof-of-principle demonstration of electric-field sensing using optically excited spin states in molecular systems, the achieved sensitivity is currently limited by the random molecular orientations, the signal-to-noise ratio of the transient echo, and the available coherence times. These limitations could be mitigated through strategies such as molecular alignment under magnetic fields [131], magnetic dilution [68], deuteration [60, 61], or the introduction of controlled strain within the host polymer matrix [132]. Combined with the capability for optical spin-state initialization, these approaches could substantially enhance sensitivity and potentially enable room-temperature operation.

A promising extension of the presented study is the exploration of molecular colour centres (MCCs), a recently synthesised class of molecules that emulate solid-state colour centres in materials such as diamond and SiC [133, 134]. MCCs offer optical spin-state initialization and readout (even at telecom wavelengths [135]), together with coherent microwave control. Quantum sensing of magnetic fields using MCCs has already been demonstrated experimentally [136], and theoretical studies have proposed their application for electric-field detection [137]. Their key advantage lies in the tunability of their spin Hamiltonian, combined with the chemical flexibility to incorporate a variety of ESR-active centres. Integrating MCCs with our device architecture, which combines microwave, optical, and electric-field control, could therefore offer a direct route to enhanced sensing performance. In the nearer term, systematic SEC measurements on molecules structurally similar to ACRSA (see, e.g., Ref. [138]) would provide valuable insight into how the spatial distribution and degree of separation of electronic wavefunctions drive the magnitude of the SEC.

This work is part of a manuscript in preparation for publication.

3 Electric Control of Hyperfine-Coupled Spin Systems

3.1 Introduction to Electronuclear Spin Systems

Our discussion has so far centred on electron, rather than nuclear, spins. This focus arises from the comparatively large gyromagnetic ratio of electrons (see Subsec. 1.1.2.1), which enables them to be driven efficiently by relatively short microwave pulses. As a result, electron spins are suited to tasks requiring fast control, such as rapid qubit operations and quantum sensing of AC fields [99]. The same property, however, also has a drawback: the large magnetic moment that facilitates efficient manipulation simultaneously makes electron spins more vulnerable to environmental fluctuations, limiting their coherence. By contrast, nuclear spins, with gyromagnetic ratios smaller by about three orders of magnitude [1], typically exhibit longer coherence times at the expense of slower control.

Electronuclear spin systems, in which electron spins are hyperfine-coupled to nearby nuclei, offer a versatile hybrid platform [140] and can be addressed through ENDOR techniques. As discussed in Subsec. 1.1.5.4, these sequences combine ESR and NMR excitations, with the rf frequency typically swept while the echo-detected electron signal is continuously monitored. When the rf pulse becomes resonant with a nuclear spin

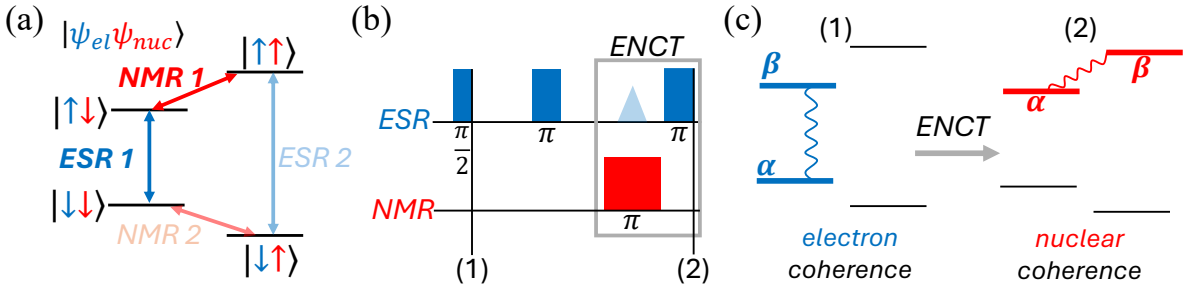

Figure 3.1: (a) Schematic energy-level diagram for a single electron coupled to a nucleus with spin $I = 1/2$. The four eigenstates are labelled as $|\psi_{\mathrm{el}}\psi_{\mathrm{nuc}}\rangle$, identifying the electron (blue) and nuclear (red) spin components of the wavefunction. Note that the ESR and NMR transitions are spectrally distinct due to the hyperfine coupling. (b) Pulse sequence for the ElectroNuclear Coherence Transfer (ENCT), comprising both mw and rf pulses, as reported in Ref. [139]. (c) After initializing the desired state within an electron coherence (1), the subsequent application of a pair of mw and rf pulses (2) resonant with, e.g., *ESR 1* and *NMR 1*, maps this state onto a nuclear coherence, which benefits from significantly longer coherence times.

transition, whose frequency is set by the hyperfine coupling strength and the nuclear Zeeman interaction, the echo exhibits a characteristic reduction in intensity.

To illustrate the main features of such systems, we consider the simplest case of a single electron spin coupled to a nuclear spin $I = 1/2$. The four resulting eigenstates, labelled $|\psi_{\mathrm{el}}\psi_{\mathrm{nuc}}\rangle$, where $|\psi_{\mathrm{el}}\rangle$ and $|\psi_{\mathrm{nuc}}\rangle$ denote the electron and nuclear parts of the wavefunction, define a basis in which the hyperfine interaction lifts the degeneracy between states sharing the same electron spin projection but differing in their nuclear component. As a result, the ESR and NMR transitions become spectrally distinct and individually addressable (Fig. 3.1(a)), providing the level structure required for selective and coherent manipulation of both spins. This spectral addressability lies at the core of the *ElectroNuclear Coherence Transfer* (ENCT) protocol, which employs an ENDOR-inspired sequence (shown in panel (b)) to leverage the complementary strengths of the electron and nuclear degrees of freedom [139, 141].

The sequence begins with a Hahn echo on the electron manifold, which generates a coherence between two states differing in their electronic but not nuclear projections (blue oscillating line in Fig. 3.1(c)). The quantum information, encoded in the complex coefficients α and β, is determined by the phase and amplitude of the initial microwave pulse, while the first π pulse serves to refocus the spin states, compensating for dephasing

caused by magnetic-field inhomogeneities (see Subsec. 1.1.5.2). A subsequent pair of rf and mw π-pulses (ENCT) transfers this coherence into the nuclear manifold, where it benefits from the much longer nuclear T_2. At a later time, the process is reversed, allowing the state to be read out through the electron spin. In this way, the electron spin component provides fast initialization, control, and measurement, while the nuclear spin serves as a robust quantum memory.

The electric-field control of electronuclear spin systems, despite the promise of combining the local addressability of E-fields with the advantages of electronuclear platforms, remains relatively unexplored. To date, research has primarily focused on the electric control of the nuclear quadrupole moment that arises in nuclei with spin $I \geq 1$, which couples to the electric field gradient (EFG) produced by the surrounding crystal environment (Subsec. 1.1.2.4) [142]. In such systems, an electric field perturbs the lattice by displacing neighbouring atoms and distorting covalent bonds, thereby modifying the local charge distribution. This distortion, in turn, changes the EFG at the nuclear site and shifts the nuclear transition frequencies, providing a means of electrically tuning nuclear energy levels.

A landmark achievement in this direction was the experimental demonstration of Nuclear Electric Resonance (NER), the electric-field analogue of NMR, realised in a single-electron transistor device hosting a single ^{123}Sb donor in silicon [40]. In this system, radiofrequency electric fields were applied across the transistor channel, generating periodic modulations of the local EFG. This modulation acted as a resonant driving field, enabling coherent control of nuclear spin transitions (see Subsec. 1.2.3 for details).

This approach, however, restricts control to quadrupolar interactions, as the system is specifically engineered to suppress electron-nuclear coupling to maximise nuclear spin coherence. Consequently, two significant challenges arise. First, the quadrupolar coupling is highly sensitive to the precise location of the implanted donor, a parameter that is inherently difficult to control. This sensitivity leads to substantial device-to-device variability in local strain and quadrupolar profiles, posing a major obstacle to scaling NER-based multi-qubit platforms. Second, relying solely on quadrupolar

control restricts the architecture to nuclear spins, whose weak magnetic moments result in comparatively low thermal polarisation, thus requiring cryogenic temperatures or magnetic fields of several Tesla for initialisation.

A complementary strategy, explored in this chapter, is to couple nuclear spins to electrons via the hyperfine interaction (Subsec. 1.1.2.3). In previous studies, either no electron was present, in order to maximise nuclear coherence times [40], or a single $S = 1/2$ electron spin was coupled to the nucleus and employed as an *ancilla*[1] for readout [143–145]. The approach pursued here differs in that, rather than avoiding or only marginally exploiting electron-nuclear coupling, we make active use of a system with $S > 1/2$ and its associated zero-field splitting (ZFS) D. In our case, a transition-metal defect embedded in a polar semiconductor crystal (see next section) provides a natural setting for such control. Here, the lack of inversion symmetry in the host enhances the interaction between the electron spin and local electric fields, giving rise to a strong dependence of D on the local electric potential. This spin-electric interaction is then channelled to the nuclear spin via the hyperfine coupling, which mixes the electron and nuclear wavefunctions. While the presence of an electron may reduce nuclear coherence times, this drawback can be outweighed if the enhanced electric control of the nuclei enables faster operations. Moreover, employing such hyperfine-coupled electronuclear systems allows nuclear-spin states to be detected through ENCT, offering a substantial gain in sensitivity, since electron spins can be read out orders of magnitude more efficiently and their coherence transferred to the nuclei.

In this chapter, we investigate both the static SEC in electron-nuclear systems and the resonant electric driving of nuclear transitions (NER), both amplified by the strong electric sensitivity of the electron anisotropy. To this end, we develop an ENDOR-inspired pulse sequence, based on ENCT, that extends the Hahn-Mims scheme to coupled electronuclear spins. In the next section, we begin by characterising the sample employed in this study, which consists of spin defects embedded in a semiconducting crystal host.

[1] In this context, an ancilla refers to an auxiliary spin used to indirectly probe or manipulate the state of another spin system.

3.2 Characterization of Mn Defects in a ZnO Crystal

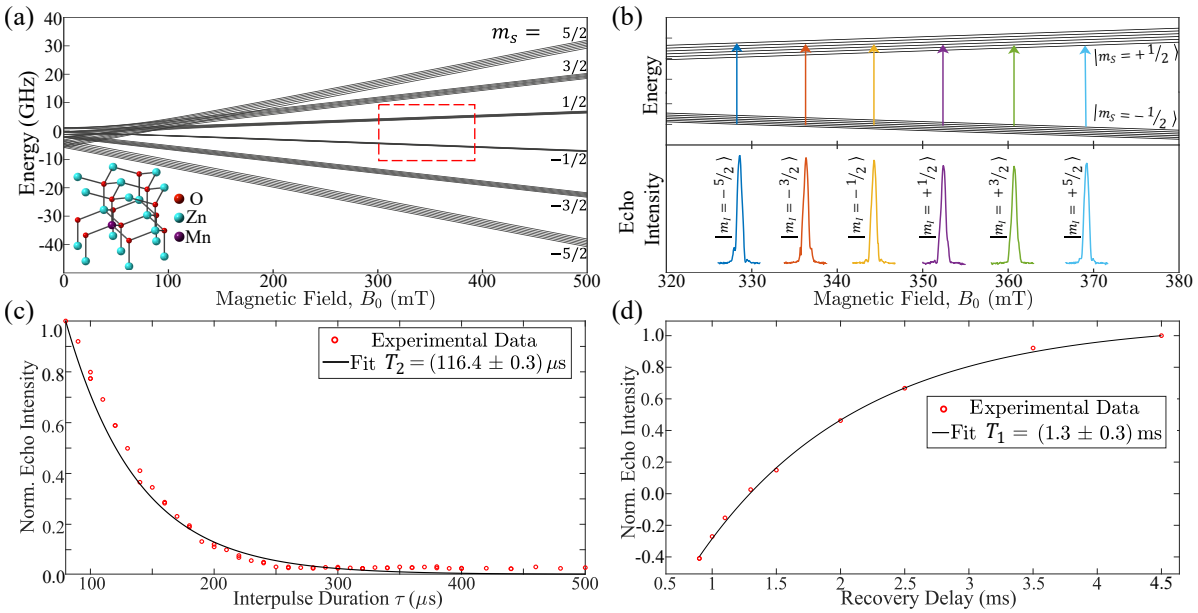

Figure 3.2: (a) Simulated energy-level diagram of Mn^{2+} defects in ZnO with the crystal axis aligned parallel to the static magnetic field B_0 ($\theta = 0°$ in Eq. 3.1). *Inset*: Structure of the wurtzite ZnO crystal with the Mn substitutional defect (purple sphere). (b) Experimental electron spin-echo signal for $|m_s = -1/2 \leftrightarrow 1/2\rangle$ (red rectangle in (a)), showing six peaks arising from the hyperfine coupling to the $I = 5/2$ nuclear spin. Similar spectra can be obtained for the other electronic transitions. Adapted from Ref. [141]. (c, d) Representative data collected at 20 K for one of the $|m_s = 3/2 \leftrightarrow 5/2\rangle$ transitions, probing the electronic T_2 and T_1, respectively.

The sample employed in this work consists of a spin ensemble of manganese (^{55}Mn) substitutional defects in wurtzite ZnO, with the crystal structure shown in the inset of Fig. 3.2(a). Here, a Mn^{2+} ion (purple sphere) replaces a Zn^{2+} lattice site. Unlike zinc, which carries no electronic spin, the Mn^{2+} ion has the electronic configuration [Ar] $3d^5 4s^0$, giving rise to a high-spin ground state with $S = 5/2$ ($^6S_{5/2}$) coupled to the manganese nuclear spin $I = 5/2$. Such an electronuclear spin system is particularly promising for electric-field control owing to its strong SEC, which, as reported in Ref. [129], originates from the pronounced polarity of ZnO resulting from the broken inversion symmetry of the wurtzite lattice.

The effective spin Hamiltonian of Mn:ZnO, established experimentally in Refs. [141,

146], can be written as[2]

$$\begin{aligned}\hat{\mathcal{H}} = \mu_e g_e B_0 \left(\hat{S}_z \cos\theta + \hat{S}_x \sin\theta\right) - \mu_N g_N B_0 \left(\hat{I}_z \cos\theta + \hat{I}_x \sin\theta\right) \\ + D\left(\hat{S}_z^2 - \tfrac{1}{3}S(S+1)\right) + Q\hat{I}_z^2 + A_{\text{iso}}\,\hat{\mathbf{S}}\cdot\hat{\mathbf{I}},\end{aligned} \tag{3.1}$$

where θ denotes the angle between the external magnetic field B_0 and the crystal c-axis ([0 0 1]), which defines the intrinsic polar direction of the wurtzite lattice [129]. Owing to the hexagonal symmetry of ZnO and the C_{3v} site symmetry of the Mn defect, the anisotropy parameter D, together with the quadrupole and the principal axis of the hyperfine interaction, are all aligned with the crystal c-axis, which thus provides the natural reference frame for the spin Hamiltonian [147].

The bottom panel of Fig. 3.2(b) presents the experimental X-band echo-detected field sweep (EDFS) at 20 K for the $|m_s = -1/2 \leftrightarrow +1/2\rangle$ electron transition with $\theta = 0°$. The spectrum displays six peaks, each corresponding to one of the nuclear spin projections ($2I + 1 = 6$), arising from the hyperfine interaction with the Mn nucleus. Similar features are observed for all other electron transitions (see panel (a) for the energy-level diagram). From these data, we extract an anisotropy parameter $D \simeq -707$ MHz and an isotropic hyperfine coupling $A_{\text{iso}} \simeq -225$ MHz. A quadrupolar interaction of $Q = 0.32$ MHz, reported in Ref. [147], was also included in the analysis, although its influence on the resonant-peak positions is too weak to be resolved directly; as discussed later, however, it plays an important role when discussing the nuclear SEC. Finally, we note that the electron g-factor in Mn:ZnO is close to the free-electron value, while the nuclear g-factor is $g_N \simeq 1.38$.

Using second- and third-order perturbation theory on Eq. 3.1, previous studies [147, 148] found that the ENDOR frequencies in Mn:ZnO depend not only on the expected Zeeman, quadrupolar, and hyperfine interactions, but also on the electron anisotropy parameter D. This dependence arises from the significant mixing between nuclear and electronic degrees of freedom induced by the relatively large hyperfine interaction. Formally, the ENDOR frequencies can then be expressed as $f_{\text{ENDOR}} = f_{\text{ENDOR}}(B_0, A_{\text{iso}}, Q, D)$,

[2]Although reported in Ref. [146], fourth-order magnetic anisotropies ($\sim \hat{S}_z^4$) are ignored in this Hamiltonian, as their contributions to the energy levels and to the discussion of E-field control are negligible.

with the influence of D confirmed by numerical simulations (see Appendix, Fig. A.5). Although this dependence is modest, it remains finite and, given the substantial electric modulation $\delta D(E)$ [129], can still influence the electric sensitivity of nuclear transitions, as discussed in Sec. 3.4.

Finally, Figs. 3.2(c) and (d) show representative measurements of the electronic coherence times T_2 and T_1, obtained for the $|m_s, m_I\rangle = |3/2 \leftrightarrow +5/2, +1/2\rangle$ transition using Hahn-echo and inversion-recovery sequences, respectively, at 20 K. The extracted values, $T_{2e} \simeq 0.12$ ms and $T_{1e} \simeq 1.3$ ms, are consistent with previous reports [141]. The temperature dependence of these coherence times has been investigated in detail in Ref. [129], where the dominant decoherence mechanisms were identified as phonon-mediated spin-lattice relaxation, which limits T_{1e}, and dipolar interactions with neighbouring Mn spins, which give rise to spectral diffusion and ultimately limit T_{2e}. Moreover, the same study reports a nuclear-spin coherence time of $T_{2n} \approx 1$ ms under conditions comparable to ours. This value is of the same order as the electronic T_{1e}, indicating that nuclear dephasing may primarily be driven by electron-spin flips, as expected given the strong hyperfine coupling.

3.3 Electric-Field Device

The device used to generate the DC and rf E-fields in this study is conceptually similar to the one described in Chapter 2, though fewer constraints apply here, such as the requirement for UV transparency. The setup consists of a parallel-plate capacitor, whose electrodes are fabricated from rigid PCBs coated via thermal evaporation with approximately 150 nm of gold, deposited on a ∼15 nm seed layer. The rationale behind this design choice is the same as previously discussed: to minimise the amount of metal within the resonator and thus reduce its perturbative effect on the resonator's electromagnetic mode structure. A schematic of the device as inserted inside the resonator is shown in Fig. 3.3.

Another key difference between this and the previous setup lies in the nature of the sample: here, we work with a crystalline system rather than a solution containing randomly oriented molecules. In ZnO, which has a well-defined polar axis along its crystallographic

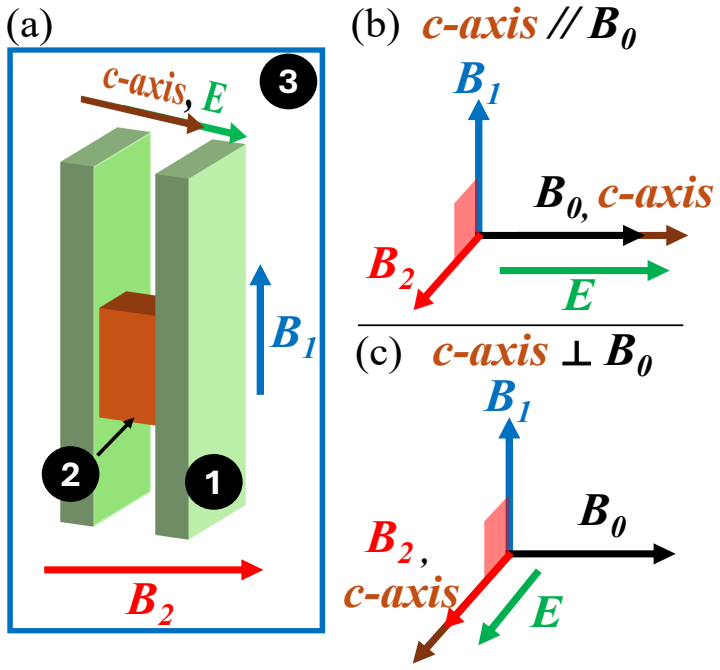

Figure 3.3: (a) Schematic of the E-field device, consisting of a parallel-plate capacitor mounted inside a mw resonator and rotatable about its axis. (1): conducting plates; (2): sample; (3): mw resonator. (b,c) Fields configurations when the crystal c-axis is (b) parallel and (c) perpendicular to the static magnetic field B_0. In both orientations, B_1 and B_2 are perpendicular to B_0, as required for standard ESR/ENDOR operation. The sample is affixed to the capacitor plates and co-rotates with them, ensuring that the applied E-field remains aligned with the crystal c-/polar axis throughout the rotation.

$c-$axis, the electrodes are arranged such that the applied electric field is parallel to this polar axis, thereby maximizing the SEC. This is achieved by mounting the crystal between the plates with its c-axis oriented normal to the electrode surfaces, i.e., along the expected direction of the E-field. This configuration is fixed and maintained throughout all measurements, ensuring a consistent alignment between the E-field and the polar axis.

As shown in Fig. 3.3(a), this device is inserted into the (4 mm-diameter) sample space of a Bruker EN 4118X-MD4 ENDOR resonator, with the inter-plate distance of the capacitor set to roughly 1 mm. This geometry allows the device to generate an electric field of $\sim$ 4 kV/cm at the sample location. While this is roughly a quarter of the field strength produced by the design used in Chapter 2 (15 kV/cm), the effect is compensated by a stronger SEC, as discussed in the following sections. It should also be noted that the resonator design ensures that the driving excitations B_1 (ESR) and

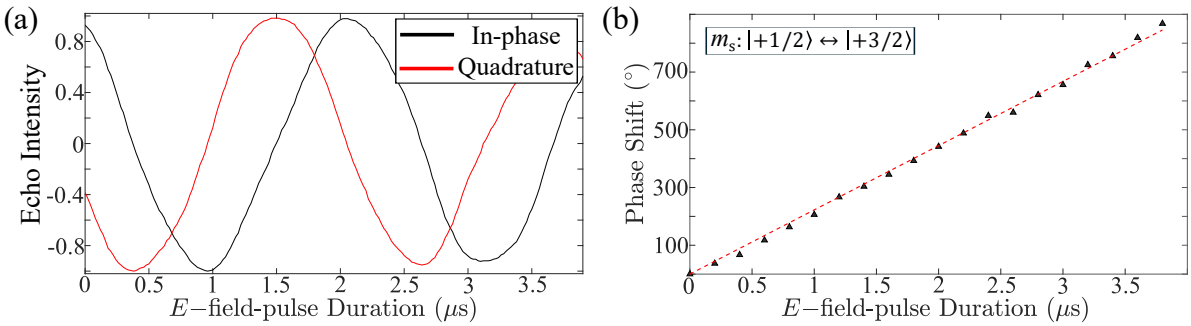

Figure 3.4: (Experimental, $B_0 \parallel c-$axis) (a) E-field-induced coherent oscillations of the in-phase (black) and quadrature (red) components of the electron Hahn-echo signal. These oscillations arise from the electric-field modulation of the axial anisotropy parameter D, as previously reported in Ref. [129]. Measurements were performed at 20 K on the $|m_s = 1/2 \leftrightarrow 3/2\rangle$ transition. (b) Corresponding Hahn-echo phase shift induced by the applied E-field. The ability to electrically control the coherence phase is central to our proposal for exploiting electronuclear systems in quantum information science, as discussed in Sec. 3.6.

B_2 (NMR) remain perpendicular to the static field B_0 regardless of the sample/device orientation (panels (b) and (c)), thereby preserving standard conditions for magnetic-resonance operation (Subsec. 1.1.3).

3.4 Spin-electric Coupling in Electronuclear Spin Systems

We now turn to the characterization of the electric response of both the electronic and nuclear manifolds in Mn:ZnO. Our objective is to determine the DC electric-field sensitivity of the spin-effective parameters appearing in the Hamiltonian of Eq. 3.1. For the electron spin, this analysis was performed using a Hahn-Mims sequence with $\tau = t_{E,\max} = 4$ μs at 20 K and an applied electric-field strength of ~ 4 kV/cm. Representative data, recorded with the crystal c-axis aligned with B_0 for the $|m_s = +1/2 \leftrightarrow +3/2\rangle$ transition at X-band, are shown in Fig. 3.4(a). The in-phase and quadrature channels display the characteristic coherent oscillations associated with electric-field modulation of the spin transition. On the other hand, panel (b) shows the corresponding Hahn-echo phase shift induced by the applied E-field, in line with the dependence predicted by Eq. 1.44; the ability to control the coherence phase provides the foundation for our proposal to harness electronuclear systems in quantum information processing, as discussed in Sec. 3.6.

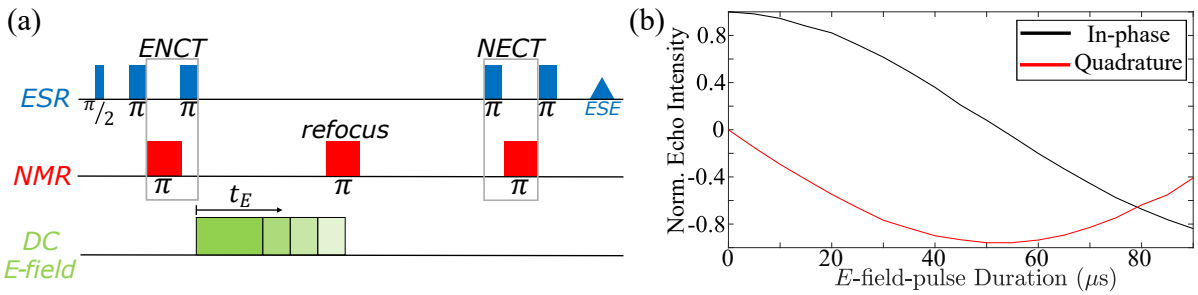

Figure 3.5: (a) Pulse sequence based on Ref. [139], incorporating a DC E-field pulse inserted between the ENCT and the refocusing pulse. This plays an analogous role to the Hahn-Mims sequence for electronuclear systems. (b) In-phase (black) and quadrature (red) components of a nuclear spin-echo signal, measured on the transition $|m_s = -1/2, m_I = +3/2 \leftrightarrow +5/2\rangle$, showing coherent oscillatory behaviour as a function of the applied E-field-pulse duration.

Following the discussion in Ref. [129], we assumed that the electron SEC is predominantly driven by the axial anisotropy parameter D. Accordingly, its electric-field dependence was modelled as $D(E) = D(0)+\kappa_D E$, and the experimental phase-shift data were fitted to this relation. The resulting fit, shown as the dotted line in Fig. 3.4(b), shows good agreement with the measurements. From this analysis, we extract an SEC constant of $\kappa_D \simeq 2.5\ \mathrm{Hz}/(\mathrm{V}\cdot\mathrm{m}^{-1})$, consistent with the value reported in that study. This response reflects the strong coupling between the applied electric field and the crystal-field environment of the Mn^{2+} ion: in the polar ZnO host, field-induced redistributions of the local charge density modify the splitting of the high-spin $S = 5/2$ manifold through the anisotropy D.

Next, we investigate the electric-field modulation of the nuclear spin terms using a modified version of the pulse sequence introduced in Ref. [139] and shown in Fig. 3.5(a). The sequence begins by transferring the initial electron coherence into the nuclear manifold through an ENCT block. A single nuclear π-pulse is then applied to refocus the nuclear coherence, serving the same function as the refocussing pulse in a standard Hahn-echo sequence. Finally, the coherence is mapped back to the electron manifold via a *Nuclear-Electron Coherence Transfer* (NECT) step, where it is detected as an electron spin echo (SE). In our implementation, we insert a variable-duration DC electric-field pulse between the ENCT block and the nuclear refocusing π-pulse, while monitoring the resulting SE. Conceptually, the sequence plays an analogous role to the Hahn-Mims protocol: once a spin coherence is established via ENCT, the application of an electric field induces a

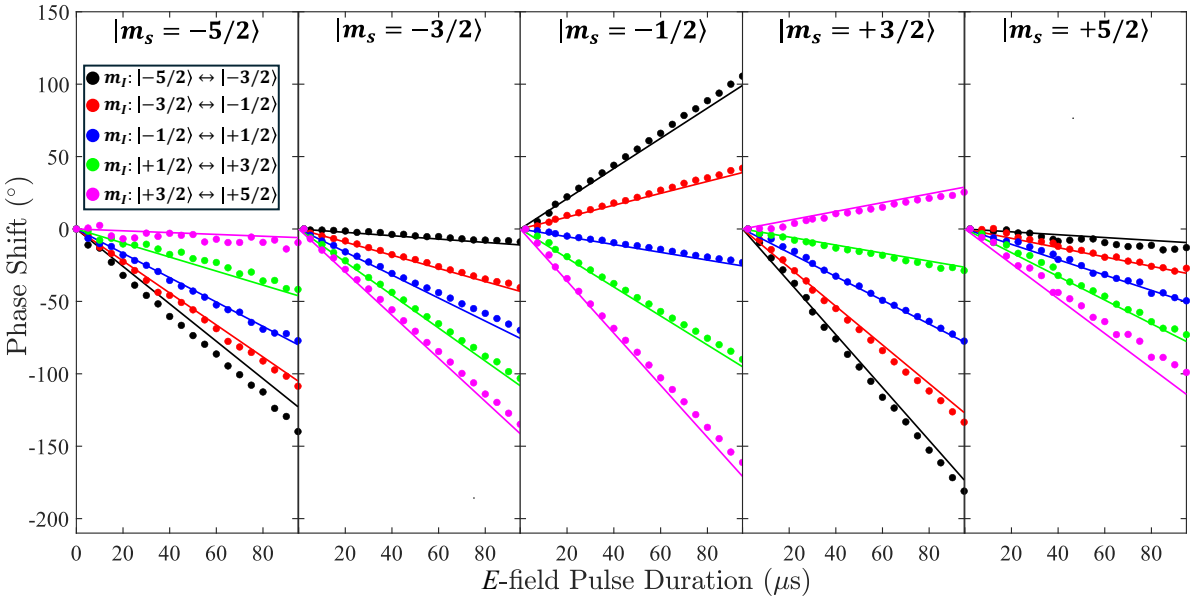

Figure 3.6: Experimental observation of E-field-induced spin-echo phase shift for 25 $\Delta m_I = \pm 1$ nuclear transitions in Mn:ZnO. Each graph corresponds to a different electronic spin manifold (indicated at the top of each plot), while different colours represent different nuclear transitions. Solid lines are obtained via numerical simulations using the E-field-induced parameters' shifts listed in Table 3.1. The absence of data for $|m_s = +1/2\rangle$ is discussed in Ref. [147] and in the main text.

phase shift in the spin echo. As in the electron-spin case, the accumulated phase increases proportionally with both the amplitude and duration of the applied E-field pulse.

Fig. 3.5(b) presents nuclear-SEC data for the $|m_s = -1/2, m_I = +3/2 \leftrightarrow +5/2\rangle$ transition, where the spin-echo signal exhibits coherent oscillatory behaviour as a function of the electric-pulse duration. Fitting these data yields an SEC constant of $\simeq 0.3$ Hz/(V $\cdot$ m^{-1}), approximately an order of magnitude smaller than the corresponding electron-spin value. To probe the microscopic origin of this (weaker) nuclear response, we measured the electric-field-induced phase shifts for 25 $\Delta m_I = \pm 1$ nuclear coherences. The results, shown in Fig. 3.6, are compared with simulations (continuous lines) based on the electrically modulated parameters listed in Table 3.1, obtained using the same fitting procedure employed in the electron case.

The extracted SEC constants for the hyperfine and quadrupolar components are $\kappa_A \simeq 1.3 \times 10^{-2}$ Hz/(V $\cdot$ m^{-1}) and $\kappa_Q \simeq 0.8 \times 10^{-2}$ Hz/(V $\cdot$ m^{-1}), respectively. These values are roughly two orders of magnitude smaller than the modulation observed for D. This

Spin Hamiltonian Term	D	A_{iso}	Q
Value @ $E = 0$ V/m (MHz)	-707	-225	0.32*
SEC Constant κ ($\times 10^{-2}$ Hz/(V/m))	252	1.34	0.82
$\delta f_{\mathrm{ENDOR}}$ @ $\lvert m_s, m_I\rangle = \lvert -1/2, -5/2 \leftrightarrow -3/2\rangle$ (kHz)	2.71	0.36	1.84
$\delta f_{\mathrm{ENDOR}}$ @ $\lvert m_s, m_I\rangle = \lvert -1/2, -1/2 \leftrightarrow +1/2\rangle$ (kHz)	0.31	0.19	0.01

Table 3.1: Spin-Hamiltonian parameters at zero applied electric field and their corresponding electric-field coupling coefficients. The field dependence is obtained by fitting the experimental data in Fig. 3.6 to $P(E) = P(0) + \kappa_P E$, where P denotes a spin-effective parameter and κ_P the associated SEC constant. The last two rows list representative frequency-shift contributions from each spin parameter for two nuclear transitions. *Value taken from Ref. [147].

difference arises because D reflects the axial crystal-field splitting of the Mn^{2+} ion, which is highly sensitive to lattice distortions and local symmetry changes induced by the applied electric field. In contrast, the hyperfine and quadrupolar parameters, although also influenced by electric fields, are primarily determined by the electronic spin density at the nucleus and the nuclear charge distribution, which exhibit comparatively weaker variations under similar field strengths.

Nevertheless, what ultimately determines the degree of electric control is not the modulation of an individual spin parameter itself, but how sensitively the *resonance frequency* responds to such modulation. In other words, the SEC constants quantify the coupling between each spin parameter and the electric degrees of freedom of the crystal, whereas the actual frequency shift observed in ENDOR experiments reflects how variations in those parameters translate into measurable resonance changes. To illustrate this relationship, Table 3.1 lists representative frequency-shift contributions for two nuclear transitions within the same electron-spin manifold: $|m_s = -1/2, m_I = -5/2 \leftrightarrow -3/2\rangle$ and $|m_I = -1/2 \leftrightarrow +1/2\rangle$. In both cases, the dominant contribution to the overall frequency shift arises from the modulation of D. This is noteworthy, as one might expect the nuclear parameters A_{iso} and Q to play a larger role in nuclear transitions. The observed behaviour, however, highlights that the electric response of the ENDOR frequencies is primarily mediated through the electron-spin manifold, whose strong electric sensitivity (via D) is "transferred" to the nuclear transitions through the hyperfine interaction.

Additionally, a marked reduction in the effective Q-related contribution is observed when comparing the $|m_I = -5/2 \leftrightarrow -3/2\rangle$ and $|m_I = -1/2 \leftrightarrow +1/2\rangle$ transitions. This arises from the dependence of the quadrupolar shift on m_I^2: for the central transition ($m_I = \pm 1/2$), this term effectively vanishes, leading to negligible sensitivity to Q. By contrast, the hyperfine parameter A_{iso} contributes to both transitions, though its effect remains smaller than that of D due to its weaker intrinsic electric coupling.

We now briefly discuss the absence of nuclear-SEC data from the $|m_s = +1/2\rangle$ electron manifold in Fig. 3.6. In this case, we found the ENDOR signal to be too weak to allow SEC measurements. As explained in Ref. [147], this arises because the $\mu_B g_e \hat{\mathbf{S}}$ term in the expression for the signal intensity (Eq. 1.29) is significantly reduced for these transitions. Such suppression is not a fundamental limitation, but rather an accidental consequence of the spin Hamiltonian: the particular mixing of spin states produces a local minimum in the ENDOR transition probability at $D \simeq -670$ MHz, close to the anisotropy of Mn:ZnO. Numerical simulations (Fig. A.6 in the Appendix) confirm this behaviour, showing that the ENDOR intensity from the $|m_s = +1/2\rangle$ transitions is markedly weaker than that from the $|m_s = -1/2\rangle$ ones.

3.5 Nuclear Electric Resonance in an Electronuclear System

We now investigate nuclear spin transitions driven by resonant rf E-fields, using the electrode setup described in Sec. 3.3 at 20 K. In this case, the static field B_0 was deliberately tilted slightly away from the crystal c-axis. This misalignment is essential: for $B_0 \parallel c$, all spin parameters (D, A_{iso}, and Q) are diagonal in the laboratory frame [147], and the rf E-field is also aligned along the c-axis. Under these conditions, the spin operators that couple to the electric field are thus of the form $\hat{S}_z$ and $\hat{I}_z$, which have no off-diagonal matrix elements in the eigenbasis of the Hamiltonian. As a result, the driving Hamiltonian contains no transverse components and cannot induce any transitions. Tilting B_0 away from the c-axis breaks this symmetry, introduces off-diagonal elements into the effective driving Hamiltonian, therefore (potentially) enabling NER.

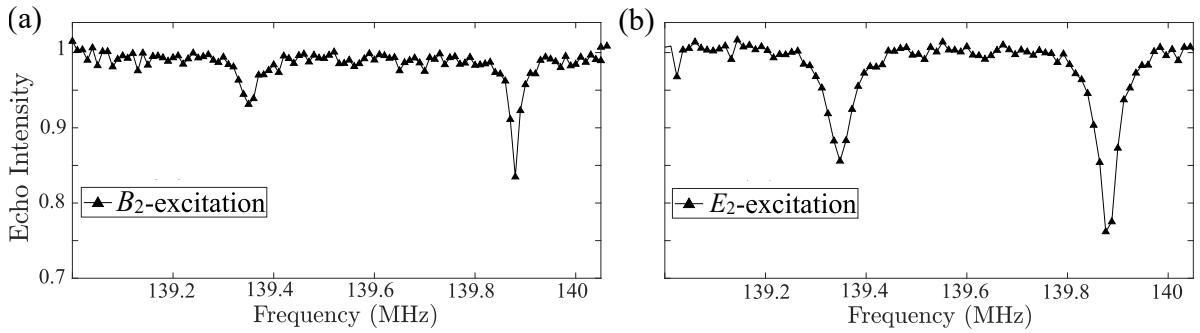

Figure 3.7: (Experimental) ENDOR spectra for the $|m_s = +1/2, m_I = -5/2 \leftrightarrow -3/2\rangle$ (left dip) and $|m_s = +1/2, m_I = -3/2 \leftrightarrow -1/2\rangle$ (right dip) nuclear transitions for (a) NMR (coils) and (b) NER (electrodes).

Fig. 3.7 shows Davies ENDOR spectra (pulse sequence in the inset of Fig. 3.8(b)), where the rf pulse is applied either magnetically via ENDOR coils[3] (left) or electrically through our custom E-field device (right). The two dips correspond to the $|m_I = -5/2 \leftrightarrow -3/2\rangle$ and $|m_I = -3/2 \leftrightarrow -1/2\rangle$ nuclear transitions within the $|m_s = +1/2\rangle$ electron manifold. This manifold was chosen because, as noted at the end of Sec. 3.4, the ENDOR signal is suppressed for these transitions [147]. Consequently, any contribution from residual magnetic-field leakage from the electrodes (even at the maximum applied power of 100 W in this experiment) is expected to be negligible. The clearer resonance dips observed under electrode excitation thus provide initial evidence that these nuclear transitions may be driven electrically.

We confirmed this point by characterising possible parasitic magnetic fields in our device. To this end, we inserted a powder sample of Koelsch radical, 1,3-bisdiphenylene-2-phenylallyl (BDPA), embedded in a PMMA matrix. BDPA, whose structure is shown in the inset of Fig. 3.8(a), is a well-established standard in electron-spin resonance, with $S = 1/2$ and $g \simeq g_e$. It provides a strong ESR and ENDOR response under magnetic excitation, yet is insensitive to electric fields, making it ideally suited for probing spurious magnetic contributions in our electrode-based design. Fig. 3.8(a) displays the ENDOR spectrum obtained using either conventional ENDOR coils (black lines) or the electrode device (red). In the coil-based configuration, clear ENDOR resonances are observed at $\omega_0 = 14.48$ MHz, corresponding to the proton Larmor frequency, together with

[3]These coils are already integrated into the commercial resonator.

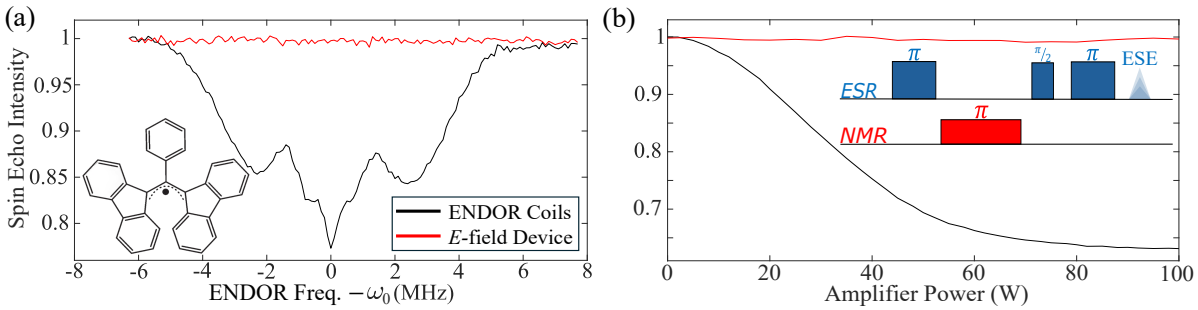

Figure 3.8: (Experimental) (a) ENDOR spectrum of the standard electron-spin sample BDPA (molecular structure shown in the inset). The $x-$axis is referenced to $\omega_0 = 14.48$ MHz, the proton Larmor frequency at ~ 345 mT. Spectra were recorded using either conventional ENDOR coils (black) or the electrode-based device (red). The absence of any resonance in the latter demonstrates that magnetic-field leakage is negligible in our E-field-based design. (b) ENDOR power-nutation measurement at ω_0, showing no detectable response across the full range of applied rf powers. *Inset:* Davies ENDOR sequence, as described in Subsec. 1.1.5.4.

additional features at $\simeq \omega_0 \pm 2$ MHz, in agreement with previously reported ^{1}H hyperfine couplings [149]. In contrast, no detectable ENDOR signal is observed with the electrode configuration, confirming that the application of a rf electric field does not generate significant magnetic-field leakage. This conclusion is also supported by the ENDOR power-nutation measurements in panel (b).

To further verify the nature of the electrode-driven transitions, we probe double-quantum nuclear transitions ($\Delta m_I = \pm 2$), which are forbidden under magnetic driving but can be activated electrically [40]. Unlike the previous $\Delta m_I = \pm 1$ case, where a slight misalignment of B_0 from the crystal c-axis introduces transverse terms [145], double-quantum transitions are optimised with B_0 perpendicular to the c-axis ($\theta = 90°$), which is the orientation employed here. The right panel of Fig. 3.9 shows the ENDOR spectra for the $|m_s = -1/2, m_I = -5/2 \leftrightarrow -1/2\rangle$ transition, excited either electrically (red) or magnetically (black). A clear, though weak, ENDOR resonance is observed under electric excitation, corresponding to a $\sim 15\%$ reduction in the spin-echo amplitude, while no response is detected under coil-driven magnetic excitation. Power- and pulse-duration-dependent nutation experiments further confirmed that no signal could be obtained with magnetic driving. For comparison, the left panel shows a $\Delta m_I = \pm 1$ single-quantum transition within the same electron manifold, where the signal is visible under both electric and magnetic excitation, consistent with standard NMR selection rules. This

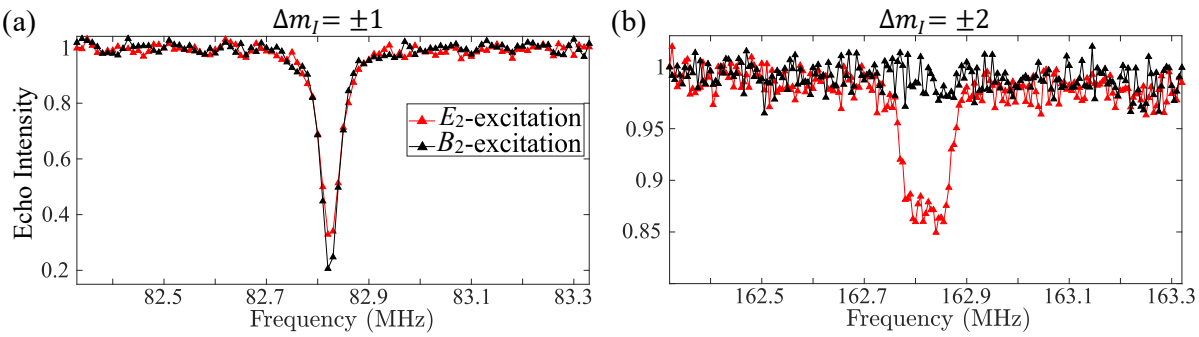

Figure 3.9: Single- (left) and double-quantum (right) nuclear transitions within the $|m_s = -1/2\rangle$ electron manifold, excited using the standard ENDOR coils (black), or with the electrodes (red). Both magnetic and electric fields drive single-quantum transitions ($\Delta m_I = \pm 1$), whereas only electric excitation induces double-quantum ones ($\Delta m_I = \pm 2$).

behaviour strongly indicates that the $\Delta m_I = \pm 2$ transitions are electrically driven, a conclusion reinforced by the absence of magnetic-field leakage in our setup, as discussed earlier. The remaining three double-quantum transitions in this manifold are presented in Fig. A.7 in the Appendix and exhibit similar behaviour.

The only term in the Hamiltonian of Eq. 3.1 that possesses the appropriate symmetry to account for the observed $\Delta m_I = \pm 2$ transitions is the quadrupolar interaction, $Q\hat{I}_z^2$. When $\theta = 90°$, the nuclear Zeeman term becomes $g\mu_B B_0 \hat{I}_x$, and thus no longer commutes with $Q\hat{I}_z^2$. In this configuration, the quadrupolar interaction can be represented in the Zeeman frame by an effective form $Q\hat{I}_x^2$, which, since $\hat{I}_x^2 \propto \hat{I}_+^2 + \hat{I}_-^2$, directly enables double-quantum transitions. Following Refs. [40, 145], the driving Hamiltonian under these conditions can be expressed as[4]:

$$\hat{\mathcal{H}}^{\mathrm{NER}}_{m_I \leftrightarrow m_I \pm 2}(t) \propto \delta Q_{xx}(t)\, \hat{I}_x^2. \tag{3.2}$$

As discussed earlier, the quadrupolar interaction exhibits only a weak spectroscopic signature and could not be directly measured. Consequently, Eq. 3.2 should be regarded as a phenomenological description, which reflects that Q is the only term in the Hamiltonian with the appropriate symmetry to drive double-quantum transitions. This model is further justified by the microscopic origin of the quadrupolar coupling, which arises

[4]In principle, time-dependent modulations such as $\delta Q_{yy}(t)$ and $\delta Q_{xy}(t)$ may also contribute to the excitation of double-quantum transitions. However, since Eq. 3.2 is not intended as a quantitative model, these terms are neglected here for clarity.

from the EFG at the nuclear site (see Subsec. 1.1.2.4). An applied rf electric field perturbs the surrounding crystal field, thereby modulating the local EFG and inducing a time-dependent variation of Q. A more rigorous treatment would require, for instance, density-functional-theory calculations to quantify the electric-field-induced perturbation of the EFG around the Mn^{2+} ion. Nevertheless, establishing a direct correspondence between the computed EFG variations and the effective Q coupling remains challenging, and experimental verification of their magnitude is equally difficult.

A similar driving mechanism can be formulated for the $\Delta m_I = \pm 1$ NER transitions. In this case, all Hamiltonian terms containing a single nuclear spin operator $\hat{I}_x$ (or $\hat{I}_y$) can, in principle, contribute, implying that off-diagonal components of either the quadrupolar or hyperfine interactions may drive such excitations:

$$\hat{\mathcal{H}}^{NER,1}_{m_I \leftrightarrow m_I \pm 1}(t) \propto \delta Q_{xz}(t)(\hat{I}_x \hat{I}_z + \hat{I}_z \hat{I}_x), \tag{3.3}$$

$$\hat{\mathcal{H}}^{NER,2}_{m_I \leftrightarrow m_I \pm 1}(t) \propto \delta A_{xz}(t)(\hat{I}_x \hat{S}_z + \hat{S}_z \hat{I}_x). \tag{3.4}$$

In the latter case, the electric field perturbs the electronic wavefunction and thereby modulates the hyperfine elements, leading to a time-dependent variation in the coupling between the electron and nuclear spins. In practice, however, such terms are difficult to resolve spectroscopically, as they appear as second-order perturbations in the energy-level structure and contribute only weakly to observable peak positions. Hence, while these terms provide a plausible explanation for the observation of electrically driven $\Delta m_I = \pm 1$ transitions, their quantitative contribution cannot be directly extracted from experiments.

A possible way to test whether the quadrupolar interaction alone can account for the observed transitions is to examine the $|m_I = -1/2 \leftrightarrow +1/2\rangle$ case. In fact, for this transition, the quadrupolar operator vanishes because, for example, $\hat{I}_z\hat{I}_x + \hat{I}_x\hat{I}_z = \frac{1}{2}(\hat{I}_+\hat{I}_z + \hat{I}_z\hat{I}_+ + \hat{I}_-\hat{I}_z + \hat{I}_z\hat{I}_-)$ couples only to states with $\Delta m_I = \pm 1$ away from the central pair, but gives zero matrix element between $|m_I = -1/2\rangle$ and $|m_I = +1/2\rangle$. Experimentally, however, Fig. 3.10(b) ($B_0 \perp c-$axis) shows that this transition does produce an electrically driven ENDOR response: at high power a signal of about 20% echo reduction is observed. Although this is weak compared to the magnetic driving of the same transition shown in

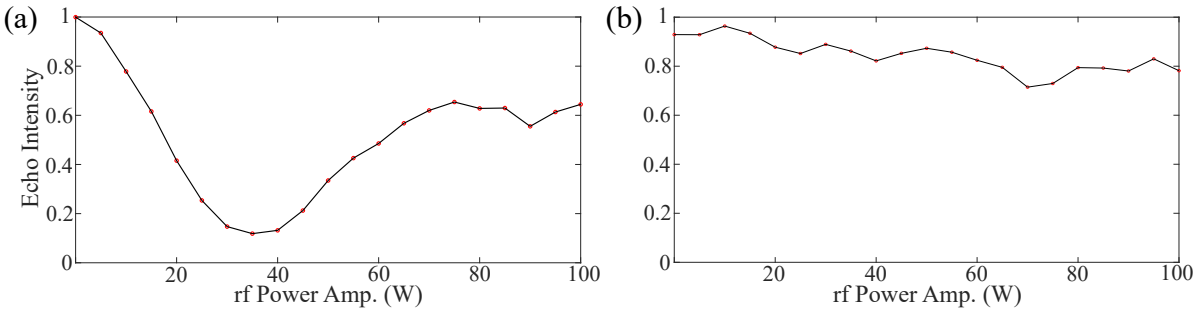

Figure 3.10: (Experimental) ENDOR nutation signals for the nuclear transition $|m_s = -1/2, m_I = -1/2 \leftrightarrow +1/2\rangle$, driven using (a) conventional rf coils and (b) electrodes. The electrically driven transition exhibits a nutation amplitude weaker than that obtained with rf excitation yet remains non-zero. This demonstrates that the interaction responsible for single-quantum NER cannot be attributed solely to the quadrupole term Q, since $|m_I = -1/2 \leftrightarrow +1/2\rangle$ transitions would otherwise be forbidden.

panel (a), it is nonetheless non-zero and of similar strength to other electrically driven single-quantum transitions (Fig. 3.7). This observation rules out a purely quadrupolar mechanism and indicates that the hyperfine-driven channel of Eq. 3.4 must also contribute.

While a more detailed investigation is required to fully clarify the mechanism responsible for these transitions, the data suggest that they likely originate from a combination of time-dependent quadrupolar and hyperfine modulations. The quadrupolar contribution is essential, as it is the only mechanism capable of inducing $\Delta m_I = \pm 2$ transitions [40]. In contrast, the observation of a finite signal for the $|m_I = -1/2 \leftrightarrow +1/2\rangle$ transition (forbidden under a purely $\delta Q(t)$ drive) indicates that hyperfine-driven components must also be involved, implying that mixing with the electron wavefunction contributes to the driving process. In this context, it is thus reasonable to expect that the strong electron-nuclear state mixing associated with the hyperfine interaction A_{iso} plays a role in mediating these transitions, suggesting that the electron anisotropy parameter D may also influence the process, as observed in the static SEC discussed in Sec. 3.4. This interpretation is consistent with the notion that electron-spin admixture can enhance nuclear transition probabilities and provide additional coupling pathways between the rf electric field and the nuclear spin degrees of freedom [147]. Therefore, while a full theoretical treatment is still needed, the available evidence indicates that both nuclear and electron contributions, including the anisotropy D, may act together to account for the observed NER response.

Importantly, these measurements were performed at 20 K using standard experimental instrumentation. Under such conditions, the nuclear polarization in a magnetically diluted system like Mn:ZnO would not be sufficient to generate detectable signals. This underscores the crucial role of ENCT-based techniques, which exploit electron-nuclear coupling to amplify the response through the much larger electron-spin polarization. As a result, they enable the observation of nuclear transitions (whether magnetically or electrically driven) that would otherwise remain undetectable. With further theoretical investigations to elucidate its microscopic mechanism, probing NER via ENCT sequences may develop into a powerful characterization method for coupled spin systems. Building on these insights, the following section outlines a route toward leveraging the electric-field control of electronuclear spin systems in quantum-information applications.

3.6 Conclusion & Future Directions

In this chapter, we have measured the nuclear SEC in an electronuclear spin system using a pulse sequence based on ElectroNuclear Coherence Transfer (ENCT). This approach exploits the complementary strengths of the electron spins (fast control and readout) and nuclear (longer coherence times) spins. Using ENCT, we characterised the electric-field modulation of nuclear spin-effective parameters. We found that the electron axial anisotropy D mediates a large part of the nuclear response through the hyperfine interaction, which mixes the electron and nuclear wavefunctions. In Mn:ZnO, D exhibits a particularly strong SEC [129], due to its coupling to the intrinsic electric dipole moment of the host crystal.

Moreover, we have reported the experimental observation of nuclear electric resonance (NER) in a spin ensemble. While previous demonstrations of NER have focused on single-spin platforms, such as molecular qubits [81] or single-electron silicon transistors [40], our results show that the effect can also be observed in a bulk spin ensemble. Detecting such modulations in purely nuclear systems would be extremely challenging in practice: in magnetically diluted samples, nuclear polarization remains weak under moderate fields and temperatures, typically requiring millikelvin conditions for direct detection. By

contrast, the ENCT approach leverages the much larger electron polarization to enhance the nuclear response, enabling the observation of these effects at 20 K using only standard magnetic-resonance instrumentation and a simple parallel-plate capacitor to apply the electric field. This comparatively mild experimental configuration highlights the potential of electronuclear systems as platforms for electrically driven spectroscopy and control.

To establish NER as a broadly useful characterization tool, however, a more complete understanding of the microscopic mechanisms underlying these transitions is required. In Mn:ZnO, our data indicate that both hyperfine and quadrupolar interactions contribute to the driving process, with possible additional modulation via the electron anisotropy parameter D. Yet, disentangling their respective roles remains challenging, as the off-diagonal components of the A and Q interactions potentially responsible for such driving produce only subtle spectroscopic signatures. Computational methods such as DFT may help elucidate these effects, although capturing dynamic (AC) spin-terms modulations reliably remains an open question.

An alternative strategy would be to explore NER in molecular nanomagnets, where the spin Hamiltonian can be chemically engineered. By incorporating different nuclear isotopes or tailoring the ligand environment, one could in principle tune the relative strengths of the hyperfine and quadrupolar couplings, as well as the influence of the electron anisotropy D. Such an approach could begin to resolve their contributions to electrically driven transitions, extending the work in Ref. [126] on the *static* SEC to the dynamic modulations. These chemically tunable systems may therefore offer a promising route to map the microscopic origins of NER while advancing electronuclear platforms as versatile tools for spin-environment characterization.

Turning to applications in quantum information science, a possible extension of the present work is to consider Mn:ZnO as a qudit, that is, a generalization of the qubit to a d-dimensional Hilbert space [150]. Moving beyond binary encodings offers several advantages: the accessible Hilbert space grows as d^N for an array of N qudits, yielding higher information density and more compact encodings of algorithms [151, 152], while also enabling the design of intrinsically more efficient gates [153]. Electronuclear spin

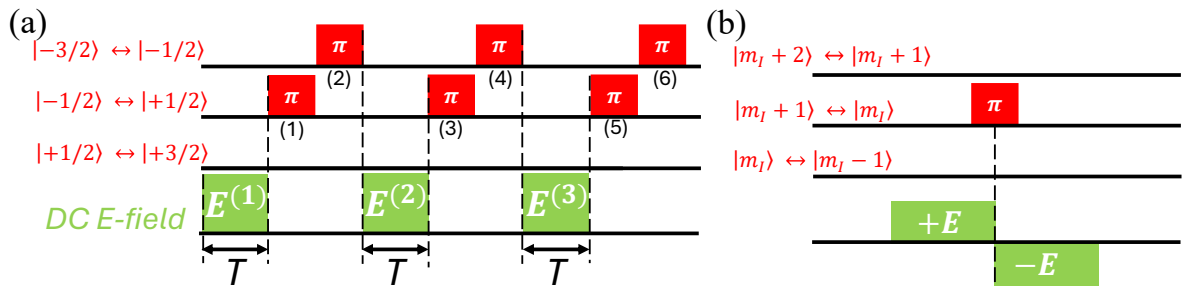

Figure 3.11: Proposed pulse sequences for electric-field control of electronuclear spin systems in quantum information processing. (a) A sequence of rf π-pulses alternated with DC E-field pulses ensures that only a single basis component (here $|m_I = +3/2\rangle$) acquires a relative phase. This realises a conditional phase gate, which is a fundamental operation of the quantum Fourier transform. (b) A conditional phase gate on the $|m_I + 1\rangle \leftrightarrow |m_I\rangle$ coherence implemented using a bipolar DC E-field sequence.

systems provide a natural setting for qudits, owing to the combination of electronic and nuclear degrees of freedom, thereby enlarging the available state space [145]. Theoretical proposals based on such systems have already outlined fault-tolerant[5] qudit operations [154], and proof-of-principle experimental demonstrations have implemented quantum-error-correction encoding within a $d = 4$ qudit in Mn:ZnO [141].

Building on this foundation, the present study points toward the possibility of realizing an all-electric quantum Fourier transform (QFT) in an electronuclear spin system. The QFT is a central subroutine in quantum computing, underpinning algorithms such as Shor's integer factorization [155] and quantum phase estimation, which has broad applications in quantum chemistry [156]. Implementing the QFT in an electronuclear qudit would thus provide a proof-of-principle demonstration of electrically driven quantum logic in spin systems, directly leveraging the results reported here. As in the qubit setting, the qudit-QFT relies on two key types of gates. The first is the Hadamard gate, which generates equal superpositions of basis states and thereby enables quantum parallelism[6]. In NMR, this gate can be implemented either through an off-resonance pulse, e.g., $\hat{\mathcal{H}} = e^{-i\pi(\hat{I}_x+\hat{I}_z)/\sqrt{2}}$ (see Eq. 1.28), or via a composite pulse sequence such

[5]Fault tolerance refers to the ability of a quantum computing architecture to continue operating correctly even in the presence of noise or errors.

[6]Quantum parallelism refers to the ability of a quantum computer to process many inputs at once, because a superposition of basis states evolves through a circuit as though each component were computed simultaneously. The Hadamard gate is the simplest example: it maps the computational Z-basis into a superposition basis lying in the equatorial plane of the Bloch sphere. Explicitly, $H|0\rangle = (|0\rangle + |1\rangle)/\sqrt{2}$ and $H|1\rangle = (|0\rangle - |1\rangle)/\sqrt{2}$.

as $\hat{I}_y(\pi/4) - \hat{I}_x(\pi) - \hat{I}_{-y}(\pi/4)$ [157]. In the present context, an equivalent operation could be realised by exploiting off-resonance NER pulses.

The second essential operation is the controlled-phase gate, which implements a conditional phase shift depending on the state of a control qubit. In the qubit case, its action can be written as $\mathrm{CPhase}(\varphi) = \begin{pmatrix} 1 & 0 \\ 0 & e^{i\varphi} \end{pmatrix}$, such that only the state $|1\rangle$ acquires the relative phase factor $e^{i\varphi}$. In the qudit setting, the same principle extends naturally: selected sublevels within the larger Hilbert space can be made to accumulate controlled phases. In an electronuclear spin system, this can be achieved by applying a static electric field, which shifts the energies of the nuclear spin projections $|m_I\rangle$ in proportion to m_I. The corresponding evolution is $\hat{E}(\varphi) = e^{-i\varphi\hat{I}_z}$ with $\varphi = \delta f\, t_E$, where δf is the E-field-induced resonance shift and t_E the E-field pulse duration. Acting on a basis state, this gives $\hat{E}(\varphi)\,|m_I\rangle = e^{-im_I\varphi}\,|m_I\rangle$, so that different nuclear spin projections acquire controllable relative phases.

As an illustrative example, Fig. 3.11(a) presents a pulse protocol that implements a conditional phase gate in a $d = 4$ qudit. The central idea is to apply a phase shift selectively to one computational basis state, while restoring all others up to global phases. This is achieved by alternating rf π-pulses with DC E-field: the rf operations reshuffle the population among basis states, ensuring that different components of the state vector are sequentially exposed to the E-field action, while the DC pulses accumulate state-dependent phases. Following the sequence in the figure, the resulting evolution of a generic four-dimensional state $|\psi\rangle$ is

$$
\begin{aligned}
|\psi\rangle = \begin{pmatrix} \alpha \\ \beta \\ \gamma \\ \delta \end{pmatrix}
&\xrightarrow{\hat{E}^{(1)}} \begin{pmatrix} \alpha e^{-i3\varphi/2} \\ \beta e^{-i\varphi/2} \\ \gamma e^{+i\varphi/2} \\ \delta e^{+i3\varphi/2} \end{pmatrix}
\xrightarrow{\pi^{(1)}} \begin{pmatrix} \alpha e^{-i3\varphi/2} \\ \gamma e^{+i\varphi/2} \\ \beta e^{-i\varphi/2} \\ \delta e^{+i3\varphi/2} \end{pmatrix}
\xrightarrow{\pi^{(2)}} \begin{pmatrix} \gamma e^{+i\varphi/2} \\ \alpha e^{-i3\varphi/2} \\ \beta e^{-i\varphi/2} \\ \delta e^{+i3\varphi/2} \end{pmatrix}
\xrightarrow{\hat{E}^{(2)}} \begin{pmatrix} \gamma e^{-i\varphi} \\ \alpha e^{-i2\varphi} \\ \beta \\ \delta e^{+i3\varphi} \end{pmatrix} \\
&\xrightarrow{\pi^{(3)}} \begin{pmatrix} \gamma e^{-i\varphi} \\ \beta \\ \alpha e^{-i2\varphi} \\ \delta e^{+i3\varphi} \end{pmatrix}
\xrightarrow{\pi^{(4)}} \begin{pmatrix} \beta \\ \gamma e^{-i\varphi} \\ \alpha e^{-i2\varphi} \\ \delta e^{+i3\varphi} \end{pmatrix}
\xrightarrow{\hat{E}^{(3)}} \begin{pmatrix} \beta \\ \gamma \\ \alpha \\ \delta e^{+i6\varphi} \end{pmatrix}
\xrightarrow{\pi^{(5)}} \begin{pmatrix} \beta \\ \alpha \\ \gamma \\ \delta e^{+i6\varphi} \end{pmatrix}
\xrightarrow{\pi^{(6)}} \begin{pmatrix} \alpha \\ \beta \\ \gamma \\ \delta e^{+i6\varphi} \end{pmatrix}. \qquad (3.5)
\end{aligned}
$$

Here, φ denotes the electric-field-induced phase introduced earlier, which can be tuned by varying the duration or amplitude of the applied DC pulses, while $\hat{E}^{(1,2,3)}$ indicate the

successive E-field operations within the sequence. The net outcome is a relative phase factor $e^{+i6\varphi}$ applied solely to the δ component, with the rest of basis states unchanged (up to an overall global phase). In this way, the protocol realises a selective controlled-phase gate on a chosen state. A practical limitation, however, is that extending this approach to a general d-dimensional qudit requires $d-2$ rf pulse sets, each consisting of $d-2$ individual π-pulses, leading to quadratic scaling $(d-2)^2$ in the number of rf operations, in addition to $d-1$ DC E-field pulses.

Another strategy, which avoids the unfavourable scaling of the previous protocol, is based on the use of *bipolar* electric-field pulses [158]. This consists of applying two DC electric-field pulses of equal magnitude but opposite polarity in sequence. For a linear SEC such as Mn:ZnO, reversing the polarity of the electric field simply changes the sign of the accumulated phase shift, so that successive positive and negative pulses produce opposite phase evolutions. A schematic of this approach is shown in Fig. 3.11(b), where a symmetric bipolar electric-field pulse is embedded across a π pulse resonant to the $|m_I \leftrightarrow m_I+1\rangle$ transition. Following the timing indicated in the figure, the evolution of a generic nuclear-spin state in a d-dimensional Hilbert space ($d \geq 2$), $|\psi^{(d)}\rangle$, is given by:

$$|\psi^{(d)}\rangle = \begin{pmatrix} \vdots \\ \kappa_2 \\ \kappa_1 \\ \kappa_0 \\ \kappa_{-1} \\ \vdots \end{pmatrix} \xrightarrow{+\hat{E}} \begin{pmatrix} \vdots \\ \kappa_2 e^{i(m_I+2)\varphi} \\ \kappa_1 e^{i(m_I+1)\varphi} \\ \kappa_0 e^{im_I\varphi} \\ \kappa_{-1} e^{i(m_I-1)\varphi} \\ \vdots \end{pmatrix} \xrightarrow{\pi_{0,1}} \begin{pmatrix} \vdots \\ \kappa_2 e^{i(m_I+2)\varphi} \\ \kappa_0 e^{im_I\varphi} \\ \kappa_1 e^{i(m_I+1)\varphi} \\ \kappa_{-1} e^{i(m_I-1)\varphi} \\ \vdots \end{pmatrix} \xrightarrow{-\hat{E}} \begin{pmatrix} \vdots \\ \kappa_2 \\ \kappa_0 e^{-i\varphi} \\ \kappa_1 e^{i\varphi} \\ \kappa_{-1} \\ \vdots \end{pmatrix}. \tag{3.6}$$

As a result, only the targeted $|m_I \leftrightarrow m_I+1\rangle$ coherence acquires an additional phase, while other components remain unchanged. Taken together, the two pulse sequences discussed above highlight complementary approaches to achieve electric-field control in multidimensional quantum systems, such as coupled electron-nuclear spins.

4
Electric Dipole Spin Resonance

4.1 Previous Experimental Realizations of EDSR

In Chapter 3, we examined how *nuclear spin transitions* in a defect embedded in a semiconductor host can be driven electrically, with the electron component of the wave-function acting as an amplifier of the system's electric sensitivity. In those experiments, however, the ESR control pulses were still applied magnetically. To achieve full E-field control of the spin system, it is therefore necessary that not only nuclear, but also *electron* spin transitions be driven directly by resonant electric fields, a mechanism known as Electron Dipole Spin Resonance (EDSR) [145].

EDSR has already been demonstrated across a variety of platforms at the single-electron level. In silicon quantum dots, for instance, integrated micromagnets create a static magnetic field gradient. When an oscillating electric field is applied, it displaces the electron, producing an effective time-varying magnetic field in the electron's rest frame; this enabled fast spin control with reported qubit fidelities reaching up to $\mathcal{F} = 99.8\%$ [159]. A different route was demonstrated in single-electron transistors based on donors in silicon (the same platform underlying the Kane proposal in Subsec. 1.3). For instance, in

Ref. [145], EDSR was used to simultaneously flip electron and nuclear spins (i.e., $\Delta m_s = \pm 1$, $\Delta m_I = \pm 1$) in a ^{123}Sb donor device, driven by modulation of the hyperfine interaction.

Another notable advance in this direction was achieved by George *et al.* [129], who investigated EDSR in bulk Mn:ZnO (the same system used for the measurements presented in Chapter 3). In their study, continuous-wave (cw) EDSR was performed by placing the crystal at the electric, rather than the magnetic, antinode of a rectangular microwave cavity. Under these conditions, the driving mechanism was identified as originating from modulation of the axial anisotropy parameter D (see Eq. 3.1), which, as discussed earlier, arises from the crystal field surrounding the Mn^{2+} ions and is therefore sensitive to the local polar environment of the host lattice. Upon the application of an oscillating electric field, such crystal field is periodically perturbed, giving rise to a time-dependent variation $\delta D(t)$, following a rationale analogous to that described by Eqs. 3.3 and 3.4. Crucially, however, these experiments were carried out under cw conditions, meaning the measurements probed changes in spin population (*polarization*) rather than manipulating spin coherence. This distinction is critical for applications in quantum information processing, where the ability to coherently drive and detect quantum superpositions is essential. Despite this, the possibility of achieving such control and detection purely through electric fields remains underexplored.

In this work, we investigate the feasibility of performing *pulsed* EDSR, that is, coherent spin manipulation driven entirely by microwave electric fields, in a spin ensemble of iron-doped ZnO. This system, closely related to that investigated in the previous chapter, exhibits stronger atomic SOC and is therefore expected to display an enhanced spin-electric coupling (Subsec. 1.2.1). In contrast to the cw experiments described in Ref. [129], the present study may enable direct control and readout of spin coherence, rather than polarization, by implementing an electrically driven Hahn-echo sequence.

The chapter begins with a characterization of the magnetic and electric properties of Fe:ZnO, followed by the theoretical framework for the possible EDSR mechanism in this system, specifically emphasizing the selection rules that differentiate it from conventional ESR. Before presenting the experimental results and analysis, we describe the design

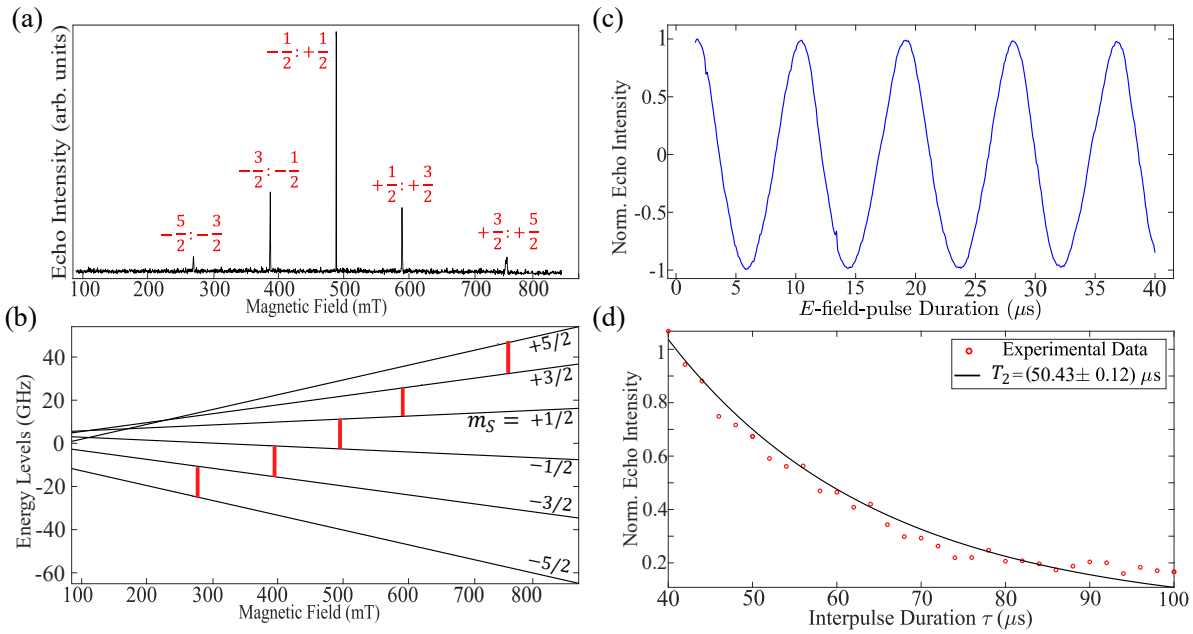

Figure 4.1: (a) Experimental echo-detected field sweep of Fe^{3+}:ZnO (with $c-$axis $\parallel B_0$, $\theta = 0°$), recorded at 20 K using our home-built resonator operating at a resonance frequency of $\sim$ 14 GHz (see Sec. 4.3). The observed transitions are labelled in the Zeeman basis. (b) Simulated energy-level diagram, highlighting the standard $\Delta m_s = \pm 1$ transitions in red. (c, d) Representative measurements taken at the $|m_s = 1/2 \leftrightarrow 3/2\rangle$ transition for the spin-electric coupling ($\kappa_D \simeq 10\,\mathrm{Hz/(V/m)}$), and electron coherence time T_2.

and performance of the custom-built cavity resonator used in these experiments, which constitutes an adaptation of the rectangular cavity employed in Ref. [129]. Note that all measurements were performed using the home-built broadband pulsed spectrometer described in Subsec. 1.5.3.

4.2 Spin and Electric-dipole Transitions in Iron defects in ZnO

The system investigated in this chapter consists of trivalent Fe^{3+} ions doped into the same polar semiconducting ZnO crystal studied in Chapter 3. Like Mn^{2+}, Fe^{3+} also possesses a high-spin ground state with $S = 5/2$. However, in contrast to manganese, approximately 98% of naturally occurring iron isotopes are nuclear-spin-free, with only ^{57}Fe having $I = 1/2$ [160]. Consequently, nuclear effects are generally negligible, as evidenced by the experimental ESR spectrum in Fig. 4.1(a), which exhibits the five allowed $\Delta m_s = \pm 1$ transitions without any hyperfine splitting. The effective spin Hamiltonian is therefore

analogous to Eq. 3.1, except for the absence of nuclear terms

$$\hat{\mathcal{H}} = D\,(\hat{S}_z \cos\theta + \hat{S}_x \sin\theta)^2 + \mu_B g B_0 \hat{S}_z. \tag{4.1}$$

Here θ is the angle between the crystal c-axis and the static field B_0. The simulated energy-level diagram for $\theta = 0°$ in Fig. 4.1(b) reproduces the ESR transitions (red), from which we extract an isotropic g-factor $g \simeq g_e$, and an axial zero-field splitting (ZFS) parameter $D \simeq -1780$ MHz, in line with previous reports [161]. Note that this ZFS is approximately 2.5 times larger than that of Mn^{2+} ions, reflecting the stronger spin-orbit coupling of Fe^{3+} and, consequently, a potentially enhanced spin-electric coupling (SEC).

To further characterise the sample, we investigated both its coherence properties and its (static) SEC. Representative data for the $|m_s = 1/2 \leftrightarrow 3/2\rangle$ transition, taken at 20 K, are shown in Fig. 4.1(c) and (d). The spin coherence times are measured to be in the range of a few tens to hundreds of μs, which is qualitatively similar to the values obtained for Mn^{2+}:ZnO. In contrast, the SEC is found to be roughly three times stronger. The measurement is performed using the Hahn-Mims sequence with an E-field device analogous to that described previously, generating fields of order ~ 1 kV/cm. Across the spectrum, the extracted values for the SEC coupling constant range from $\kappa_D \simeq 0.5$ Hz/(V/m) for the central peak $|m_s = -1/2 \leftrightarrow +1/2\rangle$ up to $\kappa_D \simeq 20.5$ Hz/(V/m) for the outermost peaks $|m_s = \pm 3/2 \leftrightarrow \pm 5/2\rangle$.

Having established the electric-field sensitivity of the sample, and following the cw EDSR results reported in Ref. [129], we now investigate EDSR in Fe:ZnO, assuming that the same mechanism applies to this isostructural system. In that study, a resonant oscillating electric field was shown to modulate the axial anisotropy parameter as $D(t) = D(E = 0) + \delta D(t)$. This effect originates from the crystal field created by the electrostatic environment around Fe^{3+}, which determines both the anisotropy parameter D and an internal electric dipole, both aligned along the crystal c-axis. The resulting time-dependent perturbation of such field enters the spin Hamiltonian as $\sim \delta D(t)\hat{S}_z^2$, acting as an alternative oscillating transition operator that can drive spin transitions under resonance conditions.

More specifically, the EDSR interaction Hamiltonian, $\hat{\mathcal{H}}_I^{\mathrm{EDSR}}(t)$, can be derived following the discussion in Subsec. 1.2.3 and it can be expressed as

$$\begin{aligned}\hat{\mathcal{H}}_I^{\mathrm{EDSR}}(t) &= \delta D(t)\ \left(\hat{S}_z\cos(\theta)+\hat{S}_x\sin(\theta)\right)^2 \\ &= \tilde{\kappa}_D\ (\mathbf{E}_1(t)\cdot\mathbf{p})\left(\hat{S}_z\cos(\theta)+\hat{S}_x\sin(\theta)\right)^2. \end{aligned} \tag{4.2}$$

Here, $\mathbf{p}$ denotes the direction of the electric dipole moment, while $\tilde{\kappa}_D$ is the intrinsic coupling of the sample to ac electric fields. The amplitude of the oscillating perturbation $\delta D(t) = \tilde{\kappa}_D \mathbf{E}_1(t)\cdot\mathbf{p}$ thus depends on both the sample's electric sensitivity and the degree of alignment between the applied electric field and the polar axis.

From Eq. 4.2, one can straightforwardly prove that EDSR follows selection rules different from those of conventional ESR. This becomes clear by setting $\theta = 90°$ and aligning the oscillating electric field with the dipole moment direction, $\mathbf{E}_1 \parallel \mathbf{p}$, which maximises the electric driving term (the configuration used in the experiment). Under these conditions, this equation reduces to

$$\hat{\mathcal{H}}_I(\theta=90°,t) = \tilde{\kappa}_D\, E_1(t)\hat{S}_x^2 = \frac{\tilde{\kappa}_D}{4}\, E_1(t)\left(\hat{S}_+ + \hat{S}_-\right)^2. \tag{4.3}$$

This shows that $\hat{\mathcal{H}}_I(\theta = 90°, t) \sim \hat{S}_\pm^2$, indicating that double-quantum ($\Delta m_s = \pm 2$) transitions can, in principle, be excited, unlike in conventional ESR.

To better illustrate the differences in selection rules between EDSR and standard ESR, we simulated the orientation-dependent spectra for both cases (using Eq. 4.2 for EDSR) at various excitation frequencies. The results are presented in Fig. 4.2. In the ESR spectra (left panels), the five resonances correspond to single-quantum transitions ($\Delta m_s = \pm 1$), whereas in the EDSR spectra, the prominent low-field peaks (absent in ESR) correspond to double-quantum transitions[1], and are highlighted by the white rectangle in panel (d). This assignment is supported by Ref. [129] and the simulations in Fig. 4.9(b), where the relevant double transitions are indicated by blue lines. Another key feature of the EDSR spectra is the pronounced angular dependence of the single-quantum ($\Delta m_s = \pm 1$) transitions, which disappear near $\theta = 0°$ and $90°$. This behaviour arises because, at $\theta = 0°$

[1] As noted, e.g., in Fig. 4.10, some of these resonances are technically "triple" $\Delta m_s = \pm 3$ transitions. For simplicity, however, we will continue referring to them as double transitions.

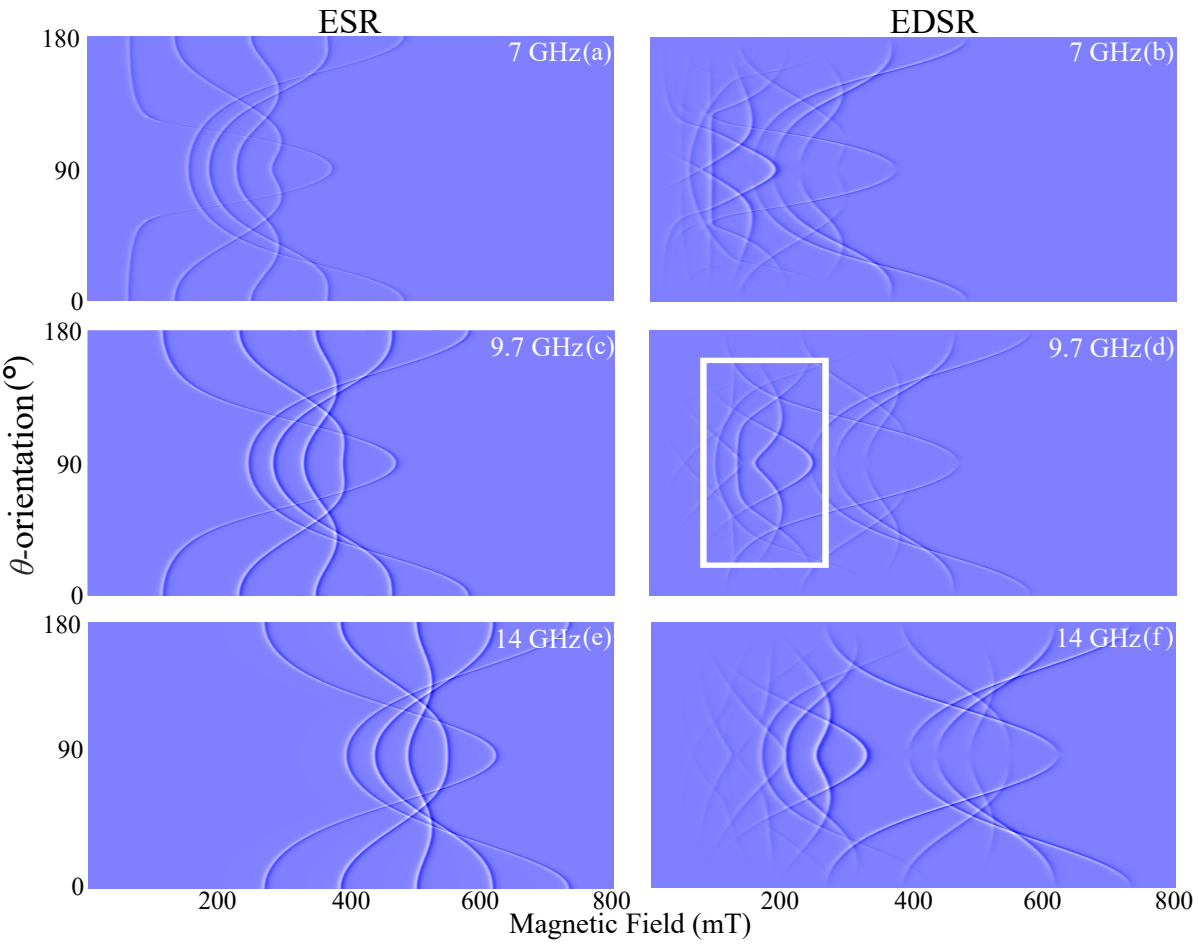

Figure 4.2: Simulated ESR (left) and EDSR (right) orientation-dependent spectra, with the magnetic field orientation defined by the angle θ in Eq. 4.1. Spectra are shown at $C-$band (7 GHz), $X-$band (9.7 GHz), and K_u-band (14 GHz). Two key differences are observed: (i) EDSR exhibits additional $\Delta m_s = \pm 2$ transitions, absent in ESR and highlighted by the white rectangle in panel (d); and (ii) EDSR shows a pronounced orientation-dependent intensity for the $\Delta m_s = \pm 1$ transitions near $\theta = 0°(180°), 90°$, unlike ESR.

(or 180°), Eq. 4.2 reduces to $\hat{S}_z^2$, which commutes with the Zeeman term and thus forbids $\Delta m_s = \pm 1$ transitions. As the orientation deviates from these extremes, contributions from $\hat{S}_x^2$ and cross terms such as $\hat{S}_x\hat{S}_z$ break this commutation, enabling both double- and single-quantum transitions. When the field lies perpendicular to the $c-$axis ($\theta = 90°$), the Hamiltonian is dominated by $\hat{S}_x^2$, connecting only states differing by $\Delta m_s = \pm 2$; as a result, single-quantum transitions vanish while double-quantum transitions are fully allowed.

Distinguishing EDSR from conventional ESR relies on achieving sufficient spectral separation between the single-quantum and double-quantum transitions. At 7 GHz (C-band, Fig. 4.2, top row), these transitions are close in field and partially overlap, making

their identification challenging. Increasing the excitation frequency improves separation because single-quantum transitions generally occur at higher magnetic fields, where the Zeeman term dominates over the zero-field splitting, resulting in an approximately linear dependence on field ($hf \simeq g\mu_B B_0$). In contrast, $\Delta m_s = \pm 2$ transitions are influenced more strongly by D, which is independent of B_0, so their positions shift less with increasing frequency. As a result, higher excitation frequencies progressively separate the single- and double-quantum transitions, enhancing spectral resolution. This trend is evident at 9.7 GHz (middle row), where the transitions are more clearly resolved, although some overlap still remains. At 14 GHz (bottom row), the separation is sufficient to unambiguously identify the double-quantum transitions and assign them confidently to EDSR. Higher frequencies would further improve this separation but at the cost of reduced sample space[2], which can limit sensitivity, particularly in a magnetically dilute system like the one studied here. In the next section, we outline the design criteria and considerations for the custom-made cavity resonator used to excite EDSR.

4.3 Reentrant Cavity Resonators for EDSR

4.3.1 Design Criteria

When designing a resonator for EDSR, several criteria must be considered:

(i) *Resonance frequency and sample volume.* The resonance frequency must be sufficiently high to spectrally separate the $\Delta m_s = \pm 1$ from the $\Delta m_s = \pm 2$ transitions, thus allowing standard ESR signals to be distinguished from EDSR-specific contributions. However, higher frequencies are typically achieved by smaller resonators, which constrains the available sample volume and can reduce sensitivity. For Fe:ZnO, this consideration necessitates operation in the K_u band (12-18 GHz, corresponding to wavelengths $\lambda \simeq 1.5$-2.5 cm), as illustrated in Fig. 4.2.

(ii) *Field distribution.* The electric and magnetic field components must be spatially separated to enable an unambiguous distinction between EDSR and ESR, since in certain operating conditions their effects can appear identical (see Subsec. 4.4.1). In

[2]As the resonance frequency generally increases with decreasing cavity dimensions.

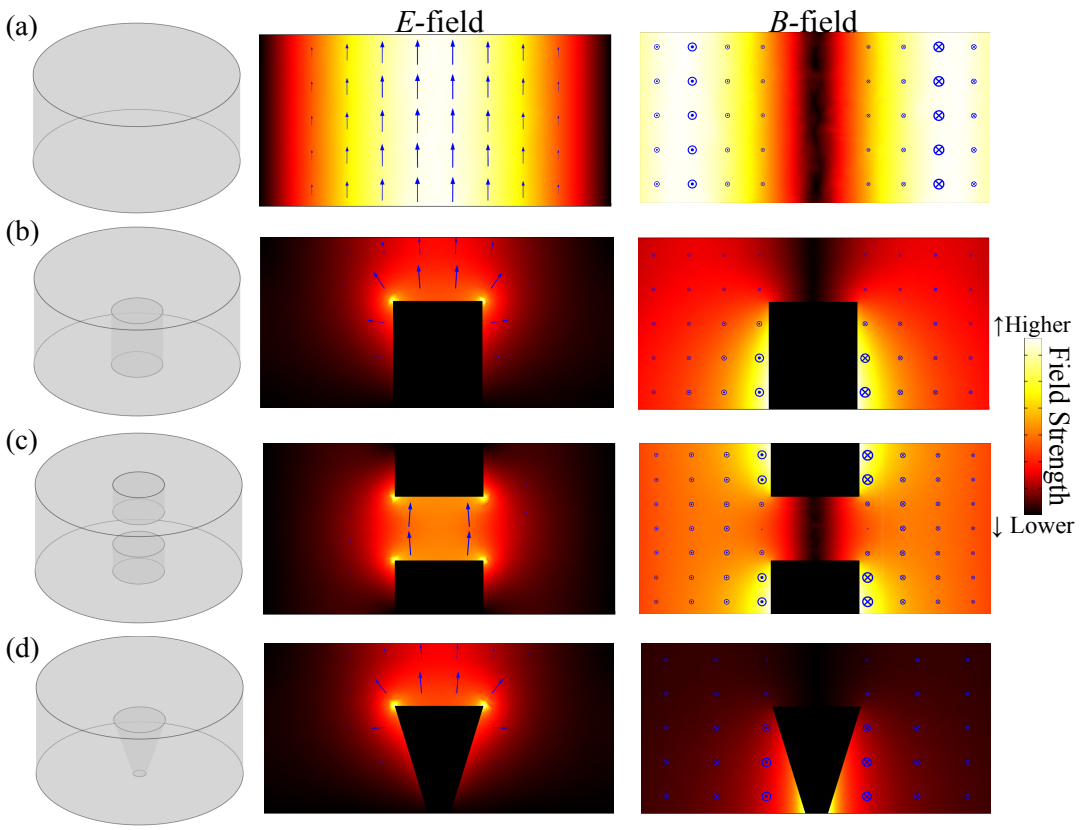

Figure 4.3: Finite-element simulations comparing the electric (left) and magnetic (right) field distributions of the TM_{010} mode in four resonator geometries: (a) standard cylindrical, (b) single-reentrance, (c) double-reentrance, and (d) tapered-conic-reentrance. In all reentrant designs, the magnetic field is concentrated around the central post(s), while the electric field is confined to the capacitive gap, resulting in reduced electric mode volumes compared to the standard cylindrical cavity of comparable size. Resonance frequencies and corresponding electric mode volumes are: (a) (14.33 GHz, $4.53\times10^{-2}\lambda^3$); (b) (8.76 GHz, $1.30\times10^{-5}\lambda^3$); (c) (10.53 GHz, $2.36\times10^{-5}\lambda^3$); (d) (7.80 GHz, $6.48\times10^{-5}\lambda^3$).

practice, cavity designs should minimise the local magnetic field while maximising the electric field at the sample position.

(iii) *Electric mode volume.* Efficient coupling to the electric field requires minimizing the electric mode volume, defined as $V_E = \frac{\int dV\, |\mathbf{E}(\mathbf{r})|^2\, \epsilon(\mathbf{r})}{|\mathbf{E}(\mathbf{r}_{\max})|^2\, \epsilon(\mathbf{r}_{\max})}$, analogous to V_B in Eq. 1.51. In fact, a smaller V_E indicates stronger field confinement at the sample site. Following Ref. [91], V_E can be expressed in units of the cube of the vacuum wavelength at resonance, λ^3 (Fig. 4.4), which provides a frequency-independent figure of merit and enables direct comparison between resonators[3].

[3]Expressing V_E in units of λ^3 normalises out the frequency dependence, since for a given resonator geometry $V_E \propto \lambda^3 \propto f^{-3}$, allowing direct comparison between resonators operating at different

(iv) *Geometric factor.* Finally, a high quality factor Q, or equivalently a material- and coupling-independent geometric factor G (Eq. 1.50), is desirable. High G is particularly important in cw operation, where it improves sensitivity by narrowing the resonance linewidth and enhancing field strength per unit input power.

To excite EDSR efficiently, we employ a *reentrant cavity resonator*, a hybrid design that combines the high filling factor of loop-gap resonators with the well-defined modes and robustness of conventional cavities. It consists of a central conducting post extending toward the bottom wall, leaving narrow capacitive gaps. In this geometry, the magnetic field circulates around the post, while the electric field is confined to the gap (Fig. 4.3(b)). This spatial separation naturally accommodates different modalities: in ESR the sample is placed at the base of the post, where the magnetic field antinode lies, whereas in EDSR the optimal location is at the top of the capacitive gap, i.e., the electric field antinode. Fig. 4.3 shows the fundamental TM_{010} mode[4] in four geometries: a standard cylindrical cavity (a), and single-post (b), double-post (c), and tapered-conic (d) reentrant designs.

To benchmark the different geometries and identify the most suitable design for our experiments, we performed finite-element modelling (FEM) simulations[5] of the three reentrant resonators, alongside a standard cylindrical cavity for comparison. In particular, we focused on point (iii) and (iv), i.e., the electric mode volume and the geometric factor. The results are summarised in Fig. 4.4, where each marker corresponds to a simulated cavity with varying dimensional parameters, and colours distinguish between the different geometrical designs. All simulations were constrained to cavities resonating within the K_u-band, with physical dimensions compatible with the cryostat and probe limitations (cavity diameter $\lesssim 3\,\mathrm{cm}$).

From these simulations, and in line with Ref. [91], introducing a central reentrance substantially reduces V_E and moderately enhances the geometric factor, compared with standard cylindrical cavities (black markers). This highlights the advantages of reentrant

frequencies.

[4] In cylindrical cavities, the TM_{010} mode is the lowest-order transverse magnetic mode, widely used because it produces a strong, uniform fields.

[5] Using the COMSOL Multiphysics software package in the AC/DC module.

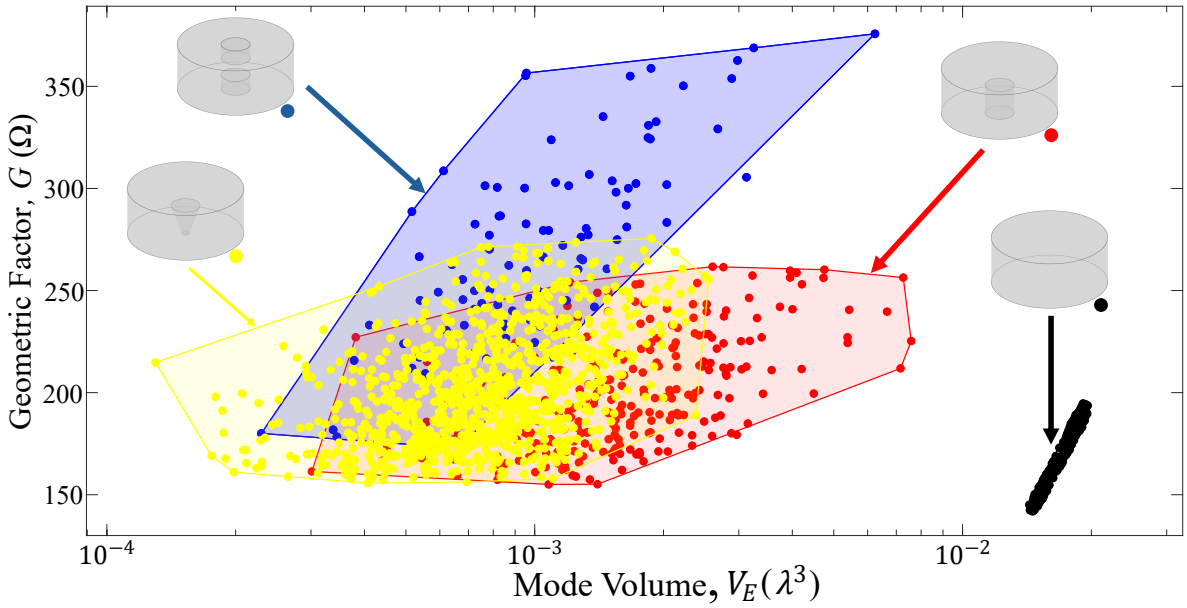

Figure 4.4: (FEM Simulations) A comparison of the four cavity geometries discussed in the main text, plotted as a function of the geometric factor, G, and the electric field mode volume, V_E. Each marker corresponds to a simulated resonator with different dimensional parameters (all simulated cavities resonate in the K_u band and cavity diameter $\lesssim 3$ cm), while marker colours indicate different cavity geometries. *Colour Legend:* Yellow: conic reentrance; Blue: double reentrance; Red: single reentrance; Black: standard cylindrical.

designs for strengthening spin-microwave coupling. Among the reentrant geometries, the tapered conic design achieves the most compact mode volume (up to two orders of magnitude smaller than the standard cylindrical case), while also providing improved spatial separation between electric and magnetic field antinodes. By contrast, double-reentrance cavities tend to yield slightly higher geometric factors.

In selecting the optimal resonator, the coupling between the microwave feedline and the cavity must also be carefully considered. While many coupling schemes have been developed [92], for this proof-of-concept study we adopted a *slot-in-waveguide* configuration (see Fig. 4.8). In this approach, the cavity is coupled to a waveguide through a narrow aperture (slot) milled into one of the waveguide walls. The electromagnetic energy leaks through this aperture, and both its position relative to the resonator and its area determine the strength of the coupling. By selecting a waveguide that supports a mode structure compatible with that of the cavity, efficient energy transfer can be achieved with minimal reflection or field distortion. Although this geometry

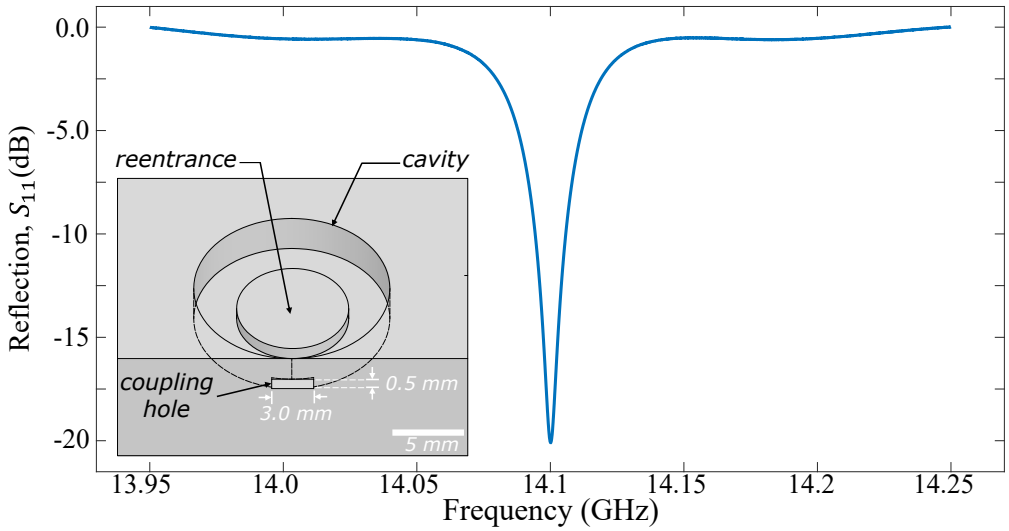

Figure 4.5: (Experimental) Resonator profile of the brass reentrant cavity measured with a vector network analyser, showing a resonance at $\sim$ 14.1 GHz. *Inset:* Scaled schematic of the cavity geometry, including the 0.5 mm $\times$ 3 mm coupling slot connecting the cavity to the waveguide.

does not easily allow fine tuning of the coupling strength (see next section), it provides a mechanically robust interface that minimises perturbations to the resonator field distribution and helps reduce dielectric losses.

In practice, we fabricated both the tapered-conic and the double-reentrance geometries. However, in neither case were we able to observe a clear reflection profile from the cavity. We attribute this to insufficient coupling efficiency. For slot-in-waveguide coupling to be effective, the waveguide must be aligned with a magnetic-field antinode in order to drive the mode. In the tapered-conic geometry, the relevant antinode lies too close to the reentrance to be properly accessed, while in the double-reentrance design the antinode is distributed between the two posts, resulting in a weakened coupling. After these considerations, we opted for and constructed a single-reentrance cavity. This design offers a balanced compromise: a lower mode volume and higher geometric factor than the standard cylindrical cavity, together with stronger coupling than the tapered-conic and double-reentrance variants. In the next section, we present the characterization of this final design.

4.3.2 Characterization of the Reentrant Cavity

The single-reentrant cavity used in the experiments was machined from brass, with a radius of 7 mm and a height of 3 mm. The central reentrance extends 1 mm from the base and has a radius of 4 mm. A schematic of the structure, drawn to scale, is shown in the inset of Fig. 4.5. The main panel displays the measured resonator profile obtained with a vector network analyser, showing the fundamental resonance at 14.1 GHz, in line with the FEM-predicted value for the TM_{010} mode (within 2%).

Once the geometry was fixed, the coupling aperture was designed to set the interaction between the cavity and the microwave feedline. As discussed in Sec. 1.5, critical coupling is ideal for cw experiments, while over-coupling is preferable for pulsed operation. In our case the coupling is not tunable: implementing an iris bolt, as in commercial ESR systems, would require drilling into the microwave components and could compromise their integrity. We therefore aimed for an intermediate regime between critical and over-coupling, allowing operation in both modes without adjustment. This choice inevitably reduces cw efficiency compared to true critical coupling and produces longer ring-down times than in strongly over-coupled systems. However, these trade-offs are minor in practice: cw data serve only for rapid sample characterization, while in pulsed experiments the electron coherence times T_2 of tens of μs at the relevant temperature easily accommodate the longer defence pulses (see Sec. 4.4).

The coupling slot dimensions were optimised through a trial-and-error approach, since the coupling strength is highly sensitive to manufacturing tolerances and FEM simulations can provide only approximate guidance [92]. The final aperture, 3 mm wide and 0.5 mm high (see inset of Fig. 4.5), is relatively small compared to the overall resonator size, which helps preserve the cavity's mode symmetry. All results presented in the following sections were obtained using this resonator design and coupling configuration.

To confirm that the resonator supports the TM_{010} mode predicted by FEM simulations, we probed its B_1-field distribution using a standard ESR test sample, dilithium phthalocyanine (Li_2Pc, $S = 1/2, g \simeq g_e$), whose molecular structure is shown in Fig. 4.6(a). This compound provides a strong ESR signal while being insensitive to electric fields,

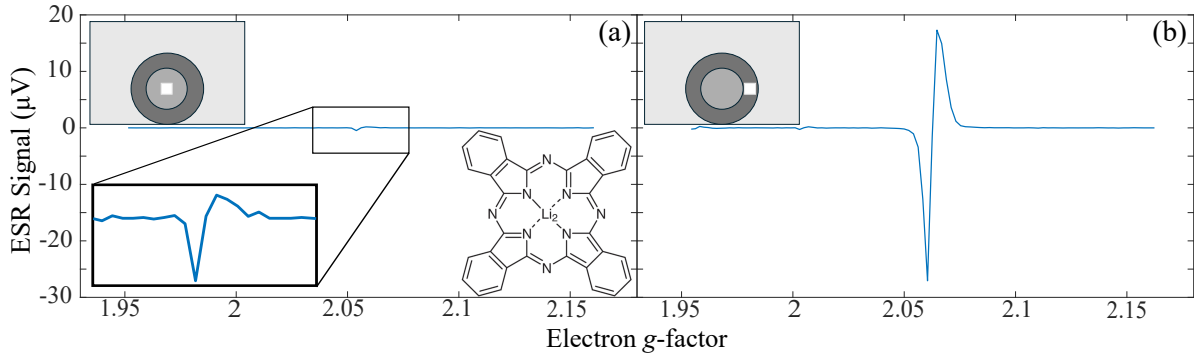

Figure 4.6: The cw ESR spectra of Li_2Pc, measured with the home-built reentrant resonator. The molecular structure is shown in the right inset. Spectra are recorded with the sample placed at the top (a) and on the side (b) of the reentrance. The latter configuration produces a signal nearly fifty times stronger, reflecting the substantially higher magnetic field amplitude at the cavity base, in agreement with FEM predictions.

making it an ideal probe of magnetic fields. Continuous-wave detection[6] was employed while placing the Li_2Pc sample at different positions within the cavity. Fig. 4.6 shows the resulting spectra for placing the sample at the top (a), and at the base (b) of the reentrance, corresponding to the expected magnetic- and electric-field antinodes of the TM_{010} mode, respectively.

The standard ESR signal measured at the cavity base is approximately fifty times stronger than that detected at the top, in agreement with the expected spatial distribution of the microwave magnetic field. Importantly, as shown by the simulations in Fig. 4.2, the ratio between the double-transition intensities around $\theta = 90°$ for EDSR and standard ESR is predicted to be four to five orders of magnitude (see the inset in Fig. 4.13(c)). This implies that any experimentally observed double transitions around those $\theta-$orientation are highly unlikely to originate from conventional ESR excitation. In both measurement positions, the microwave power was carefully adjusted to prevent signal saturation, ensuring a reliable comparison of the relative intensities. The weak residual signal observed when the sample is positioned at the top (left inset in Fig. 4.6(a)) is attributed to the finite dimensions of the sample, which result in partial overlap with regions where the mw magnetic field does not vanish completely.

[6]Since the cavity is made of brass, slow field modulation (a few hundred Hz) is necessary to ensure full penetration of the modulation field.

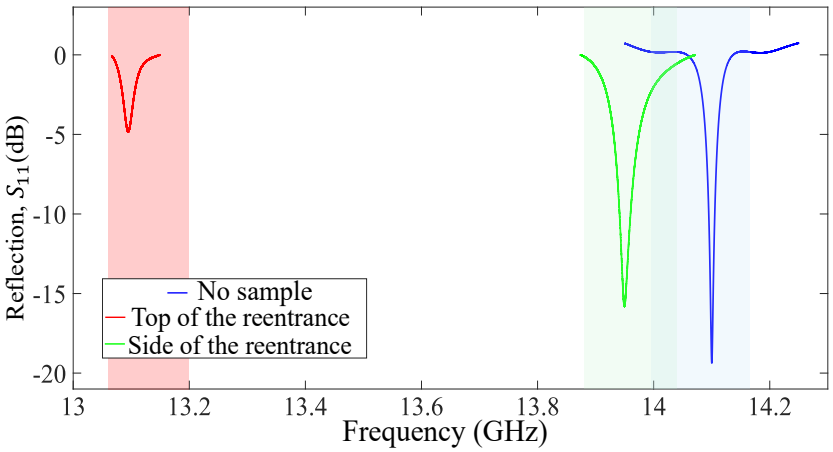

Figure 4.7: Resonator profile of the home-built reentrant cavity at room temperature measured without a sample (blue), and with a 2 mm × 2 mm × 1 mm ZnO crystal placed at the cavity base (green), or at the top of the reentrance (red). The pronounced frequency shift and reduction in Q-factor observed in the latter case are consistent with the stronger electric field in the cavity's gap. Shaded regions indicate the resonant frequency range predicted by FEM simulations, accounting for manufacturing tolerances of ±0.015 mm.

Another important consideration is the effect of dielectric losses introduced by our polar ZnO sample, which has dimensions $2 \times 2 \times 1$ mm^3 (as the sample is diluted, it must be spatially extended to ensure sufficient signal) and an anisotropic[7] electric permittivity $\varepsilon_r = \{10, 10, 12\}$ [162]. Fig. 4.7 compares the resonator response in three configurations at room temperature: unloaded (blue), with the ZnO sample placed at the top of the reentrance (red), and at its base (green). When positioned at the top, the sample produces a pronounced shift (resonance at $\sim$ 13.1 GHz) and broadening of the resonance. This arises from the high-dielectric of ZnO, which modifies the local electromagnetic field distribution within the cavity when placed in high E-field regions, leading to changes in the spin-cavity coupling and a resulting shift of the resonance frequency. FEM simulations quantitatively reproduce this behaviour, with the expected resonance-frequency ranges (accounting for machining tolerances of ±0.015 mm) shown as shaded regions.

Finally, we address the design of the *probe*, i.e., the structure to which the resonator is attached when inserted into the cryostat. The probe provides mechanical support, maintains vacuum integrity, and enables controlled rotation of the resonator for orientation-dependent measurements; its schematic is shown in Fig. 4.8. At the top of the assembly

[7]Originating from the Wurtzite crystal structure.

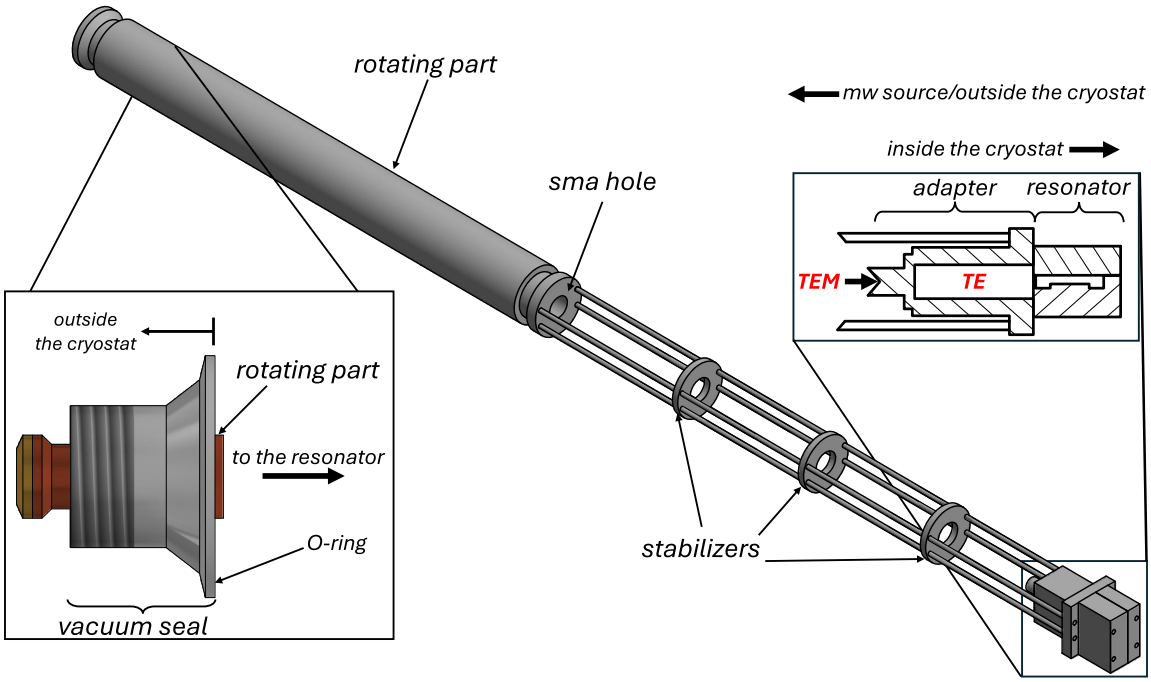

Figure 4.8: *Main:* Probe structure used in the experiment, as described in the main text. *Right inset:* Cross-section of the SMA-waveguide adapter converting the coaxial TEM mode into the rectangular TE mode. *Left inset:* Vacuum seal at the top of the probe, clamped to the cryostat to maintain vacuum, while allowing probe rotation for orientation-dependent EDSR/ESR measurements.

(outside the cryostat), a vacuum seal secures the probe to the cryostat body, while an O-ring ensures airtight closure and supports a central pillar (red component in the left inset). This pillar, which connects directly to the resonator, is hollow (*SMA hole*) to accommodate the coaxial SMA cable delivering the microwave signal to the cavity.

Below this section, the central shaft splits into four thinner pillars (each 1.5 mm in diameter) that extend to the probe base, where the resonator is mounted. This geometry reduces the thermal load on the resonator by limiting conductive heat transfer, while its mechanical stability is maintained by inserting intermediate *stabilisers*. At the bottom of the probe (cross-section shown in the right inset), an SMA-to-waveguide adapter (Pasternack WR-62 UBR140) converts the transverse electromagnetic (TEM) mode of the coaxial SMA cable into the rectangular transverse electric (TE) mode supported by the waveguide, which is directly compatible with the cavity mode.

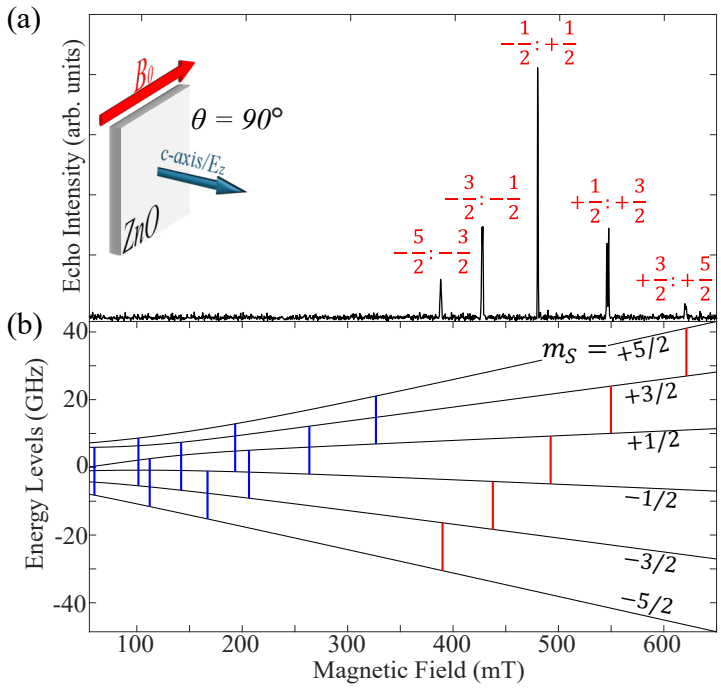

Figure 4.9: (a) Echo-detected field sweep at $\theta = 90°$ with the sample positioned at the base of the reentrance (magnetic-field antinode). The absence of low-field signals is consistent with the simulations shown in Fig. 4.2. (b) Corresponding simulated energy-level diagram illustrating the allowed standard ESR (red lines) and EDSR (blue lines) transitions at ∼14 GHz.

4.4 E-field Driven Electron Transitions in Fe:ZnO

We employ our custom-built singly reentrant resonator to perform EDSR measurements on a 2 mm × 2 mm × 1 mm Fe:ZnO crystal at 20 K. As a preliminary step, we verify the expected ESR selection rules, namely that the probability of exciting $\Delta m_s = \pm 2$ transitions is vanishingly small (Fig. 4.2(e)). To this end, a Hahn-echo sequence is carried out with the sample positioned at the magnetic antinode, i.e., at the base of the reentrance. The resulting spectrum at $\theta = 90°$, shown in Fig. 4.9(a), displays only single-quantum transitions, with no low-field features, in agreement with magnetically driven ESR excitations. To ensure artefact-free detection, we account for the resonator's ring-down time, which becomes relevant due to the cavity not being fully overcoupled (see Fig. 4.7, green trace). To mitigate this, a 2 μs defence pulse (discussed in Subsec. 1.5.3) is applied following the π-pulse, thereby setting a lower bound on the interpulse delay, $\tau > 2.0\,\mu$s. For this reason, τ is set to 5 μs in all our measurements. This does not represent a limitation for the present sample, as the total sequence duration remains

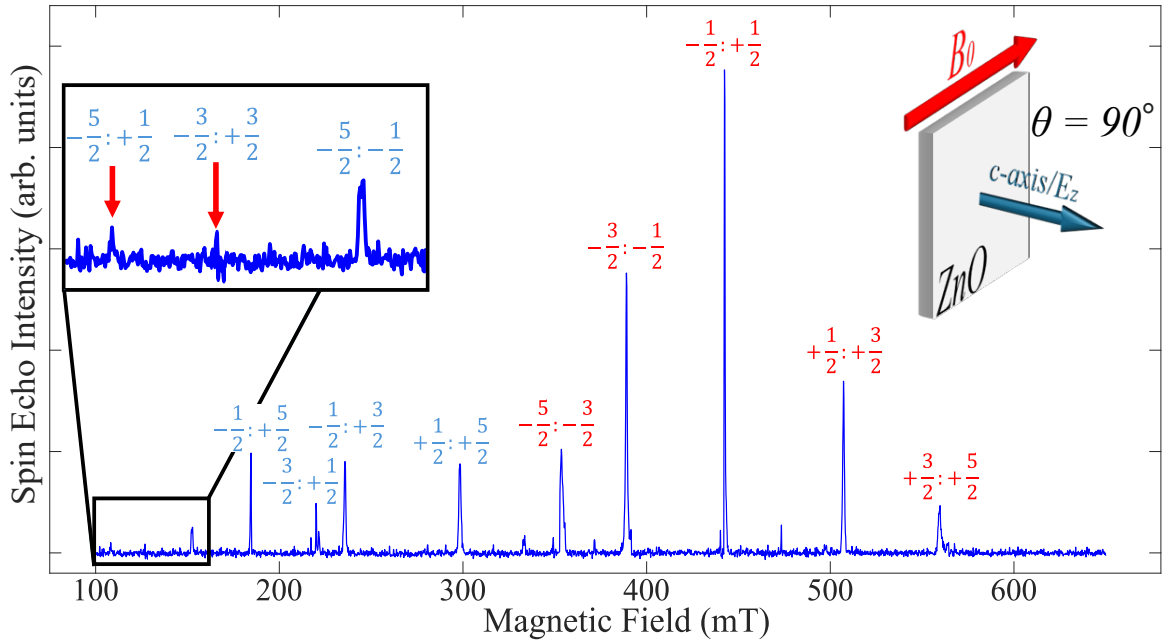

Figure 4.10: Spectrum measured with a 2 mm × 2 mm × 1 mm Fe:ZnO sample placed at the top of the resonator's reentrance, i.e., the E-field antinode, with $\theta = 90°$ at 20 K ($f \simeq 13.1$ GHz). As outlined in the main text, both $\Delta m_s = \pm 1$ (red labels) and $\Delta m_s = \pm 2$ (blue) transitions are observed. The former are attributed to magnetic-field leakages exciting standard ESR transitions, while the latter may arise from EDSR or parallel-mode ESR (see next subsection). The spin states involved in the transitions were identified via the simulated energy levels shown in Fig. 4.9(b). *Left inset:* Close-up of the low-field region (100-160 mT).

short compared to its spin coherence time at 20 K ($T_2 \sim$ tens of μs; Fig. 4.1(d)).

To drive EDSR, we reposition the sample at the expected electric-field antinode, located at the top of the reentrance (Sec. 4.3.2). All other experimental parameters, including the orientation $\theta = 90°$, are kept unchanged. The corresponding EDFS is shown in Fig. 4.10, revealing two distinct sets of resonances. The high-field transitions (labelled in red) can be readily identified as the single-quantum $\Delta m_s = \pm 1$ transitions, occurring at the same field positions as those observed previously (adjusted for the different excitation frequency). In contrast, the low-field resonances (labelled in blue) indicate the occurrence of double-quantum transitions. The labels in the figure specify the corresponding transition for each observed peak, as determined from the simulated energy-level diagram in Fig. 4.9(b).

To clarify the nature of the low-field transitions, we carried out an angular-dependence study by rotating the crystal from $\theta = 90°$ to 30°. The complete set of orientation-dependent spectra is presented in Fig. A.8 (App. A.4.1), while Fig. 4.11 summarises

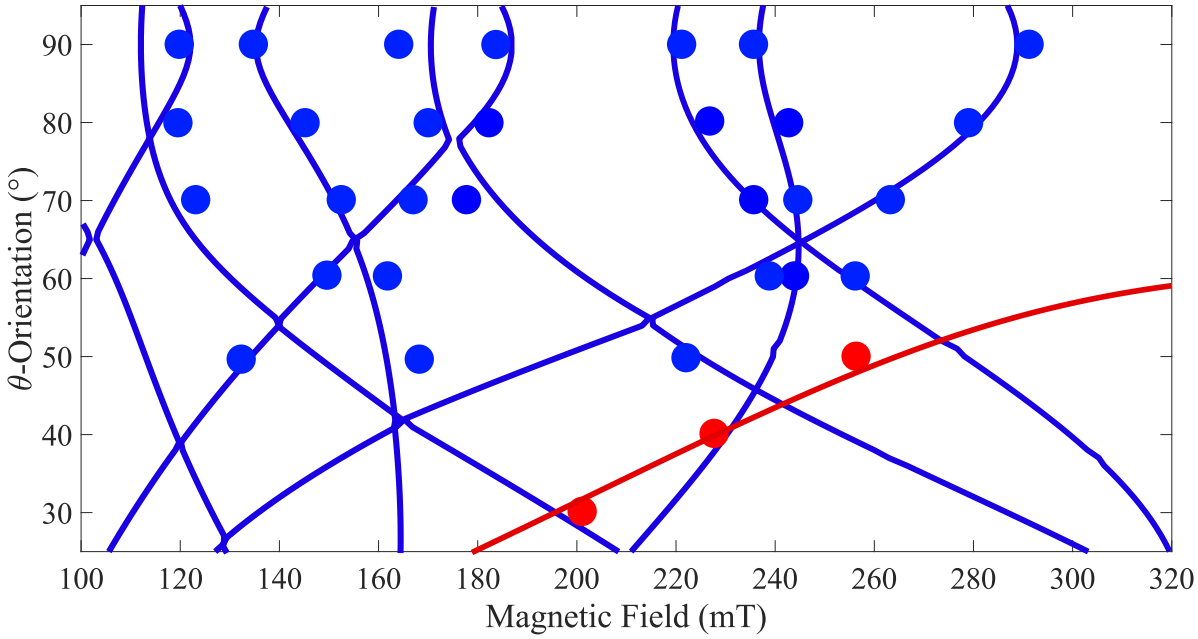

Figure 4.11: Experimental (dots) and simulated (solid lines) resonant B_0-positions for the low-field $\Delta m_s = \pm 2$ transitions (see Fig. A.8 for the full orientation-dependent spectra). As discussed in the main text, the red signals at $\theta \leq 50°$, corresponding to the single-quantum $|m_s = -5/2 \leftrightarrow -3/2\rangle$ transition, likely originating from conventional ESR.

the corresponding resonant-B_0 field positions extracted from these spectra, alongside the simulated EDSR transition fields (solid blue lines) at 13.1 GHz. The low-field peaks can be reliably tracked up to $\theta \approx 40°$-$50°$, beyond which the reduced signal-to-noise ratio hinders precise identification. This trend is consistent with expectations: as the sample is rotated away from $\theta = 90°$, the intensity of the $\Delta m_s = \pm 2$ transitions diminishes, as seen in the simulations shown in the right column of Fig. 4.2 and in prior work [129]. The close correspondence between the experimental and simulated resonance positions thus provides strong evidence that the low-field features originate from double transitions.

However, despite this overall agreement, an important discrepancy arises: under purely electric driving at around $\theta = 90°$, the same simulations predict that single-quantum transitions should be absent, yet they clearly appear in the data of Fig. 4.10. This suggests that the driving mechanism cannot be attributed to mw electric excitation alone, but likely also involves a magnetic field that drives ESR transitions. In the next subsection, we examine the origin of this magnetic coupling and discuss how it may contribute to the observed $\Delta m_s = \pm 2$ transitions.

4.4.1 Magnetic-field Contributions to Double Transitions

To elucidate the mechanism underlying the previously described signals, we analyse how the cavity field distribution is modified when a dielectric sample such as ZnO is placed at the top of the reentrance. To this purpose, we performed FEM simulations of the resonator both without and with the sample inserted, following the same approach used to compute the expected resonance-frequency range in Fig. 4.7. The corresponding electric (top) and magnetic (bottom) field distributions are shown in Fig. 4.12(a, b). The observed change between these two cases can be explained as follows. Owing to the dielectric nature of the sample, the material becomes polarised in the presence of an electric field, inducing bound surface charges that generate an opposing field. This results in a reduction of the net electric field within the sample, analogous to the behaviour of a simple parallel-plate capacitor, where $E \propto 1/\varepsilon_r$ (see the field lines in the top panel of Fig. 4.12(b)). Concurrently, the parasitic magnetic field intensity inside the sample increases (see right inset in (b)) due to the redistribution of the electromagnetic field within the resonator.

We further compute the average electric and magnetic fields inside the sample as functions of its relative dielectric constant and linear size, defined here as the crystal dimension perpendicular to the c-axis (2 mm in our case). The corresponding results are shown in panels (c) and (d) of the same figure, respectively. As expected, increasing either parameter reduces the internal electric-field strength while enhancing the magnetic field, indicating that larger or higher-ε_r samples favour magnetic driving at the expense of EDSR. Thus, in principle, employing materials with lower dielectric constants or smaller samples could mitigate this effect. However, a lower ε_r also diminishes the electric-field coupling, since, as discussed earlier and in Ref. [129], the SEC in defects in ZnO is strongly linked to the crystal's polar nature. Likewise, reducing the sample size decreases the number of spins and therefore degrades the signal-to-noise ratio (SNR). While increasing the spin density could enhance the SNR without increasing the sample volume, it would do so at the expense of shorter coherence times. These competing considerations ultimately motivate the use of the present sample, which provides a balance between signal strength and spin coherence.

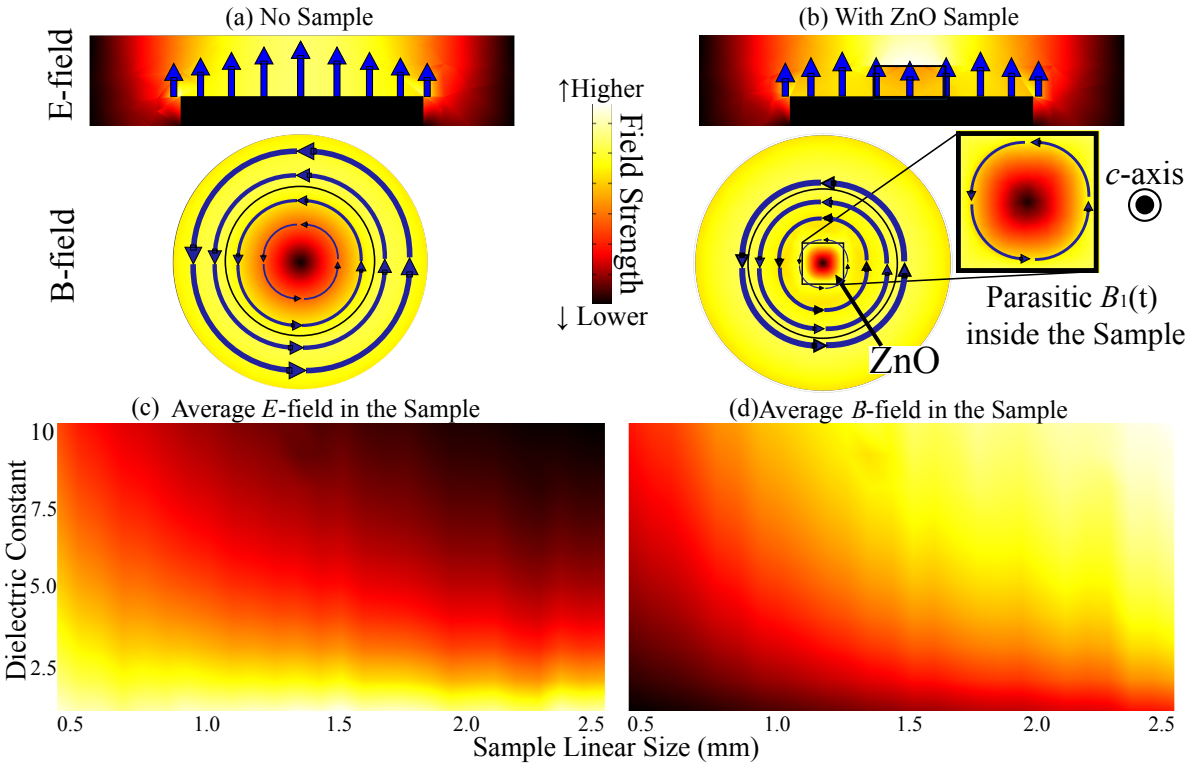

Figure 4.12: (a, b) Simulated electric (top) and magnetic (bottom) field distributions inside the custom-made cavity without (a) and with (b) the ZnO polar crystal inserted. The high dielectric constant of ZnO draws part of the magnetic field into the sample while repelling the electric field. (c, d) Simulated average electric and magnetic fields inside the sample, respectively, as functions of its size and dielectric constant. These simulations show that both magnetic-field penetration and electric-field repulsion become increasingly pronounced as either parameter increases.

As illustrated in the inset of Fig. 4.12(b), the parasitic magnetic field inside the sample forms circulating loops that follow the cylindrical symmetry of the cavity. As a result, the local $B_1(t)$ field has components in multiple directions within the plane perpendicular to the c-axis, rather than being purely transverse. This geometry implies that, in addition to standard ESR, *parallel-mode* ESR (parESR) can also contribute to the observed signal. A more detailed picture of how both ESR and parESR arise in this configuration is presented in Fig. A.9 and discussed in App. A.4.2. As briefly introduced in Subsec. 1.1.3, parESR occurs when the oscillating magnetic field $B_1(t)$ is aligned, rather than perpendicular, with the static field B_0. For pure $|m_s\rangle$ states, parESR does not induce any transitions because its associated interaction term, $B_1(t)\hat{S}_z$, commutes with the Zeeman Hamiltonian. However, in systems with strong magnetic anisotropy, such as the axial zero-field splitting

D in Fe:ZnO, and for $\theta \neq 0°$, the eigenstates become mixed at low B_0. As a result, the spin states deviate from pure Zeeman levels and form superpositions of different $|m_s\rangle$ components, thus relaxing the conventional selection rules $\Delta m_s = \pm 1$ for magnetic driving [163]. Crucially for our discussion, such mixing may enable parESR to drive otherwise forbidden $\Delta m_s = \pm 2$ transitions around $\theta = 90°$ where state-mixing is maximised [164].

This behaviour is confirmed by the numerical simulations shown in Fig. 4.13(a, b), which display the orientation-dependent spectra for (a) EDSR and (b) parESR. Due to the D-induced mixing of spin states, both mechanisms give rise to $\Delta m_s = \pm 2$ transitions, while their single-quantum responses exhibit a comparable angular dependence, with vanishing intensity around $\theta = 0°$ and 90°. This angular trend suggests that the $\Delta m_s = \pm 1$ peaks observed in Fig. 4.10 at $\theta = 90°$, which are stronger than the double-quantum features, are most likely driven by standard ESR. The similarity between EDSR and parESR arises from the analogous symmetry of their respective driving terms, i.e., $\sim \delta D(t)\hat{S}_z^2$ for EDSR and $B_1(t)\hat{S}_z$ for parESR. Consequently, the mere observation of $\Delta m_s = \pm 2$ transitions, or variations in the intensity of $\Delta m_s = \pm 1$ features with θ, cannot, *per se*, be regarded as definitive evidence of electrically induced spin transitions (unlike in Ref. [129], where the intensity change of the signal near $\theta = 0°$ provided direct confirmation of EDSR).

Since a qualitative identification of the possible driving processes cannot be established with certainty, a quantitative comparison of amplitudes may offer a more reliable means of determining the dominant contribution. To this end, we carry out simulations that combine the interaction Hamiltonian with the FEM-simulated field strengths inside the sample. As outlined in App. A.4.2, we first compute the electromagnetic fields (as in Fig. 4.12) and then determine the corresponding Rabi frequencies, $\omega \simeq \langle\psi_i|\hat{\mathcal{H}}^I(t)|\psi_j\rangle$, where $\hat{\mathcal{H}}^I(t)$ denotes the interaction term for standard ESR, parESR, and EDSR, expressed in terms of the appropriate spin operators and magnetic or electric fields (see Tab. A.2 for details). Focusing on the $\Delta m_s = \pm 2$ transitions, we find that the standard ESR contributions are (exactly) zero at $\theta = 90°$ and generally four orders of magnitude weaker than those of EDSR and parESR, as shown in the inset of Fig. 4.13(c) for, e.g., $\theta = 85°$. This effectively rules out standard ESR as the source of these signals.

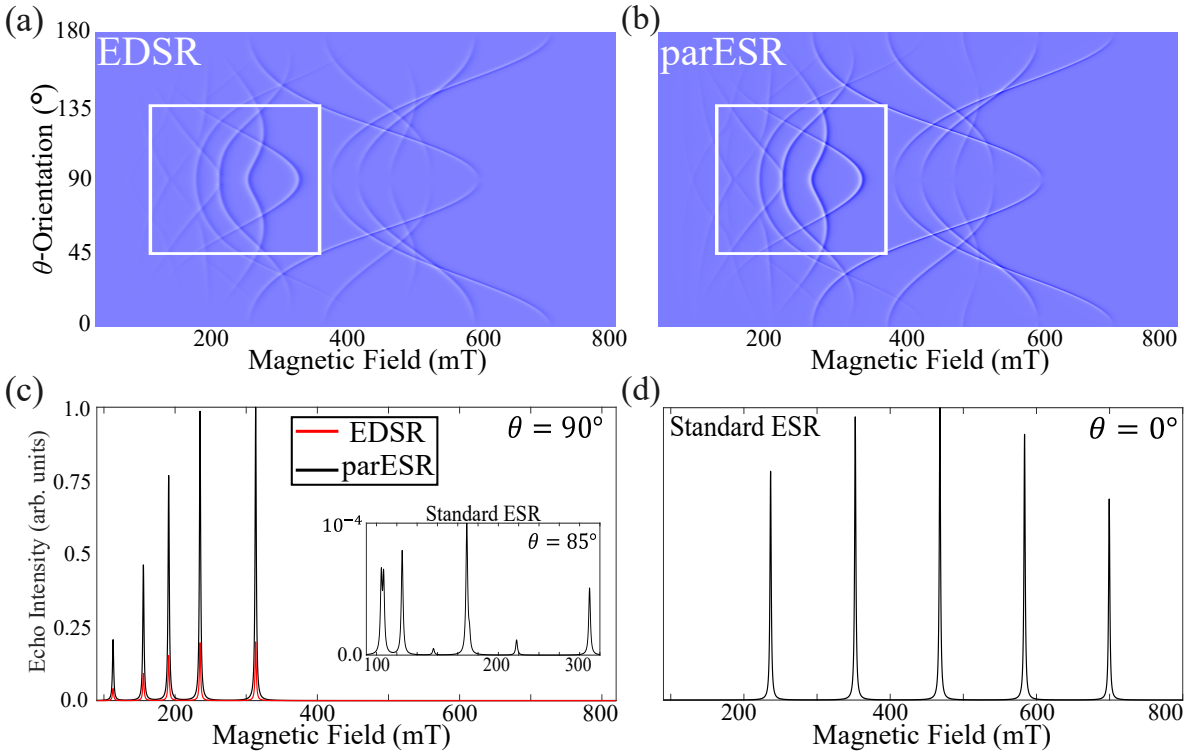

Figure 4.13: (a, b) Simulated orientation-dependent spectra for EDSR and parallel-mode ESR (parESR). Both mechanisms display $\Delta m_s = \pm 2$ transitions (highlighted by the white rectangles) and show similar angular dependence for the $\Delta m_s = \pm 1$ excitations, vanishing around $\theta = 0°$ and 90°. (c) (Simulations) Quantitative comparison of the double-quantum transition intensities (Rabi frequencies) at $\theta = 90°$ for EDSR and parESR, normalised to the maximum parESR value, showing a ratio of $\sim$ 1:5. Standard ESR is effectively zero at this orientation and remains significantly weaker at nearby angles (see inset). The analysis details are provided in App. A.4.2. (d) When the c-axis is aligned with B_0, both parESR and EDSR vanish, and standard ESR dominates.

Conversely, when the c-axis is aligned with B_0 (panel (d)), parESR and EDSR vanish while ESR dominates. These results suggest that the strong signal in Fig. A.8 for $\theta \leq 50°$ (red dots in Fig. 4.11), predicted to correspond to the $\Delta m_s = \pm 1$ transition $|m_s = -5/2 \leftrightarrow -3/2\rangle$, likely arises from standard ESR.

Comparison between EDSR and parESR, however, is less straightforward. For orientations $\sim \pm 45°$ from $\theta = 90°$, where the $\Delta m_s = \pm 2$ response reaches its maximum (highlighted by the white rectangles in Fig. 4.13(a, b)), the ratio of the calculated Rabi frequencies for EDSR and parESR is approximately 1:5, as shown in Fig. 4.13(c) for $\theta = 90°$. This suggests that the observed signals in Fig. 4.11 are likely dominated by parESR, though a contribution from EDSR cannot be entirely ruled out. Given the current

experimental set-up and sample properties, it remains challenging to unambiguously attribute the observed double-quantum transitions to either purely electric-field-driven or parasitic magnetic-field-induced processes.

Although our data are consistent with the observation of $\Delta m_s = \pm 2$ transitions, the dominant driving mechanism, whether primarily EDSR or parESR (with the latter likely contributing most), cannot be determined unambiguously. This uncertainty arises from two factors in Fe:ZnO: (i) the polar nature of ZnO, which enhances electric-field sensitivity but, at the same time, amplifies parasitic magnetic fields within the sample, and (ii) the large magnetic anisotropy, which mixes spin states and enables non-zero parESR transition probabilities with angular dependencies similar to those of EDSR. In the final section of this chapter, we outline potential strategies to disentangle these contributions and propose future experiments aimed at achieving electric control of electron-spin coherence.

4.5 Conclusion & Future Directions

In this chapter, we have described the development and implementation of an experimental protocol to investigate ensemble EDSR using Fe substitutional defects in a wurtzite ZnO crystal. A key challenge lies in managing the interplay between the dielectric properties of the sample and the resonator's field distribution. On one hand, the relatively large dielectric constant of ZnO enhances the electric sensitivity of the spin system, which is advantageous for driving EDSR. On the other hand, this same property also distorts the cavity mode structure, introducing parasitic magnetic fields at the electric-field antinode (precisely where the sample must be placed to perform EDSR). Compounding this issue is the strong axial anisotropy D of Fe:ZnO, which mixes the spin eigenstates at low-fields, thus modifying the selection rules. As a result, double-quantum transitions, normally forbidden in conventional ESR, become allowed via parallel-mode ESR. Indeed, our measurements show signals consistent with such double transitions. However, based on angular dependence and simulations, we cannot unambiguously determine the dominant driving mechanism. While our analysis points toward parESR as the primary driver, a partial contribution from electric driving via EDSR cannot be fully ruled out.

Future experiments should aim to mitigate these limitations. One promising approach is to use samples where the spin-electric coupling does not depend on the polar nature of the host lattice. Molecular magnets with intrinsic high electric sensitivity embedded in a diamagnetic matrix represent an ideal candidate. These systems combine significant SEC with a non-polar environment, thereby minimizing dielectric effects that distort the cavity field distribution and enhance parasitic ESR contributions.

This strategy, however, faces two major challenges. First, molecular systems typically exhibit shorter coherence times, although these may be extended through targeted chemical design [60]. Second, their spin Hamiltonians are generally more complex, necessitating a detailed understanding of how the relevant parameters respond to an oscillating electric field. Ideally, one would study a system with a spin Hamiltonian as straightforward as that of Fe:ZnO, where the electrically modulated terms and their effects are well characterised. An additional complication is that, while EDSR transitions have been demonstrated in Mn:ZnO [129], they have yet to be observed in molecular samples. Consequently, whether strong static SEC in molecular systems can be harnessed to enable EDSR remains an open question.

Another possibility is to redesign the resonator to improve the spatial separation between electric and magnetic fields, even in the presence of a sample with strong dielectric properties. One design under consideration is a loop-gap resonator featuring a single gap and two loops, with an adjustable loop coupler integrated into either loop. In this geometry, EDSR transitions would be driven by placing the sample within the gap, whose width can be reduced to closely match the sample dimensions. The primary advantage of this configuration lies in the ability to fabricate wide capacitor plates, potentially enhancing the separation of electric and magnetic fields. However, practical constraints arise from the limited volume available within the cryostat, as well as the requirement to maintain resonance within the desired frequency range (at least K_u). These challenges must be carefully addressed for the design to be experimentally viable.

Regardless of the sample or the resonator design, a potential way to disentangle EDSR from ESR contributions would be to perform measurements in which the relative orientation

α between the applied oscillating field $\mathbf{E}_1(t)$ and the sample's polar axis $\mathbf{p}$ can be systematically varied. If the transitions are driven electrically, the signal intensity should follow a sinusoidal modulation arising from the $(\mathbf{E}_1(t) \cdot \mathbf{p}) \sim \cos(\alpha)$ term in Eq. 4.2. By contrast, no such controlled modulation is expected if the transitions are driven purely ESR. A practical implementation would involve a setup in which the sample remains fixed within the cryostat, while a (e.g., loop-gap) resonator can be mechanically rotated with respect to the crystal axis.

This work is part of a manuscript in preparation for publication.

5 Electric-field Control of Lanthanide-based Molecules

5.1 Spin-Electric Coupling in Lanthanide-based Compounds

In this chapter, we investigate the electric-field control of lanthanide-based molecular nanomagnets and outline a proposal for their use in multi-qubit architectures. Lanthanide ions are appealing for this purpose due to their strong spin-orbit coupling (SOC), arising from large atomic constants λ in $\hat{\mathcal{H}}^{\mathrm{SOC}} = \lambda\,\hat{\mathbf{S}}\cdot\hat{\mathbf{L}}$. As shown in Eq. 1.38, electric-field-induced variations in spin parameters scale directly with λ, as, e.g., $\delta D^{\mathrm{SOC}}(\mathbf{E}) = \lambda^2\,\delta\mathbf{\Lambda}(\mathbf{E})$, implying that the response is strong in lanthanides, where the magnetic anisotropies originate primarily from SOC rather than spin-spin interactions [165]. Such SOC-mediated enhancement enables high electric sensitivity and has inspired both theoretical [166] and experimental [29, 30] studies exploring the electric control in these systems.

The strength of SOC in lanthanides originates from two factors [5]. First, the SOC constant λ scales with the atomic number Z as Z^4, meaning that heavier elements exhibit much stronger SOC than lighter ones. Second, the extent to which orbital angular momentum is *quenched* depends sensitively on the radial distribution of the valence orbitals. In fact, in

transition-metal ions, the $3d$ orbitals are spatially extended and poorly shielded, leading to strong interactions with the surrounding crystal field (CF). This CF splitting dominates over SOC and suppresses the orbital angular momentum L that would otherwise be expected from Hund's rules. By contrast, lanthanide ions are typically found in the trivalent state (e.g., Ho^{3+}) [167]. Their valence electrons occupy $4f$ orbitals that lie closer to the nucleus and are effectively screened by the filled $5s$ and $5p$ shells. As a result, the influence of the CF is significantly reduced, allowing the orbital angular momentum to remain largely unquenched, with SOC thus remaining the dominant interaction.

This physical picture can be formalised following Ref. [5]. In $3d$ ions the Hamiltonian is largely governed by the crystal-field interaction, $\hat{\mathcal{H}}^{3d} \simeq \hat{\mathcal{H}}^{\mathrm{CF}}$, which arises from Coulomb interactions with surrounding charges and is therefore real in position space. Its eigenfunctions can accordingly be chosen real, $|\psi^{3d}\rangle \in \mathbb{R}$, whereas the orbital angular momentum operator, $\mathbf{L} = -i\hbar\,\mathbf{r} \times \nabla$, is purely imaginary. Any nonzero matrix element $\langle\psi^{3d}|\mathbf{L}|\psi^{3d}\rangle$ would therefore be imaginary, in conflict with the requirement that Hermitian operators such as $\mathbf{L}$ yield real expectation values. The only consistent conclusion is $\langle\mathbf{L}\rangle = 0$, which explains the quenching of orbital angular momentum in $3d$ transition metals.

While strong SOC can enable efficient electric control, it also enhances the coupling to environmental degrees of freedom, such as phonons [168, 169] and molecular vibrations [170], thus introducing decoherence channels[1]. This challenge was one of the motivations behind the experiment discussed in Chapter 2, where an organic molecule lacking heavy atoms was used to suppress SOC-mediated relaxation pathways. An alternative strategy is to operate at clock transitions (CTs), where the energy levels are first-order insensitive to fluctuations in external fields, thereby enhancing protection against environmental noise and yielding significantly longer coherence times [69]. This approach, detailed in the following section, provides a way to combine the potentially strong electric sensitivity of lanthanides with improved coherence performance [30].

[1]Ref. [171] challenges this idea by showing that SOC is not always the dominant decoherence source, comparing spin coherence across three monometallic (*3d-5d*) systems with varying SOC strength. However, these findings have not been generalised to lanthanide complexes, or to all coordination environments.

5.1.1 Previous work: Clock Transitions in HoW_{10}

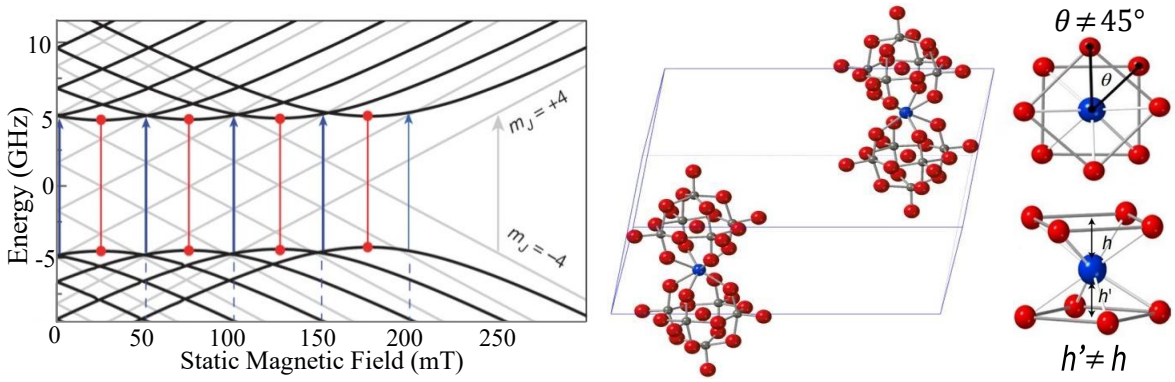

Figure 5.1: *Left:* Energy level diagram of the $m_J = \pm 4$ ground-state doublet in HoW_{10}. The red vertical arrows indicate the four clock transitions between $|m_J = -4, m_I\rangle \leftrightarrow |m_J = +4, m_I\rangle$, while the light grey ones represent the absence of avoided crossings/CTs in the case of perfect D_{4d} symmetry, i.e., $B_4^4 = 0$. *Right:* Crystal structure of the $[LnW_{10}]$ compounds, showing the unit cell with two inversion-symmetry-related (and magnetically decoupled) molecules, along with the two structural distortions that break the ideal D_{4d} symmetry. Blue spheres represent Ln ions; red spheres represent oxygen atoms. The left panel is adapted from Ref. [69].

The chemical synthesis of molecules exhibiting *clock transitions*, also known as zero-first-order-Zeeman transitions [172], offers a promising strategy to alleviate such limitations [173]. These transitions are characterised by resonance frequencies that are, to first order, insensitive to fluctuations in the external magnetic field [174]. More precisely, at the clock-transition field B_{CT}, the resonance frequency f_{res} between two spin states satisfies:

$$\left.\frac{\mathrm{d}f_{\text{res}}}{\mathrm{d}B_0}\right|_{B_0=B_{CT}} = 0. \tag{5.1}$$

Due to their inherent robustness against magnetic-field noise, CTs typically exhibit significantly enhanced coherence times and reduced susceptibility to unwanted cross-talk, both of which are highly advantageous for quantum information processing.

A notable example of a CT in molecular magnets is provided by the polyoxometalate compound $[Ho(W_5O_{18})_2]^{9-}$, hereafter referred to as HoW_{10}, embedded in a diamagnetic matrix of $Na_9[Y_{1-x}Ho_x(W_5O_{18})_2]\cdot 35H_2O$ with $x = 0.1\%$. HoW_{10} has been extensively investigated, as its clock transitions lie at X-band and yields a coherence time of $T_2 \sim 10\ \mu$s at 5 K (cf. $T_2 \sim 2\ \mu$s at fields 5 mT away from the CT), or an order of magnitude enhancement compared to similar systems [69, 175–178].

The molecular structure is shown in the right panel of Fig. 5.1, where the Ho^{3+} ion is represented as a blue sphere. The crystal unit cell contains two magnetically decoupled anions related by inversion symmetry. Each individual anion closely approximates an ideal D_{4d} geometry. The Ho^{3+} electronic configuration is $4f^{10}$ ($^5I_8$), which, according to Hund's rules, yields a spin-orbit-coupled ground state with $L = 6$, $S = 2$, and total angular momentum $J = 8$, characteristic of strong atomic SOC[2]. In addition, the only naturally occurring isotope of holmium, ^{165}Ho, has a nuclear spin quantum number of $I = 7/2$, giving rise to hyperfine coupling. The effective spin Hamiltonian for each molecule is then:

$$\hat{\mathcal{H}}_{D_{4d}} = \sum_{k=2,4,6} B_k^0 \hat{O}_k^0 + \mathbf{J} \cdot \mathbf{A} \cdot \mathbf{I} + \mu_e g_e \mathbf{B}_0 \cdot \mathbf{J} - \mu_N g_N \mathbf{B}_0 \cdot \mathbf{I}, \tag{5.2}$$

where the first term corresponds to axial high-rank Stevens operators with $B_2^0 = D/3 =$ 18 GHz, $B_4^0 = 209$ MHz, and $B_6^0 = 1.53$ MHz (see App. A.1.3 for the full expression of these operators). The (isotropic) hyperfine coupling constant is $A = 830$ MHz, and the electronic g-factor is $g_e = 1.25$ [69].

The energy levels corresponding to the ground-state doublet[3] $|m_J = \pm 4\rangle$ in a perfectly $D_{4d}-$symmetric environment are shown as grey lines in the left panel of Fig. 5.1. Thus, the Hamiltonian in Eq. 5.2 alone does not produce any avoided crossings or clock transitions. The missing term is a non-axial crystal-field of the form $B_4^4 \hat{O}_4^4 \sim \hat{J}_\pm^4$ (*tetragonal anisotropy*), which arises from small deviations from the ideal geometry. As illustrated in the figure, two such distortions are present: (i) each anionic moiety is rotated by 44.2° relative to the other (rather than the ideal 45°), and (ii) the Ho^{3+} ion is displaced slightly from the molecular centre by a distance $d = (h - h')/2$ [165, 175]. These deviations lead to the formation of four CTs with an energy splitting of approximately $B_4^4 = 94.2$ MHz, which conveniently generate CTs in the $X-$band range. These are shown as black lines in the energy-level diagram of the figure.

[2]In the presence of strong spin-orbit coupling, the total angular momentum $J = L + S$ is used.

[3]Although one might expect $|m_J = \pm 8\rangle$ under perfect D_{4d} symmetry to form the ground-state doublet in an axially symmetric crystal field, in HoW_{10} the $m_J = \pm 4$ levels are stabilised instead. This results from the dominant interaction between the *4f* electrons and the crystal-field component along the Ho-O bond direction. See Ref. [165] for a detailed explanation.

Liu *et al.* [30] demonstrated the (linear) electric modulation of the resonance frequency at the CTs of HoW_{10} using a Hahn-Mims echo sequence, providing an experimental evidence of SEC in such systems. Their model proposes that the electric field primarily modulates the B_4^4 parameter, motivated by the observation that the deviation from perfect symmetry induces the tetragonal anisotropy and simultaneously break inversion symmetry, which in turn generates an electric dipole moment. Their measurements led to an estimated $\delta B_4^4(E) \simeq 8.8$ kHz (5.9×10^{-2} Hz/(V/m)) at an applied field of roughly 1 kV/cm. Nevertheless, direct experimental confirmation that *solely* B_4^4 is modulated was not possible, since only transitions within the ground-state doublet along the easy axis, largely insensitive to axial terms such as D, could be probed via magnetic resonance. This limitation arises as the first excited doublet ($m_J = \pm 5$) lies approximately 480 GHz (16 cm^{-1}) higher in energy [175].

Building on this experiment, a theoretical proposal for electrically generating quantum entanglement in a dipolar-coupled dimer of HoW_{10} molecules has recently been introduced [179]. The significance and details of this proposal will be discussed in the last section of this chapter. For now, it is worth noting that while the approach is promising, it suffers from a notable limitation: the dipolar coupling between the two molecules is always active. This leads to uncontrolled spin evolution outside the targeted operations, ultimately impairing the application of such scheme in multi-qubit platforms.

This chapter is organised around two main themes. In the first part, we experimentally test the hypothesis made by Liu *et al.* [30] concerning the origin of SEC in LnW_{10} compounds. To this end, we employ a Hahn-Mims sequence on an isostructural analogue of HoW_{10}, in which the Ho^{3+} ion is replaced with Gd^{3+}. Owing to its $4f^7$ electronic configuration, Gd^{3+} possesses $S = 7/2$ and $L = 0$ ($^8S_{7/2}$), resulting in significantly weaker anisotropies. This facilitates access to transitions beyond the ground-state doublet, allowing a more comprehensive investigation of the SEC mechanism. The second part of the chapter introduces a novel mechanism for generating CTs, leveraging the competition between spin anisotropy and the Zeeman interaction, and proposes a new approach to electrically control these transitions beyond simply modulating their resonance frequency. This

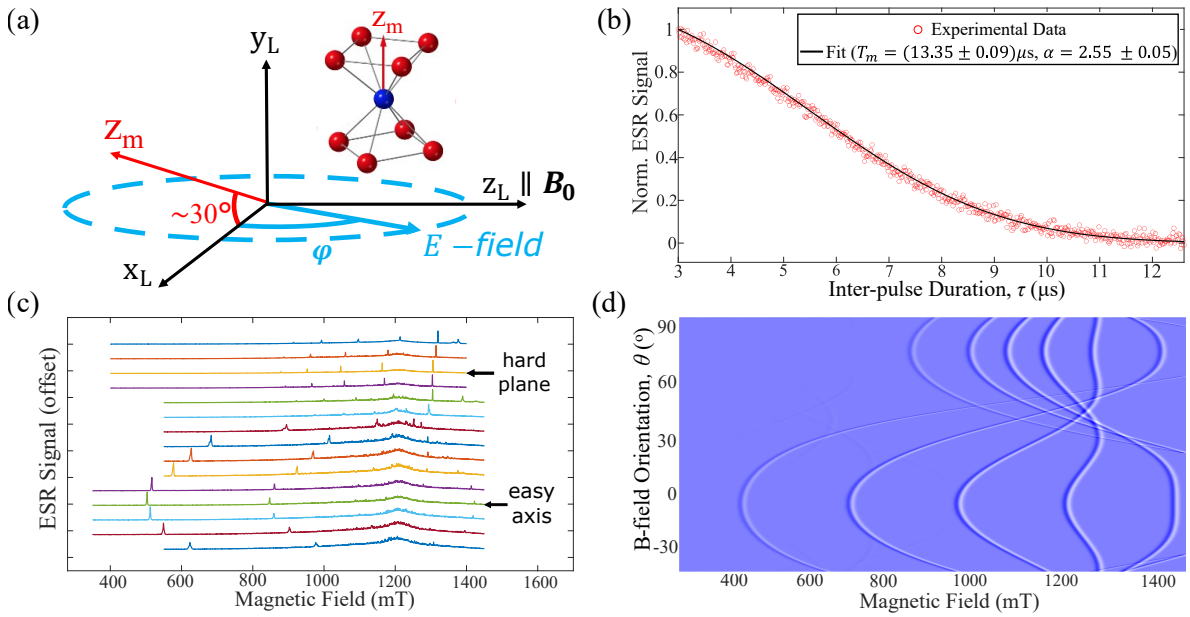

Figure 5.2: (a) Orientation of the molecular easy axis (z_m, inset) with respect to the laboratory frame ($\{x_L, y_L, z_L\}$), with the sample aligned in the hard plane. As previously reported [30, 69], the static magnetic field B_0 is misaligned from z_m by about 30°. The electric field (blue arrow) was applied within the $\{x_L, z_L\}$ plane, and its orientation was systematically varied. (b) Representative data for the electron spin coherence time T_m at 4 K, with all detected transitions exhibiting $T_m > 8$ μs, the interpulse delay in the Hahn-Mims sequence. The stretch parameter $\alpha = 2.55$ arises for nuclear spin flip-flop nearby the electron spin (see Subsec.1.1.4) (c,d) Experimental and simulated orientation-dependent ESR spectra, computed using the Hamiltonian in Eq. 5.3. The easy-axis and hard-plane orientations are highlighted in (c).

discussion lays the groundwork for our proposal to use E-fields to manipulate spin-spin interactions, addressing the *always-on interactions* challenge highlighted in Ref. [179].

5.2 Spin-electric Coupling in GdW_{10}

Here we present the ESR and SEC characterization of the polyoxometalate molecular anion GdW_{10}, which is isostructural with HoW_{10} and embedded in the same host lattice. Gd^{3+} has a $4f^7$ electronic configuration, corresponding to $S = 7/2$ and $L = 0$. The lack of orbital angular momentum in Gd^{3+} makes it an ideal model system for probing crystal-field effects. This contrasts with HoW_{10}, where magnetic anisotropy originates primarily from atomic SOC, which is strongly suppressed in Gd^{3+}. As a result, GdW_{10} exhibits much weaker anisotropy, allowing more spin transitions to be accessed via magnetic resonance (unlike in HoW_{10}).

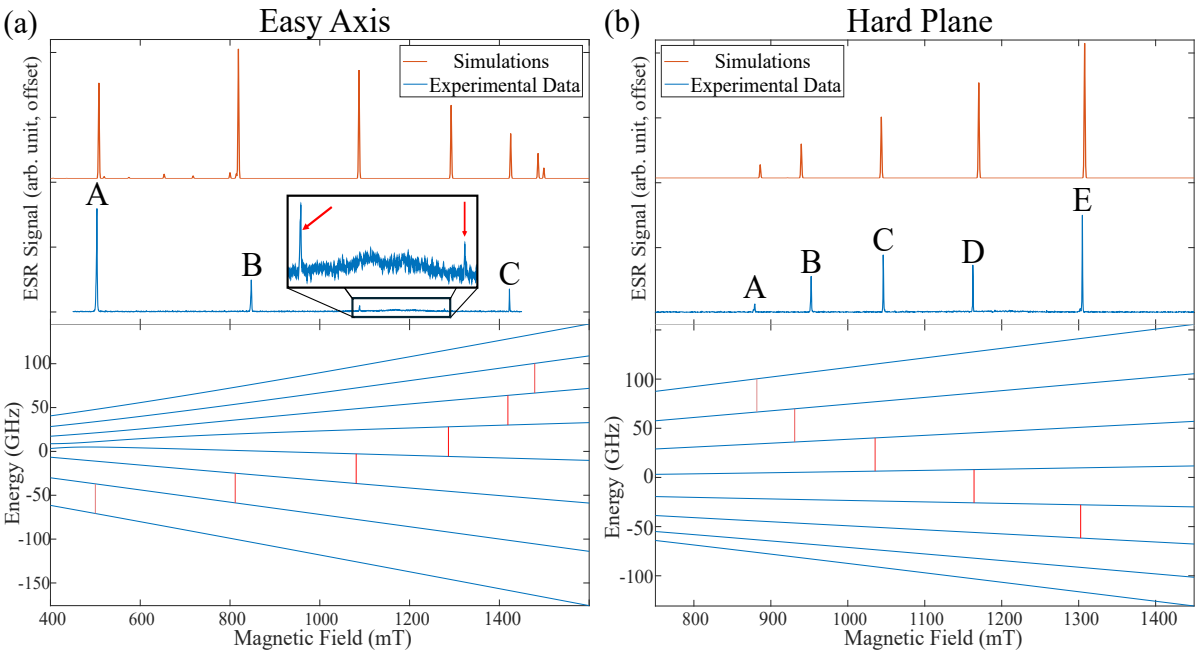

Figure 5.3: *Top:* Simulated (red) and experimental (blue) ESR spectra for the easy-axis (a) and hard-plane (b) orientations. The inset in (a) highlights two weak peaks whose signal-to-noise ratio was insufficient for spin-electric coupling measurements. *Bottom:* Corresponding energy-level diagrams, where the Q-band transitions are indicated by vertical red lines.

The effective spin Hamiltonian for each GdW_{10} anion is given by [180]:

$$\hat{\mathcal{H}}_{GdW_{10}} = D\left(\hat{S}_z^2 - S(S+1)\right) + B_4^4\hat{O}_4^4 + \mu_B g_e B_0\left(\hat{S}_z\cos\theta + \hat{S}_x\sin\theta\right), \qquad (5.3)$$

where the fourth-order term $B_4^4\hat{O}_4^4$ captures the effects of tetragonal anisotropy arising from local distortions around the lanthanide ion, analogous to HoW_{10}. The effect of nuclear spins in GdW_{10} is spectroscopically unresolved, and it is therefore ignored in the following discussion[4].

Using orientation-dependent ESR measurements on a single crystal at Q-band (Fig. 5.2), we extract the parameters $B_4^4 \simeq 9.0$ MHz, $D \simeq -3.7$ GHz, and $g \simeq g_e$, the free-electron g-factor; these are in line with previous investigations [180]. The weak anisotropies compared to Eq. 5.2 is a direct consequence of the vanishing orbital angular momentum. As in previous HoW_{10} studies [30, 69], a misalignment of approximately 30° between the molecular easy axis and the applied magnetic field was observed, illustrated by the red arrow labelled z_m in panel (a). Such offset originates from the crystallisation geometry,

[4]Roughly 30% of naturally occurring Gd is either ^{155}Gd or ^{157}Gd, both with nuclear spin $I = 3/2$. However, no nuclear hyperfine features were observed in the ESR spectra.

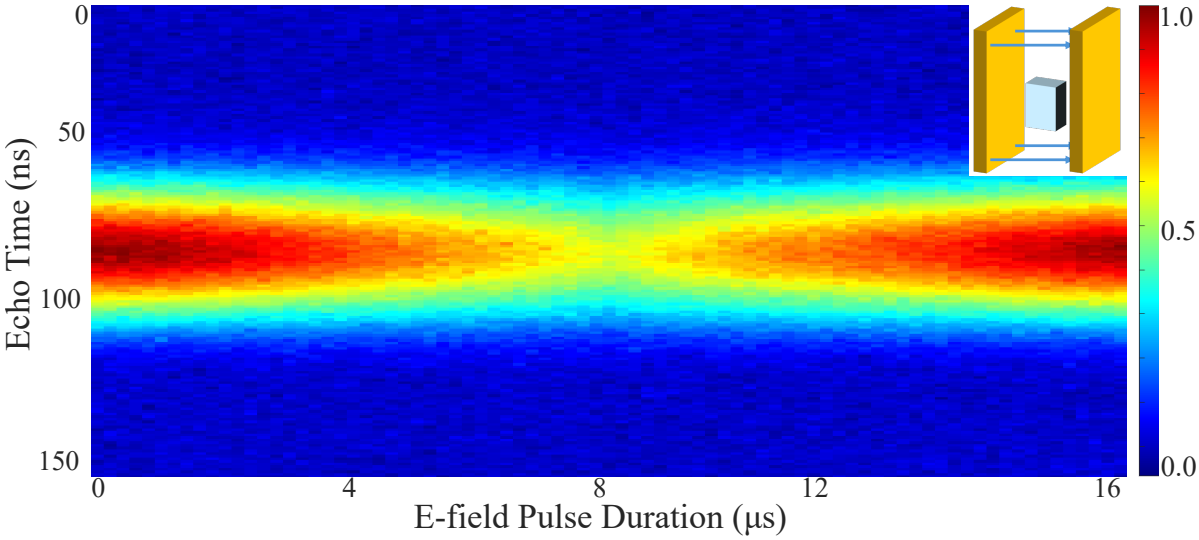

Figure 5.4: Representative data showing the modulation of the spin-echo intensity induced by the electric field at peak B in the hard plane. *Inset:* Schematic of the parallel-plate capacitor used to probe the SEC in GdW_{10}.

where the easy axis does not coincide with any crystal facet or edge [176], combined with the limitation that our experiments employ only single-axis rotation. In the following, we focus on two specific field orientations: one near the easy axis (with the aforementioned 30° misalignment, hereafter referred to as the "easy-axis" orientation), and the other in the hard plane, i.e., with B_0 oriented 90° from the easy axis. Experimental and simulated spectra for both cases are shown in Fig. 5.3, alongside energy level diagrams indicating the allowed Q-band transitions.

To characterise the SEC, we performed Hahn-Mims sequences on each labelled resonance peak (three in the easy-axis and five in the hard-plane orientations), probing how electric fields modulate the spin Hamiltonian parameters in Eq. 5.3. For this experiment, we employed an electric-field probe similar to that used in Chapter 3, schematically shown in the inset of Fig. 5.4. It consists of two parallel PCB plates, each coated with a thin conductive layer ($\sim$ 100 nm Au over $\sim$ 20 nm Cr), separated by 2 mm. This design generates electric fields up to $\sim 2\,\mathrm{kV/cm}$ at the sample site. However, unlike in Chapter 3, the sample is not affixed directly to the plates but is instead housed within a quartz tube and inserted into a Bruker EN5107D2 resonator. This setup enables independent rotation of the static magnetic field B_0 and the electric field, as indicated by the φ-rotation in

Fig. 5.2(a). Consequently, one can maintain a fixed magnetic field orientation, e.g., in the hard plane, while rotating the electric field.

Representative SEC data are shown in Fig. 5.4, taken at peak B in the hard-plane orientation at 4 K with an E-field intensity of $\sim$2 kV/cm. With an inter-pulse delay of $\tau = 8$ μs ($< T_m$ of the sample; see Fig. 5.2(b)), we observe a typical recovery of the spin echo as the electric-field pulse duration is swept between τ and 2τ, indicating coherent modulation has been achieved. Notably, the SEC signal observed in GdW_{10} is significantly weaker than that in HoW_{10} [30]. We attribute this difference to the much weaker SOC and anisotropies in Gd^{3+} relative to Ho^{3+}, reinforcing the critical role of SOC in enabling strong molecular SEC in lanthanide-based compounds.

The linearity of the SEC is checked by measuring the modulation frequency δf at a fixed B_0 and sample orientation, while varying the applied voltage across the capacitor and recording the change in spin-echo intensity as a function of the electric field. The resulting spin-echo modulation (similar to that in Fig. 5.4) is then fitted to a $|\cos(\delta f t_E)|$ function, from which δf is extracted. The modulation frequency as a function of the applied voltage for peak B in the hard-plane orientation is shown in Fig. 5.5(a), exhibiting a clear linear dependence (with slope ~ 80 $^{\mathrm{Hz}}/_{\mathrm{V}}$), as expected from the broken inversion symmetry in the GdW_{10} anions[5].

We further measured δf as a function of the angle φ between the applied E-field and the x_L-axis in the laboratory frame (Fig. 5.2(a)), with $\varphi = 0°$ corresponding to $E \perp B_0$. Fig. 5.5(b) shows the angular dependence for peak B in the hard-plane orientation, together with a $|\cos(\varphi)|$ fit, consistent with previous observations [30]. The maximum at $\varphi = 0°$ and the vanishing signal at $\varphi = 90°$ ($E \parallel B_0$) indicate that the molecular electric dipole moment lies in the $\{x_L, y_L\}$ plane. This is broadly consistent with DFT calculations in Ref. [30], which predict the dipole to roughly align along one of the the

[5]Since there are two inversion-symmetry-related anions per unit cell, the application of an electric field induces equal and opposite phase shifts, $\pm\delta f t_E$, in each anion. As discussed at the end of Subsec. 1.2.2, this implies that, despite the sample being an oriented single crystal, the linearity of the response can be inferred from the absence of a quadrature signal, as previously demonstrated for disordered ensembles (Chapter 2). Although not shown here, this behaviour has been experimentally confirmed for GdW_{10}.

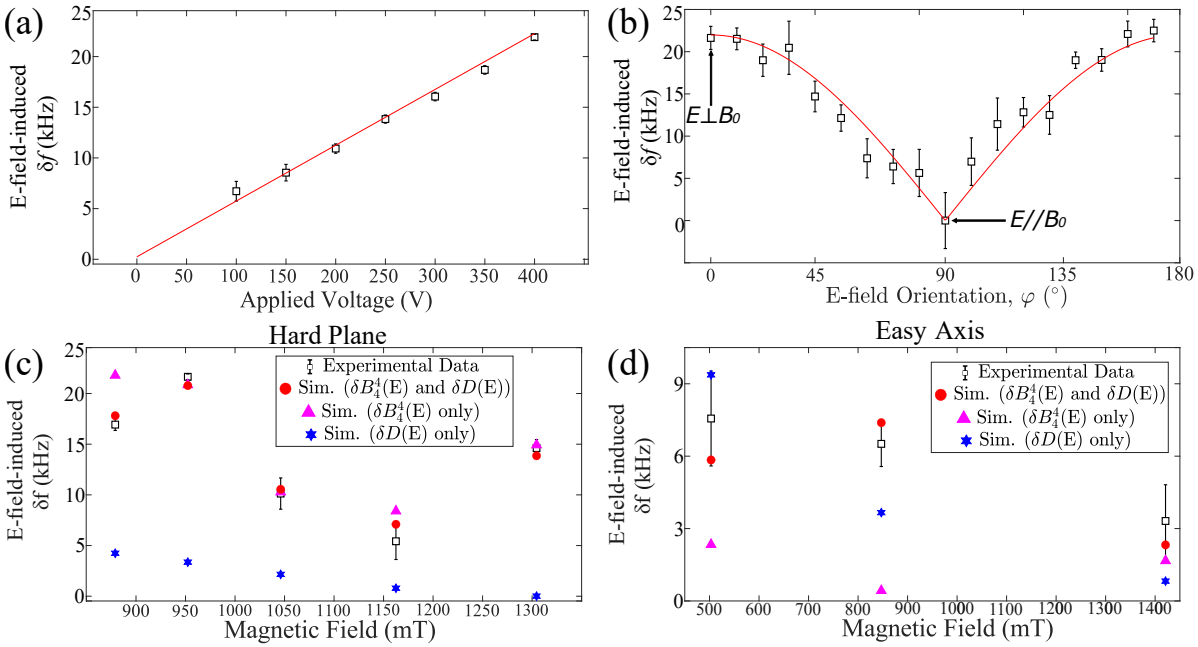

Figure 5.5: (a) Linearity of the SEC effect demonstrated by measuring the resonance frequency shift δf for peak B in the hard-plane orientation under varying applied voltages. (b) Angular dependence of δf at the same peak as the electric field is rotated from $\varphi = 0°$ ($E \perp B_0$, along the x_L-axis in Fig. 5.2(a)) to $\varphi = 90°$ ($E \parallel B_0$, along the z_L-axis). (c, d) Experimentally measured δf values (black) compared with the three simulations described in the main text.

Ho-O bond. A definitive determination of the dipole orientation in the molecular frame would, however, require a two-axis E-field study, which lies beyond the scope of this work.

After fixing the E-field orientation relative to the sample to maximise δf ($\varphi = 0°$), we repeated the SEC measurements for all eight resonance peaks. The resulting shifts are shown in Fig. 5.5(c,d) for both the easy-axis and hard-plane orientations. These data reveal that the SEC modulation in the hard-plane orientation is approximately four to five times larger than in the easy-axis case.

To test the hypothesis by Liu *et al.* [30] regarding the origin of SEC in LnW_{10} compounds, we assume that both anisotropy parameters in GdW_{10} (D and B_4^4) are susceptible to electric-field modulation. We expect transitions in the easy-axis orientation to be more sensitive to variations in the axial anisotropy D, while those in the hard plane should predominantly reflect changes in B_4^4. In fact, when B_0 is aligned close to the easy axis, the wavefunctions $|\psi_i\rangle$ are approximately eigenstates of $\hat{S}_z$ (or $\hat{S}_z^2$), resulting in dominant contributions from the axial anisotropy term to the spin energies, i.e.,

$|\langle\psi_i|D\hat{S}_z^2|\psi_i\rangle| \gg |\langle\psi_i|B_4^4\hat{O}_4^4|\psi_i\rangle|$. In contrast, when B_0 is rotated away from the easy axis, the eigenstates acquire significant $\hat{S}_x$ and $\hat{S}_y$ components. In this basis, the operator $\hat{O}_4^4$ yields first-order contributions to the energy levels, making them more sensitive to electric-field-induced modulations in B_4^4.

To model this, we performed simulations in which the anisotropy terms were modulated as $B_4^4(E) = B_4^4(0) + \delta B_4^4(E)$ (and similarly for D). A search algorithm (see App. B.2) was used to determine the shifts δD and δB_4^4 that best matched the measured δf values. The simulated data are overlaid with experiment in Fig. 5.5(c,d), showing three cases: both parameters modulated (red circles), only B_4^4 varied (magenta triangles), and only D varied (blue stars). The best-fit values at an applied field of 2 kV/cm were $(\delta B_4^4, \delta D) = (3.00\text{ kHz}, 7.37\text{ kHz})$ (or, alternatively, 1.50 $\times 10^{-2}$ Hz/(V/m), 3.69 $\times 10^{-2}$ Hz/(V/m)), $\delta B_4^4 = 3.20$ kHz (1.60 $\times 10^{-2}$ Hz/(V/m)), and $\delta D = 16.39$ kHz (8.19 $\times 10^{-2}$ Hz/(V/m)), respectively. While the SEC strength in GdW_{10} is overall weaker than in HoW_{10}, the extracted shifts in spin-Hamiltonian parameters are comparable. This is likely due to the difference in SOC: in GdW_{10}, the eigenstates are less susceptible to the same level of anisotropy modulation due to the zero orbital momentum.

In both orientations, the best agreement with experiment was obtained (unsurprisingly) when both anisotropy terms were allowed to vary. In this case, all simulated values fell within experimental uncertainties. In the hard plane, varying B_4^4 alone reproduced the measured shifts well, while changing only D resulted in shifts about three times too weak. The opposite held true in the easy-axis orientation: modulating only D provided reasonable agreement, while variations in B_4^4 alone were insufficient. These modulation parameters were extracted by minimising the weighted residuals using the search algorithm outlined in App. B.2. The previous analysis indicates that, while the tetragonal anisotropy B_4^4 is the dominant contributor to SEC in GdW_{10} (as SEC is stronger in the hard plane), the axial anisotropy also plays a non-negligible role. This nuanced picture contrasts with the simpler hypothesis proposed in Ref. [30] and underscores the rich physics of SEC in polyoxometalates.

5.3 Electric Control of Clock Transitions

Having established the spin parameters involved in the SEC in GdW_{10}, we now turn to alternative strategies to generate and electrically control CTs, laying the theoretical foundation for our proposal in Sec. 5.4.

To understand the modalities by which CTs in spin systems can be electrically controlled, we begin by considering the simple axial Hamiltonian for $S \geq 1$ systems:

$$\hat{\mathcal{H}}^{(0)} = D\hat{S}_z^2 + \mu_B g B_0 \hat{S}_z, \tag{5.4}$$

where we have neglected the $S(S+1)/3$ term from Eq. 1.14, as it contributes only a constant energy shift and is irrelevant to the present discussion. The eigenstates of $\hat{\mathcal{H}}^{(0)}$ are the pure $|m_S\rangle$ states, with corresponding energies[6] $E_{m_S} = Dm_S^2 + \mu_B g B_0 m_S$. Since all terms in $\hat{\mathcal{H}}^{(0)}$ commute with $\hat{S}_z$, these eigenstates do not mix. As a result, when two levels intersect at specific values of B_0, the crossings remain exact rather than avoided. In other words, the spectrum of a purely axial Hamiltonian does not exhibit CTs.

To generate CTs, the Hamiltonian must include terms that do not commute with $\hat{\mathcal{H}}^{(0)}$, i.e., non-axial contributions. The first route is through lowering the symmetry of the spin system, which introduces terms such as the transverse zero-field splitting $E(\hat{S}_x^2 - \hat{S}_y^2)$ from Eq. 1.14. As discussed in Sec. 5.2, this mechanism is responsible for CTs in HoW_{10}, where the tetragonal anisotropy term $B_4^4\hat{O}_4^4$ produces avoided crossings. This is corroborated by the simulations in Fig. 5.1 from Ref. [69], which show that CTs appear only when this anisotropy is included. We refer to these as *intrinsic* CTs, as they originate from the symmetry properties of the spin system. In GdW_{10}, although a tetragonal anisotropy is present, it is more than an order of magnitude weaker than in HoW_{10}. Consequently, CTs appear at significantly lower resonance frequencies, lying outside the conventional X- and K_u-band windows, and thus necessitating larger, lower-frequency resonators (see Fig. A.11 in the Appendix).

[6]The exact form of the eigenvalues depends on the spin quantum number S. However, changing S only rescales the scalar prefactors of D and $\mu_B g B_0$, which does not affect the overall argument.

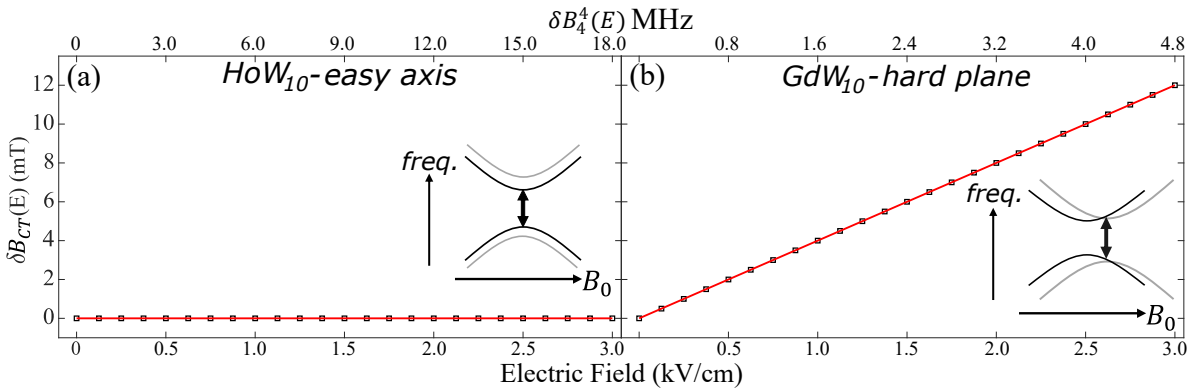

Figure 5.6: (Simulations) Electric-field-induced shift of the CT field position, $\delta B_{\mathrm{CT}}(E)$, for (a) the intrinsic CTs along the easy axis of HoW_{10} and (b) the extrinsic CTs in the hard plane of GdW_{10}. The simulations were obtained by varying the B_4^4 parameter (top axis) and tracking the corresponding CT position. In the former case, $\delta B_{\mathrm{CT}}(E)$ remains unaffected by the electric field, whereas in the latter it exhibits a linear dependence, consistent with the discussion in the main text. *Insets:* Schematic representation of the modulation of (a) the resonance frequency and (b) the CT field position.

A second mechanism to induce CTs is by tilting the static magnetic field B_0 away from the principal symmetry axis. This introduces a term of the form $\mu_B g B_0 \sin\theta \hat{S}_x$, where θ is the angle between the applied field and the symmetry axis. Such a perturbation is equivalent to introducing a transverse contribution, i.e., a non-diagonal term in the spin Hamiltonian. In this case, the CT frequency depends on the (controllable) tilt angle θ (Fig. A.10), and we therefore refer to these as *extrinsic* CTs, since they are mostly due to external experimental conditions rather than by the intrinsic symmetry of the spin system. An example relevant here is the case of GdW_{10} in its hard plane, whose energy levels and corresponding CTs are displayed in Fig. 5.7.

Two distinct mechanisms can enable the modulation of CTs with an electric field. The first involves shifting the resonance frequency, i.e., inducing $\delta f(E) \neq 0$, which can be detected through standard Hahn-Mims sequences, as demonstrated in Ref. [30], and forms the basis of the theoretical framework in Ref. [179]. The second, central to Sec. 5.4, relies on tuning the magnetic field at which the CT occurs, B_{CT}, rather than its resonance frequency. As discussed in App. A.5.1, this effect originates from the axial crystal-field contributions ($\sum_{k=2,4,6} B_k^0 \hat{O}_k^0$) in the easy-axis configuration, while in the hard plane both axial and non-axial terms can influence B_{CT}. This explains why $\delta B_{CT}(E) = 0$ in

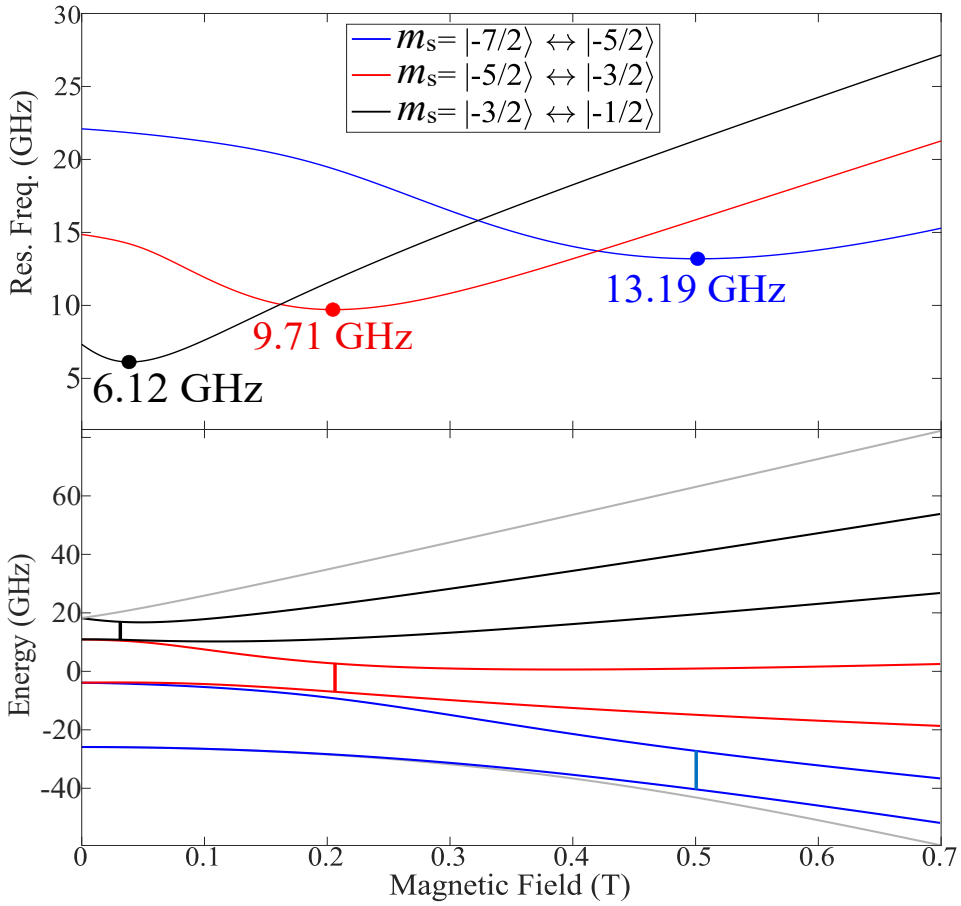

Figure 5.7: *Top:* Resonance frequencies of selected transitions in GdW_{10}, measured as a function of magnetic field B_0 in the hard-plane orientation. Three *extrinsic* clock transitions are identified, with their corresponding frequencies indicated. *Bottom:* Energy level diagram showing the magnetic-field positions of the clock transitions.

HoW_{10} [30], where the relevant X-band CTs occur around the easy axis, so that their B_{CT} are insensitive to changes in non-axial parameters such as B_4^4. In contrast, modulation of this same term in the hard-plane CTs of GdW_{10} is expected to directly alter the CT field. This is confirmed by the simulations in Fig. 5.6, where varying B_4^4 (top axis) reveals that B_{CT} in HoW_{10} remains unchanged, whereas in GdW_{10} it exhibits a clear linear shift with B_4^4, or, equivalently, with the applied electric field (see next subsection for details).

Experimentally, the E-field variation in the CT field position ($\delta B_{CT}(E)$) can be probed by monitoring the variation of the electron coherence time T_{2e} as we apply an increasingly strong E-field. As discussed earlier, T_{2e} reaches its maximum at the CTs, and in HoW_{10}, Ref. [69] reported that it nearly doubles compared to its value measured only ~ 2 mT

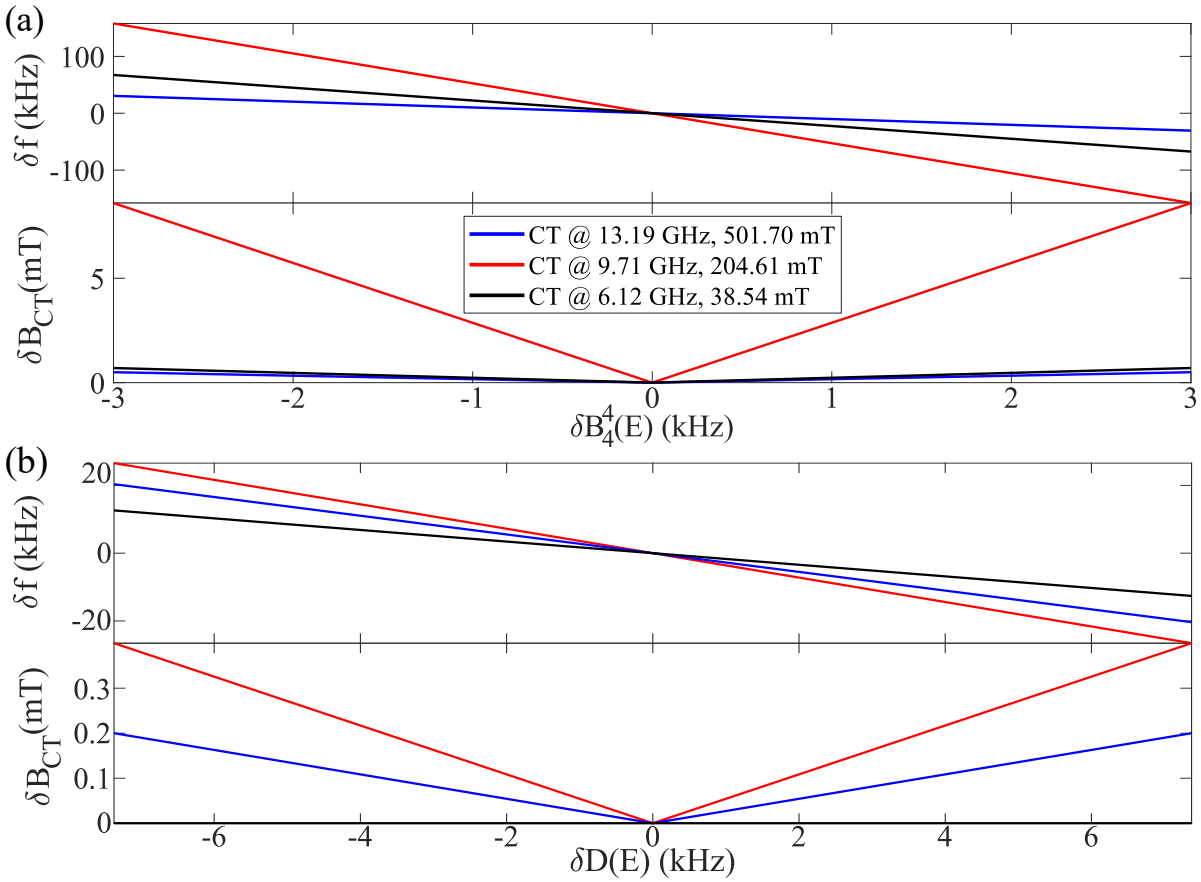

Figure 5.8: Simulated shifts in the resonance frequency δf (top panels) and the CT field position δB_{CT} (bottom) for the three clock transitions in the hard-plane orientation, plotted as a function of variations in (a) B_4^4 and (b) D. The parameter ranges are consistent with the spin-Hamiltonian modulations experimentally evaluated at an applied electric field of 2 kV/cm.

away. In GdW_{10}, simulations in Fig. 5.6(b) predict that an electric field of 2 kV/cm (the experimental value) shifts the CT field by $\delta B_{CT} \simeq 8$ mT. Assuming the same narrow magnetic-field dependence of coherence in HoW_{10}, such a shift would reduce T_{2e} by up to $\sim 75\%$. Therefore, fixing the magnetic field at the $B_{CT}(E = 0)$ field and applying increasing electric fields should lead to a systematic reduction in T_{2e}. Observing such a trend would provide clear experimental evidence of a finite $\delta B_{CT}(E)$. The precise functional form of $T_{2e}(E)$ will depend on the dominant decoherence mechanisms, which are sample-specific and may require ab initio or DFT-level modelling for accurate prediction.

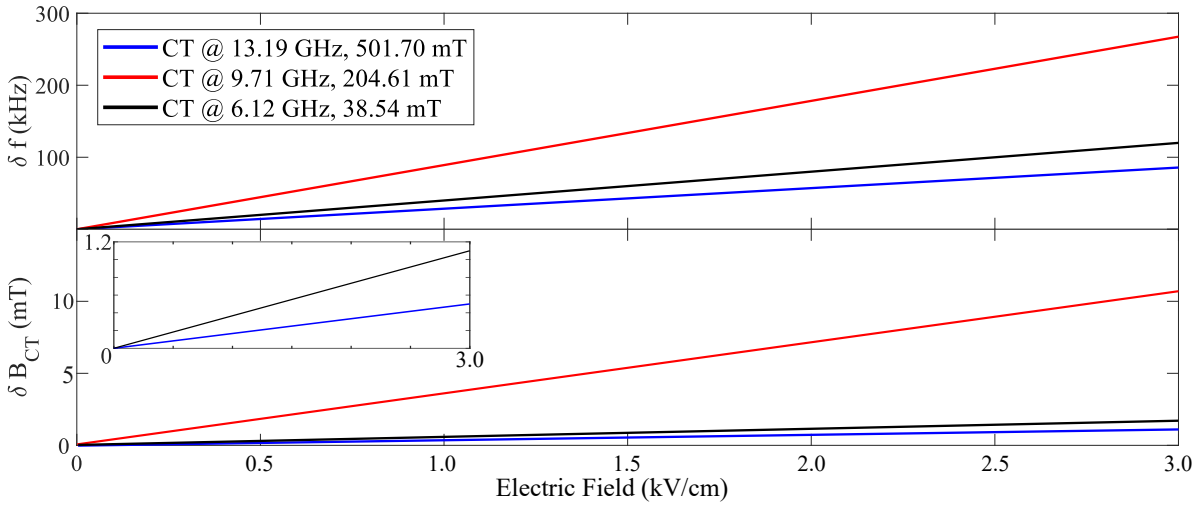

Figure 5.9: (Simulated) Electric-field-induced variations of the resonance frequency δf (top) and clock-transition field position δB_{CT} (bottom) for the three CTs in the hard-plane orientation. From an operational standpoint, the frequency shift remains within a few hundred kHz (well inside the bandwidth of standard ESR resonators), ensuring that the system stays on resonance. In contrast, δB_{CT} can reach values up to ∼10 mT, a substantial effect relevant to the control scheme discussed in the following section.

5.3.1 The GdW_{10} Case

We now examine the electric-field modulation of the CTs in GdW_{10}. As shown in Fig. 5.7, three *extrinsic* CTs appear in the hard-plane orientation, including one at X-band. This orientation is particularly suitable for SEC studies, as the coupling is strongest and can be predominantly attributed to modulation of the $B_4^4\hat{O}_4^4$ term, with negligible contributions from D (Fig. 5.5).

Fig. 5.8 displays simulations of the frequency shift δf and CT field shift δB_{CT} as a function of variations in the anisotropy parameters B_4^4 and D. The parameter ranges were chosen to be consistent with the experimentally observed SEC shifts from Sec. 5.2 (at 2 kV/cm). These simulations were carried out by varying each parameter independently while tracking the resulting changes in both δf and δB_{CT}. As expected, the dominant contribution comes from B_4^4, yielding frequency shifts of ∼0.1 MHz and CT shifts of ∼7 mT, whereas modulating D produces effects nearly an order of magnitude weaker.

We further compute these shifts explicitly as a function of the applied electric field, using $B_4^4(E) = B_4^4(0) + \kappa_4 E$ and $D(E) = D(0) + \kappa_D E$. The results in Fig. 5.9 indicate

that even the X-band CT (red trace), which displays the largest field shift of $\delta B_{\mathrm{CT}} \simeq$ 10 mT at 3 kV/cm, is accompanied by frequency variations of only a few hundred kilohertz, well within the bandwidth of standard ESR resonators. This is operationally significant: it implies that the spin system can remain on resonance with a fixed-frequency resonator (negligible δf), while still being electrically tuned into and out of a CT (large δB_{CT}). This enables dynamic electrical control of the spin system sensitivity to its environment. In the next section, we will examine how to use this property to generate two-qubits operations using E-fields.

5.4 Toward Entangling Gate via Electric Fields

We now summarise the theoretical proposal by A. Ullah *et al.* [179] for generating quantum entanglement in a dipolar-coupled homodimer of HoW_{10} using DC electric fields. In contrast to the earlier sections, where the two molecular anions per unit cell were magnetically decoupled and behaved spectroscopically as monomers, we now consider the dimer case where dipolar interactions are significant. Here, the electric modulation of the *intrinsic* CTs in HoW_{10} is used solely to shift the system's energy levels, without inducing any B_{CT} changes.

The computational two-qubit space[7] in Ullah's scheme is defined such that the $|01\rangle$ and $|10\rangle$ states are degenerate at zero electric field, and the transition frequencies $|00\rangle \leftrightarrow |01\rangle$ and $|10\rangle \leftrightarrow |11\rangle$ are nearly equal. The protocol operates *near* a CT (as will become important shortly) and begins by initializing the dimer in the $|00\rangle$ state using a sequence of microwave and radio-frequency pulses. Applying a static electric field lifts the degeneracy between $|01\rangle$ and $|10\rangle$ via a Stark shift, enabling a selective magnetic π-pulse to transfer population into $|01\rangle$. The field is then switched off, restoring the degeneracy and allowing coherent oscillations between $|01\rangle$ and $|10\rangle$, mediated by the isotropic dipolar interaction $J\,\hat{\mathbf{S}}_1 \cdot \hat{\mathbf{S}}_2$. In the computational basis, this interaction

[7]The "computational space" refers to the four spin energy levels labelled as $|00\rangle$, $|01\rangle$, $|10\rangle$, and $|11\rangle$, used to encode the two-qubit states.

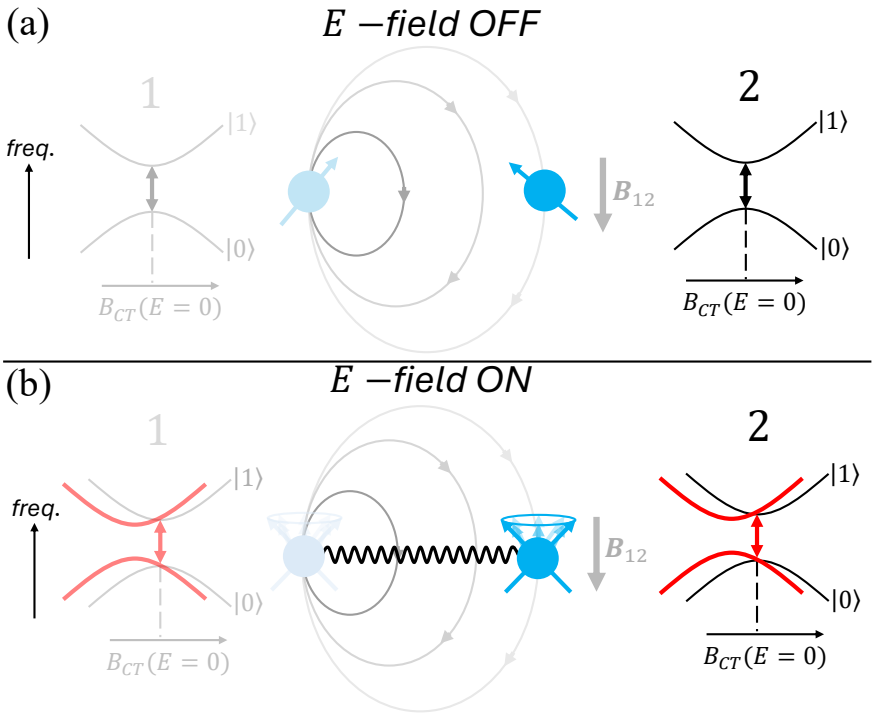

Figure 5.10: Pictorial representation of the proposed protocol to enable switchable two-qubit interactions using E-fields. (a) When both spins are tuned to a CT, they are first-order insensitive to external magnetic-field fluctuations, including the mutual dipolar field (B_{12}). In this regime, the effective dipolar coupling is suppressed and the spins behave as if decoupled. (b) Under the conditions described in Sec. 5.3, applying an electric field shifts the CT position B_{CT}. If the external magnetic field is held fixed at $B_{\mathrm{CT}}(E=0)$, this shift moves the system away from the CT, restoring sensitivity to magnetic fields and reactivating the dipolar coupling. In this way, the spin-spin interaction can be switched on and off electrically.

is captured by the effective Heisenberg Hamiltonian:

$$\hat{\mathcal{H}}_{\mathrm{Heis}} = \begin{pmatrix} \frac{J}{2} & 0 & 0 & 0 \\ 0 & -\frac{J}{2} & J & 0 \\ 0 & J & -\frac{J}{2} & 0 \\ 0 & 0 & 0 & \frac{J}{2} \end{pmatrix}. \tag{5.5}$$

Taking the time-evolution operator $U(t) = \exp(-i\hat{\mathcal{H}}_{\mathrm{Heis}}t/\hbar)$ and setting the free evolution time $t = \pi/(4J)$, the coherent exchange yields a $\sqrt{\mathrm{SWAP}}$ operation (up to a global phase) that transforms the state as $|01\rangle \longrightarrow \frac{1}{\sqrt{2}}(|01\rangle + i|10\rangle)$. Thus, the free-evolution under the Heisenberg Hamiltonian generates an entangled state between the two HoW_{10} molecules. A second electric-field pulse, combined with a selective π-pulse, maps $|01\rangle \rightarrow |00\rangle$ and $|10\rangle \rightarrow |11\rangle$, yielding the Bell's state $(|00\rangle + i|11\rangle)/\sqrt{2}$.

Crucially, the protocol operates *near*, but not exactly at, the CT. This is because, as

detailed later in this section, each spin at the CT is first-order insensitive to *all* external magnetic fields, including mutual dipolar interactions. As a result, the effective dipolar coupling between qubits vanishes: each qubit behaves as if it were magnetically isolated. In other words, operating exactly at the CT transforms the dimer into two magnetically decoupled copies, with each molecule effectively behaving as diamagnetic. By detuning slightly from the CT, a finite dipolar coupling is restored, enabling the desired $\sqrt{\text{SWAP}}$ interaction while still benefiting from partial protection against magnetic noise.

While this protocol represents an elegant use of electrically sensitive CTs, it faces two notable limitations. The first is practical: the initialization sequence for HoW_{10} requires control over a broad frequency range, spanning from hundreds of MHz to tens of GHz, well beyond the capabilities of standard ESR resonators and commercial pulse generators. This complexity arises from the intricate internal level structure of HoW_{10}, driven by strong hyperfine coupling and pronounced magnetic anisotropy [178]. Although this challenge might be mitigated via molecular engineering, it presents a nontrivial experimental hurdle.

The second, more fundamental limitation stems from the fact that the dipolar interaction is never truly "off": detuning even slightly from the CT reintroduces a nonzero coupling. While this is acceptable in a two-qubit setup like the one described, it becomes a significant obstacle when scaling to multi-qubit architectures. In such cases, the ability to switch J on and off on demand is essential. Residual dipolar couplings between qubits/spins can lead to unwanted entanglement, crosstalk, and gate errors, reducing fidelity. Without a mechanism to independently modulate the interaction strength between selected qubit pairs, the protocol lacks the selectivity and flexibility required for larger quantum registers.

This is where the extrinsic CTs in GdW_{10}, discussed in the previous section, become advantageous. Unlike the easy-axis CTs in HoW_{10}, their CT position can be shifted by an applied electric field, enabling dynamic control of the dipolar coupling. By toggling in and out of the CT, one can effectively switch the dipolar interaction strength J. Fig. 5.10 schematically illustrates this concept. With the electric field off, both spins are tuned to their CT at zero field, $B_{\text{CT}}(E = 0)$ (top panel). In this state, the local magnetic field produced by one spin (B_{12}) is not sensed by the other due to the CT-induced first-order

magnetic insensitivity. As a result, the dipolar coupling effectively vanishes, since the spins behave as if magnetically "silent" or diamagnetic to each other.

Upon applying an external electric field, the CT shifts to a new value $B_{\mathrm{CT}}(E)$, as shown in the lower panel of Fig. 5.10. If the external magnetic field remains fixed at $B_{\mathrm{CT}}(E = 0)$, the spins are now detuned from their CTs and thus regain magnetic sensitivity, including to each other's dipolar fields. This introduces a finite J, turning on the spin-spin interaction. This mechanism therefore enables a switchable two-qubit gate controlled purely by electric fields. Notably, this protocol is general and could, in principle, be extended to other platforms exhibiting clock transitions, such as donor spins in silicon [173], trapped ions [181], or superconducting qubits [174], where the insensitivity may extend to other control parameters beyond magnetic fields.

To make such a scheme practically viable, however, it is necessary to consider the full Hamiltonian of the coupled system rather than treating the qubits as isolated. It is not *a priori* obvious that clock-transition behaviour will be preserved once dipolar interactions are introduced, or that the single-qubit interpretation of CTs remains valid in the enlarged Hilbert space. Nonetheless, Ref. [182] has demonstrated that molecular spin systems such as Cr_7Mn can indeed be coupled into dimers whose eigenstates retain clock-transition character. Other dimeric systems provide further opportunities. For instance, Yb(trensal) has well-characterised magneto-chemical properties [183, 184] and has already been shown to host entangled states [185]. In another example, pairs of Gd^{3+} ions exploit the large spin $S = 7/2$ to span a 64-dimensional Hilbert space (2^6), effectively corresponding to six qubits[8] [12]. Together, these systems highlight the versatility of molecular dimers for engineering multi-qubit architectures. Their practical use, however, is currently limited by relatively short coherence times (typically only a few hundred nanoseconds at cryogenic temperatures) posing a significant challenge for scalability and fault-tolerant quantum computation.

We tried to test this idea experimentally using a single crystal containing GdW_{10} homodimers, which occur statistically within the lattice so that the sample contains a

[8] Or, equivalently, two coupled eight-level qu*d*its.

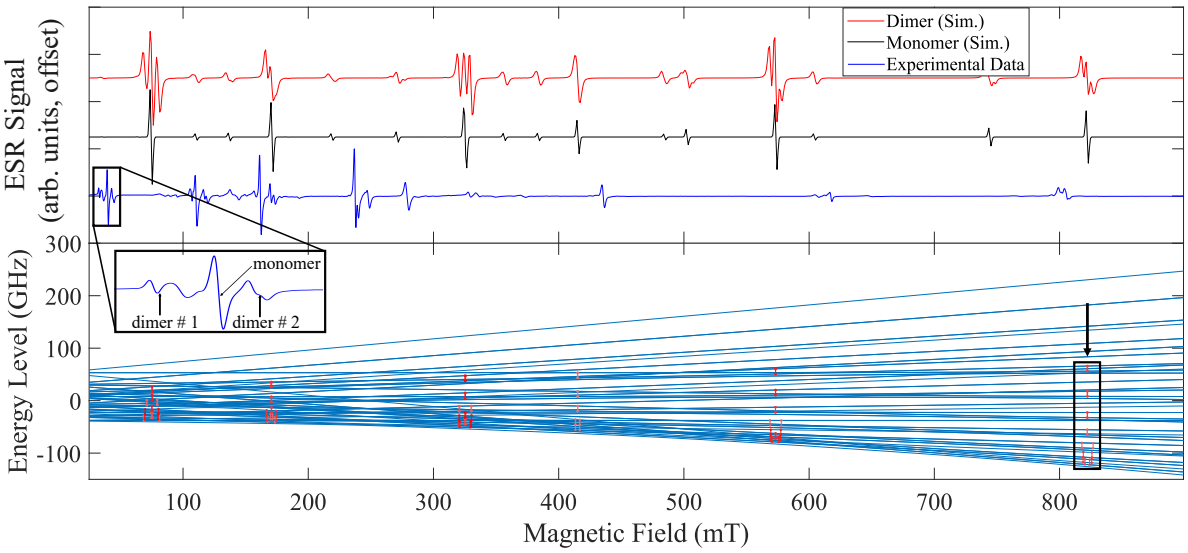

Figure 5.11: *Top:* Simulated spectra of the GdW_{10} monomer (black) and dimer (red) in the hard-plane orientation at X-band. The simulations use the same Hamiltonian parameters as in Eq. 5.3, with the dimer coupling modelled as a weak isotropic exchange interaction with $J = 20$ MHz. The experimental cw spectrum (blue) corresponds to a sample containing both monomers and dimers. *Bottom:* Energy level diagram of the dimer system, with allowed $X-$band transitions indicated by red vertical lines. The high-field transitions inside the black box show clock-transition character. *Inset:* Close-up of an experimental peak, showing the signal from the monomer (centre) and the two dimers (sides).

mixture of monomeric and dimeric species. The coupling between the two monomers within each dimer can be modelled similarly to the HoW_{10} case, via a weak isotropic dipolar interaction with $J = 20$ MHz; each monomer retains the same spin Hamiltonian and parameters as defined in Eq. 5.3. Fig. 5.11 shows the calculated energy level diagram and the allowed X-band transitions in the hard plane of the molecule. Among these, we identified a group of transitions (highlighted by the black rectangle) that exhibit clock-transition-like behaviour.

While the presence of CT-like transitions in the dimer spectrum is suggestive, further evidence is needed to confirm their origin. To this end, we performed a continuous-wave ESR experiment, shown as the blue trace in the top panel of Fig. 5.11. Simulated spectra for both the dimer (red) and monomer (black) are overlaid for comparison. The additional spectral features introduced by the J-coupling in the dimer enable us to distinguish dimer-specific transitions from monomeric ones. This distinction is highlighted in the inset, where characteristic splittings and shifts provide clear spectral signatures of the

dimeric contribution. Based on this comparison, we can confidently assign some of the CT-like transitions to dimer species.

However, there are two significant challenges associated with working with GdW_{10} dimers. First, during synthesis, the molecules preferentially form monomers, resulting in a comparatively weak ESR signal from dimers in bulk measurements, as illustrated in the inset of the lower panel of Fig. 5.11. Resolving the dimeric contributions thus requires either engineering the system at the single- or few-molecule level (for instance, through surface deposition with nanoscale control [71]), or increasing the dimer concentration in the crystal. In the data shown, detection of the dimer spectrum required a relatively high GdW_{10} concentration of 2.1%, significantly higher than the 0.1% used in monomer measurements. This higher concentration, however, results in a marked reduction in coherence time: T_2 is reduced to less than 1 μs, roughly ten times shorter than in the monomer case, thereby precluding the implementation of SEC experiments or T_2 vs. E-field characterizations.

An open question is whether the CTs observed in GdW_{10} dimers retain the same physical meaning as in the monomer case. In dimers, inter-monomer coupling reshapes the eigenstates and may introduce hybridization or entanglement, making it unclear if the CTs can still be mapped cleanly onto a two-qubit computational space. For the proposed scheme to serve as a genuine two-qubit gate, two conditions needs to be met simultaneously: (i) the dimer CT must be physically connected to the corresponding monomer CT, and (ii) the logical subspace must retain a well-defined, controllable qubit encoding. Whether such a "sweet spot" exists in GdW_{10} dimers or related systems remains an open problem for both theory and experiment.

5.5 Conclusion

In this chapter, we explored the electric control of lanthanide-based molecular nanomagnets. Building on previous work on the polyoxometalate HoW_{10} [30], where the tetragonal anisotropy was proposed as the origin of both clock transitions (CTs) and electric sensitivity, we turned to the isostructural compound GdW_{10} to gain direct

experimental evidence. In HoW_{10}, only transitions within the ground-state doublet $m_J = \pm 4$ are accessible due to large anisotropies, preventing a full test of this proposal. In contrast, Gd^{3+} has negligible orbital angular momentum and therefore much weaker anisotropy, allowing us to directly probe spin-electric coupling across multiple transitions. Our analysis reveals that while B_4^4 provides the dominant contribution, the axial zero-field splitting D also plays a role, underscoring the complex interplay of anisotropy terms that can be harnessed via SEC.

On the quantum-information side, we proposed using the hard-plane CTs of GdW_{10} within a multi-qubit architecture. Unlike previous schemes [179], where only the resonance frequency was electrically tuned, here also the CT magnetic-field position shifts. By toggling the system in and out of the CT condition, the spin sensitivity to magnetic fluctuations, and thus spin-spin interactions, can be electrically controlled, enabling tunable interaction times between qubits. Realising this scheme poses both theoretical and experimental challenges. Theoretically, one must clarify how enlarging the Hilbert space affects the preservation of CT character, building on work such as Ref. [182]. Moreover, suitable molecular dimers are required. While GdW_{10} is attractive in principle, synthesising and spectroscopically addressing dimers of this compound is challenging. This calls for alternative candidates that could be designed through chemical engineering strategies.

6
Conclusion

In this thesis, we examined the electric field control across a broad range of spin systems, from frozen solutions of organic molecules to crystalline defects and molecular crystals. These studies, while targeting different physical settings, collectively illustrate the versatility of spin-electric coupling (SEC) and its relevance for both fundamental physics and emerging quantum technologies.

Our investigation of optically excited molecules (Chapter 2) demonstrated how the Hamiltonian tunability of molecular nanomagnets can be combined with optical initialization and simultaneous magnetic and electric field control. Although initially conceived as a proof-of-principle spin-based quantum sensor, the study revealed broader opportunities for quantum architectures. In particular, the prospect of optical initialization at telecom frequencies, as recently demonstrated in Ref. [135], together with electric-field control, suggests a promising strategy that unites high-fidelity initialization with nanoscale manipulation. Complementary to this, we explored the use of resonant electric fields to drive spin transitions (Chapters 3 and 4). For nuclear spins, we exploit the strong coupling between the electric field and the electronic degrees of freedom in the sample. Through the hyperfine interaction, this electric sensitivity is transferred to the nucleus, enabling nuclear transitions to be driven by radio-frequency electric fields.

Attempts to achieve an analogous effect for electron spins proved more challenging, as the outcome was strongly influenced by the interplay between the electromagnetic field distribution of our custom resonator, the sample's permittivity, and its pronounced magnetic anisotropy. Nonetheless, this study identified practical and theoretical criteria for realizing electrically driven electron-spin resonance in ensembles. The final part of the thesis (Chapter 5) addressed electrically modulated clock transitions in polyoxometalate complexes. Here, we obtained a more comprehensive picture of the microscopic origins of spin-electric coupling compared to earlier work in similar samples [30], and we proposed how these insights could be harnessed to implement multi-qubit architectures based on such systems.

One of the most important directions for future work is to establish a microscopic model that rationalises the origin of SEC. In this thesis, as in previous studies [16, 30, 34, 40], SEC has been described phenomenologically by fitting the electric-field dependence of effective spin Hamiltonians (see App. B.1). While this provides valuable high-level insight, it remains limited in two ways. On one hand, it does not allow reliable prediction of which systems will display strong SEC; current expectations are based largely on qualitative structural features, such as the presence of strong spin-orbit coupling (SOC) or the lack of inversion symmetry (necessary for a first-order effect). On the other hand, the absence of a microscopic description prevents the use of SEC as a quantitative probe for extracting detailed structure-property relationships, such as how variations in electronic configuration govern magnetic anisotropy, or how spin-orbit and dipolar interactions contribute to the observed couplings. A deeper microscopic picture would not only clarify the origin of SEC but also guide the design of new systems where SEC can be optimised for specific applications. Recent developments have pointed towards this direction by using DFT calculations to reveal the microscopic mechanisms by which external electric fields affect spin Hamiltonian parameters [126]. Such approaches promise not only a clearer microscopic picture, but also the ability to anticipate which molecular or crystalline systems are most likely to display strong SEC, thereby moving beyond purely empirical, parameter-fitting descriptions. Despite these advances, the

strength and nature of SEC are strongly dependent on the specific system, and no general predictive methodology currently exists.

Finally, we consider the broader relevance of this work within the field of quantum information science. The experiments presented here were designed as exploratory demonstrations rather than implementations *directly* suitable for quantum computing or quantum sensing architectures. A key reason is the use of spin ensembles instead of individually addressable spins, which inevitably limits scalability and direct applicability to device-level quantum technologies. Nevertheless, working with ensembles offers important advantages: it enables systematic testing of SEC mechanisms and related control strategies using established magnetic-resonance techniques and equipment, thus avoiding the technical challenges associated with probing single-spin systems. In this sense, the results of this thesis provide both conceptual insights and methodological progress that may inform the future development of quantum technologies based on spin systems. While their ultimate impact will depend on future research and experimental progress, the work presented here represents a constructive step toward their systematic advancement.

Appendices

A

Supplementary Material

A.1 Chapter 1

A.1.1 Spin-Orbit Coupling Contribution to the Spin Parameters

This derivation follows closely the treatment in Ref. [94]. We start by considering the orbital and spin contributions to the effective spin Hamiltonian, which can be written as

$$\hat{\mathcal{H}} = \mu_B \, \mathbf{B_0} \cdot (\hat{\mathbf{L}} + g_e \, \hat{\mathbf{S}}) + \lambda \, \hat{\mathbf{L}}^{\top} \cdot \hat{\mathbf{S}}, \tag{A.1}$$

where $\hat{\mathbf{L}}$ and $\hat{\mathbf{S}}$ are the orbital and spin angular momentum operators, μ_B is the Bohr magneton, g_e is the free-electron g-factor, and λ is the spin–orbit coupling (SOC) constant. We assume that the ground state $|\psi_0\rangle = |l_G, m_s\rangle$ is orbitally non-degenerate, meaning that it experiences orbital quenching, i.e., $\langle L \rangle = 0$. Under this condition, the first-order orbital correction to the ground-state energy is

$$E^{(1)} = \mu_B g_e \, \langle l_G, m_s | \, B_0 \hat{S}_z \, | l_G, m_s \rangle + \langle l_G, m_s | \, (\mu_B B_0 + \lambda \hat{S}_z) \hat{L}_z \, | l_G, m_s \rangle \, . \tag{A.2}$$

The first term corresponds to the standard Zeeman energy. The second term vanishes because it factorises as $\langle m_s | \, (\mu_B B_0 + \lambda \hat{S}_z) \, | m_s \rangle \, \langle l_G | \, \hat{L}_z \, | l_G \rangle$ and $\langle l_G | \, \hat{L}_z \, | l_G \rangle = 0$ for an orbitally non-degenerate ground state.

The leading correction then comes from the second-order perturbation term:

$$E^{(2)} = - \sum_{n \neq l_G} \frac{\left| \langle l_G, m_s | \, \mu_B g_e \, \mathbf{B_0} \cdot \hat{\mathbf{S}} + (\mu_B \mathbf{B_0} + \lambda \hat{\mathbf{S}}) \cdot \hat{\mathbf{L}} | n, m_s' \rangle \right|^2}{E_n^{(0)} - E_G^{(0)}}, \tag{A.3}$$

where the sum runs over all orbitally excited states. Expanding the numerator gives

$$E^{(2)} = -\sum_{n \neq l_G} \frac{\langle m_s | \left(\mu_B \mathbf{B_0} + \lambda \hat{\mathbf{S}}\right) | m_s' \rangle \langle l_G | \hat{\mathbf{L}} | n \rangle \langle n | \hat{\mathbf{L}} | l_G \rangle \langle m_s | \left(\mu_B \mathbf{B_0} + \lambda \hat{\mathbf{S}}\right) | m_s' \rangle}{E_n^{(0)} - E_G^{(0)}}. \quad \text{(A.4)}$$

We now define the symmetric tensor

$$\mathbf{\Lambda} = \frac{\langle l_G | \hat{\mathbf{L}} | n \rangle \langle n | \hat{\mathbf{L}} | l_G \rangle}{E_n^{(0)} - E_G^{(0)}}, \quad \text{(A.5)}$$

so that the SOC correction can be expressed as

$$E = \langle m_s | \, \mu_B^2 \, \mathbf{B_0} \cdot \mathbf{\Lambda} \cdot \mathbf{B_0} + 2\lambda \mu_B \, \mathbf{B_0} \cdot \mathbf{\Lambda} \cdot \hat{\mathbf{S}} + \lambda^2 \, \hat{\mathbf{S}} \cdot \mathbf{\Lambda} \cdot \hat{\mathbf{S}} \, | m_s \rangle \, . \quad \text{(A.6)}$$

The first term is spin-independent and contributes only to the orbital part of the magnetic susceptibility, so it can be ignored in the effective spin Hamiltonian. The remaining two terms have the same operator structure as the Zeeman interaction and the zero-field splitting term, respectively: the first is linear in spin operators, and the second is quadratic. Thus, the effective spin Hamiltonian including SOC corrections is

$$\hat{\mathcal{H}}_{\text{eff}} = \mu_B \, \mathbf{B_0} \cdot \left(g_e \, \mathbb{I} + 2\lambda \mathbf{\Lambda} \right) \cdot \hat{\mathbf{S}} + \hat{\mathbf{S}} \cdot (\lambda^2 \mathbf{\Lambda}) \cdot \hat{\mathbf{S}}, \quad \text{(A.7)}$$

from which the SOC contributions to the **g**-tensor and the **D**-tensor can be directly identified. The SOC contribution to the hyperfine interaction can be derived in an analogous way (see, e.g., Ref. [1]), yielding $\mathbf{A}^{\text{SOC}} \sim 2\lambda \, \mathbf{\Lambda}$, in direct analogy to the SOC contribution to the g-tensor.

A.1.2 Rotating-Frame Transformation and Bloch–Siegert Shift

We outline the unitary-frame transformation used in Subsec. 1.1.3. Starting from the time-dependent Schrödinger equation, $i\hbar \, \partial_t \, |\psi(t)\rangle = \hat{\mathcal{H}} \, |\psi(t)\rangle$, we define a rotated state $|\tilde{\psi}(t)\rangle = U(t) \, |\psi(t)\rangle$. Differentiating and substituting gives

$$i\hbar \, \partial_t \, |\tilde{\psi}(t)\rangle = \left(i\hbar \dot{U} U^\dagger + U \hat{\mathcal{H}} U^\dagger \right) |\tilde{\psi}(t)\rangle \, , \quad \text{(A.8)}$$

so the Hamiltonian in the rotating frame is $\tilde{\mathcal{H}} = i\hbar \dot{U} U^\dagger + U \hat{\mathcal{H}} U^\dagger$.

For a driven ESR Hamiltonian, $\hat{\mathcal{H}}(t) = \mu_B g (\mathbf{B_0} + \mathbf{B_1}(t)) \cdot \hat{\mathbf{S}}$, with $\mathbf{B_0} = B_0 \hat{z}$ and $\mathbf{B_1}(t) = 2B_1 \cos(\omega_{\text{mw}} t) \, \hat{x}$, we choose $U(t) = \exp(i\omega_{\text{mw}} t \hat{S}_z)$ to go to the frame co-rotating

with the microwave field. Using $U\hat{S}_x U^\dagger = \hat{S}_x \cos\theta - \hat{S}_y \sin\theta$, one finds $\tilde{\mathcal{H}}(t) = (\omega_0 - \omega_{\mathrm{mw}})\hat{S}_z + \Omega(\hat{S}_x + \hat{S}_x \cos(2\omega_{\mathrm{mw}}t) - \hat{S}_y \sin(2\omega_{\mathrm{mw}}t))$. Under the rotating-wave approximation (RWA), the fast terms oscillating at $\pm 2\omega_{\mathrm{mw}}$ average to zero, leading to the effective Hamiltonian $\tilde{\mathcal{H}}_{\mathrm{RWA}} = \Delta\,\hat{S}_z + \Omega\,\hat{S}_x$, where $\Delta = \omega_0 - \omega_{\mathrm{mw}}$. This is valid when B_1 (or the Rabi frequency Ω) is small compared to ω_{mw}.

When the drive is strong, the fast-oscillating terms neglected in the RWA give rise to a small correction to the resonance condition, known as the *Bloch–Siegert shift*. This can be derived using Floquet or Magnus theory by treating the drive as a periodic perturbation. For a T-periodic Hamiltonian of the form $\hat{\mathcal{H}}(t) = \hat{\mathcal{H}}_0 + \sum_{m\neq 0} V_m e^{im\omega t}$ (with $V_{-m} = V_m^\dagger$), the first-order correction to the time-averaged Hamiltonian is [1]

$$\hat{\mathcal{H}}^{(1)} = \sum_{m\neq 0} \frac{[V_m, V_{-m}]}{2m\omega}. \tag{A.9}$$

Only the $m = \pm 2$ terms contribute in the case of an $S = 1/2$ spin driven at $\omega = \omega_{\mathrm{mw}}$: although the field oscillates as $e^{\pm i\omega t}$ in the laboratory frame, once we transform into the rotating frame those terms appear at $e^{\pm 2i\omega t}$. Identifying these components as $V_{\pm 2} = (\Omega/2)\hat{S}_\pm$ one therefore obtains

$$\hat{\mathcal{H}}^{(1)} = \frac{\Omega^2}{8\omega}\hat{S}_z, \tag{A.10}$$

which adds a small shift along $\hat{S}_z$. The total effective Hamiltonian (up to first order in Ω/ω) becomes

$$\hat{\mathcal{H}}_{\mathrm{eff}} = \Delta\,\hat{S}_z + \Omega\,\hat{S}_x + \frac{\Omega^2}{8\omega}\,\hat{S}_z. \tag{A.11}$$

Physically, this additional $+\frac{\Omega^2}{8\omega}\hat{S}_z$ term means that the resonance frequency is shifted by an amount proportional to Ω^2/ω. In ESR, where $\Omega \ll \omega$ (typically $\Omega/2\pi \sim$ MHz and $\omega/2\pi \sim$ GHz [1]), this shift is on the order of a few kHz and hence usually negligible, though it becomes observable in strongly driven or high-fidelity control experiments [186].

A.1.3 Stevens Operator Table

k	q	High-order Stevens Operator, $\hat{O}_k^q$
2	0	$3\hat{S}_z^2 - s\hat{\mathbb{I}}$
	±1	$c_\pm[\hat{S}_z, \hat{S}_+ \pm \hat{S}_-]_+$
	±2	$2c_\pm(\hat{S}_+^2 \pm \hat{S}_-^2)$
4	0	$35\hat{S}_z^4 - (30s-25)\hat{S}_z^2 + (3s^2-6s)\hat{\mathbb{I}}$
	±1	$c_\pm[7\hat{S}_z^3 - (3s+1)\hat{S}_z, \hat{S}_+ \pm \hat{S}_-]_+$
	±2	$c_\pm[7\hat{S}_z^2 - (s+5)\hat{\mathbb{I}}, \hat{S}_+^2 \pm \hat{S}_-^2]_+$
	±3	$c_\pm[\hat{S}_z, \hat{S}_+^3 \pm \hat{S}_-^3]_+$
	±4	$2c_\pm(\hat{S}_+^4 \pm \hat{S}_-^4)$
6	0	$231\hat{S}_z^6 - (315s-735)\hat{S}_z^4 + (105s^2-525s+294)\hat{S}_z^2 - (5s^3-40s^2+60s)\hat{\mathbb{I}}$
	±1	$c_\pm[33\hat{S}_z^5 - (30s-15)\hat{S}_z^3 + (5s^2-10s+12)\hat{S}_z, \hat{S}_+ \pm \hat{S}_-]_+$
	±2	$c_\pm[33\hat{S}_z^4 - (18s+123)\hat{S}_z^2 + (s^2+10s+102)\hat{\mathbb{I}}, \hat{S}_+^2 \pm \hat{S}_-^2]_+$
	±3	$c_\pm[11\hat{S}_z^3 - (3s+59)\hat{S}_z, \hat{S}_+^3 \pm \hat{S}_-^3]_+$
	±4	$c_\pm[11\hat{S}_z^2 - (s+38)\hat{\mathbb{I}}, \hat{S}_+^4 \pm \hat{S}_-^4]_+$
	±5	$c_\pm[\hat{S}_z, \hat{S}_+^5 \pm \hat{S}_-^5]_+$
	±6	$2c_\pm(\hat{S}_+^6 \pm \hat{S}_-^6)$

Table A.1: Stevens operator $\hat{O}_k^q$ expressed in terms of $\hat{S}_z$, $\hat{S}_\pm$, and the identity matrix $\hat{\mathbb{I}}$ [14]. The coefficients are defined as $c_+ = 1/4$, $c_- = 1/4i$, and $s = S(S+1)$, where S denotes the spin quantum number; $[\hat{A}, \hat{B}]_+ = \hat{A}\hat{B} + \hat{B}\hat{A}$ represents the anticommutator.

A.2 Chapter 2

A.2.1 Details on Density Functional Theory

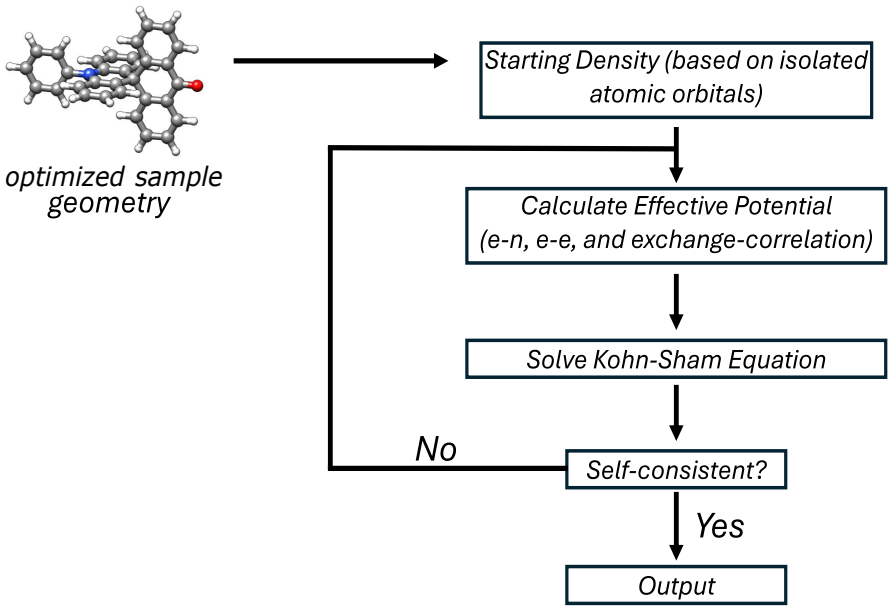

Figure A.1: Schematic representation of the self-consistent procedure in density functional theory. The cycle begins with an initial guess of the electron density, followed by the construction of the effective potential and the solution of the Kohn-Sham equations. The electron density is then updated until convergence is reached.

Here we outline the details of the Density Functional Theory (DFT) used to compute the electron-hole distribution in the triplet state, as well as the spin-spin and spin-orbit contributions to the ZFS (Eq. 1.15). The key principle of DFT is that a system can be fully described in terms of the electron density $\rho(\mathbf{r})$, rather than the many-body wavefunction. This represents a major simplification: while the wavefunction of an N-electron system depends on $3N$ spatial coordinates, the density depends only on three, regardless of N.

After the molecular structure is optimised, i.e., when the net forces on the nuclei are minimised, the electronic density is determined using the *self-consistent field* (SCF) method [187], which forms the basis of our DFT calculations. As shown in Fig. A.1, the SCF cycle starts from an initial guess for $\rho(\mathbf{r})$, typically taken as a superposition of atomic densities from the constituent atoms. From this density, the effective potential is constructed, incorporating the external nuclear potential, electron-electron Coulomb

repulsion, and the exchange-correlation contribution. The Kohn–Sham equations, a set of Schrödinger-like equations, $\hat{\mathcal{H}}_{\mathrm{KS}} |\psi_i\rangle = \epsilon_i |\psi_i\rangle$, are then solved to obtain a new set of molecular orbitals $|\psi_i\rangle$ and eigenvalues ϵ_i. These orbitals are then used to build an updated electron density, which is compared with the previous iteration. If the difference falls below a predefined threshold, the SCF cycle is considered converged. Otherwise, the new density is mixed with the previous one, and the resulting density is fed back in the cycle; this process is repeated until self-consistency is reached.

While conventional DFT provides access primarily to ground states, our goal with ACRSA is to study the excited triplet state, which requires time-dependent DFT. This method that extends the Kohn–Sham formalism to include the explicit time evolution of the electron density [188]. Specifically, our choice of functional and basis set followed established benchmarks for organic molecules such as ACRSA [189, 190], as we employed the B3LYP functional together with the EPR-II basis set. This constitutes a well validated combination for calculating spin Hamiltonian parameters including ZFS and hyperfine interactions, making it well suited for this investigation.

A.2.2 ^{1}H Hyperfine Couplings in ACRSA

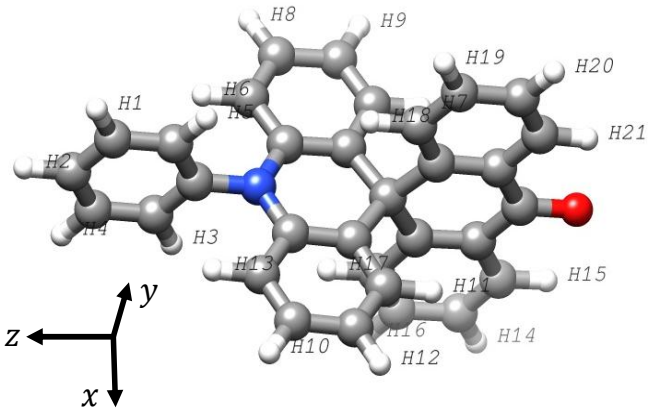

Id	A_{xx}	A_{yy}	A_{zz}
1H	1.18	1.35	0.19
2H	0.01	-0.21	-0.00
3H	0.39	-1.69	-1.32
4H	1.53	1.02	-0.27
5H	-1.11	-0.31	0.63
6H	-3.48	-5.66	1.01
7H	2.10	3.02	1.22

Id	A_{xx}	A_{yy}	A_{zz}
8H	1.60	1.48	0.24
9H	-8.38	-6.05	-2.05
10H	1.58	1.55	0.08
11H	1.79	3.34	0.07
12H	-7.06	-7.27	3.13
13H	-4.06	-5.21	-1.14
14H	2.83	1.89	-0.66

Id	A_{xx}	A_{yy}	A_{zz}
15H	-4.39	-5.87	-0.19
16H	-5.00	-8.35	-2.51
17H	2.06	2.13	-0.30
18H	2.48	1.75	-0.91
19H	-8.45	-5.13	1.76
20H	2.19	2.46	0.09
21H	-4.34	-5.93	-0.26

Figure A.2: (Top) ACRSA structure with labelled hydrogen atoms. (Bottom) Hyperfine tensor components in MHz for the 21 hydrogen atoms in ACRSA simulated with DFT. Their direction is defined as the axes frame by the axes in the top picture.

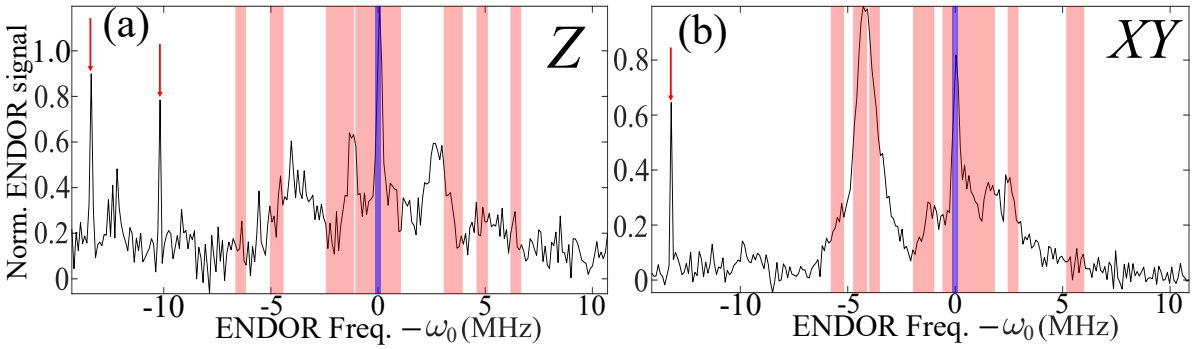

Figure A.3: Mims ENDOR spectra for the Z (a) and XY (b) magnetic-field positions, as defined in the main text. Moreover, the blue shaded area indicates the hydrogen Larmor frequency, while the red ones correspond to the predicted ENDOR frequency for each of the H atoms in ACRSA, as determined by the DFT calculations described in the previous section. The features on the left side of both spectra are attributed either to the single Nitrogen atom in the molecule or to artifacts.

A.2.3 Details on the Sensitivity Calculations

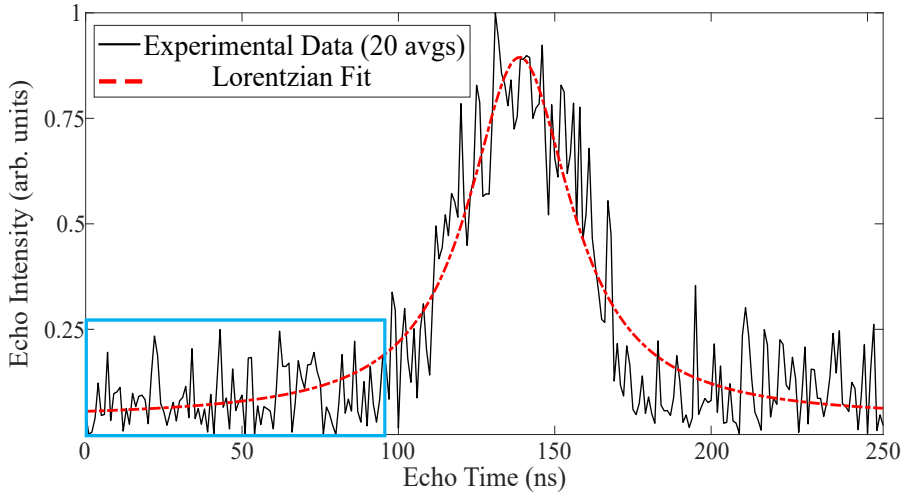

Figure A.4: Transient echo signal of ACRSA embedded in the E-field device described in the main text, measured at 20 K after 20 averages (black line). The signal-to-noise is calculated as the ratio between the amplitude of the Lorentzian fit (in red) and the root-mean-square noise within the region indicated by the blue rectangle, normalised by the number of averages.

Here we outline the procedure used to estimate the electric-field sensitivity reported in the main text. This is based on the signal-to-noise ratio (SNR) of the transient echo from ACRSA embedded in the electric-field device, which determines the weakest E-field-induced change in echo intensity that can be reliably detected.

Fig. A.4 shows the experimental echo signal (black) measured at the Z-B_0 position at 20 K after 20 averages, together with a Lorentzian fit (red). Such fit provides the signal amplitude, while the noise level is estimated as the root-mean-square deviation within the blue-marked region (away from the echo). The ratio of these quantities, normalised by the square root of the number of averages, yields an SNR of about 3.5, leading to the smallest resolvable fractional change in the normalised echo amplitude of $1/3.5 \simeq 29\%$. For the experimentally used $\tau = 2$ μs (limited by the electron T_2 of the sample), this translates to a frequency modulation of $\delta f(E_{\min}) \simeq 63$ kHz, obtained from $1 - \cos(2\pi\delta f(E_{\min})\tau) = 0.29$. Using the measured SEC constant $\kappa = 0.51$ Hz/(V/m), we obtain a minimum detectable electric field of $E_{\min} = \delta f(E_{\min})/\kappa \simeq 1.22$ kV/cm.

As discussed in the main text, two possible routes to enhance this sensitivity are: (i) increasing the triplet-state yield (e.g., through chemical modification of the molecular

environment) to strengthen the echo signal without increasing the overall molecular density, and (ii) extending the spin coherence time T_2, which would lead to the same SNR with a larger τ, hence enabling the same modulation to the spin echo with a weaker E-field.

A.3 Chapter 3

A.3.1 Extended Figures

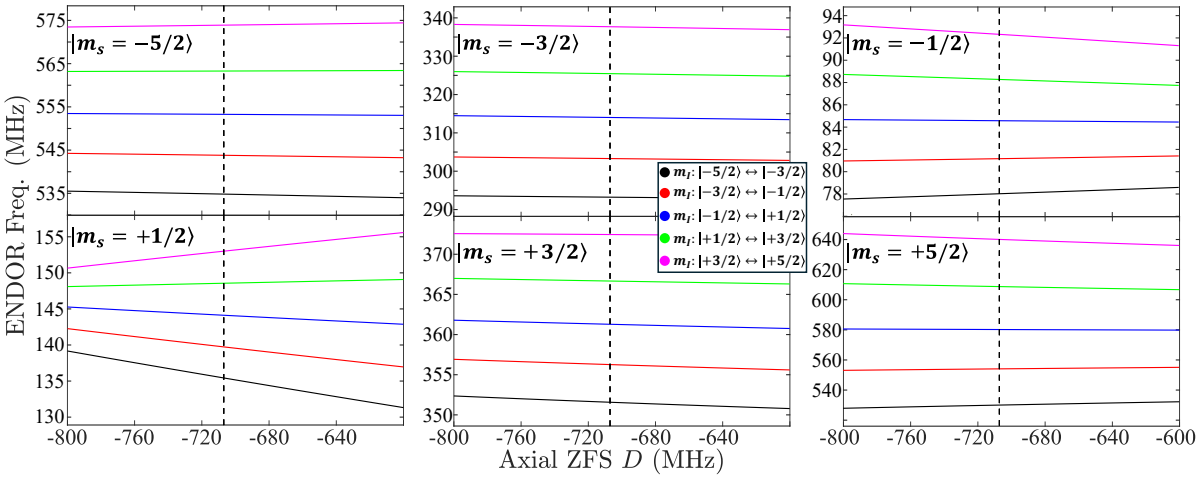

Figure A.5: Simulated ENDOR transition frequencies obtained from the Hamiltonian in Eq. 3.1 as a function of the axial anisotropy D. The dotted black line marks the experimentally determined anisotropy value of $D = -707$ MHz for the Mn:ZnO sample. Each panel corresponds to a distinct electron manifold (as indicated), while different nuclear transitions within a given manifold are distinguished by colour (see legend).

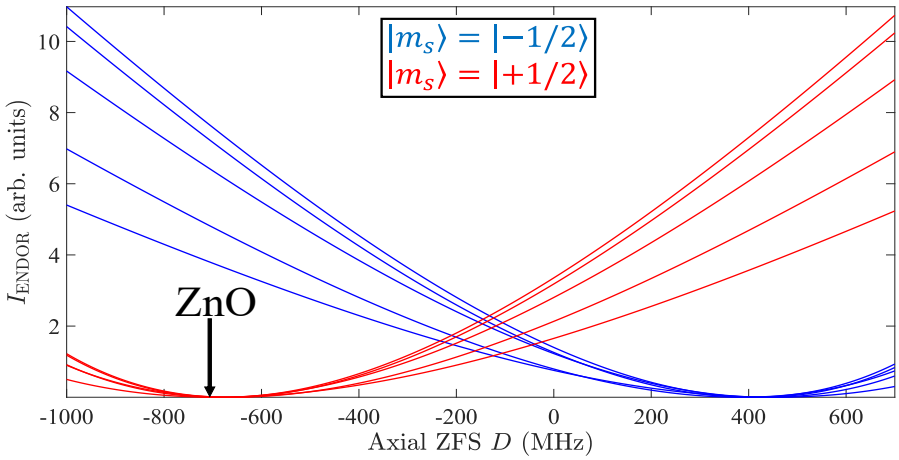

Figure A.6: Simulated ENDOR transition strengths for all single-quantum nuclear transitions within the $|m_s = -1/2\rangle$ (blue) and $|m_s = +1/2\rangle$ (red) manifolds, plotted as a function of the axial magnetic anisotropy D. As discussed in the main text, at $D = -707$ MHz, i.e., the experimentally determined value for Mn:ZnO, the ENDOR transition strength within the $|m_s = +1/2\rangle$ manifold is strongly suppressed. These results are consistent with and adapted from Ref. [147].

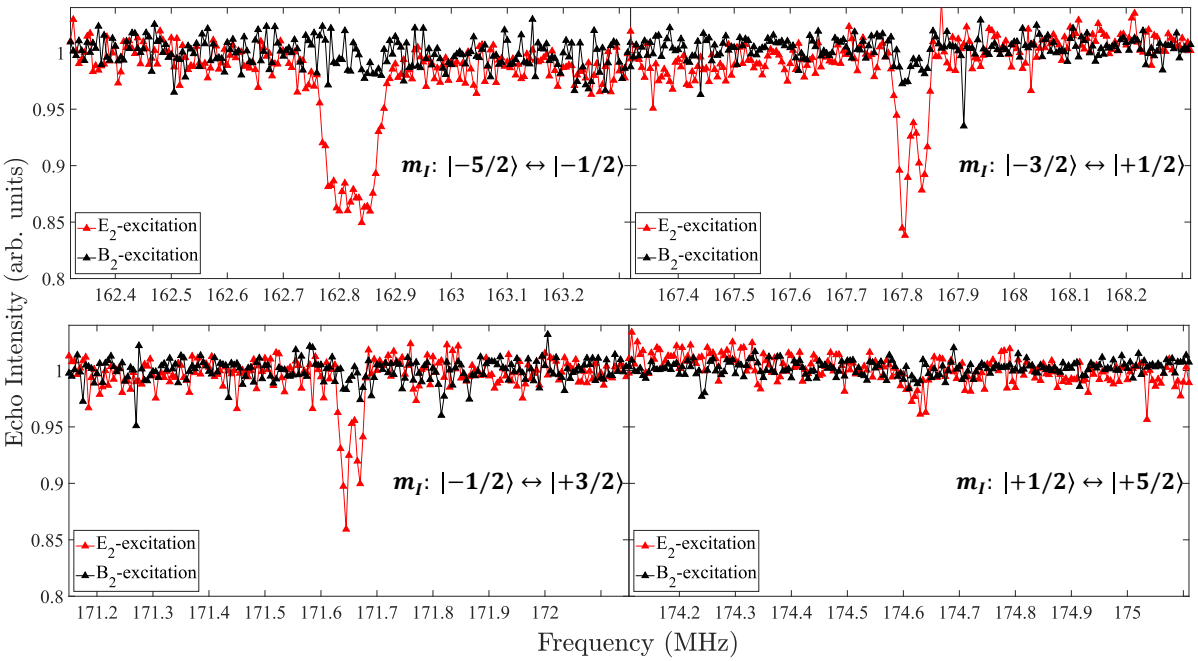

Figure A.7: Experimental data for the four possible double-quantum transitions within the $|m_s = -1/2\rangle$ electron manifold in Mn:ZnO. The corresponding nuclear states are indicated on each plot. As in the main text, black traces represent NMR excitations via coils, while red traces correspond to NER excitations via the capacitor.

A.4 Chapter 4

A.4.1 Orientation-dependence of the Low-field Transitions

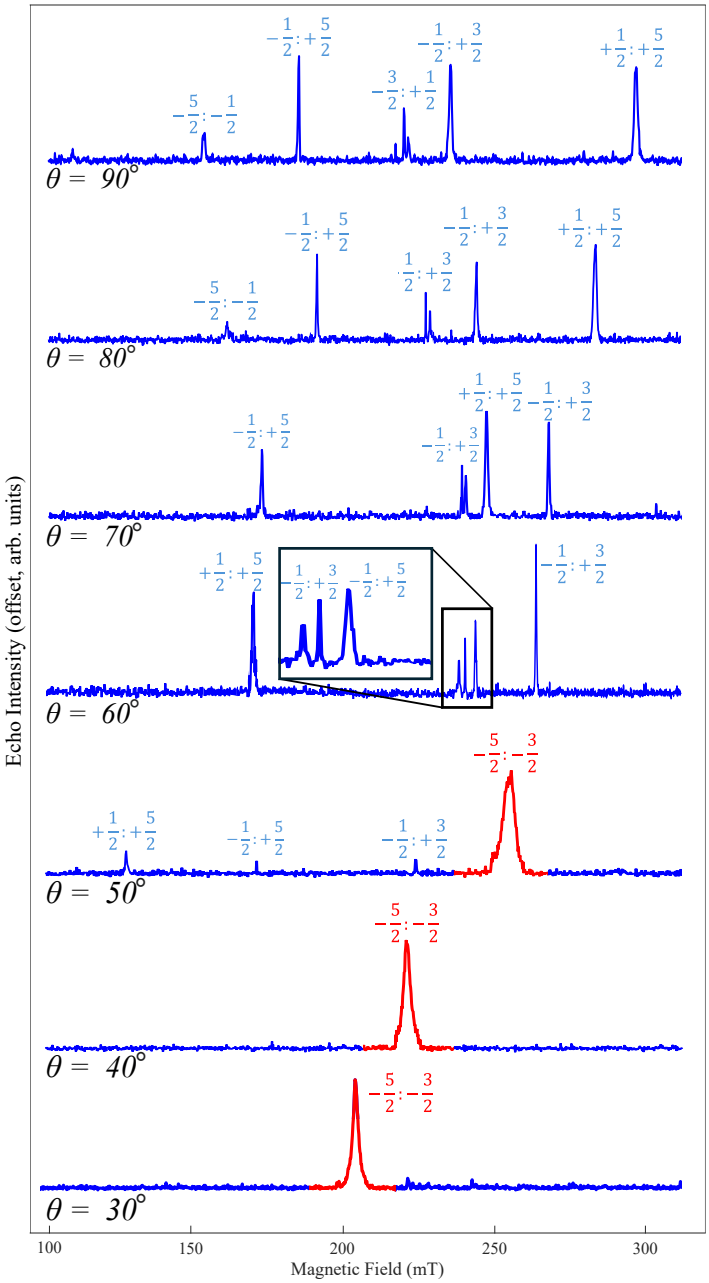

Figure A.8: Full dataset for the orientation-dependent spectra at low fields between $\theta = 90°$ and 30°. The transition labels were assigned using simulated energy-level diagrams, such as the one in Fig. 4.9(b). As discussed in the main text, the blue peaks originate from either parallel-mode ESR or EDSR, with the former likely being the dominant contributor, although this cannot be concluded definitively. The single red peak for $\theta \leq 50°$, in contrast, corresponds to a $\Delta m_s = \pm 1$ transition and arises from conventional ESR.

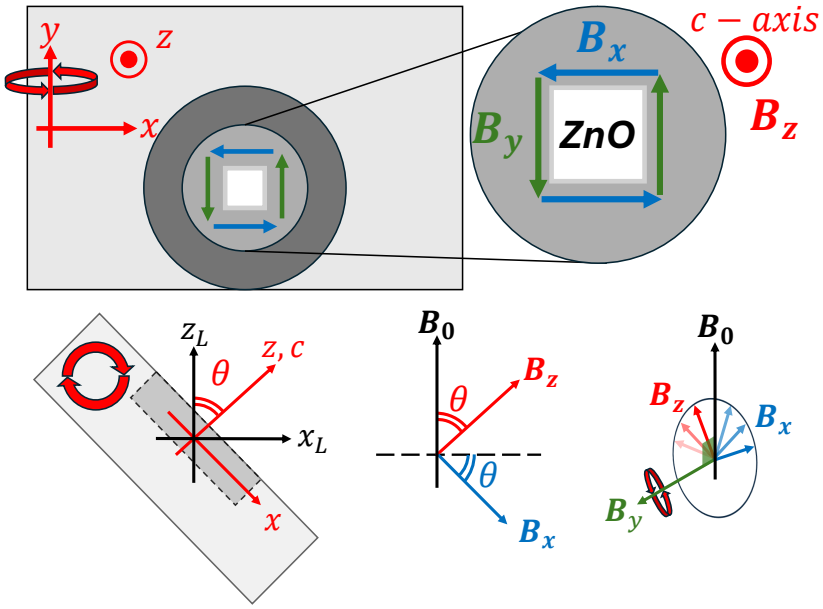

Figure A.9: The cavity frame $\{x, y, z\}$ (shown in red) relative to the laboratory frame $\{x_L, y_L, z_L\}$ (black). The crystal c-axis (and therefore its polar axis) is always aligned with the z-axis of the resonator, while B_0 is rotated around the $y \equiv y_L$-axis, forming an angle θ (as defined in Eq. 4.1) with the c-axis. As described in the main text, the B_x and B_z components contribute to both standard and parallel-mode ESR depending on θ, whereas B_y contributes to standard ESR only. The corresponding interaction terms are summarised in Table A.2.

A.4.2 Modelling the Electric and Magnetic Contributions to the Observed Signal

Here, we detail the simulations of the Rabi frequencies for ESR, parallel-mode ESR (parESR), and EDSR, as discussed in the main text. To quantitatively assess the relative contributions of these mechanisms, it is first necessary to understand how each arises within the cavity geometry. This is illustrated in Fig. A.9, which provides a simplified version of Fig. 4.12(b). The figure shows the parasitic microwave magnetic field $\mathbf{B}_1(t)$ decomposed into its two orthogonal components within the cavity reference frame $\{x, y, z\}$ (red labels). The z-axis defines both the symmetry axis of the resonator and the polar ($c-$) axis of the ZnO sample; these are aligned in the experiment to maximise the electric coupling. In contrast, the laboratory frame $\{x_L, y_L, z_L\}$ (shown in black) follows the conventional definition $\mathbf{B}_0 = (0, 0, B_0)^\top$.

Under rotation around the $y_L \equiv y$ axis, the cavity field components transform as follows. The B_y field remains always perpendicular to the static field B_0, while the B_x and B_z com-

Interaction $\hat{\mathcal{H}}^I(t)$	Technique
$(B_x(t)\cos\theta + B_z(t)\sin\theta)\,\hat{S}_x + B_y(t)\hat{S}_y$	Standard ESR
$(-B_x(t)\sin\theta + B_z(t)\cos\theta)\,\hat{S}_z$	Parallel ESR
$(\hat{S}_x\sin\theta + \hat{S}_z\cos\theta)^2 E_z(t)$	EDSR

Table A.2: Spin operators used in the transition-matrix calculations for standard ESR, parallel-mode ESR, and EDSR, employed to determine the corresponding Rabi frequencies and to identify the dominant driving mechanism responsible for the $\Delta m_s = \pm 2$ transitions. The magnetic and electric field components, $\{B_x, B_y, B_z\}$ and E_z, are defined in the cavity reference frame and were obtained from finite-element simulations.

ponents acquire both parallel and perpendicular projections with respect to B_0, depending on the angle θ from Eq. 3.1 (this can be inferred by the central bottom panel in the figure). This implies that B_y contributes exclusively to conventional ESR, whereas B_x and B_z may drive both ESR and parESR, depending on the cavity's orientation. A straightforward calculation shows that the transverse and longitudinal components of the microwave field in the laboratory frame are given by $B_1^{\perp}(t) = (B_x(t)\cos\theta + B_z(t)\sin\theta)\,\hat{x}_L + B_y(t)\hat{y}_L$ and $B_1^{\parallel}(t) = (-B_x(t)\sin\theta + B_z(t)\cos\theta)\,\hat{z}_L$, respectively. Thus, combining all contributions, the total time-dependent interaction Hamiltonian reads

$$\begin{aligned}\hat{\mathcal{H}}_I(t) &= \hat{\mathcal{H}}_I^{\mathrm{ESR}}(t) + \hat{\mathcal{H}}_I^{\mathrm{parESR}}(t) + \hat{\mathcal{H}}_I^{\mathrm{EDSR}}(t) \\ &= \mu_B g\left(B_1^{\perp}(t)\hat{S}_x + B_1^{\parallel}(t)\hat{S}_z\right) + \tilde{\kappa}E_1(t)\left(\hat{S}_z\cos\theta + \hat{S}_x\sin\theta\right)^2, \end{aligned} \tag{A.12}$$

where the first two terms describe the magnetic driving (ESR and parESR), while the third corresponds to EDSR, with $\tilde{\kappa}$ denoting the ac spin-electric coupling constant (Eq. 4.3). The corresponding effective operators, incorporating both field strengths and spin operators for each of these driving mechanisms, are summarised in Tab. A.2.

Using the interaction terms $\hat{\mathcal{H}}^I(t)$ listed in this table as well as the average magnetic and electric fields inside the sample obtained from finite-element simulations (see, for instance, Fig. 4.12(b)), we calculate the Rabi rates for both EDSR and parESR as $\omega_{\mathrm{Rabi}} \simeq \langle\psi_i|\hat{\mathcal{H}}^I(t)|\psi_j\rangle$ for two spin states $|\psi_{i,j}\rangle$. As detailed in the main text, the Rabi frequencies expected from standard ESR are more than three orders of magnitude weaker for double-quantum transitions and are therefore neglected. Focussing on EDSR and parESR, we evaluate the ratio $\omega_{\mathrm{EDSR}}/\omega_{\mathrm{parESR}} \simeq 1/5$ across all the low-field peaks. This

result shows that although EDSR contributions are systematically weaker, they remain within the same order of magnitude as parESR and therefore cannot be disregarded. In practice, both mechanisms are expected to play a role in driving the observed transitions.

A.5 Chapter 5

A.5.1 $\delta\mathbf{B_{CT}}(\mathbf{E})$ in the Easy-axis Orientation

Here we provide the mathematical details underlying the discussion in Sec. 5.3 on the contribution of axial Stevens operators ($\hat{O}_k^0$) to the clock-transition (CT) field, B_{CT}, in the easy-axis orientation. The general spin Hamiltonian in this case can be written as

$$\hat{\mathcal{H}}(\theta = 0^\circ) = \underbrace{\left[g\mu_B B_0 \hat{S}_z + \sum_{k=2,4,6} B_k^0 \hat{O}_k^0 \right]}_{\text{axial}} + \underbrace{\sum_{k=2,4,6} \sum_{q=-k}^{k} B_k^{q\neq 0} \hat{O}_k^{q\neq 0}}_{\text{non-axial}}, \tag{A.13}$$

where the first and second brackets collect the axial and non-axial contributions, respectively. Assuming that the two states $|i\rangle$ and $|j\rangle$ involved in the CT are only weakly hybridised with the remaining spin states, the Hamiltonian can be reduced to the two-dimensional subspace they span:

$$\hat{\mathcal{H}} = \begin{pmatrix} E^{(i)} & V^{\mathrm{eff}} \\ (V^{\mathrm{eff}})^* & E^{(j)} \end{pmatrix}. \tag{A.14}$$

Here, the diagonal terms $E^{(i,j)}$ arise from the axial terms, while the effective coupling $V^{\mathrm{eff}} = \sum_{k,q\neq 0} B_k^q \langle i|\hat{O}_k^q|j\rangle$ collects the non-axial ones that directly mix the two levels. In practice, most of these matrix elements vanish, leaving only the operator that couples the selected pair. For instance, in HoW_{10}, the only non-zero contribution comes from $B_4^4\hat{O}_4^4$ since the CT occurs between the $|m_J = \pm 4\rangle$ doublet.

In this simplified two-level framework, the resonance frequency around the CT can be approximated to leading order as

$$hf_{\mathrm{res}} \propto \sqrt{\left(g\mu_B B_0 + \sum_{k=2,4,6} B_k^0 \hat{O}_k^0 \right)^2 + \left(\sum_{k=2,4,6} \sum_{q\neq 0} B_k^q \hat{O}_k^q \right)^2}, \tag{A.15}$$

and taking its derivative with respect to the static field B_0 gives

$$\frac{\partial f_{\mathrm{res}}}{\partial B_0} \propto \frac{g\mu_B B_0 + \sum_{k=2,4,6} B_k^0}{hf_{\mathrm{res}}}. \tag{A.16}$$

Applying the CT condition ($\partial f_{\mathrm{res}}/\partial B_0 = 0$) yields $B_{\mathrm{CT}} \propto -\frac{1}{g\mu_B}\sum_{k=2,4,6} B_k^0$, demonstrating that the CT field is determined only by the *axial* crystal-field parameters in the easy-axis configuration.

In HoW_{10}, only transitions within the ground-state doublet along the easy axis could be experimentally accessed [175]. In this case, the electric field modulates exclusively the non-axial B_4^4 term, which affects the resonance frequency (Eq. A.15) but not the position of the clock transition, yielding $\delta B_{\mathrm{CT}}(E) \simeq 0$. This explains the absence of an experimentally observed shift in B_{CT} in Ref. [30] and in the simulations displayed in Fig. 5.6(a).

For any orientation with $\theta \neq 0°$ (including the hard plane), the simplified two-level picture no longer applies. In this case, the Zeeman interaction involves the transverse operator $\hat{S}_x$, which couples different $|m_s\rangle$ states rather than preserving them. Consequently, the eigenstates become mixed superpositions, and both axial and non-axial crystal-field terms contribute to the level structure and to the position of the clock transition. In this regime, electric-field modulations of non-axial parameters can therefore also influence B_{CT}, in contrast to the previous case (Fig. 5.6(b)).

A.5.2 Extended Figures

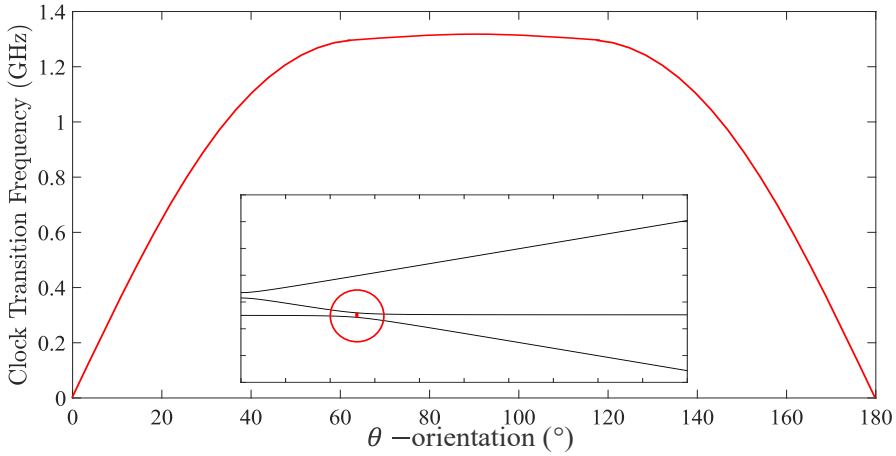

Figure A.10: (Simulations) Resonance frequency of *extrinsic* clock transitions as a function of the tilt angle θ between the static field B_0 and the molecular axis. *Inset:* Representative energy-level diagram of an $S = 1$ system at $\theta = 10°$, with the clock transition highlighted (red circle).

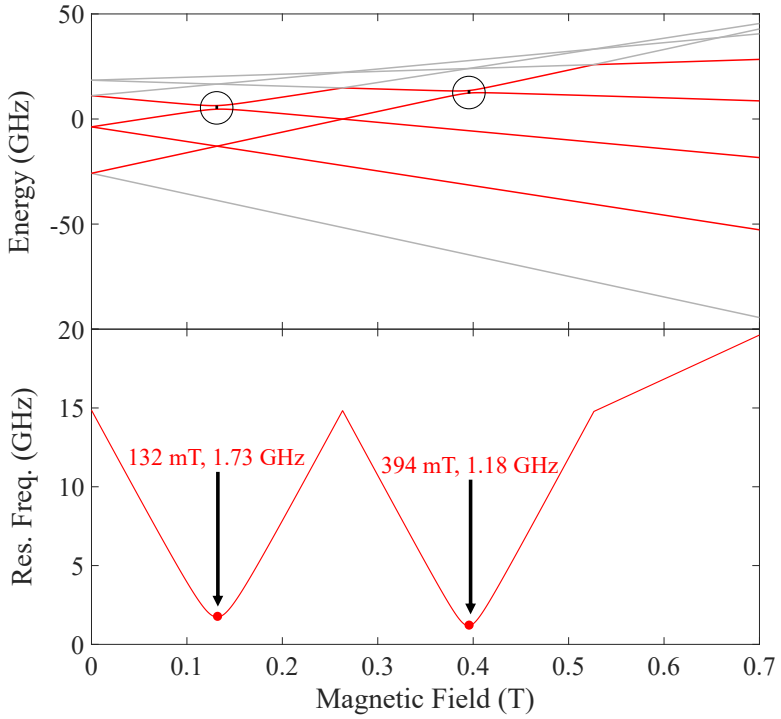

Figure A.11: (Simulations) Energy-level diagram (top) and corresponding resonance frequencies of the highlighted states (bottom) for GdW_{10} along the easy axis. Two CTs are observed (magnetic fields and frequencies indicated), but both occur below 2 GHz, implying that their experimental investigation would require larger, low-frequency resonators.

B
Analysis Scripts

B.1 Magnetic Resonance and Spin-Electric Coupling Simulations

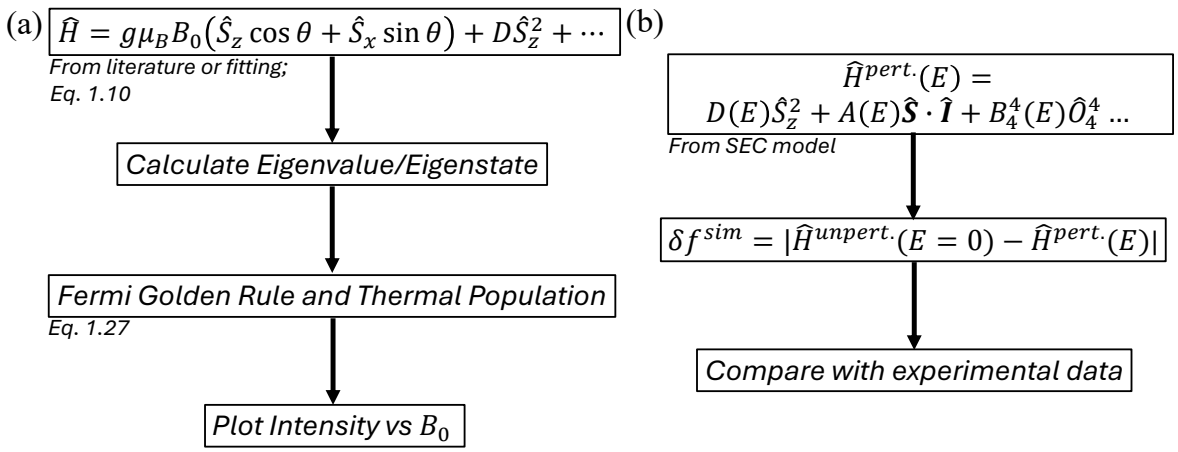

Figure B.1: (a) ESR spectra are simulated from the spin Hamiltonian, which defines the energy levels (eigenvalues) and eigenstates. Transition probabilities are then computed using Fermi's golden rule and weighted by the Boltzmann populations; repeating this procedure across a range of B_0 yields the field dependence of the allowed transitions, from which the ESR spectrum is constructed. (b) Electric-field-induced frequency shifts are obtained analogously, but with Hamiltonian parameters expressed as field-dependent quantities, e.g., $D(E)$. The simulated δf^{sim} are given by the difference between eigenvalues of the E-field-perturbed and unperturbed Hamiltonians and compared directly with experiment. In both cases, the Hamiltonian form and parametrisation of the spin-electric coupling are chosen based on physical insight and prior studies, ensuring consistency with the relevant microscopic mechanisms.

B.2 Search Algorithm for Chapter 5

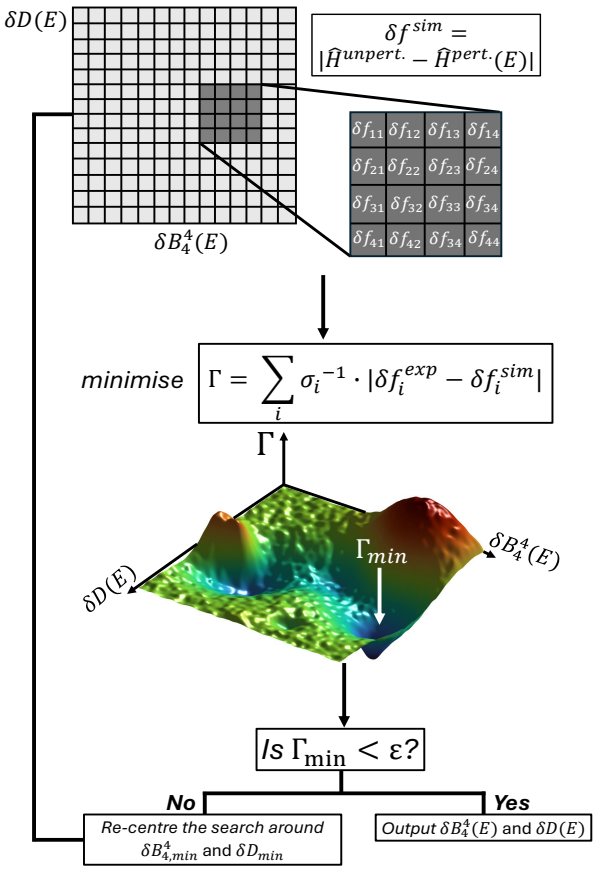

Figure B.2: Schematic representation of the search algorithm used to find the resonance frequency shifts δf in GdW_{10}, as shown in Fig. 5.5 in the main text.

This section outlines the procedure used to calculate the resonance-frequency shifts δf and the corresponding spin-parameter variations shown in Fig. 5.5(c,d) in the main text. A schematic of the search algorithm is presented in Fig. B.2.

The calculation begins by evaluating δf as the absolute difference between the resonance frequencies obtained from (i) the unperturbed Hamiltonian in Eq. 5.3, with parameters determined experimentally from orientation-dependent ESR spectra, and (ii) the electrically modulated Hamiltonian, obtained by varying the anisotropy terms $\delta D(E)$ and $\delta B_4^4(E)$. The explored parameter space (illustrated by the darker grid in the top panel of the schematic) was chosen to be physically reasonable and consistent with previous studies [30].

The next step is to identify the parameter shifts that best reproduce the experimental SEC data. For this, we define the cost function

$$\Gamma(\delta B_4^4, \delta D) = \sum_i \sigma_i^{-1} \left| \delta f_i^{exp} - \delta f_i^{sim} \right|, \tag{B.1}$$

where the sum runs over all measured peaks ($i = 1, \ldots, 8$; five in the hard-plane and three in the easy-axis orientations), and σ_i is the standard error of the experimental δf_i^{exp}. This weighted sum quantifies the mismatch between experiment and simulation.

The (linear) search algorithm scans the chosen parameter space to find the pair ($\delta B_{4,\min}^4$, $\delta D_{\min}$) that minimises Γ. If the minimum cost $\Gamma_{\min}$ lies below a target threshold ε, these values are taken as the optimal parameter shifts, and the corresponding δf^{sim} is computed using $D(E) = D(0) + \delta D_{\min}$ and $B_4^4(E) = B_4^4(0) + \delta B_{4,\min}^4$. If $\Gamma_{\min} > \varepsilon$, the search is repeated with a parameter space re-centred at $(\delta B_{4,\min}^4, \delta D_{\min})$, iterating until the convergence criterion is met.

References

[1]A. Schweiger and G. Jeschke, *Principles of Pulse Electron Paramagnetic Resonance* (Oxford University Press, 2001).

[2]M. A. Nielsen and I. L. Chuang, *Quantum Computation and Quantum Information* (Cambridge University Press, 2000).

[3]A. Abragam and M. H. L. Pryce, 'Theory of the nuclear hyperfine structure of paramagnetic resonance spectra in crystals', Proc. Roy. Soc. London **A205**, 135–153 (1951).

[4]S. Takahashi et al., 'Discrete easy-axis tilting in Mn_{12}-acetate, as determined by EPR: Implications for the magnetic quantum tunneling mechanism', Phys. Rev. B **70**, 094429 (2004).

[5]S. J. Blundell, *Magnetism in condensed matter*, Vol. 140 (Oxford University Press, 2001).

[6]C. A. J. Hutchison and B. Weinstock, 'Paramagnetic Resonance Absorption in Neptunium Hexafluoride', J. Chem. Phys. **32**, 56–61 (1960).

[7]G. Moise et al., 'The impact of spin–orbit coupling on fine-structure and spin polarisation in photoexcited porphyrin triplet states', J. Magn. Reson. **355**, 107546 (2023).

[8]H. Kurreck et al., 'ENDOR Spectroscopy- A Promising Technique for Investigating the Structure of Organic Radicals', Angew. Chem. **23**, 173–194 (1984).

[9]E. Fermi, 'Über die magnetischen momente der atomkerne', Z. Phys. **60**, 320 (1930).

[10]A. Abragam and B. Bleaney, *Electron Paramagnetic Resonance of Transition Ions* (Oxford University Press, 1970).

[11]B. M. Roberts et al., 'Bohr-Weisskopf effect: From hydrogenlike-ion experiments to heavy-atom calculations of the hyperfine structure', Phys. Rev. A **105**, 052802 (2022).

[12]F. Luìs et al., 'A dissymmetric $[Gd_2]$ coordination molecular dimer hosting six addressable spin qubits', Comm. Chem. **3**, 176 (2020).

[13]A. Janossy et al., 'Antiferromagnetic Domains in $YBa_2Cu_3O_{6+x}$ Probed by Gd^{3+} ESR', Phys. Rev. B **59**, 1176 (1999).

[14]K. W. H. Stevens, 'Matrix Elements and Operator Equivalents Connected with the Magnetic Properties of Rare Earth Ions', Proc. Phys. Soc. A **65**, 209–215 (1952).

[15]C. Rudowicz and C. Y. Chung, 'The generalization of the extended Stevens operators to higher ranks and spins, and a systematic review of the tables of the tensor operators and their matrix elements', J. Phys. Condens. Matter **16**, 1–23 (2004).

[16]M. Fittipaldi et al., 'Electric field modulation of magnetic exchange in molecular helices', Nat. Mater. **18**, 329–334 (2019).

[17]W. J. Brya and P. E. Wagner, 'Direct, Orbach, and Raman Relaxation in Dilute Cerous Magnesium Nitrate', Phys. Rev. **147**, 239–246 (1966).

[18]C. J. Wedge et al., 'Chemical Engineering of Molecular Qubits', Phys. Rev. Lett. **108**, 107204 (2012).

[19]D. Kaminski et al., 'Quantum spin coherence in halogen-modified Cr_7Ni molecular nanomagnets', Phys. Rev. B **90**, 184419 (2014).

[20]S. S. Eaton and G. R. Eaton, 'Relaxation times of organic radicals and transition metal ions', in *Biological Magnetic Resonance*, Vol. 19, edited by G. R. Eaton, S. S. Eaton and L. J. Berliner (Springer-Verlag, 2000) Chap. 2, pp. 29–52.

[21]D. G. Cory et al., 'Ensemble quantum computing by NMR spectroscopy', Proc. Natl. Acad. Sci. U.S.A. **94**, 1634–1639 (1997).

[22]E. L. Hahn, 'Spin Echoes', Phys. Rev. **80**, 580–594 (1950).

[23]E. R. Davies, 'A new pulse endor technique', Phys. Lett. A **47**, 1–2 (1974).

[24]W. B. Mims, 'Pulsed endor experiments', Proc. R. Soc. Lond. A **283**, 452–455 (1965).

[25]W. T. Morrillo et al., 'Ab Initio Design of Molecular Qubits with Electric Field Control', J. Am. Chem. Soc. **146**, 26978–26987 (2024).

[26]D. R. McCamey et al., 'Electrically detected magnetic resonance in ion-implanted Si:P nanostructures', Appl. Phys. Lett. **89**, 182115 (2006).

[27]P. Chuang et al., 'All-electric all-semiconductor spin field-effect transistors', Nat. Nanotechnol. **10**, 35–39 (2015).

[28]K. C. Nowack et al., 'Coherent Control of a Single Electron Spin with Electric Fields', Science **318**, 1430–1433 (2007).

[29]Z. Liu et al., 'Electric field manipulation enhanced by strong spin-orbit coupling: promoting rare-earth ions as qubits', Natl. Sci. Rev. **7**, 1557–1567 (2020).

[30]J. Liu et al., 'Quantum Coherent Spin–electric Control in a Molecular Nanomagnet at Clock Transitions', Nat. Phys. **17**, 1205–1209 (2021).

[31]D. Khomskii, 'Classifying multiferroics: mechanisms and effects', Physics **2**, 20 (2009).

[32]M. Trif et al., 'Spin-Electric Coupling in Molecular Magnets', Phys. Rev. Lett. **101**, 217201 (2008).

[33]M. Trif et al., 'Spin electric effects in molecular antiferromagnets', Phys. Rev. B **82**, 045429 (2010).

[34]J. Liu et al., 'Electric Field Control of Spins in Molecular Magnets', Phys. Rev. Lett. **122**, 037202 (2019).

[35]W. Mims, 'Measurement of the linear electric field effect in EPR using the spin echo method', Rev. Sci. Instrum. **45**, 1583 (1994).

[36]E. I. Rashba, 'Cyclotron and combined resonances in a perpendicular field', Sov. Phys. Solid State **2**, 1109–1122 (1960).

[37]Y. Liu et al., 'Emergent linear Rashba spin-orbit coupling offers fast manipulation of hole-spin qubits in germanium', Phys. Rev. B **105**, 075313 (2022).

[38]E. I. Rashba and A. L. Efros, 'Orbital Mechanisms of Electron-Spin Manipulation by an Electric Field', Phys. Rev. Lett. **91**, 126405 (2003).

[39]E. I. Rashba, 'Theory of electric dipole spin resonance in quantum dots: Mean field theory with Gaussian fluctuations and beyond', Phys. Rev. B **78**, 195302 (2008).

[40]S. Asaad et al., 'Coherent electrical control of a single high-spin nucleus in silicon', Nature **579**, 205–209 (2020).

[41]N. Bloembergen, 'Linear Stark effect in magnetic resonance spectra', Science **133**, 1363–1364 (1961).

[42]S. Thiele et al., 'Electrically driven nuclear spin resonance in single-molecule magnets', Science **344**, 1135 (2014).

[43]D. Loss and D. P. DiVincenzo, 'Quantum computation with quantum dots', Phys. Rev. A **57**, 120–130 (1998).

[44]B. Kane, 'A silicon-based nuclear spin quantum computer', Nature **393**, 133–137 (1998).

[45]D. Holmes et al., 'Isotopic enrichment of silicon by high fluence $^{28}Si^{-}$ ion implantation', Phys. Rev. Mat. **5**, 014601 (2021).

[46]F. Arute et al., 'Quantum supremacy using a programmable superconducting processor', Nature **574**, 505–510 (2019).

[47]K. R. Brown et al., 'Materials challenges for trapped-ion quantum computers', Nat. Rev. Mater. **6**, 892–905 (2021).

[48]S. J. Evered et al., 'High-fidelity parallel entangling gates on a neutral-atom quantum computer', Nature **622**, 268–272 (2023).

[49]Google Quantum AI and Collaborators, 'Quantum error correction below the surface code threshold', Nature **638**, 920–926 (2025).

[50]D. Garisto, 'Microsoft quantum-computing claim still lacks evidence: physicists are dubious', Nature News, Available at: `https://www.nature.com/articles/d41586-025-00829-2` (Accessed: 02 December 2025), (2025).

[51]A. Morello et al., 'Single-shot readout of an electron spin in silicon', Nature **467**, 687–691 (2010).

[52]M. Gulka, D. Wirtitsch, V. Ivády, J. Vodnik, J. Hruby, G. Magchiels, E. Bourgeois, A. Gali, M. Trupke and M. Nesladek, 'Room-temperature control and electrical readout of individual nitrogen-vacancy nuclear spins', Nat. Commun. **12**, 4421 (2021).

[53]H. Ou, 'Silicon carbide, the next-generation integrated platform for quantum technology', Light Sci. Appl. **13**, 219 (2024).

[54]A. Gaita-Ariño et al., 'Molecular spins for quantum computation', Nat. Chem. **11**, 301–309 (2019).

[55]C.-J. Yu et al., 'A Molecular Approach to Quantum Sensing', ACS Cent. Sci. **7**, 712–723 (2021).

[56]F. Xie et al., 'Quantum Sensing of Electric Fields Using Spin-Correlated Radical Ion Pairs', J. Am. Chem. Soc. **45**, 14922–14931 (2023).

[57]W. Wu et al., 'Modulating the optical properties and functions of organic molecules through polymerization', Mater. Horiz. **9**, 99–111 (2022).

[58]S. Saha et al., 'From Molecules to Interactions to Crystal Engineering: Mechanical Properties of Organic Solids', Acc. Chem. Res. **11**, 2957–2967 (2018).

[59]M. Wasielewski et al., 'Exploiting chemistry and molecular systems for quantum information science', Nat. Rev. Chem. **4**, 490–504 (2020).

[60]J. M. Zadrozny et al., 'Millisecond Coherence Time in a Tunable Molecular Electronic Spin Qubit', ACS Cent. Sci. **9**, 488–492 (2015).

[61]A. Ardavan et al., 'Will Spin-Relaxation Times in Molecular Magnets Permit Quantum Information Processing?', Phys. Rev. Lett. **98**, 057201 (2007).

[62]E. Moreno-Pineda and W. Wernsdorfer, 'Measuring molecular magnets for quantum technologies', Nat. Rev. Phys. **3**, 645–659 (2021).

[63]G. Aromí et al., 'Design of magnetic coordination complexes for quantum computing', Chem. Soc. Rev. **41**, 537–546 (2012).

[64]K. Bader et al., 'Room temperature quantum coherence in a potential molecular qubit', Nat. Commun. **5**, 5304 (2014).

[65]R. L. Orbach, 'On the Theory of Spin-Lattice Relaxation in Paramagnetic Salts', Proc. Phys. Soc. **77**, 821–831 (1961).

[66]S. Gómez et al., 'Origin of slow magnetic relaxation in Kramers ions with nonuniaxial anisotropy', Nat. Commun. **5**, 4300 (2014).

[67]S. G. McAdams, 'Molecular single-ion magnets based on lanthanides and actinides: design considerations and new advances in the context of quantum technologies', Coord. Chem. Rev. **346**, 216–239 (2017).

[68]C. E. Jackson et al., 'A reaction-coordinate perspective of magnetic relaxation', Chem. Soc. Rev. **50**, 6684–6699 (2021).

[69]M. Shiddiq et al., 'Enhancing coherence in molecular spin qubits via atomic clock transitions', Nature **531**, 348–351 (2016).

[70]E. Coronado, 'Molecular magnetism: from chemical design to spin control in molecules, materials and devices', Nat. Rev. Mater. **5**, 87–104 (2020).

[71]S. Baumann et al., 'Electron paramagnetic resonance of individual atoms on a surface', Science **350**, 417–420 (2015).

[72]F. H. Cho et al., 'A continuous-wave and pulsed X-band electron spin resonance spectrometer operating in ultra-high vacuum for the study of low dimensional spin ensembles', Rev. Sci. Instrum. **95**, 063904 (2024).

[73]B. Xiang and W. Xiong, 'Molecular Polaritons for Chemistry, Photonics and Quantum Technologies', Chem. Rev. **124**, 25841–25851 (2024).

[74]S. C. Yelishala et al., 'Phonon interference in single-molecule junctions', Nat. Mater. **24**, 1258–1264 (2025).

[75]Y. Gu et al., 'Resonance fluorescence of single molecules assisted by a plasmonic structure', Phys. Rev. B **81**, 193103 (2010).

[76]C. Bonizzoni et al., 'Coherent coupling between Vanadyl Phthalocyanine spin ensemble and microwave photons: towards integration of molecular spin qubits into quantum circuits', Scientific Reports **7**, 13096 (2017).

[77]M. D. Jenkins et al., 'A scalable architecture for quantum computation with molecular nanomagnets', Dalton Trans. **45**, 16857–16866 (2016).

[78]I. Gimeno et al., 'Enhanced Molecular Spin-Photon Coupling at Superconducting Nanoconstrictions', ACS Nano **14**, 8359–8366 (2020).

[79]Z. Zhang et al., 'Controllable Spin Switching in a Single-Molecule Magnetic Tunneling Junction', Nanoscale Res. Lett. **16**, 77 (2021).

[80]E. Moreno-Pineda and W. Wernsdorfer, 'Magnetic Molecules as Building Blocks for Quantum Technologies', Adv. Quantum Technol. **8**, 2300367 (2025).

[81]C. Godfrin et al., 'Operating Quantum States in Single Magnetic Molecules: Implementation of Grover's Quantum Algorithm', Phys. Rev. Lett. **119**, 187702 (2017).

[82]J. A. Mol et al., 'Graphene-porphyrin single-molecule transistors', Nanoscale **7**, 13181–13185 (2015).

[83]Q. Chen et al., 'Porphyrin-fused graphene nanoribbons', Nat. Chem. **16**, 1133–1140 (2024).

[84]I. Kassal et al., 'Simulating chemistry using quantum computers', Annu. Rev. Phys. Chem. **62**, 185–207 (2011).

[85]F. Shi et al., 'Single-protein spin resonance spectroscopy under ambient conditions', Science **347**, 1135–1138 (2015).

[86]I. Lovchinsky et al., 'Nuclear magnetic resonance detection and spectroscopy of single proteins using quantum logic', Science **351**, 836 (2016).

[87]S. Das et al., 'Observation of room-temperature polar skyrmions', Nature **568**, 368–372 (2019).

[88]K. F. Mak et al., 'Tightly bound trions in monolayer MoS_2', Nat. Mater. **12**, 207–211 (2013).

[89]P. C. Bunting et al., 'Magnetic bubble chambers and sub-GeV dark matter direct detection', Phys. Rev. D **95**, 095001 (2017).

[90]C. V. Topping et al., 'A.C. susceptibility as a probe of low-frequency magnetic dynamics', J. Phys.: Condens. Matter **31**, 014601 (2019).

[91]H. Choi and D. Englund, 'Ultrastrong magnetic light-matter interaction with cavity mode engineering', Commun. Phys. **6**, 105 (2023).

[92]D. Alesini, 'Power Coupling', in CERN Accelerator School: Course on RF for Accelerators, Available at: `https://arxiv.org/abs/1112.3201` (Accessed: 02 December 2025), (2011).

[93]M. Tseitlin et al., 'Combining absorption and dispersion signals to improve signal-to-noise for rapid-scan EPR imaging', J. Magn. Reson. **203**, 305–310 (2010).

[94]J. A. Weil, J. R. Bolton and J. E. Wertz, *Electron Paramagnetic Resonance: Elementary Theory and Practical Applications*, 2nd ed. (John Wiley & Sons, 1994).

[95]D. Schmalbein et al., 'The Bruker high-frequency-EPR system', Appl. Magn. Reson. **16**, 185–205 (1999).

[96]D. L. Goodwin et al., 'Feedback control optimisation of esr experiments', J. Magn. Reson. **297**, 9–16 (2018).

[97]P. Krantz et al., 'A quantum engineer's guide to superconducting qubits', App. Phys. Rev. **6**, 021318 (2019).

[98]S. W. Jolin et al., 'Calibration of mixer amplitude and phase imbalance in superconducting circuits', Rev. Sci. Instrum. **91**, 124707 (2020).

[99]N. Aslam et al., 'Quantum sensors for biomedical applications', Nat. Rev. Phys. **5**, 157–169 (2023).

[100]C. Degen et al., 'Quantum Sensing', Rev. Mod. Phys. **89**, 035002 (2017).

[101]Z. Qiu et al., 'Nuclear spin assisted magnetic field angle sensing', npj Quantum Inf. **7**, 39 (2021).

[102]M. Bal et al., 'Ultrasensitive magnetic field detection using a single artificial atom', Nat. Commun. **3**, 1324 (2012).

[103]D. Schäffner et al., 'Quantum sensing in tweezer arrays: optical magnetometry on an individual-atom sensor grid', PRX Quantum **5**, 010311 (2024).

[104]C. Fancher et al., 'Rydberg atom electric field sensors for communications and sensing', IEEE Trans. Electron Devices **2**, 3501313 (2020).

[105]J. Yoo et al., 'Trapped-ion based nanoscale quantum sensing', Nano Converg. **12**, 12 (2025).

[106]S. Danilin et al., 'Quantum sensing with tunable superconducting qubits: optimization and speed-up', New J. Phys. **26**, 103029 (2024).

[107]F. Troiani et al., 'Towards quantum sensing with molecular spins', J. Magn. Magn. Mater. **491**, 165534 (2019).

[108]Y.-H. Fang et al., 'Spin-electric coupling with anisotropy-induced vanishment and enhancement in molecular ferroelectrics', J. Am. Chem. Soc. **144**, 19 (2022).

[109]A. Cini et al., 'Electric control of magnetic exchange in a molecular spin triangle', Nat. Commun. **16**, 6564 (2025).

[110]S. Harvey et al., 'Photogenerated spin-correlated radical pairs: from photosynthetic energy transduction to quantum information science', J. Am. Chem. Soc. **38**, 15508–15529 (2021).

[111]B. Rugg et al., 'Photodriven quantum teleportation of an electron spin state in a covalent donor–acceptor–radical system', Nat. Chem. **11**, 981–986 (2019).

[112]L. Franca et al., 'Spiro donor–acceptor TADF emitters: naked TADF free from inhomogeneity caused by donor acceptor bridge bond disorder. Fast rISC and invariant photophysics in solid state hosts', J. Mater. Chem. C **10**, 1313 (2022).

[113]L. Franca et al., 'Donor, Acceptor, and Molecular Charge Transfer Emission All in One Molecule', J. Phys. Chem. Lett. **14**, 2764–2771 (2023).

[114]I. Lyskov and M. Marian, 'Climbing up the Ladder: Intermediate Triplet States Promote the Reverse Intersystem Crossing in the Efficient TADF Emitter ACRSA', J. Phys. Chem. C **121**, 21145–21153 (2017).

[115]H. Nakanotani et al., 'High-efficiency organic light-emitting diodes with fluorescent emitters', Nat. Commun. **5**, 4016 (2014).

[116]Z. Yang et al., 'Recent advances in organic thermally activated delayed fluorescence materials', Chem. Soc. Rev. **46**, 915–1016 (2017).

[117]Y. Tao et al., 'Thermally Activated Delayed Fluorescence Materials Towards the Breakthrough of Organoelectronics', Adv. Mater. **26**, 7931–7958 (2014).

[118]G. Meng et al., 'High-efficiency and stable short-delayed fluorescence emitters with hybrid long- and short-range charge-transfer excitations', Nat. Commun. **14**, 2394 (2023).

[119]N. Aizawa and R. J. Vázquez, 'Thermally Activated Delayed Fluorescence (TADF) Active Systems: Mechanism, Applications, and Future Directions', J. Phys. Chem. C **129**, 3359–3360 (2025).

[120]P. Atkins and R. Friedman, *Molecular Quantum Mechanics* (Oxford University Press, 2018).

[121]K. Nasu et al., 'A highly luminescent spiro-anthracenone-based organic light-emitting diode exhibiting thermally activated delayed fluorescence', Chem. Comm. **49**, 10385 (2013).

[122]V. Coropceanu et al., 'Charge-transfer electronic states in organic solar cells', Nat. Rev. Mater. **4**, 689–707 (2019).

[123]S. Richert, C. Tait and C. Timmel, 'Delocalisation of photoexcited triplet states probed by transient EPR and hyperfine spectroscopy', J. Magn. Reson. **280**, 103–116 (2017).

[124]F. Neese et al., 'The ORCA quantum chemistry program package', J. Chem. Phys. **152**, 224108 (2020).

[125]S. Stoll and A. Schweiger, 'EasySpin, a comprehensive software package for spectral simulation and analysis in EPR', J. Magn. Reson. **178**, 42–55 (2006).

[126]M. V. Vaganov et al., 'Chemical tuning of quantum spin-electric coupling in molecular magnets', Nat. Chem. **17**, 1903–1909 (2025).

[127]A. J. Redman et al., 'EPR of Photoexcited Triplet-State Acceptor Porphyrins', J. Phys. Chem. C **125**, 11782–11790 (2021).

[128]N. R. Armstrong et al., 'Interface modification of ito thin films: organic photovoltaic cells', Thin Solid Films **445**, 342–352 (2003).

[129]R. E. George et al., 'Coherent Spin Control by Electrical Manipulation of the Magnetic Anisotropy', Phys. Rev. Lett. **110**, 027601 (2013).

[130]J. M. Song et al., 'Exploring Spin-Electric Coupling in an Electrically-Controlled Rare-Earth Molecular Qubit', Angew. Chem. **64**, e202513081 (2025).

[131]M. Boamfa et al., 'Magnetic field alignment of liquid crystals for fast display applications', Adv. Mater. **17**, 610 (2005).

[132]G. Stoclet et al., 'Strain-induced molecular ordering in polylactide upon uniaxial stretching', Macromolecules **43**, 1488 (2010).

[133]S. Bayliss et al., 'Optically addressable molecular spins for quantum information processing', Science **370**, 1309–1312 (2020).

[134]D. Laorenza et al., 'Tunable Cr^{4+} molecular color centers', J. Am. Chem. Soc. **143**, 21350–21363 (2021).

[135]L. R. Weiss et al., 'A high-resolution molecular spin-photon interface at telecommunication wavelengths', Science **390**, 76–81 (2025).

[136]K. R. Mullin et al., 'Quantum sensing of magnetic fields with molecular color centers', Phys. Rev. Res. **5**, L042023 (2023).

[137]K. R. Mullin et al., 'Electric field sensitivity of molecular color centers', Appl. Phys. Lett. **125**, 144004 (2024).

[138]Y.-K. Qu et al., 'Spiro Compounds for Organic Light-Emitting Diodes', Acc. Mater. Res. **2**, 1261–1271 (2021).

[139]J. J. L. Morton et al., 'Solid-state quantum memory using the ^{31}p nuclear spin', Nature **455**, 1085–1088 (2008).

[140]A. J. Campanella et al., 'Quantum Mimicry With Inorganic Chemistry', Comments Inorg. Chem. **44**, 11–53 (2024).

[141]S. Lim et al., 'Demonstrating experimentally the encoding and dynamics of an error-correctable logical qubit on a hyperfine-coupled nuclear spin qudit', Phys. Rev. Lett. **134**, 070603 (2025).

[142]R. Dixon and N. Bloembergen, 'Electrically induced perturbations of halogen nuclear quadrupole interactions in polycrystalline compounds. II. Microscopic theory', J. Chem. Phys. **41**, 1739–1747 (1964).

[143]J. J. Pla et al., 'High-fidelity readout and control of a nuclear spin qubit in silicon', Nature **496**, 334–338 (2013).

[144]B. Joecker et al., 'Error channels in quantum nondemolition measurements on spin systems', Phys. Rev. B **109**, 085302 (2024).

[145]I. Fernández de Fuentes et al., 'Navigating the 16-dimensional Hilbert space of a high-spin donor qudit with electric and magnetic fields', Nat. Commun. **15**, 1380 (2024).

[146]A. Hausmann and H. Huppertz, 'Paramagnetic resonance of ZnO:Mn^{++} single crystals', J. Phys. Chem. Solids **29**, 1369 (1968).

[147]R. Böttcher et al., '^{55}Mn pulsed ENDOR spectroscopy of Mn^{2+} ions in ZnO thin films and single crystal', J. Magn. Reson. **245**, 79 (2014).

[148]K. V. Narasimhulu et al., 'Single Crystal ^{55}Mn ENDOR of Concanavalin A: Detection of Two Mn^{2+} Sites with Different ^{55}Mn Quadrupole Tensors', J. Am. Chem. Soc **129**, 5391–5402 (2007).

[149]I. Tkach et al., '^{1}H High-Field Electron-Nuclear Double Resonance Spectroscopy at 263 GHz/9.4 T', J. Magn. Reson. **303**, 17–27 (2019).

[150]Y. Wang et al., 'Qudits and High-Dimensional Quantum Computing', Front. Phys. **8**, 589504 (2020).

[151]D. Janković, J.-G. Hartmann, M. Ruben and P.-A. Hervieux, 'Noisy qudit vs multiple qubits: conditions on gate efficiency for enhancing fidelity', npj Quantum Inf. **10**, 59 (2024).

[152]S. Ivanov et al., 'Time-efficient implementation of quantum search with qudits', Phys. Rev. A **85**, 062321 (2012).

[153]S. Pirandola et al., 'Minimal qudit code for a qubit in the phase-damping channel', Phys. Rev. A **77**, 032309 (2008).

[154]S. Lim et al., 'Fault-tolerant qubit encoding using a spin-7/2 qudit', Phys. Rev. A **108**, 062403 (2023).

[155]P. W. Shor, 'Algorithms for quantum computation: discrete logarithms and factoring', Proceedings 35th Annual Symposium on Foundations of Computer Science, 124–134 (1994) `10.1109/sfcs.1994.365700`.

[156]A. Y. Kitaev, *Quantum measurements and the Abelian stabilizer problem*, (1996) `https://eccc.weizmann.ac.il/report/1996/003/`.

[157]J. A. Jones et al., 'Quantum Logic Gates and Nuclear Magnetic Resonance Pulse Sequences', J. Magn. Reson. **135**, 353–360 (1998).

[158]G. Wolfowicz et al., 'Conditional Control of Donor Nuclear Spins in Silicon Using Stark Shift', Phys. Rev. Lett. **113**, 157601 (2014).

[159]A. Noiri et al., 'Fast universal quantum gate above the fault-tolerance threshold in silicon', Nature **601**, 338–342 (2022).

[160]N. Huet et al., 'Isotope shifts and hyperfine structure of the laser-cooling Fe I 358-nm line', Phys. Rev. A **92**, 052507 (2015).

[161]W. M. Walsh and L. J. Rupp, 'Paramagnetic Resonance of Trivalent Fe^{57} in Zinc Oxide', Phys. Rev. **126**, 952 (1962).

[162]S. Shokhovets et al., 'Spectroscopic Ellipsometry of Wurtzite ZnO and GaN: Examination of a Special Case', J. Appl. Phys. **107**, 023509 (2010).

[163]J. Haak et al., 'X-Band Parallel-Mode and Multifrequency Electron Paramagnetic Resonance Spectroscopy of $S = 1/2$ Bismuth Centers', Inorg. Chem. **61**, 11173–11181 (2022).

[164]S. Piligkos et al., 'Single-crystal parallel-mode EPR spectroscopy of an $S = 6$ ground-state transition-metal cluster', Phys. Rev. B **69**, 134424 (2004).

[165]R. Steward et al., 'Engineering Clock Transitions in Molecular Lanthanide Complexes', J. Am. Chem. Soc. **146**, 11083–11094 (2024).

[166]A. Sarkar and G. Rajaraman, 'Modulating magnetic anisotropy in Ln(III) single-ion magnets using an external electric field', Chem. Sci. **11**, 10324–10330 (2020).

[167]S. Reale et al., 'Electrically driven spin resonance of 4f electrons in a single atom on a surface', Nat. Commun. **15**, 5289 (2024).

[168]J.-L. Du et al., 'Electron Spin Relaxation in Vanadyl, Copper(II), and Silver(II) Porphyrins in Glassy Solvents and Doped Solids', J. Magn. Reson., Ser. A **119**, 240 (1996).

[169]A.-J. Fielding et al., 'Electron spin relaxation of copper(II) complexes in glassy solution between 10 and 120 K', J. Magn. Reson., Ser. A **179**, 92–104 (2006).

[170]A.-M. Ariciu et al., 'Engineering electronic structure to prolong relaxation times in molecular qubits by minimising orbital angular momentum', Nat. Commun. **10**, 3330 (2019).

[171]M. J. Graham et al., 'Influence of Electronic Spin and Spin–Orbit Coupling on Decoherence in Mononuclear Transition Metal Complexes', J. Am. Chem. Soc. **136**, 21 (2014).

[172]D. L. McAuslan et al., 'Reducing decoherence in optical and spin transitions in rare-earth-metal-ion–doped materials', Phys. Rev. A **85**, 032339 (2012).

[173]G. Wolfowicz et al., 'Atomic clock transitions in silicon-based spin qubits', Nat. Nanotechnol. **8**, 561–564 (2013).

[174]D. Vion et al., 'Manipulating the Quantum State of an Electrical Circuit', Science **145**, 886–88 (2002).

[175]M. AlDamen et al., 'Mononuclear lanthanide single molecule magnets based on the polyoxometalates $[Ln(W_5O_{18})_2]^{9-}$ and $[Ln(\beta\text{-}SiW_{11}O_{39})_2]^{13-}$', Inorg. Chem. **48**, 3467–3479 (2009).

[176]S. Ghosh et al., 'Multi-frequency EPR studies of a mononuclear holmium single-molecule magnet based on the polyoxometalate $[Ho(W_5O_{18})_2]^{9-}$', Dalton Trans. **41**, 13697–13704 (2012).

[177]S. Gimenez-Santamarina et al., 'Exploiting clock transitions for the chemical design of resilient molecular spin qubits', Chem. Sci. **11**, 10718–10728 (2020).

[178]K. Kundu et al., 'Electron-nuclear decoupling at a spin clock transition', Comm. Phys. **6**, 38 (2023).

[179]A. Ullah et al., 'Electrical two-qubit gates within a pair of clock-qubit magnetic molecules', npj Quantum Inf. **8**, 133 (2022).

[180]M. J. Martínez-Pérez et al., 'Gd-based single-ion magnets with tunable magnetic anisotropy: molecular design of spin qubits', Phys. Rev. Lett. **108**, 247213 (2012).

[181]T. Rosenband et al., 'Observation of the $^1S_0 \rightarrow^3 P_0$ clock transition in $^{27}Al^+$', Phys. Rev. Lett. **98**, 220801 (2007).

[182]C. A. Collett et al., 'Constructing clock-transition-based two-qubit gates from dimers of molecular nanomagnets', Phys. Rev. Res. **2**, 032037 (2020).

[183]K. S. Pedersen et al., 'Toward Molecular 4f Single-Ion Magnet Qubits', J. Am. Chem. Soc. **138**, 18 (2016).

[184]R. Hussain et al., 'Coherent Manipulation of a Molecular Ln-Based Nuclear Qudit Coupled to an Electron Qubit', J. Am. Chem. Soc. **140**, 31 (2018).

[185]B. E. Bode et al., 'Dipolar-Coupled Entangled Molecular 4f Qubits', J. Am. Chem. Soc. **145**, 5 (2023).

[186]I. Pietikäinen et al., 'Observation of the Bloch-Siegert shift in a driven quantum-to-classical transition', Phys. Rev. B **96**, 020501 (2017).

[187]D. Ganyushin and F. Neese, 'A fully variational spin-orbit coupled complete active space self-consistent field approach: application to electron paramagnetic resonance g-tensors', J. Chem. Phys. **138**, 104113 (2013).

[188]C. Adamo and D. Jacquemin, 'The calculations of excited-state properties with time-dependent density functional theory', Chem. Soc. Rev. **42**, 845–856 (2013).

[189]S. Sinnecker and F. Neese, 'Spin-Spin Contributions to the Zero-Field Splitting Tensor in Organic Triplets, Carbenes and Biradicalss: A Density Functional and Ab Initio Study', J. Phys. Chem. A **110**, 12267–12275 (2006).

[190]O. Vahtras et al., 'Ab initio calculations of zero-field splitting parameters', Chem. Phys. **279**, 133–142 (2002).